“Strategic Association of Aqueous/Non-aqueous Liquid Wettability to Derive Functional Materials/Interfaces”

A thesis submitted by

Saurav Kumar
Roll No. 196122029

In Partial Fulfilment of the Requirements
for the Degree of
Doctor of Philosophy

Department of Chemistry
Indian Institute of Technology Guwahati
Guwahati - 781039
Assam, India

31st July 2025

Dedicated to

My Parents

Indian Institute of Technology Guwahati

Department of Chemistry

Statement

I hereby declare that the work comprised in the thesis entitled **"Strategic Association of Aqueous/Non-aqueous Liquid Wettability to Derive Functional Materials/Interfaces"** is the result of investigations carried out by me in the Department of Chemistry, under the supervision of Prof. Uttam Manna, Professor, Department of Chemistry, Indian Institute of Technology Guwahati, Guwahati, Assam, India.

Research materials used in this thesis from any other sources have been fully cited and acknowledged. This work is original and has not been submitted elsewhere for the award of any degree.

Saurav Kumar

31st July, 2025
IIT Guwahati

Saurav Kumar
Roll No.- 196122029

Indian Institute of Technology Guwahati

Department of Chemistry

CERTIFICATE

This is to certify that the work presented in the thesis entitled **“Strategic Association of Aqueous/Non-aqueous Liquid Wettability to Derive Functional Materials/Interfaces”** by Saurav Kumar, a Ph.D. student of Department of Chemistry, Indian Institute of Technology Guwahati, for the award of degree of Doctor of Philosophy has been carried out under my supervision and this work has not been submitted elsewhere for any degree.

Uttam Manna

31st July, 2025

Prof. Uttam Manna
Thesis Supervisor
Department of Chemistry
Indian Institute of Technology Guwahati
Guwahati - 781039
Assam, India

Acknowledgements

First and foremost, I would like to express my deepest gratitude to my supervisor, Prof. Uttam Manna, for his exceptional guidance, unwavering encouragement, and insightful advice throughout my Ph.D. program. His profound knowledge, thoughtful mentorship, and constant support have been instrumental in shaping both my research and personal growth. I consider myself truly fortunate to have had the opportunity to work under his supervision. This work would not have been possible without his invaluable suggestions, and I could not have asked for a more inspiring mentor and advisor.

I extend my sincere gratitude to the members of my doctoral committee Prof. Gopal Das (Chairman), Prof. Aditya Narayan Panda, Prof. Kalyan Raidongia and Dr. Kalishankar Bhattacharyya for their insightful suggestions, constructive critiques and invaluable guidance, which significantly enhanced the quality of this thesis. I am equally thankful to all the faculty members of the Department of Chemistry, IIT Guwahati, for their constant support and encouragement. I would like to thank Dr. Mizuki Tenjimbayashi, Prof. Debasis Manna, and Prof. Biman B. Mondal for their advice and assistance in the collaborative work. I gratefully acknowledge the Central Instruments Facility (CIF), IIT Guwahati, for access to various characterization facilities that played a crucial role in my experimental work. I would like to thanks my special teacher Neeraj Kumar for their inspiring teaching, supportive guidance, and continuous motivation, which laid a strong foundation for higher studies.

It has been a truly a new experience to learn and carry out research in the Bioinspired Polymeric Materials Laboratory at IIT Guwahati. Over time, this lab became a second home to me, not only because of the exciting scientific work but also due to the presence of many wonderful individuals who made each moment special and memorable. I am deeply grateful to all my labmates, Dr. Adil Majeed Rather, Dr. Dibyangana Parbat, Dr. Avijit Das, Dr. Kousik Maji, Dr. Arpita Shome, Dr. Supriya Das, Dr. Angana Borbara, Dr. Manideepa Dhar, Dr. Upama Baruah, Dr, Hayder Ali, Dr. Samiran Morang, Dr. Susanta Dinda, Nirban Jana, Nishanta Barman, Debasmita Sarkar, Jaishri Das, Hrishikesh Sarma, Chittranjan Mishra, Madhav Dwivedi, Pritam Giri, Ajoy Chand and Sumit Sarkar for fostering a warm, collaborative, and motivating environment. Their companionship and support have made my journey both enjoyable and fulfilling. I also extend my sincere appreciation to the project students, Karan Jain, Priyam Mondal, Pritha Bhattacharyya and Akash Bose for their valuable assistance in various experiments during my research.

I will always cherish the joyful memories shared with Tumapa Manna Jana and Irsia Manna, whose warmth and presence added so much meaning to my journey. I am also deeply thankful to my friends, Sidharth Senapati, Mongoli Brahma, Anita Chanu, Anjali Roy, Sinchini Barman, Nandan Roy, Prachuryya Kaushik, Vikas Vinjamoori, Rahul Kumar, Madhav Dwivedi, Hrishikesh Sarma, Mukesh Kumar, Vipul Vaibhav, Valmiki Kumar, Priyam Ghosh and Santanu Mandal and for their companionship, unwavering support, and for filling my time at IIT Guwahati with laughter, unforgettable moments, and lasting friendships. Their presence made my stay truly memorable and enriching. I am highly thankful to my home's friends like Prashant Bhusan Mishra, Ajay Kumar, Deepak Kumar, Preeti Mishra, without whom my life would have been incomplete.

Finally, this Ph.D. journey would not have been possible without the boundless love, unwavering support, patience, and prayers of my family. I am deeply honoured and sincerely grateful to each of them for standing by me through every step of this endeavour. Their constant encouragement gave me the strength to persevere during the most challenging times. I feel truly fortunate and blessed to have such loving and supportive parents, Mr. Ramjee Prasad and Mrs. Sita Devi. It is their sacrifices, tireless efforts, and heartfelt prayers that have made it possible for me to pursue and fulfil my dream of completing PhD in IIT Guwahati. My heartfelt thanks also go to my younger sister, Sima Kumari, and my younger brother, Sonu Prakash, whose unconditional love, emotional strength, and cooperation were invaluable throughout this journey.

I want to thank my wife, Mrs. Geetanjali, for his constant love and support throughout this journey and in every part of my life. Thank you for always being there for me, listening patiently, encouraging me, and helping me in every possible way.

Saurav Kumar
31st July 2025

Abbreviation

SEM	Scanning electron microscope
FESEM	Field emission Scanning electron microscope
SHP	Superhydrophobic
SHS	Superhydrophobic surfaces
CA	Contact angles
WCA	water contact angles
SCA	Static contact angles
CAH	Contact angle hysteresis
SLIPS	Slippery liquid-infused porous surfaces
SA	Sliding angles
CNF	Cellulose nanofibers
OTS	Octadecyltrichlorosilane
PU	Polyurethane
PAL	Palygorskite
MTMS	Methyltrimethoxysilane
SiO_2	Silicon dioxide
HD-POS	Hexadecyl-polysiloxane
LMs	Liquid marbles
PDEA	Poly 2-(diethylamino)ethyl methacrylate
DHSA	9,10-Dihydroxy stearic acid
BFI	1-bromo-3-fluoro-4-iodobenzene
PNIPAM	Poly (N-isopropyl acrylamide)
LCST	Lower critical solution temperature
GLM	Graphene liquid marble
MOF	Metal-organic framework
BMA	Butyl methacrylate
EDMA	Ethylene dimethacrylate
PS	Polystyrene

TiO_2	Titanium dioxide
DMF	Dimethylformamide
PTFE	Polytetrafluoroethylene
$ZrCl_4$	Zirconium tetrachloride
NIR	Near-infrared
TO-SHS	Titanium dioxide embedded superhydrophobic surfaces
HP side	Hydrophobic side
HL side	Hydrophilic side
PET	Polyethylene terephthalate
CPHA	Cation-π hydrophilic agent
CF	Cotton fabric
JCF	Janus cotton fabric
PCF	Pattern cotton fabric
BN	Boron Nitride
SDS	Sodium dodecyl sulphate
FETEM	Field emission transmission electron microscope
NMR	Nuclear magnetic resonance
XRD	X-ray powder diffraction
XPS	X-ray photoelectron spectroscopy
FTIR-ATR	Fourier transform infrared attenuated total reflectance spectra
H_2ATA	2-Aminoterephthalate
$FeCl_3$	Iron (III) chloride
KSCN	Potassium thiocyanate
DMSO-d_6	deuterated dimethyl sulfoxide
CR-MOF	Chemically reactive metal-organic framework
3-Acl	Trimethylolpropane triacrylate
DA	Decyl amine
OA	Octyl amine
HA	Hexyl amine
PA	Pentyl amine

BA	Butyl amine
ODA	Octadecyl amine
ODAc	Octadecyl acrylate
OAc	Octyl acrylate
HAc	Hexyl acrylate
BAc	Butyl acrylate
$Fe(SCN)_3$	Iron (III) thiocyanate
NO_2^-	Nitrite ion
PODAc	Poly(octadecylacrylate)
DMSO	Dimethyl sulfoxide
DCS	Differential scanning calorimeter
HT-GPC	High-temperature gel permeation chromatography
AFM	Atomic force microscope
GMA	Glycidyl methacrylate
PGMA	Poly Glycidyl methacrylate
CRNC	Chemically reactive nano complex
FITC	Fluorescein isothiocyanate
TMRC	Tertramethylrhodamine cadaverine
FBS	Fetal bovine serum
NBF	Neutral buffer formalin
BSA	Bovine serum albumin
BPEI	Branched poly(ethyleneimine)
5-Acl	Dipentaerythritolpenta-acrylate
NaCl	Sodium Chloride
$MgSO_4$	Magnesium sulphate
$MgCl_2$	Magnesium chloride
$CaCl_2$	Calcium chloride
DTAB	(1-dodecyl)trimethylammonium bromide
LM	Leachate medium
HDF	Human dermal fibroblast

CCM	Cell culture medium
MTT	Thiazolyl blue tetrazolium bromide
PBS	Phosphate-buffered saline
JT	Janus textile
PT	Patterned textile
P_{Lap}	Laplace pressure
PDMS	Polydimethylsiloxane
DMAP	4-(dimethylamino)pyridine
EDC	1-(3-dimethylaminopropyl)3-ethylcarbodiimide hydrochloride
DCM	Dichloromethane
CH_3CN	Acetonitrile
HRMS	High-resolution mass spectra
APTES	(3-aminopropyl)triethoxysilane
RM	Reaction mixture
NP	Nanoparticle
DLS	Dynamic light scattering
DI	Distilled
SA	Sliding angle
PMMA	Poly (methyl methacrylate)
PC	Polycarbonate
MF	Melamine Foam

Abstract:

Nature-inspired anti-wettable material, like superhydrophobic coating, liquid marble, pattern interface with contrast of wettability and slippery surfaces, have shown immense potential for their wide range of applications—including self-cleaning, water harvesting, environmental remediation, and so on. In this relevance, significant strides have been made in replicating the wettability present in natural materials like lotus leaf, desert beetle, rice leaf, honeydew, nepenthes pitcher plants and so on. However, further design of such materials with their improved shelf-life, tolerance under harsh environmental conditions, better resistance to mechanical abrasion, following environment friendly fabrication process is essential for its advancement. Here, in this synopsis report, I have accounted the strategic use of facile chemistry (i.e., 1,4-conjugate addition and water based amidation reaction), reactive small molecules and crystalline polymer for developing functional coating as materials to demonstrate on-demand release of liquid, droplet chemistry, antigravity liquid transport, self-cleaning etc. The content of this synopsis report is comprises of six chapters. **Chapter 1** provides a brief overview of bio-inspired liquid wettability, explores the common techniques used to create different artificial anti-wetting surfaces, highlights existing relevant challenges, and outlines this thesis work's objectives. **Chapter 2** demonstrates the post-modification of porous and reactive crystalline material (MOFs) with selected alkyl amines through 1,4-conjugate addition reaction to tailor the liquid wettability from hydrophobic to superhydrophobic. It allowed to develop liquid marble for on-demand and customized release of the inner liquid in the presence of different pH of water pool. In **Chapter 3,** I have introduced omniphobic capsules/colloidosomes from crystalline and hydrophobic comb-polymer to prevent loss of inner liquid because of surface adhesion and evaporation of encapsulated volatile liquid. **Chapter 4** accounts for the fabrication of chemically reactive superhydrophobic polymeric coating on a textile to develop chemically modulated wettability pattern for antigravity water transport. **Chapter 5** introduces a completely waterborne, highly transparent, abrasion-tolerant and substrate-independent solid slippery and superhydrophobic interface through an amidation reaction between thioester and aminosilane. **Chapter 6** provides a concise summary and the future directions of the work presented here.

Chapter 1. Introduction

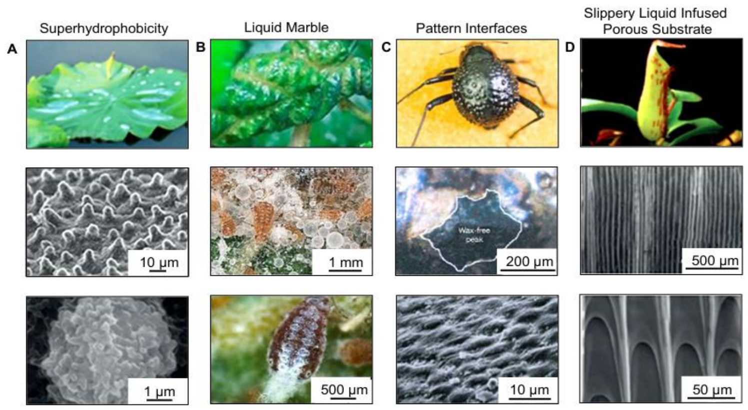

Figure 1. A-D) Digital images and field emission scanning electron microscopy images of various natural species including lotus leaf (A) Aphids on gall leaf (B) Desert bettle (C) and Nepenthes pitcher plant (D). Figure 1.1A, D is adapted with permission from *Nat. Rev. Mater.*, 2017, **2**, 17036. Macmillan Publishers Limited, Copyright 2017. Figure 1.1B is adapted from *Langmuir*, 2019, **35**, 6169-6178. American Chemical Society, Copyright 2019. Figure 1.1C is adapted from *Nature.*, 2001, **14**, 33-34. Springer Nature Limited, Copyright 2001.

Nature-inspired materials have received great attention from scientists and engineers due to their unique properties. Many natural plants and creatures embedded with special features have influenced the development of innovative materials and technologies. For example, lotus leaf, aphids on gall leaves, desert beetle, nepenthes pitcher plant, (Figure 1) etc. exhibit excellent antiwetting property. Such natural species offer new understandings to the design of artificial superhydrophobic surfaces, liquid marble, patterned interfaces and slippery surfaces. Lotus leaf surfaces exhibit superhydrphobicity due to the existence of micro/nano hierarchical structures and low surface energy coating of epiticular wax. It displayed a very high water contact angle (>150°) and low contact angle hysteresis (<10°). This phenomenon is explained by the Cassie-Baxter model. According to this wettability model, air gets trapped within the grooves of the microporous structure, creating an air pocket and contributes to heterogeneous liquid wettability. When a water droplet beads on and contacts the rough solid surface, it restricted access to rough solid surface due to the third phase i.e., meta stable trapped air, results in extreme water repellence. In the past, various artificial superhydrophobic surfaces have been developed and used in different prospective applications including self-cleaning, oil/water separation, anti-corrosion, anti-icing, etc. On the other side, in a seminal report, Aussillous and Quére introduced a functional soft material, called liquid marbles from superhydrophobic powder, i.e., lycopodium grains. It exhibits non-stick properties on solid and liquid surfaces due to the presence of superhydrophobic solid particles around the liquid droplets. Since the first ground-breaking report on liquid marble in 2001, numerous exciting studies have been reported in the literature. Their unique properties, such as non-wetting, deformability, and controlled permeability, make them valuable in various applications, including chemical sensing, drug delivery, miniaturized chemical reaction, etc. Different types of materials including silica nanoparticles, graphene, carbon black, carbon nanotubes, polytetrafluoroethylene particles, polymeric particles, metal oxide nanoparticles, porous crystalline nanoparticles are utilized to prepare such soft materials. While the hydrophobic shell of liquid marble provides a protective environment, but the on-demand release of inner liquid is essential for various other prospective applications. In the past, different approaches were introduced to demonstrate the instant release of inner liquid in the presence of a specific stimulus with acidic, alkaline, light, heat, etc., but reports on controlling the lifetime of floating liquid marbles on water pool in the presence of a stimulus are extremely rare in the literature. On the other side, a porous shell of liquid marble fails to prevent evaporation of the encapsulated volatile liquid. In this context, different types of capsules or colloidosomes were introduced in the literature, but they often suffer from the inability to prevent adhesion, losses of inner liquid and on-demand release of inner liquid. In nature, another fascinating creature, the desert beetles, possess contrasting wettability (superhydrophobic and superhydrophilic) patterns on their back surfaces, which they utilize for efficient fog water collection. Inspired by the desert beetle, different superhydrophobic/superhydrophilic patterned interfaces were introduced in the literature. For example, Bai *et al.* used the spin coating method and selective UV light illumination to develop a superhydrophobic/superhydrophilic patterned interface with the help of hazardous fluorine chemistry. Later, researchers have shown significant interest in utilizing patterned interfaces with contrasting wettability for moisture management in addition to other applications, including microfluidics, self-cleaning surfaces, liquid manipulation, and so on. In the previous literature, mostly, noncontact patterning methods (UV-ray, plasma treatment, etc.) were spatially and selectively applied to perturb the hydrophobic chemical groups (e.g., fluorinated hydrocarbons) on hydrophobic/superhydrophobic interface to achieve patterned textile, however, controlled and uniform penetration of UV-radiation or plasma across the highly opaque fibrous substrate would be a challenging task to achieve. Thus, it is difficult to introduce wettability gradient with precision across the selected fibrous substrate. Low surface tension liquids, such as organic solvents, readily wet superhydrophobic interfaces by penetrating the micro-nano grooves of the rough solid surface. In general, antiwetting property for both low and high surface tension liquids through association of complex topography (i.e., re-entrant surface curvature) mostly topped with fluorinated chemical modifications. However, fabricating such intricate surface structures on a large scale presents significant challenges, and the use of fluorinated chemicals and organic solvent possesses environmental hazards. A new approach has been developed to overcome this limitation, drawing inspiration from the Nepenthes pitcher plant that displays an effortless sliding of beaded droplet of liquids. While significant advancements have been made in liquid-repellent interfaces, challenges related to durability still pose concerns over their potential real-world applications.

So, in this context, design of a complete water-borne, ultra-robust, highly transparent, lubrication-free dry slippery interface and superhydrophobic surface would be appropriate for prospective applications. To address above mentioned challenges, I have introduced different strategies to achieve i) adjustable and programmed release of inner liquid from liquid marble, ii) omniphobic colloidosome for no adhesion and evaporation loss of inner liquid and its on-demand release, iii) chemically controlled patterned textile for accelerated anti-gravity water

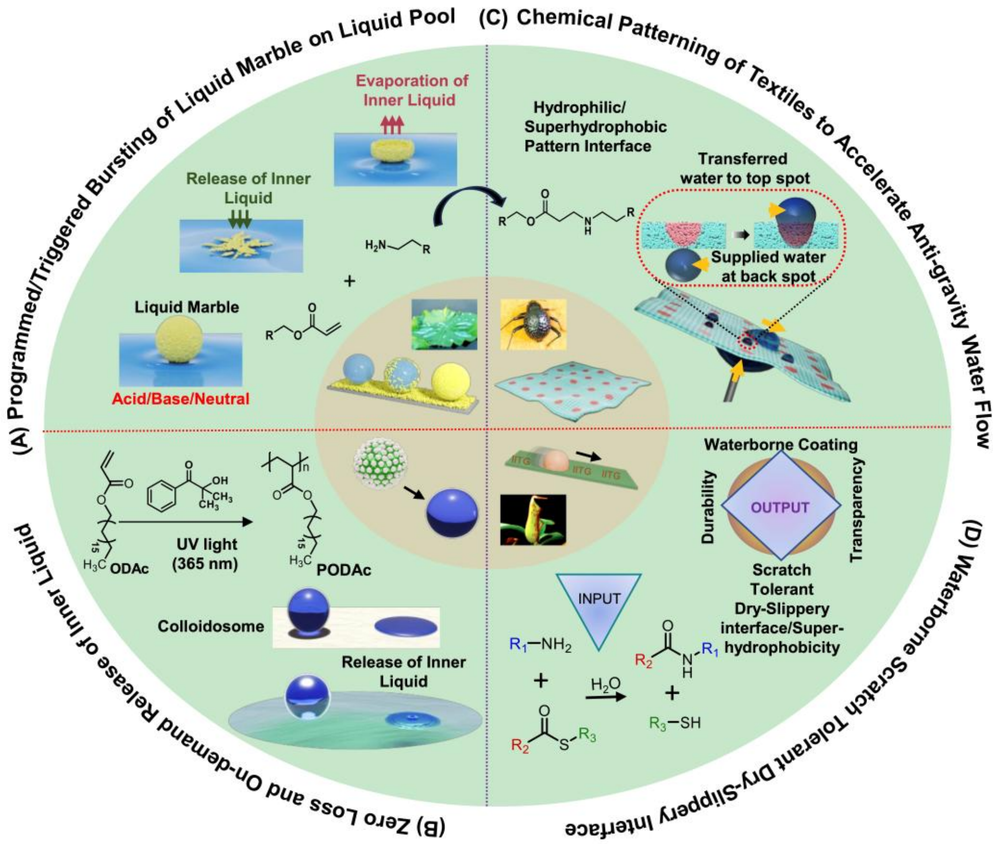

Figure 2: A) Schematic Illustrating the controlled bursting of LMs with adjustable release of the loaded liquid by modulating the lifetime of the prepared LMs. B) Scheme depicting zero loss and on-demand release of inner liquid from colloidosome on a solid surface and water pool upon heating. C) Schematic demonstrating the unidirectional transport of beaded droplets through patterned textiles against gravity. D) Schematic presentation of the designing of waterborne slippery and superhydrophobic coatings through an amidation reaction between amine and thioester groups.

transfer, and iv) water-borne, fluorine-free, durable and optically transfer, slippery and superhydrophobic coating as shown in Figure 2.

Chapter 2. pH-triggered Adjustable Bursting of Liquid Marbles in Water Pools

Non-sticking millimetric droplets wrapped with micron/submicron-sized liquid-repellent solid particles and aggregates are recognized as liquid marbles (LMs). LMs behave like a non-wetting solid, which enables zero-loss transportation on solid surfaces and liquid pools. The challenge is controlling the liquid-releasing behavior, especially on a liquid pool. For example, releasing the inner liquid of LMs at a specified time in adaptation to liquid pool conditions has not been achieved. In the past, different approaches were introduced to demonstrate the instant release of inner liquid in the presence of a specific stimulus, but reports on controlling the lifetime of floating LMs in the presence of a stimulus are extremely rare in the literature. In this chapter, I have strategically associated metal-organic framework and protonizable chemistry in combination with tailored hydrophobicity to design LMs enabling the stimulus-responsive adjustable "lifetime till breakage" on a water pool. In this context, the prepared NH_2-UiO-66 was subjected to covalently react with trimethylolpropane triacrylate (3-Acl) to achieve chemically reactive MOF (CR-MOF, Figure 3A and B). The residual acrylate reactivity of CR-MOF allowed its post-modification with selected alkyl amines, following a common and facile 1,4-conjugate addition reaction under ambient conditions (Figure 3B). Depending on the length of hydrocarbon tails in the selected alkyl (i.e., pentyl ($–C_5H_{11}$), hexyl ($–C_6H_{13}$), octyl ($–C_8H_{17}$) and decyl ($–C_{10}H_{21}$)) amine, the modified MOFs provided either dual (acid/alkaline)-responsive (pentyl, hexyl) or non-responsive (octyl, decyl) water repellence (hydrophobicity/superhydrophobicity). Covering the water droplet with such chemically modulated MOF (Figure 3C), we aimed to introduce a new class of responsive LMs that provides an automated (under neutral conditions) and adjustable (depending on the pH) triggered release of the inner liquid on the water pool, as shown in Figure 3D and E. The choice of chemical modulation decides the floating time of the same LM under acidic and alkaline conditions. Then, LMs were prepared from different amine-modified MOFs and placed on the water pool to examine their lifetime (Figure 3F–I). I found that the lifetime of the LMs drastically changed with the variation in the embedded hydrophobicity. In that, LMs derived from OA ($–C_8H_{17}$) or DA ($C_{10}H_{21}$) modified MOFs did not collapse, rather the inner liquid evaporated completely (Figure 3H and 3I), whereas LMs prepared from HA($–C_6H_{13}$) or PA($–C_5H_{11}$) modified MOFs collapsed with a lifetime of 2.8 or 1.2 hours (Figure 3F and 3G), respectively. Further, the lifetime of the same MOF-based LM is also varied in response to the water pool's pH (Figure 3J). However, the lifetime of the LM on water pools mostly depends on the chemical modification of the prepared CR-MOF with selected alkyl amines.

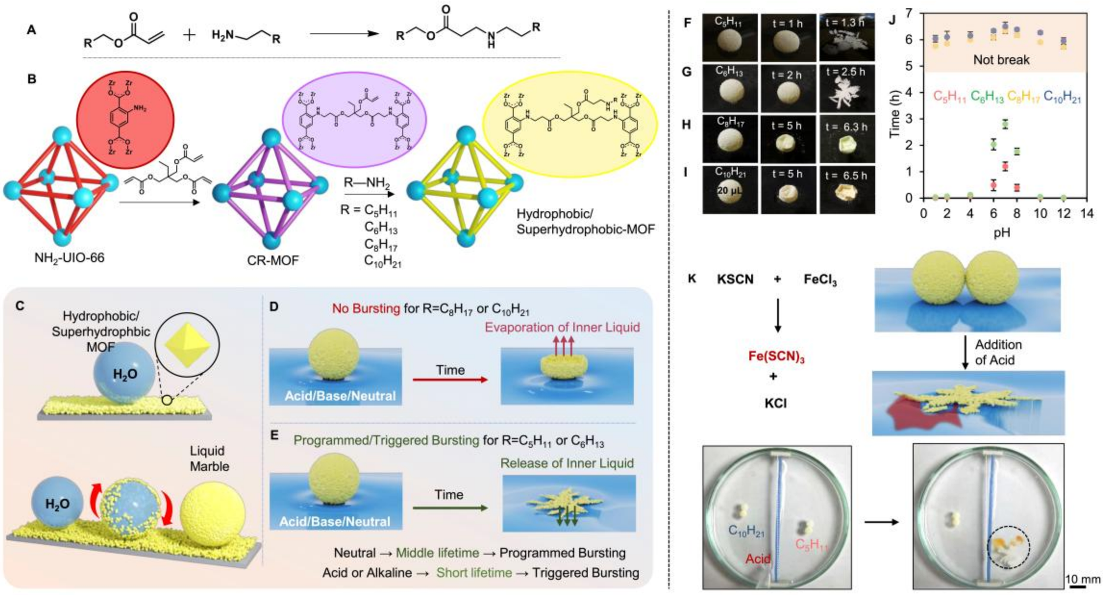

Figure 3: A) Illustrating a catalyst-free 1,4-conjugate addition reaction between amine and acrylate. B) Accounting the conversion of the prepared MOF (NH_2-UIO-66) into a chemically reactive MOF (CR-MOF), following the covalent modification with 3-Acl through the 1,4-conjugate addition reaction. The residual acrylate group in CR-MOF provided a facile basis for post-covalent modification with selected alkyl amines at ambient conditions to tailor water wettability (hydrophobicity and superhydrophobicity). C) Depicting the process of forming liquid marbles (LMs) by rolling the beaded water droplet on the pile of either hydrophobic or superhydrophobic MOFs. D) Schematic depicting the LMs prepared from hydrophobic MOFs displaying both programmed (moderate lifetime of liquid marble) and triggered release of the inner liquid at the water pool, without having any external intervention at neutral pH and in the presence of acidic/alkaline stimuli, respectively. E) Schematically depicting the LMs derived from superhydrophobic MOFs failing to release the inner liquid irrespective of the pH of the water pool, rather encapsulated water evaporated out from the LM. F-I) Digital images illustrating the buckling and bursting of LMs that were prepared from differently modified superhydrophobic (F and G) and hydrophobic (H and I) MOFs. J) Plot accounting for the stability of LMs at various pH values of the water pool. K) Demonstrating the triggered chemical reaction on the water pool in the presence of acidic stimuli by triggering release of mutually reactive reactants (ferric chloride and potassium thiocyanate) from the two LM prepared from hydrophobic MOFs. The formation of a ferric thiocyanate complex resulted in the appearance of red colour in the water pool. However, LMs that were prepared from superhydrophobic MOFs failed to release the encapsulated reactants under the identical setup. Published in *J. Mater. Chem. A*, 2024, **12**, 3362.

On the other side, the LMs prepared using differently modified MOFs did not collapse to release the inner liquid on a solid surface rather the encapsulated water evaporated over time, which resulted in the buckling of the prepared LMs. These phenomena could be used for demonstratingon demand chemical reactions on the water pool (Figure 3K). Thus, in this chapter, a porous and chemically reactive nanomaterial is developed for controlled and precise chemical modulation through a 1,4-conjugate addition reaction at ambient conditions to derive LMs embedded with tunable and adaptive wettability at different pH.

Chapter 3: Droplet Green Chemistry Using Thermally Shape-Reconfigurable Omniphobic Colloidosomes

A high-yield, lossless chemical reaction conducted under ambient conditions is promising for green chemistry. However, owing to the sticky feature of liquids on solid surfaces and the high volatility of useful primary solvents, "droplet chemistry" is far from practical use. Thus, a droplet platform that prevents both droplet evaporation and adhesion losses is promising. Here, in this present study, I report a versatile method for droplet encapsulation with superhydrophobic polymer powder, i.e. poly(octadecylacrylate) (PODAc; a thermoplastic solid-slippery polymer) based on the colloidosome technique. This process enabled the on-demand capsulation/extraction of various liquid droplets, regardless of their surface tension and volatility, without any loss. In this current design of thermally shape-reconfigurable omniphobic colloidosome, a thermoplastic comb-like polymer PODAc was synthesized by free-radical polymerization of octadecyl acrylate (ODAc) (Figure 4A) following previous report. The conversion of ODAc into PODAc was monitored by AT-FTIR analysis, as shown in Figure 4B, where the IR peak for vinylic C−H deformation of the acrylate moiety at 1407 cm^{-1} was significantly compromised with respect to another IR peak for stretching of carbonyl groups at 1720 cm^{-1} after free radical polymerization of ODAc. Next, the PODAc capsule was processed based on the "colloidosome" technique, which is depicted in Figure 4C, D. First, PODAc is ground to a powder state, possessing very low wettability to glycerol. Thus, PODAc powder is adsorbed on the droplet surface, forming a liquid marble instead of being dispersed in the glycerol droplet. Next, the liquid marble was heated locally by using NIR light to melt the PODAc powder around the glycerol droplet to form the PODAc shell. After that, the thermoresponsive property of the PODAc was strategically utilized to remove encapsulated glycerol from the PODAc shell by thermal poring. The glycerol was completely removed from the capsule due to its liquid-repellent feature. Then, target chemicals or solvents were filled into the empty PODAc capsule, which we term the PODAc colloidosome. Due to nanometrically smooth surface of PODAc, it displays omniphobicity. The PODAc shell is chemically stable to any commonly used solvent, which enables the encapsulation of various chemicals for a long time without any spillage (Figure 4E). The colloidosome retains its spherical shape even after decanting any target liquids, regardless of their volatility or surface tension (γ_{LV} = 17-72.8 mN m^{-1}).The sphericity of the PODAc is quantified with static contact angle θ (Figure 4F). Moreover, on-demand release of inner liquid of colloidosome was schematically depicted on the solid surface and liquid pool by applying either heating or NIR light as shown in Figure 4G, H.

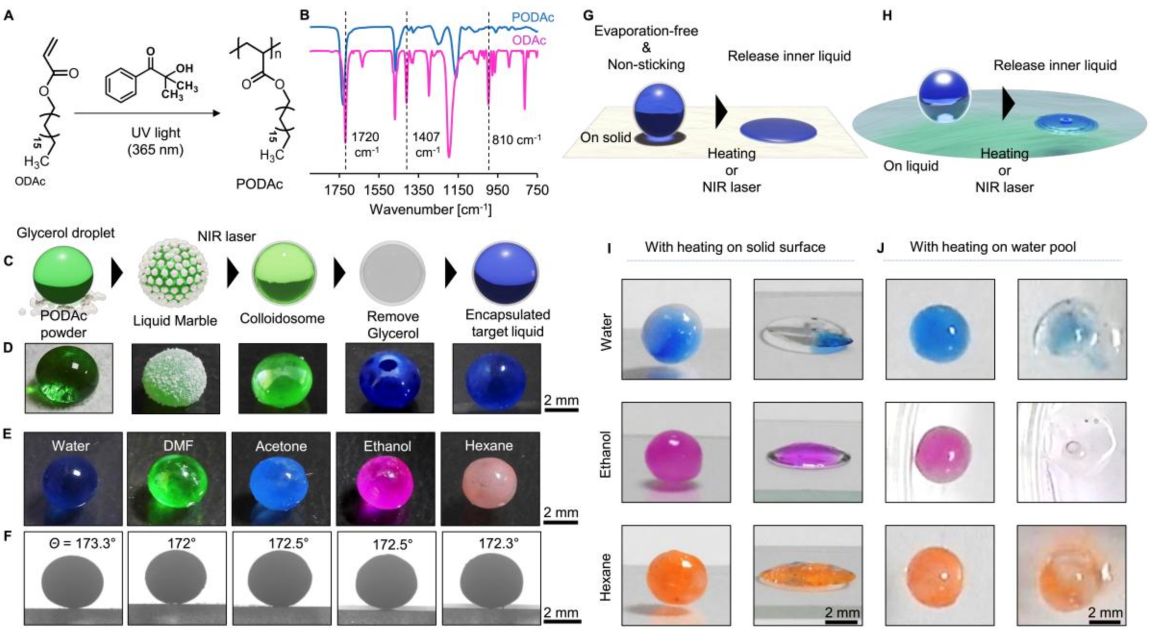

Figure 4: A) Reaction scheme representing the synthesis of polyoctadecyl acrylate (PODAc) through photopolymerization reaction of octadecyl acrylate (ODAc) in the presence of a photoinitiator. B) Attenuated total reflection-Fourier transform infrared (AT-FTIR) analysis of PODAc (blue) and ODAc (pink). C, D) Schematic and digital images depicting the process involved in preparing a colloidosome (volume = 20 μL). E, F) Liquid encapsulation in colloidosome, digital (E) and static contact angle (F) images of colloidosomes (volume = 20 μL) filled with different solvents having a wide range of surface tensions. G, H) Scheme depicting the release of inner liquid from colloidosome on a solid surface (G) and water pool (H) upon heating. I) Digital images showing the release of different solvents from colloidosome (volume = 20 μL) induced by heating with near-infrared (NIR) light and hot plate. J) Digital images representing the release of different solvents from colloidosome (volume = 20 μL) on water pool induced by heating. Published in *Chem. Mater.*, 2024, **36**, 8692.

Colloidosome was heated on a hot plate above 51 °C or irradiated with NIR light, confirmed the release of water, ethanol and hexane liquids, as shown in Figure 4G. A similar outcome was observed on water pools, as shown in Figure 4H. When the PODAc shell is heated above 51 °C, the crystalline packing of PODAc is compromised. The PODAc shell rapidly melted, releasing the encapsulated inner liquid into solid or liquid pools. Owing to its facile processability and chemical stability, the PODAc colloidosome would be a powerful tool to customize droplet chemistry more efficiently and systematically.

Chapter 4: Controlled Chemical-patterning of Textile to Accelerate Anti-gravity Water Flow

Bio-inspired unidirectional flow of tiny aqueous droplets across the fibrous substrate paved the way for the emergence of various advanced materials. In the past, textiles decorated with noncontact-based wettability-patterns enabled unidirectional water flow—without flooding the top surface by the transferred water. However, such approaches mostly suffer from a low ($\approx 0.176\ \mu L\ mm^{-2}\ s^{-1}$) flow rate, likely due to delay in the overall liquid ejection process. So, in this context, I have developed controlled chemical-patterning of textiles to accelerate the overall liquid ejection process without flooding the top surface via contact-based wettability-patterns. Here, chemically reactive nanocomplex (CRNC) was dip coated on a selected fibrous substrate for direct and spatially selective modulation of wettability through 1,4-conjugate addition reaction in aqueous medium at ambient condition (Figure 5A-D). In the current approach, no sophisticated instrumental set-up is required—rather, the diameter and depth of the patterned spot can be regulated easily—just by controlling the contact area between the textile and aqueous droplet of selected modifier, i.e. glucamine and the duration of exposure time to the beaded droplet of modifier. The hydrophilic moiety is installed—without perturbing the hydrophobic moiety (e.g., hydrocarbon) to modulate the water wettability on the water-repellent interface spatially selectively. The prepared patterns provided superior anti-gravity transport of water through patterned channels on fibrous substrate (Figure 5E). Importantly, the volume of beaded aqueous droplets of glucamine controls the dimension of patterned channels on a superhydrophobic background. Thus, the droplet contact area to the fabric controls the diameter of patterning and the patterning time decides the depth of the pattern, as illustrated in Figure 5F. Thus, the current approach provided a basis to tune the dimension of the patterned channel through a direct chemical modification at ambient conditions. The surface of the prepared superhydrophobic textile that was directly exposed to an aqueous solution of glucamine is denoted as the patterned top spot, and the other surface of the textile is referred to as the patterned back spot, as shown in Figure 5G. Next, a droplet of water was placed on the patterned top spot of a patterned textile prepared by exposing it to glucamine solution spatially selectively for 60 and 75 min, denoted as PT_{60} and PT_{75}, respectively. On exposing a tiny droplet of dyed water (blue color) on the patterning back spot, an immediate anti-gravity transfer of the water was noticed—without having any arbitrary spreading of transferred water on the top surface. Initially, an instant anti-gravity transfer of water was observed for both patterned textiles—but the backflow of the transferred liquid to the bottom surface was noted only for PT_{75} as shown in Figure 5H. It is likely due to the decrease in the breakthrough pressure—that resists the backflow of transferred water under gravity.

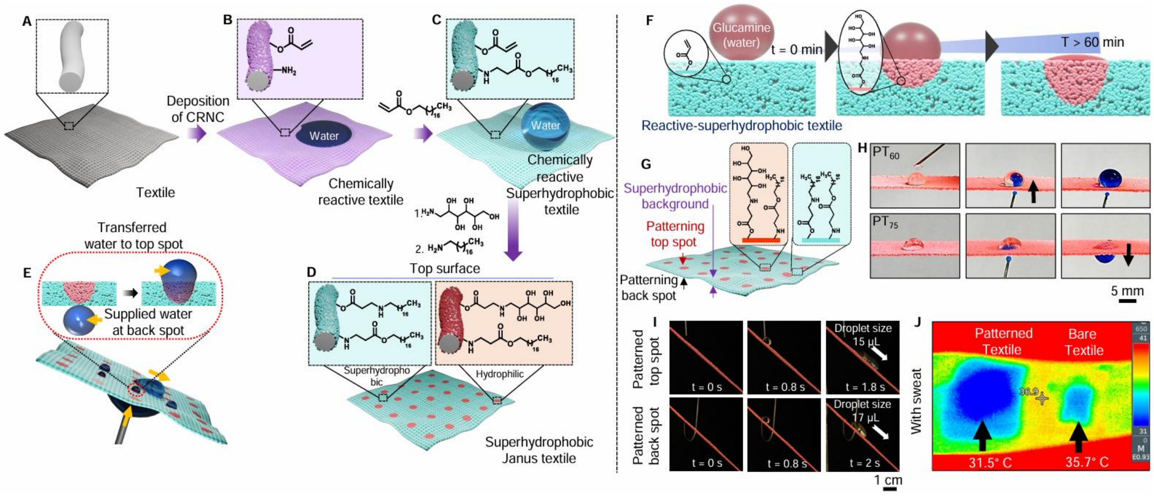

Figure 5: A–D) In situ, deposition of chemically reactive nano complex (CRNC) derived from a reaction mixture of 5Acl and BPEI on a A) selected textile following the dip coating process B) yielded chemically reactive textile. C) Its post-chemical modifications with octadecyl acrylate (ODAc) conferred superhydrophobicity and denoted as a chemically reactive superhydrophobic textile. D) The spatially selective modification of a chemically reactive superhydrophobic textile with glucamine, followed by octadecylamine, provided Janus channels on a chemically inert superhydrophobic background. E) Schematic illustrating the unidirectional transport of beaded droplets through patterned textiles against gravity. F) This schematic illustrates the spatially selective glucamine modification on reactive-superhydrophobic textile—through gradual infiltration of beaded aqueous droplets of glucamine. G) Schematic of a chemically patterned superhydrophobic interface, where hydrophilic spots, denoted by red colors, were achieved on a superhydrophobic background via spatially selective chemical modifications. H) Digital images account for the ability of two distinct patterned textiles (PT_{60} and PT_{75}) toward anti-gravity water transportation. I) Digital images accounting for the rolling of beaded (from the top side) and transported water droplets (from the back side) on patterned textile that was kept inclined at an angle of 45°. J) Infrared camera images of the patterned and bare textiles applied on the skin in artificial sweat's presence, recorded outdoors at a surrounding temperature of 40 °C. Published in *Adv. Funct. Mater.*, 2024, **34**, 2410955.

Next, the optimized patterned textile was applied to demonstrate an anti-gravity transfer of water in the absence of a beaded water droplet on its top side—without flooding the top surface of the patterned material, rather the transferred water rolls on the inclined patterned interface as shown in Figure 5I. The prepared Janus patterns displayed a high (2.57 ± 0.28 µL mm^{-2} s^{-1}) flow rate of water against gravity with an ability to roll the accumulated liquids on the top surface. This is likely due to the chemically controlled optimization of pattern dimension with a gradient of wettability on a water-repellent background. Thereafter, both bare and patterned textiles were placed on the prewetted skin of a volunteer before recording the body surface temperature using an infrared camera. The temperature difference was noticed to be 4.2 °C. The ability of unidirectional transport of artificial sweat resulted in better cooling (31.5 vs 35.7 °C) of patterned textile in comparison to bare textile, where the temperature of skin was recorded to be 36.9 °C. This is likely due to faster evaporation of ejected artificial sweat by the patterned textile (Figure 5J), which is not possible to achieve with bare textile.

Chapter 5. Amidation Reaction to Derive Waterborne, Tolerant, and Optically Transparent Solid Slippery and Superhydrophobic Coatings

The derivation of durable solid slippery and superhydrophobic coatings maintaining high optical transparency—following a simple, completely waterborne, non-fluorinated and scalable fabrication approach is an extremely challenging task to achieve. In this chapter, I unprecedentedly extended an inherently amine reactive thioester molecule to report abrasion tolerant and optically transparent two distinct bio-inspired wettability—i.e., lubrication-free slippery and superhydrophobic coatings. This current synthetic approach involved a simple aqueous and covalent processing of appropriately selected chemical functional groups (hydrophilic, hydrophobic and self-polymerizable moieties) considered as important 'Inputs' through a mutual chemical reaction between primary amine and thioester groups to achieve desired 'Outputs' (i.e., waterborne coating with durability, transparency and bio-inspired wettability) as shown in Figure 6A-C. In this waterborne chemical approach, the selectively reactive thioester group provided a simple basis to integrate two essential chemical functional groups—i.e. hydrophobic and polymerizable moieties—and simultaneously, it also enabled the release of the hydrophilic moiety during the amide bond formation process. Eventually, this chemical approach allowed to prepare a stable dispersion of nanoparticles for co-optimization of essential topography and chemistry to confer both slippery property and superhydrophobicity—where the choice of substrates (fibrous/porous or flat/featureless interfaces) played an important role in associating the desired liquid wettability as shown in Figure 6D, E. The prepared waterborne, optically transparent (~97 %) coatings embedded with bio-inspired wettability remained highly tolerant in various challenging and abrasive conditions as shown in Figure 6F. Selected sodium 3-(steartoylthio)propane-1-sulfonate (labelled as R-1) was reacted with a self-polymerizable small molecule, i.e. (3-aminopropyl)triethoxysilane (APTES, denoted as R-2) with 1:1 M ratio in DI water at 80 °C for 8 h to form a stable dispersion of nanoparticles (denoted as RM) (Figure 6G). During the course of the mutual reaction between the selected reactants (R-1 and R-2), the thioester group of R-1 selectively reacted with the primary amine of R-2 to form a robust a amide bond as evident from the ATR-FTIR analysis in Figure 6H.

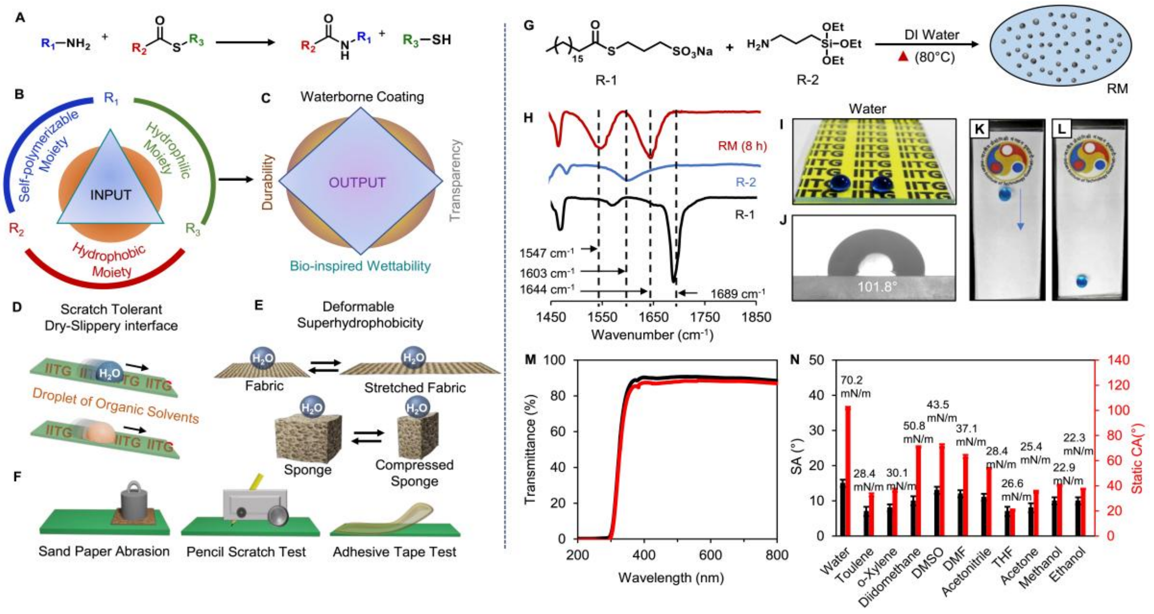

Figure 6: A-C) Schematic presentation of the designing principle of 'Processor-Input-Output, where the aqueous processing of small molecules having strategically selected chemical 'inputs' (i.e. self-polymerizable, hydrophilic, and hydrophobic moieties) through an amidation reaction (processor) between amine and thioester groups puts'—including provided desired bio-inspired wettability, waterborne process, durable and optically transparent coating. D) Depicting the slippery behaviour of beaded droplets of different liquids on a solid slippery coating. E) Illustrating the physical (tensile and compressive) deformations of fibrous and porous substrates embedded with superhydrophobic coating. F) Schematic presenting tolerance of prepared coating towards some relevant and widely accepted abrasive exposures. G) Illustrating the amidation reaction between selected reactants (i.e. 3-(steartoylthio)propane-1-sulfonate (labelled as R-1) and (3-Aminopropyl)triethoxysilane (APTES, denoted as R-2)), where the reaction mixture of R-1 and R-2 in DI water at 80 °C provided a stable dispersion of nanoparticle (NP). H) FTIR- ATR spectra for the individual reactants, i.e. 3-(steartoylthio)propane-1-sulfonate (labelled as R-1, black), (3-Aminopropyl)triethoxysilane (APTES, labelled as R-2), blue) and reaction mixtures (1:1) of R-1 and R-2 after 8 h, (labelled as RM (8 h)). The IR peaks at 1689 cm^{-1}, 1603 cm^{-1}, 1644 cm^{-1} and 1547 cm^{-1}correspond to the carbonyl stretching of the thioester group of R-1, N–H bending of the primary amine group, amide-I and amide-II bands respectively. The carbonyl stretching of the thioester group completely disappeared after 8 h of the mutual reaction between amine and thioester moieties. I-L) digital (I) and Static contact angle images (J) of the beaded droplet (5 μL) of water on coated glass, digital images (K and L) of coated glass depicting the sliding of the beaded water droplet. M) Depicting Optical transmittance (normalised with respect to bare glass) of the coated glass (red). N) Bar diagram accounting for the static contact angle and sliding angles (SA) of various non-polar and polar liquids with a wide range of surface tension on prepared slippery coating. Published in *Chem. Eng. J.* 2023, **465**, 142776.

The IR signature of carbonyl stretching of the thioester group of R-1 at 1689 cm^{-1} was gradually reduced with the progress of the reaction—and completely disappeared after 8 h of mixing of the selected reactants as shown in Figure 6H. As expected, additional IR signatures appeared at 1644 cm^{-1} and 1547 cm^{-1} corresponding to amide-I and amide-II bands, respectively. Thereafter, this aqueous reaction mixture (RM) of selected reactants (R-1 and R-2) was strategically extended to develop a lubrication-free solid slippery interface. To achieve the lubrication-free slippery coating, a microscopic glass slide was submerged in the aqueous reaction mixture for 8 h of the selected reactants (Figure 6I). A droplet of water (15 µL) was beaded on the coated substrate with a static water contact angle of $\sim 102^{\circ}$ (Figure 6J) and the beaded droplet started sliding on tilting the coated substrates, as shown in Figure 6K, L. Further, the optical transparency was compared with bare glass—and the coated glass displayed nearly similar (above 97%, normalized with respect to bare glass) optical transparency, as shown in Figure 6M. In addition to water, the prepared coating displayed the ability to slide various other polar (dimethyl sulfoxide, dimethylformamide, acetonitrile, tetrahydrofuran, acetone, ethanol and methanol) and non-polar (toluene, o-xylene and diiodomethane) organic solvents—having a wide range of surface tensions (from 50.8 mN/m to 22.3 mN/m), as shown in Figure 6N. Next, the prepared solid slippery coating was successfully used to demonstrate the self-cleaning ability, where the deposited dust and dirt on the slippery coating was readily removed on exposure to the aqueous stream—and provided a dry and clean interface as shown in Figure 7B. In the absence of such coating, the glass substrate remained inefficient to provide an instantly dry and clean interface, as shown in Figure 7A.

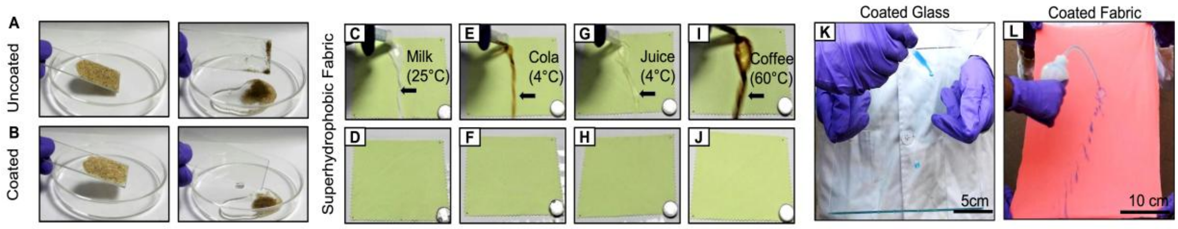

Figure 7: A, B) Digital images demonstrating the self-cleaning ability of deposited sand particles on both uncoated (A) and coated (B) glass slide with stream of tap water. C-J) Digital images showing the antifouling performance of superhydrophobic coating with the stream of cow-milk (C, D), cold (4 °C) cola (E, F), cold (4 °C) juice (G, H), hot (60 °C) coffee (I, J). V-W) Digital images demonstrating the slippery (K) and superhydrophobic (L) coatings on large objects. Published in *Chem. Eng. J.*, 2023, **465**, 142776.

Thereafter, the prepared superhydrophobic fabric was exposed to various commercially available hot and cold beverages—including milk, cold (4 °C) soft drinks, fruit juice and hot coffee (60 °C) to examine its ability to protect the selected porous/fibrous and inherently hydrophilic substrates from unwanted aqueous exposures, and the liquids were extremely repelled and readily removed—without having any trace of these used liquids on the coated fabric as shown in Figure 7C-J. Thus, I have introduced a scalable and facile chemical approach to develop an optically transparent slippery (Figure 7K) and superhydrophobic coating (Figure 7L)—which remained appropriate to survive various practically relevant and challenging conditions, and thus, such coating would be useful in relevant and realistic applications.

Chapter 6. Conclusion and Future Directions

In conclusion, I have strategically applied aqueous and non-aqueous liquid wettability to develop durable functional liquid repellent material/interfaces through adopting facile fabrication methods. The strategic association of 1,4-conjugate addition reaction allowed for embedded chemical 'reactivity' into porous crystalline nanoparticles (MOFs), which gives the scope of post-modification with selected small molecule at ambient conditions to derive hydrophobic MOFs yielded LMs to achieve adaptive water wettability at different pH, for controlling the liquid release behavior on liquid pool. Further, a crystalline comb-like polymer, i.e., PODAc, was used to design recyclable omniphobic capsule based on the "colloidosome'' technique to achieve a crystalline, solid, and continuous solid slippery shell around the encapsulated liquid droplet for on-demand capsulation/extraction of various liquid droplets, regardless of their surface tension and volatility, without having any adhesion or evaporation loss. Further, a chemically reactive superhydrophobic coating on the fibrous substrate was developed to derive Janus patterns of chemically modulated wettability with an extremely water-repellent background through spatially selective 1,4-conjugate addition reaction with hydrophilic small molecules. The prepared Janus pattern can transfer tiny aqueous droplets against the gravity across the fibrous substrates, demonstrating efficient ejection of artificial sweat and management of body surface temperature. Moreover, a completely waterborne, non-fluorinated, tolerant, optically transparent and scalable fabrication approach was developed to derive amphiphobic solid slippery and superhydrophobic interfaces through a simple water based amidation reaction.

This synopsis report introduces different types of anti-wettable materials/interfaces, which can be used for various relevant applications. Liquid marble and colloidosome have been used in numerous "droplet-scale" applications like on-demand drug release, miniaturized chemical reaction, sensing of toxic pollutants, etc. Further, these materials could be extended for catalytic miniature reactors, lab-on-a-chip devices applications, etc. Further, in the recent past, liquid marble has been used in 3D cell culture applications. Liquid marbles often suffer from weak mechanical property. On the other side colloidosomes are mechanically stable but lack porosity. To achieve desired mechanical property retaining the property of liquid marble, i.e. porous shell structure it could be possible to develop a hybrid material combining the concept of both liquid marble and colloidosome, adequately. Furthermore, the Janus pattern, which was discussed in Chapter 4 is used for demonstrating directional liquid transport and it would also be extended for water harvesting applications. The asymmetric wettability of patterned Janus membranes and fast ejection rate of water droplets could be efficient for water harvesting, wound healing, etc., making them valuable in real-life applications. Further, a robust waterborne dry transparent solid slippery interface was developed, which could be used in solar panels, smart windows, spectacle, airplane wings, etc., to prevent the unwanted fouling by liquids and dust particles. Thus, the developed materials would be useful in various other prospective applications.

Table of Contents

Chapter 1: Introduction

1.1 Biomimicry: Nature-inspired innovation

Nature remains an inspiration for various important inventions. Many natural structures and mechanisms have influenced the development of functional materials and technologies.[1,2] Examples of biomimicry include the design of a bullet train in Japan, inspired by the beak of the kingfisher bird.[3] To minimise noise pollution because of air resistance challenges when the train exited the tunnels. Redesigning the train's nose to a streamlined shape of the beak of a kingfisher bird decreased noise pollution, minimized air resistance, and enhanced energy efficiency. Similarly, the study of gecko feet has led to the development of advanced adhesives and climbing robots. Geckos can adhere to smooth surfaces due to millions of microscopic hairs on their feet.[4] Scientists have used this concept to create synthetic adhesives that allow objects to stick without glue or residue. Another example is spider silk, which has an exceptional strength-to-weight ratio and high elasticity. Researchers aim to develop synthetic fibers that mimic these properties.[5] Such fibers could be useful in textiles, medical sutures and biodegradable materials. Leonardo da Vinci's study on the movement and anatomy of birds inspired him to design flying machines. Even though his designs were never actually built, they inspired future inventors to develop flying machines. The Wright brothers successfully introduced the flying machine in 1903.[6] Their achievement demonstrated how nature-inspired designs could lead to revolutionary advancements. Biomimicry has many applications across different fields, including daily life, agriculture and medicine.[7] The lotus leaf displays extreme water repellence, which is formally defined as superhydrophobicity that allows to repel deposited dust and dirt to self-cleaning. This property has inspired the creation of self-cleaning surfaces, oil-water separation, anti-corrosion and anti-icing.[8,9] Another example is the Nepenthes pitcher plant, which is naturally embedded with slippery surfaces that help to trap insects. The upper edge of the plant's rim, called the peristome, has a slippery property, where insects slip into the pitcher plant. This mechanism has led to the development of coatings that resist ice accumulation, fouling, unwanted substances, etc.[10,11] The stenocara beetle, which lives in arid regions, collects water using hydrophilic and hydrophobic patterns on its back.[12] This adaptation has inspired the design of materials that efficiently gather water from the air. Bioinspired surface properties, such as superhydrophobicity and slipperiness, have paved the way for functional materials with advanced wetting behaviour. These innovations provide opportunities for technological advancements in many industries, such as anti-icing, drag reduction, anti-corrosion, anti-fouling performance, etc.[13-15] The following sections will explore design principle of deriving various anti-wetting materials and interfaces in detail.

1.2 Examples of Liquid Repelling Materials and Interfaces Available in Nature

Nature provides many examples of surfaces with special functionalities. Wettability is an important property that influences how surfaces interact with liquids. Many organisms have developed distinct surface chemistry and topography that control wetting behaviour.

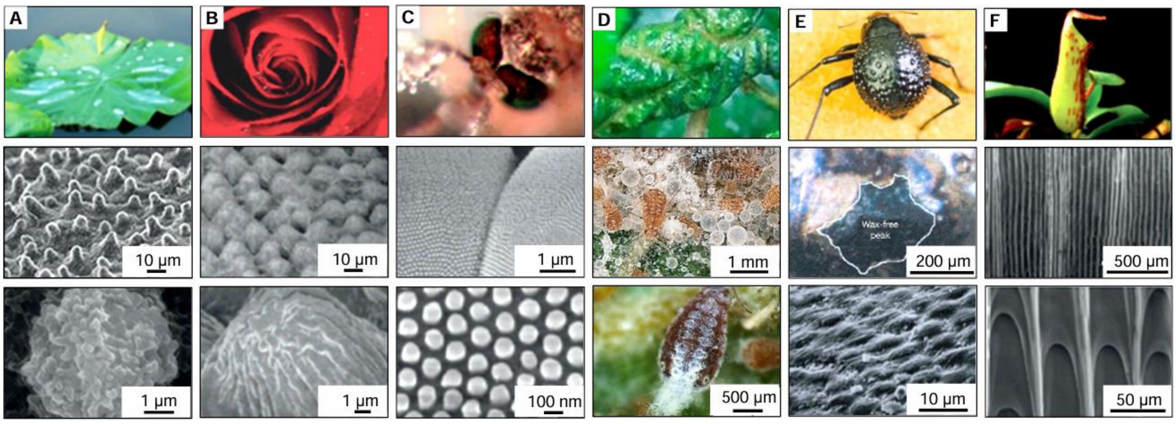

Figure 1.1 Few existing examples of naturally anti-wettable surfaces and materials. A-F) Digital and scanning electron microscope images of highly non-adhesive superhydrophobic surfaces of a lotus leaf (A), adhesive superhydrophobic surface of rose petal (B), transparent superhydrophobic mosquito eye (C), liquid marbles fabrication by honeydew droplets with wax particles in aphids on leaf (D), Desert beetle possessing pattern interface (E) and slippery nepenthes pitcher plant (F). Figure 1.1A-C, F is adapted from ref. 10 with permission from Macmillan Publishers Limited, Copyright 2017. Figure 1.1D, F is adapted from ref. 29 with permission from American Chemical Society, Copyright 2019. Figure 1.1E is adapted from ref. 30 with permission from Springer Nature Limited, Copyright 2001.

Water droplets beaded on a lotus leaf with a high water contact angle and roll off easily on tilting, removing dust and dirt from such interfaces (Figure 1.1A). Scientists studied the lotus leaf's surface under a scanning electron microscope (SEM) and revealed that such surface has micro and nano topography covered with hydrophobic wax crystals,[16,17] resulting in superhydrophobicity (Figure 1.1A). Inspired by the lotus leaf, scientists have developed artificial superhydrophobic surfaces for applications such as anti-fouling,[18,19] water harvesting,[20,21] anti-icing,[22,23] self-cleaning materials,[24,25] etc. Rose petals also displays superhydrophobicity but show high water adhesion property (Figure 1.1B). Water droplets maintain their spherical shape but do not roll down, even though the rose petal is flipped upside down; this phenomenon is known as the "petal effect". Feng et al. explored the rose petal's surface by using SEM imaging.[26] They found that the petals had closely packed micropapillae, each with a height of 7 µm and a diameter of 16 µm. These micropapillae hold densely nanometer-sized cuticular folds (Figure 1.1B). Like lotus leaves, rose petals have hierarchical roughness; however, differences in microstructure lead to higher adhesive forces in rose petals. The larger size of the microstructures allows water droplets to penetrate microgrooves but not the nanostructures, causing the droplets to stick to the surface.[27] Another example of naturally existing liquid repellent surface, the mosquito eye's embedded with anti-fogging properties and optically transparent superhydrophobicity (Figure 1.1C).[28] Gao et al. explored the mosquito eye's surface by using SEM imaging. The mosquito's eye is made up of many tiny dome-shaped units called ommatidia. Each ommatidium is about 26 μm wide and arranged in a hexagonally close-packed pattern. Each dome is covered with many tiny bumps, having an average diameter of approximately 101 nm and a spacing of around 48 nm between each (Figure 1.1C). Certain aphid species that inhabit leaf galls of their host plants are known to produce liquid marbles where honeydew are coated with wax particles, as revealed by FESEM analysis. Micrometer-sized wax particles coat the surface of the honeydew droplets, imparting a protective and non-wetting environment to the honeydew (Figure 1.1D).[29] The Stenocara beetle, or Namib beetle, has a tremendous ability to collect water from fog in an extremely dry condition. The beetle's back features hydrophilic bumps encircled by hydrophobic valleys, enabling it to harvest water from the fog-laden winds common in the Namib Desert (Figure 1.1E).[30] SEM images show randomly scattered hydrophilic bumps, each about 0.5 mm in diameter and spaced between 0.5 and 1.5 mm apart, along with intervening hydrophobic valleys (Figure 1.1E). Water collects on the hydrophilic bumps and rolls down from hydrophobic valleys to the beetle's mouth. This mechanism has inspired to derive artificial fog-harvesting systems. Other natural species, such as Nepenthes pitcher plants, have a peristome that, when insects sit on, causes them to fall into the traps due to its slippery surface. The peristome of the plant has microscopic cavities that hold water, creating a lubricated surface (Figure 1.1F).[11]

In summary, natural surfaces such as lotus leaves, rose petals, mosquito eyes, aphid species, Namib beetle backs and Nepenthes pitcher plants have inspired significant advancement in biomimetic special liquid wettability. These biomimetic materials can be used in different applications, including self-cleaning, water harvesting, anti-icing and other relevant purposes.

1.3 Liquid Wettability of Solid Surfaces

Liquid wettability determines how effectively liquid droplets interact with solid surfaces.[31,32] The behaviour of a liquid droplet on a solid surface is governed by the balance between cohesive and adhesive forces. Cohesive forces occur between similar molecules and reduce the contact area between the solid and liquid, while adhesive forces, acting between unlike molecules, promote spreading. The extent of wetting is determined by the equilibrium of these forces and it is measured by the contact angle of the beaded liquid droplets on solid surface. The contact angle is defined as the tangential angle formed by a liquid droplet at the triple-phase contact point on a solid surface.

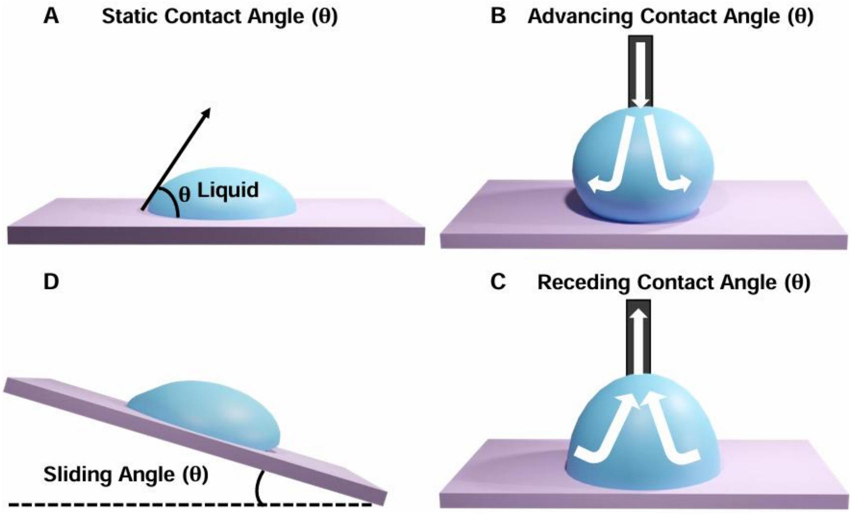

Figure 1.2 Schematic illustration of static contact angle (A), advancing contact angle (B), receding contact angle (C) and sliding angle (D), respectively.

Contact angles (θ) are broadly classified into static and dynamic contact angles. Static contact angle (Figure 1.2A) represents the equilibrium contact angle at which a liquid droplet maintains a constant solid-liquid contact area during measurement. In contrast, the dynamic contact angle is measured when the three-phase contact line is in motion relative to the solid surface. The dynamic contact angle is further categorized into advancing (Figure 1.2B) and receding (Figure 1.2C) contact angle. The advancing contact angle on an anti-wettable surface is measured when the liquid droplet volume is progressively increased, whereas the receding contact angle is determined when the liquid is withdrawn, leading to a reduction in droplet volume. The difference between the advancing and receding contact angles is known as contact angle

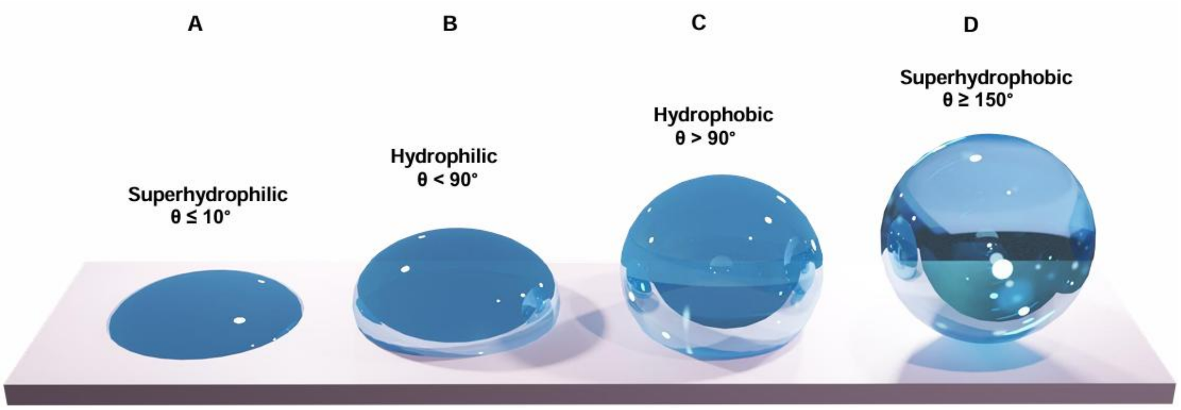

Figure 1.3 Schematic representation of different types of anti-wettable surfaces, including superhydrophilic (A), hydrophilic (B), hydrophobic (C) and superhydrophobic (D).

hysteresis (CAH).[33,34] Additionally, the sliding angle (Figure 1.2D) is defined as the inclination angle of a surface at which liquid droplets begin to slide due to gravitational force. Solid surfaces are classified into four categories based on the measured contact angle values of water droplets: a) superhydrophilic surfaces (0° ≤ θ ≤ 10°) (Figure 1.3A), hydrophilic surfaces (10° < θ < 90°) (Figure 1.3B), hydrophobic surfaces (90°< θ < 150°) (Figure 1.3C) and superhydrophobic surface (θ ≥150°) (Figure 1.3D). Moreover, superhydrophobic surfaces are subcategorized based on the CAH value, with adhesive superhydrophobic surfaces exhibiting (CAH > 10°) and non-adhesive superhydrophobic surfaces (CAH < 10°).[35,36]

1.4 Theoretical Models to Understand Liquid Wettability of Solid Surfaces

The ability of a solid surface to repel liquids is a vital property that helps to control how liquid droplets behave on solid materials. Over time, scientists have developed different models to explain how liquids interact with solid surfaces. This section provides a brief discussion of these wettability theories.

1.4.1 Young's model

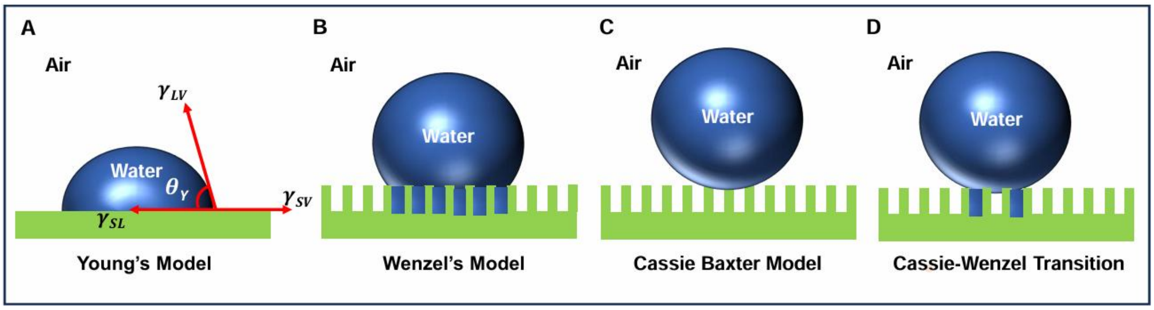

Figure 1.4 Schematic illustrates different wettability models on solid surfaces in air: A) Young's model, B) Wenzel's model, C) Cassie-Baxter model and D) Cassie-Wenzel Transition state.

In 1805, a model was proposed by Thomas Young to explore the wetting phenomenon of smooth, homogeneous solid surfaces.[37] When a liquid droplet is placed on a smooth solid surface, a stable contact angle (θ_Y) is attend after balancing the surface tension of a liquid in the air (γ_{LV}), the interfacial tension between solid and liquid (γ_{SL}) and surface free energy of solid in the air (γ_{SV}) at equilibrium (Figure 1.4A). Young's equation is expressed as follows:

$$\cos\theta_Y = \frac{\gamma_{SV} - \gamma_{SL}}{\gamma_{LV}} \qquad \ldots\ldots\ldots\ldots\ldots\ldots\ldots\ldots\ldots\ldots\ldots\ldots\ldots\ldots (1.1)$$

The above equation is obtained based on the principle of thermodynamic equilibrium at the three-phase boundary interface (solid-liquid-vapor) formed by the liquid droplet on the solid surface, where net force acting on the beaded droplet is zero.

1.4.2 Wenzel model

Young's equation works only for ideal smooth and homogeneous solid surfaces. Nevertheless, real surfaces are mostly followed with some degree of roughness. For surfaces that are chemically homogeneous yet exhibit roughness, the actual surface area exceeds the apparent surface area by a factor ‘r’ referred to as the roughness factor. This concept was introduced by Wenzel in 1936.[38] Wenzel improved Young’s model by integrating a roughness factor (Figure 1.4B). As mentioned by the Wenzel model, the liquid fully infiltrates the rough structures of the solid surface, which leads to a modification of both the solid-liquid and solid-vapor interfacial tensions. The Wenzel equation describes the equilibrium condition of this model:

$$r\gamma_{SV} = r\gamma_{SL} + \gamma_{LV}cos\theta_W$$

which can be rewritten as:

$$cos\theta_W = r\frac{(\gamma_{SV} - \gamma_{SL})}{\gamma_{LV}} \quad \text{……………………………………} \quad (1.2)$$

Here, θ_W represents the apparent contact angle of the solid surface in the Wenzel model. By using equation (1.1) and equation (1.2), the relationship between θ_Y and θ_W is established as:

$$\cos\theta_W = r\cos\theta_Y$$

For rough surfaces where $r \geq 1$, surface roughness improves a solid surface's wetting and non-wetting characteristics, which are influenced by its inherent wettability. For instance, on ideal smooth surfaces with $\theta_Y < 90^\circ$, the addition of surface roughness increases hydrophilicity. On the contrary, if the hydrophobic smooth surfaces with $\theta_Y > 90^\circ$, the introduction of roughness further enhances their hydrophobicity.

1.4.3 Cassie and Baxter model

The Wenzel model applies to a rough, solid surface where the liquid maintains a homogenous contact with the surface. Nevertheless, this model is ineffective in describing extreme liquid repellence by some interfaces (e.g., lotus leaf, rice leaf, etc.). To address this limitation, Cassie and Baxter proposed an alternative wettability model in 1944, incorporating the concept of heterogenous contact of liquid on solid.[39] Based on the Cassie-Baxter model, the liquid remains cling to the peaks of the asperities in the microstructured surface due to the trapped air phase within the grooves (Figure 1.4C). Consequently, the apparent solid-liquid contact area comprises two different interfaces: the solid-liquid interface and the liquid-vapor interface, leading to a heterogeneous wetting state. The apparent contact angle in this model is described as:

$$\cos\theta_{CB} = f_1\cos\theta_1 + f_2\cos\theta_2 \quad \text{……………………………….} \quad (1.3)$$

$$f_1 + f_2 = 1$$

Here, f_1 and f_2 represent the fraction of the contact area of the solid-liquid and liquid-vapor interface, respectively. While θ_1 and θ_2 indicate the contact angle of liquid droplets on a flat solid surface ($\theta_1 = \theta_Y$) and the contact angle (θ_2) of the liquid droplet in the air, which is taken as 180°. Substituting this value into Equation (1.3) yields:

$$\cos \theta_{CB} = f1 \cos \theta_Y + (1-f_1) \cos (180^\circ)$$

$$\cos \theta_{CB} = f1 \, (1 + \cos \theta_Y) - 1 \qquad \text{....................................(1.4)}$$

This equation applies only to contact angle measurements on rough surfaces, where liquid does not penetrate the grooves. In some cases, surfaces display a mixed wetting state, where the liquid partially penetrates the asperities while remaining suspended on the trapped air layer. This phenomenon represents a transition from the Wenzel state to the Cassie-Baxter state (Figure 1.4D). [40] The apparent contact angle for this mixed wetting state is represented as:

$$\cos \theta_{mix} = r f_l \cos \theta_Y + f_l - 1 \qquad \text{....................................(1.5)}$$

Where r denotes the roughness factor of the solid surface.

1.4.4 Liquid Wettability of Slippery Liquid Infused Porous Surfaces (SLIPS)

On the other hand, slippery liquid infused porous surface (SLIPS) is an example of special homogenous interface developed, inspired by the Nepenthes pitcher plant (Figure 1.5A). It exhibits exceptional repellency to different types of liquids, including water, oils and biological fluids. It is created by infusing a lubricant into a porous or textured solid substrate (Figure 1.5B), providing a stable and smooth layer, leading to a homogeneous wetting state, that acts as a slippery interface.[41] Such interfaces allow effortless sliding of liquid droplets on tilting.

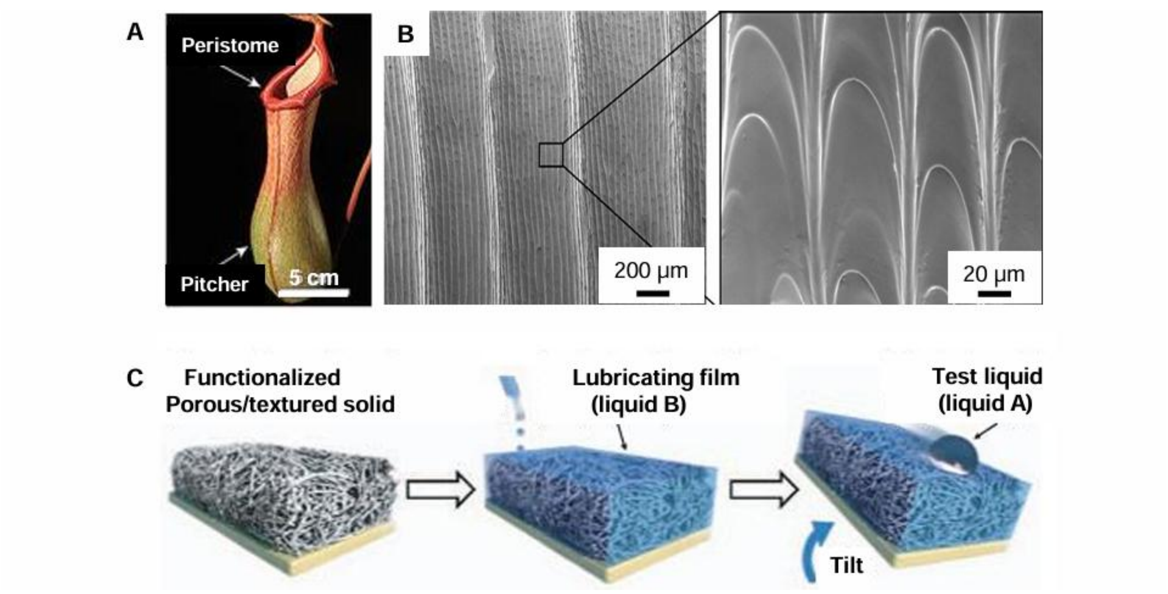

Figure 1.5 A) Digital images of Nepenthes pitcher plant. B) Scanning electron microscope images of porous/textured solid surfaces. This figure is adapted from ref. 41 with permission from Springer Nature Limited, Copyright 2011. C) Schematic illustrating the fabrication of a slippery liquid-infused surface to form a smooth surface, that allows effortless sliding liquid droplets. This figure is adapted from ref. 42 with permission from Springer Nature Limited, Copyright 2011.

Inspired by the Nepenthes pitcher plant, Wong et al. first developed the slippery liquid-infused porous surface, where a fluorinated lubricant was infused into a porous Teflon substrate and the porous substrate provides a framework to stabilize the lubricant through capillary action and the fluorinated lubricant spread on the porous substrate forms a thin layer on it (Figure 1.5C). The lubricant's surface tension and chemical compatibility with the substrate ensure its retention.[42] It is effective against high as well as low surface tension liquids, which include water, oils, organic solvents, and even blood. It prevents biofouling,[43] icing[44] and accumulation of contaminants.[45]

1.5 Essential Criteria for Designing Liquid Repellent Surfaces

Designs of bio-inspired special, heterogeneous (superhydrophobicity) and homogeneous (SLIPS), demand different chemical and physical optimization strategies. Her, I will discuss key factors necessary for creating artificial superhydrophobic surfaces and slippery liquid-infused porous surfaces (SLIPS).

1.5.1 Design of Criteria of Artificial Superhydrophobic Surface

The lotus leaf is a prominent example of a naturally existing, superhydrophobic surface. Detailed surface analysis reveals a hierarchical micro and nano structural topography topped with an epicuticular wax layer.[9, 46]

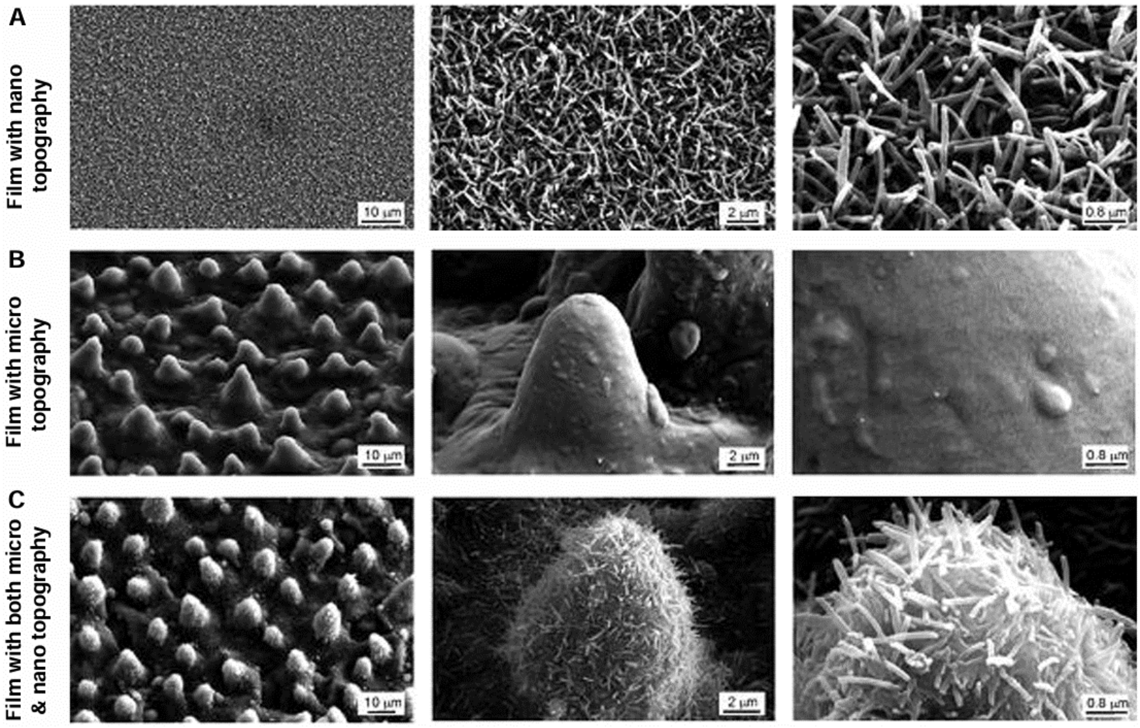

Figure 1.6 A-C) Scanning electron microscopy images of nano structures (A), micro-structures (B) and hierarchical structured (C) surfaces developed using replicas of lotus leaf. This figure is adapted from ref. 16 with permission from The Royal Society of Chemistry, copyright 2009.

Such interface displays exceptionally high water contact angle due to the combined effect of the hierarchical roughness and the wax layer.

The hierarchy (combination of nano and micro) in topography facilitates the entrapment of metastable air layer within the surface grooves, while the wax coating contributes to low surface free energy. SEM studies indicate that only a nanostructured surface is insufficient to retain air pockets for achieving superhydrophobicity (Figure 1.6A). Additionally, a microstructured surface with a wax coating alone achieves a maximum water contact angle of only 147°. This contradiction arises because of the rapid displacement of entrapped air from the microgrooves (Figure 1.6B). Consequently, combining both micro and nano hierarchical features and a low surface energy coating is important for replicating the superhydrophobic characteristics of the lotus leaf (Figure 1.6C). In conclusion, successfully fabricating artificial superhydrophobic surfaces requires the fulfilment of two essential criteria: a) a rough surface with hierarchical topography and b) low surface free energy.[16]

1.5.2 Design Criteria of Artificial SLIPS

Nepenthes pitcher plant-inspired, lubricant-infused slippery surface is typically fabricated by impregnating a rough, porous structure with a lubricant, generating a smooth and highly functional interface that allows effortless sliding of liquid droplets. However, the development of a stable lubricant-infused slippery surface required several criteria. Wong et al. first established three fundamental design principles for artificial slippery surfaces, as shown in Figure 1.5C.[42]

I. The textured substrate must exhibit chemical compatibility with the lubricant, ensuring complete wetting of the lubricant to the surface.

II. The surface should exhibit a superior affinity for the lubricant over the liquid to be repelled, preventing displacement of the lubricant layer.

III. The infused lubricant must be immiscible and chemically incompatible with the liquid intended to repel, ensuring sustained stability of the slippery interface.

If any of the above-mentioned criteria are missing, interface would failed to display slippery property. The chemical compatibility between the solid matrix lubricating liquid and the working liquid can be described using the following equations.[47]

$$R(\gamma_l \cos\theta_l - \gamma_w \cos\theta_w) - \gamma_{lw} > 0 \quad \ldots\ldots\ldots\ldots (1.6)$$

$$R(\gamma_l \cos\theta_l - \gamma_w \cos\theta_w) + \gamma_w - \gamma_l > 0 \quad \ldots\ldots\ldots\ldots (1.7)$$

Here, R denotes the roughness factor and it is defined as the ratio of the actual surface area to the projected surface area of the solid. γ_l and γ_w denote the surface tensions of the lubricating liquid and the working liquid, respectively, while γ_{lw} is the interfacial tension between the two liquids. The symbols θ_l and θ_w indicate the static contact angles of the lubricating and working liquids, respectively, when measured on a smooth, homogenous solid surface.

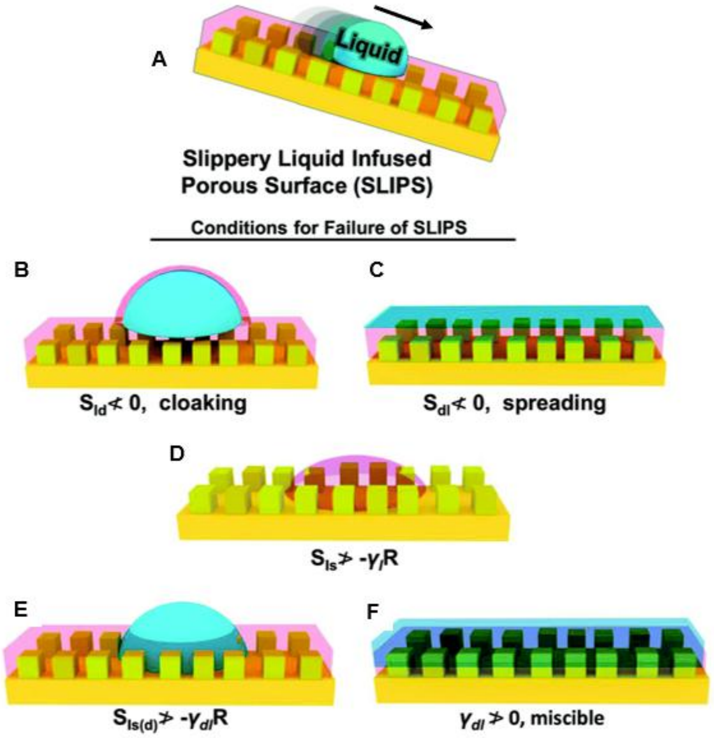

Figure 1.7 A) Schematic representation of slippery liquid infused porous surfaces (SLIPS). (B-F) Schematic illustrating the conditions that fail to form a stable SLIPS. These include: (B) the lubricant forming a cloaking layer over the working droplet; (C) the lubricant being displaced by the working droplet; (D) the lubricant's inability to uniformly wet the solid substrate; (E) the working droplet spreading across the lubricant layer; and (F) the lubricant being miscible with the working liquid. Here, *l*, *d*, and *s* denote the lubricant, the probe (working) liquid, and the solid substrate, respectively. S_{xy} represents the spreading coefficient of liquid *x* on surface *y*, and *R* denotes the surface roughness factor. This figure is adapted from ref. 48 with permission from The Royal Society of Chemistry, copyright 2022.

In addition to these key criteria for SLIPS, the working liquid must remain in the form of distinct, beaded droplets on the lubricating layer without spreading out or forming a cloaking layer. The scenarios in which these conditions are not satisfied, would led in attending slippery property, depicted in Figure 1.7A-F.[48]

1.6 Strategies for Fabricating Different Bio-inspired Liquid Wettability and Functional Materials

Wettability, which describes how liquids interact with solid surfaces, is a crucial feature that significantly impacts on our daily lives. Inspired by nature and advancements in technologies, scientists have created many functional materials embedded with bio-inspired wettability through carefully associating surface structures and chemically inert environment. These materials have found a wide range of uses in fields like farming, environment remediation, and healthcare.

1.6.1 Superhydrophobic Surfaces

Over the years, various strategies have been used to fabricate superhydrophobic surfaces. As discussed earlier, fabrication of superhydrophobic surface demands two key features: micro-nano topography and low surface energy coating. The strategies for creating superhydrophobic surfaces are categorized into two principal approaches: top-down and bottom-up approaches. Basically, in a top-down approach, the roughness was introduced by different techniques like lithography,[49-53] plasma etching,[54-58] laser ablation,[59-61] etc. However, in bottom-up methods, it involves building rough structures from hydrophilic components through self-assembly or deposition techniques like sol-gel process,[62-64] layer-by-layer deposition,[65-70] chemical vapor deposition, [71-73] etc., followed by its modification with low surface energy materials. Traditional superhydrophobic coatings rely on weak chemical bonds, such as metal-thiol interactions and metal-ion bonding, which lose their property under harsh conditions.[36] When the coating's top layer is abraded, its hydrophilic interior is exposed, compromising its anti-wetting properties. Researchers have explored post-repairable approaches, such as stimuli-responsive materials or regenerating surface structures to restore embedded extreme repellent.[74,75] However, these methods require external intervention, are time-consuming, and become ineffective over time as low surface energy molecules deplete. Nevertheless, for real-world applications, it is crucial to focus on the facile fabrication and long-term durability of these superhydrophobic surfaces. In recent years, various fabrication methods have been explored to improve their robustness and longevity.

Zhang et al. developed a strategy for a durable superhydrophobic surface using a long-chain organosilane molecule with a partial amount of water, which creates hierarchical micro-nano siloxane aggregates, which can be diluted in hexane solvent for further coating, as shown in Figure 1.8A, B.[76] This dispersible suspension of siloxane aggregates can be deposited on various types of substrates through dip coating and spray coating techniques. The reactive sites on the siloxane aggregate particles, such as -Si-OH or -Si-Cl groups, can form covalent bonds with substrates that have hydroxyl groups on their surfaces. This interaction allows the particles to attach to the substrate strongly and build hierarchical structures. The long chain of organosilane provides low surface energy, whereas hierarchical micro-nano provides morphology. All solid substrates treated with the coating solution exhibited extremely high water contact angles, ranging from 168° to 171°, along with very low sliding angles between 0.5° and 1.0°. The mechanical stability of the surface coatings was evaluated through sandpaper abrasion and water impact tests. The modified superhydrophobic glass substrate maintained its superhydrophobicity, with a water contact angle greater than 160°, even after sandpaper abrasion under a pressure of 2.5 kPa over a distance of 50 cm, or after being subjected to water jetting for 10 minutes.

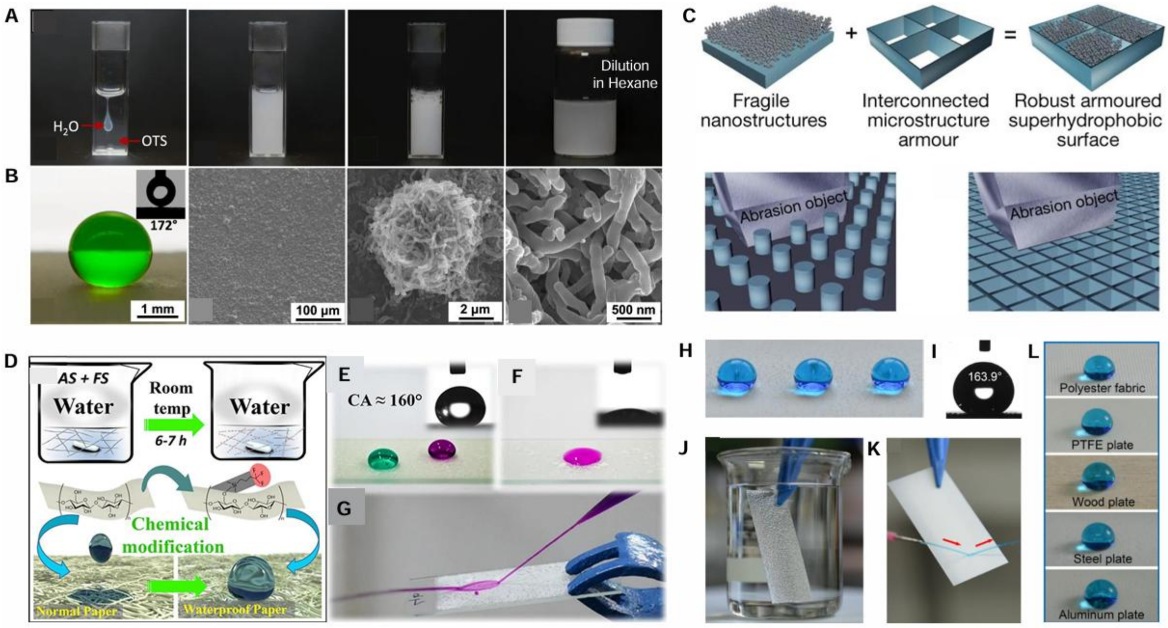

Figure 1.8 A) Digital images representing the preparation of a superhydrophobic coating solution upon mixing of OTS and water, followed by dilution with hexane. B) Digital and contact angle images (inset) with SEM image of superhydrophobic glass slide with the same diluted solution. This figure is adapted from ref. 76 with permission from Springer Nature Limited, Copyright 2020. C) Schematic representing the fabrication of a robust armoured superhydrophobic surface with a mechanism of discrete and interconnected microstructure. This figure is adapted from ref. 78 with permission from Springer Nature Limited, Copyright 2020. D) Schematic illustrating the fabrication of superhydrophobic cellulose nanofiber-based waterborne superhydrophobic coating. E, F) Digital and contact angle (inset) images of a beaded water droplet on a superhydrophobic coated substrate (E) and a hydrophilic CNF substrate (F). G) Digital images depicting the bouncing off of a dyed water jet from superhydrophobic glass. This Figure is adapted from ref. 79 with permission from American Chemical Society, Copyright, 2017. H, I) Digital image (H) and contact angle image (I) of the superhydrophobic PU/SiO_2@HD-POS substrate. J, K) Photograph representing an air cushion with intense light reflection when the superhydrophobic coating was submersed in water (J), bouncing off a dyed water jet from the coated substrate. L) A photograph representing the superhydrophobic coating was applied on the various substrates. This figure is adapted from ref. 80 with permission from WILEY-VCH Verlag GmbH & Co. KGaA, Weinheim, Copyright 2017.

Following the abrasion tests, the glass slide retained a high contact angle of 161 ± 2° and a low sliding angle of approximately 1°. This outstanding abrasion resistance is attributed to the covalent bonding of the siloxane aggregates to the surface. In another report, Xu et al. developed a transparent, superhydrophobic surface using the spin coating method by modifying hydrophilic silica nanoparticles with the (heptadecafluoro-1,1,2,2,-tetrahydrodecyl) dimethylchlorosilane (HDFTHD). The obtained fluorinated silica nanoparticles formed stable dispersions only in fluorinated solvents, such as Novec 7300 and decafluoropentane, which were used for spin-coating on a glass substrate.[77]

Next, Wang et al. demonstrated that durable superhydrophobicity can be achieved by designing surfaces with two distinct structural scales: nanoscale features that provide water repellency and microscale features that enhance mechanical strength. The microscale design consists of an interconnected surface framework that serves as protective ‘armour’, shielding the nanostructures from damage caused by abrasion, as shown in Figure 1.8C.[78] This superhydrophobic coating displayed exceptional tolerance toward 1,000 sand paper abrasion cycles, that was 10 times higher than conventional superhydrophobic coating. The mechanical durability of armoured superhydrophobic coating was verified through various tests, including tape-peeling, Taber abrasion, and scratching with an ultra-sharp object. In addition, they carried out more rigorous durability assessments, such as testing thermal stability at 100 °C for 16 days, evaluating resistance to chemical corrosion by immersing the surfaces in aqua regia or a 2.5 M NaOH solution for 4 hours, examining the impact of a high-speed water jet and check performance under high humidity to test resistance to condensation-induced failure. Even under these extreme conditions, the armoured surfaces retained their superhydrophobic properties. However, in earlier reported literature, they used tedious fabrication methods and organic solvents to develop the superhydrophobicity, which raises an environmental concern, a safety issue, and this approach is substrate selective. Further, Baidya et al. created a robust superhydrophobic coating by spray deposition technique, on cellulose nanofibers by chemically modifying them with two distinct silane-based compounds, 1H,1H,2H,2H-perfluorooctyltriethoxysilane and 3-(2-aminoethylamino)propyltrimethoxysilane, in an aqueous medium, as shown in Figure 1.8D-G.[79] This superhydrophobic surface shows excellent chemical and mechanical durability even under harsh conditions such as, sand paper abrasion, knife scratch test, water jet flow, spillage of organic solvents, etc. However, they used a toxic fluorinated compound (1H,1H,2H,2H-perfluorooctyltriethoxysilane), which is harmful to our environment. Zhang et al. developed a complete waterborne durable superhydrophobic coating without the use of fluorinated compounds by the integration of natural nanorods, palygorskite (PAL), methyltrimethoxysilane (MTMS), and polyurethane aqueous solution.[80] Li et al. also developed completely waterborne, fluorine free and mechanically durable superhydrophobic surafces. The superhydrophobic surafces were prepared by spray coating of PU aqueous solution and a hexadecyl polysiloxane treated SiO_2 aqueous suspension onto substrates, with PU serving as the adhesive (Figure 1.8H-L).[81] Despite its promise, developing mechanically durable, facile fabrication, transparent, scalable and complete waterborne superhydrophobic coating remains a challenge.

1.6.2 Liquid marbles (LMs)

Instead of a hydrophobic or superhydrophobic coating on a substrate, hydrophobic or superhydrophobic powders are used to fabricate a new type of material, i.e., liquid marbles (LMs). LMs are non-sticky droplets covered with micro- or nanometrically-scaled particles. It is defined as a liquid droplet wrapped with hydrophobic/superhydrophobic particles that blur the boundaries between solid and liquid states of matter, as shown in Figure 1.9A.[82-84]

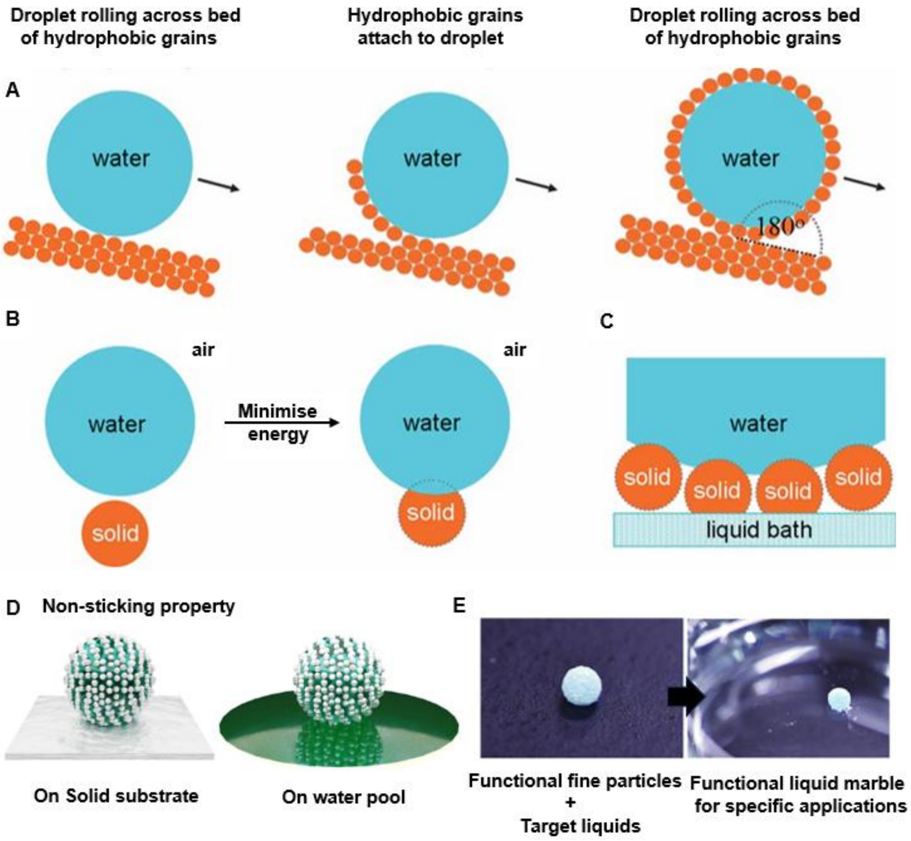

Figure 1.9 A-C) Schematic illustration of the formation of an LMs from a rolling droplet from liquid repellent powder (A), change in surface free energy on the attachment of liquid repellent particle to a droplet (B) and liquid-separation of liquid-liquid by LMs on a liquid bath. D, E) Non-sticking property of LMs on solid and liquid surface (D) and functional liquid marble for the desired application (E). This figure is adapted from ref. 85 with permission from The Royal Society of Chemistry, copyright 2023.

The anti-wettable particles adhere to the liquid-air interface due to minimise the energy of interface, preventing the liquid from direct contact with the surrounding environment.

This process developed a non-wetting system where the liquid remains isolated yet mobile.[84] The creation of LMs depends on the principle of minimizing surface energy (Figure 1.9B). When particles coat a droplet, the total system energy is reduced between the liquid and the surrounding medium (Figure 1.9C). The reduced total system energy can be described by Equation (1.6) and is at a maximum when $\theta = 90^{\circ}$.

$$\Delta G = -\gamma_{gl}\pi a^2(1-\cos\theta)^2 \qquad (1.8)$$

Here, a represents the particle radius, θ denotes the contact angle of the liquid on a particle, and γ_{gl} signifies the surface tension between the liquid and air.

This stability is a hallmark of LMs and strengthens their unique characteristics. LMs exhibits non-stick properties due to the low wettability of solid particles surrounding liquid droplets. It can roll off a solid surface or liquid pool because of a stabilized air layer known as the Cassie-Baxter state (Figure 1.9D). Low-wettability functional solid particles are used in different specific applications (Figure 1.9E).[85] In 2001, Aussillous and Quére discovered LMs for the first time.[82] They add a drop of water to a powder of lycopodium grains, typically sized at 20 µm, which are covered with fluorinated silanes, followed by gently stirring the mixture until it yields nearly spherical, composite droplets. Since the first groundbreaking report on LMs in 2001, numerous exciting studies have been reported in the literature. Their unique properties, such as non-wetting, deformability, and controlled permeability, make them valuable in various applications, including chemical sensing, drug delivery, miniaturized chemical reaction, etc.[9, 86] Different types of materials including silica nanoparticles, graphene, carbon black, carbon nanotubes, polytetrafluoroethylene particles, polymeric particles, metal oxide nanoparticles, porous crystalline nanoparticles are utilized to prepare such soft materials.[85-93] While the hydrophobic shell of LMs provides a protective environment, but the on-demand release of inner liquid is essential for various other prospective applications. In the past, various approaches were introduced to demonstrate the rapid release of inner liquid in the presence of a specific stimuli, with acidic, alkaline, light, heat, etc.,[85-93] but reports on controlling the lifetime of floating LMs on a water pool in the presence of a stimuli are extremely rare in the literature.

S. Fuji et al. created pH-responsive LMs, prepared by polystyrene particles and poly 2-(diethylamino)ethyl methacrylate (PDEA). Under basic conditions, the PDEA chain exhibits negligible charge density, resulting in precipitation. However, the PDEA chains get protonated, leading to the bursting of LMs instantly in acidic media, as shown in Figure 1.10A.[92] In another report, Zhang et al. created pH-responsive LMs prepared by 9,10-dihydroxystearic acid (DHSA), which are stable on solid, under acidic conditions, but disintegrate in alkaline conditions ($pH > 7.5$).[93] Moreover, the LMs of DHSA disintegrate in a few seconds under NH_3-rich conditions, as shown in Figure 1.10B. Next, Nakai et al. reported a thermo-responsive LMs prepared by 1-bromo-3-fluoro-4-iodobenzene (BFI), inherently hydrophobic and solid below a melting point of 46.5 °C.[88] LMs easily float on water at room temperature because it is cooler than BFI's melting point.

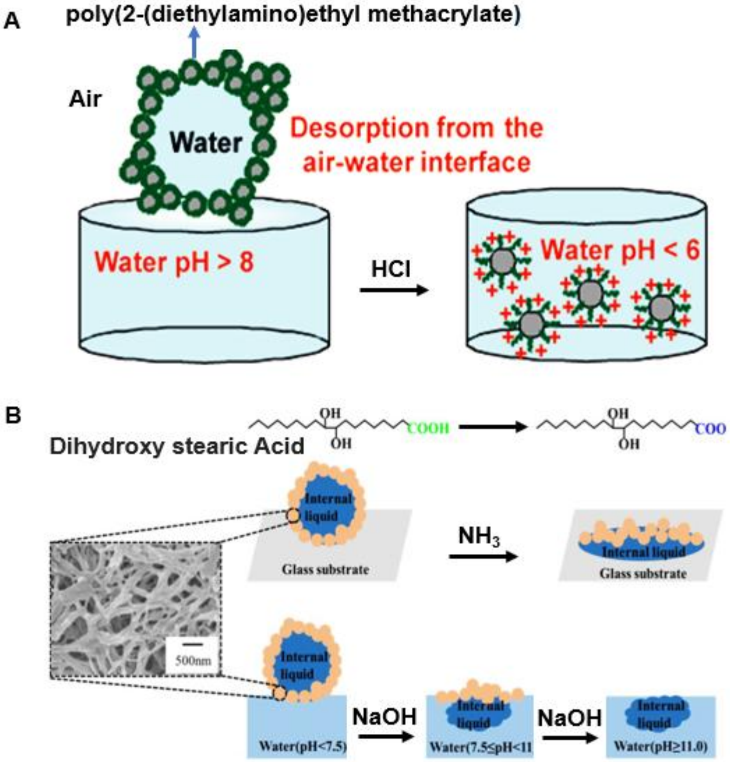

Figure 1.10 A) Schematic representing a functional liquid marble placed at the air/water interface and releasing dye on the addition of acid. This Figure is adapted from ref. 92 with permission from American Chemical Society, Copyright 2011. B) Schematic depicting a functional liquid marble placed at the air/solid and air/water interface and releasing internal liquid on exposure to NH_3 and addition of NaOH. This Figure is adapted from ref. 93 with permission from American Chemical Society, Copyright 2022.

However, when the water temperature rises above 46.5 °C, the LMs break apart, releasing the water inside into the surrounding water. This heating process can start a chemical reaction between the substances inside the LMs and those in the surrounding water. Yusa et al. reported another type of thermo-responsive LMs synthesized by poly(N-isopropyl acrylamide) (PNIPAM) powder. At room temperature (32 °C), PNIPAM is hydrophilic and dissolves in water, due to random coil conformation, causing hydrogen bonding between the pendant amide groups and water molecules.[89] However, PNIPAM behaves as a hydrophobic and separates from the water when heated above 32 °C, which is the lower critical solution temperature (LCST) of PNIPAM. A stable LMs formed using PNIPAM powder floated on the water's surface in the container. However, the LM broke apart when the bulk water temperature dropped lower than the room temperature. Gao et al. developed graphene LM (GLM) and used them as small reactors that can be heated remotely. They showed that GLM can heat up instantly due to its conducting nature. The surface temperature can be adjusted from 21 to 135

°C by changing the laser irradiation power. They studied how methylene blue containing GLM breaks down at certain temperatures.[90] Sun et al. reported a LM, synthesized through post-modification of hydrophilic NH_2-UiO 66(Zr) MOF with phenyl silane, yielding a superhydrophobic MOF. Further, this superhydrophobic MOF particle was used to form magnetic LM, where, a Fe_3O_4-containing water droplet rolled on a pile of superhydrophobic MOF particles.[91] The motion of the LM can be controlled with a magnet. The porous superhydrophobic MOF shell allows small molecules to pass through easily. This made it useful for detecting gases and vapours. To show this, they tested ammonia sensing. They used a LM containing a $CO(NO_3)_2$ solution. When ammonia was added to the water, where the LM was floating, the colour changed quickly, occurring within one minute due to formation of a complex ion. This shows that it has strong potential for sensing applications.

On the other side, a porous shell of liquid marble fails to prevent evaporation of the encapsulated volatile liquid. In this context, a similar type of liquid marble, but with a non-porous, completely closed outer shell, was designed, i.e., capsules or colloidosomes.[94-96] However, they often suffer from the inability to prevent adhesion, loss of inner liquid, and on-demand release of inner liquid.

1.6.3 Pattern Wettability

Wettability patterned interfaces are embedded with spatial variations in wettability, ranging from hydrophilic to hydrophobic/superhydrophobic regions.[97-101] In nature, desert beetles possess contrasting wettability (superhydrophobic and superhydrophilic) patterns on their back surfaces, which they utilize for efficient fog water collection.[30] The hydrophilic peaks on their backs serve as nucleation sites where water droplets initially condense. As the droplets grow and reach a critical size, gravitational and surface tension forces overcome adhesion at the hydrophilic regions. The droplets then roll over adjacent waxy hydrophobic bumps, facilitating their transport and collection. This interplay between hydrophilic and hydrophobic regions is a highly effective natural adaptation for harvesting water in arid environments. These patterns control droplet coalescence and shedding. Inspired by the desert beetle, different superhydrophobic/superhydrophilic patterned interfaces were introduced in the literature.[30, 97-101] In 2008, Pastine et al. created a superhydrophobic surface through chemical vapour deposition of multiwalled carbon nanotube forests on substrates, followed by insertion of nitrene by perfluoroarylazide moiety.[99] Further, the specific azide was selected with a carboxyl group, allowing various functionalities to be added through coupling reactions. This was used to modify surface properties. Superhydrophobic-superhydrophilic patterned interfaces were developed by exposing the surface to UV light (254 nm) for 5 minutes using a photomask.

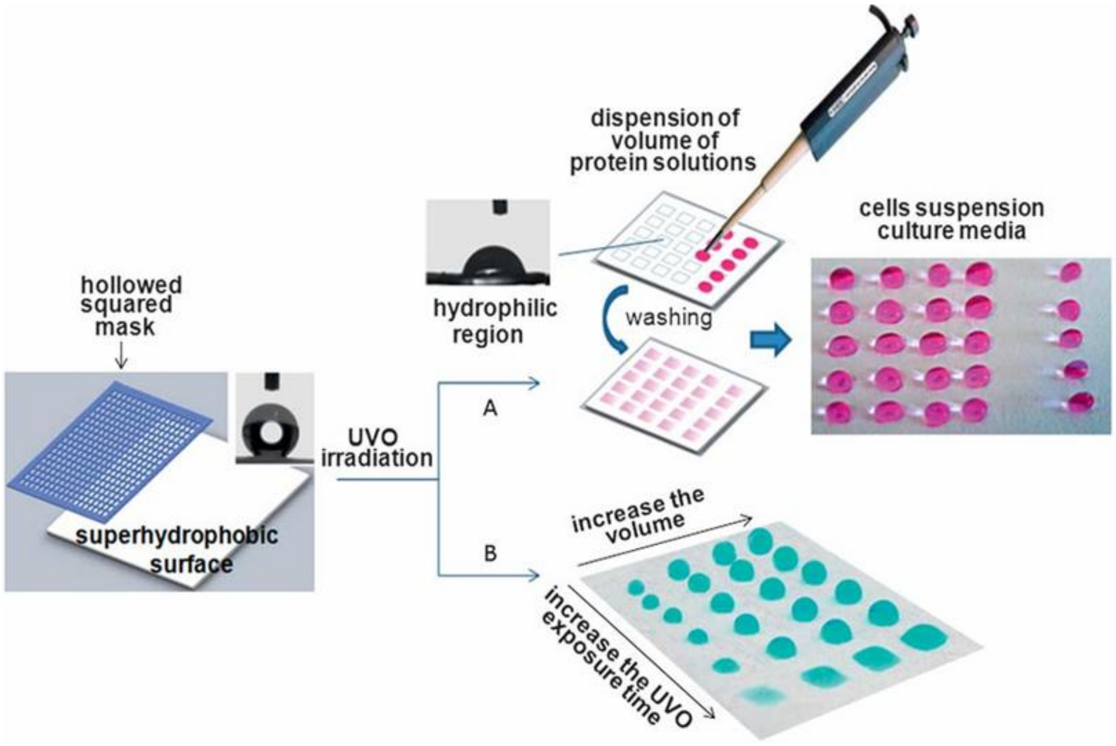

Figure 1.11 Schematic illustrating to produce the patterned interfaces (hydrophilic region on superhydrophobic background) by spatially selective ultraviolet irradiation on a superhydrophobic surface and test them for cell-protein interactions. This Figure is adapted from ref. 101 with permission from The Royal Society of Chemistry, copyright 2011.

Next, in 2011, Zahner et al. adopted a photografting method to create superhydrophobic surfaces with the help of butyl methacrylate (BMA), and ethylene dimethacrylate (EDMA). They had a static water contact angle of 163°. A single-step surface modification method using UV-initiated photografting was employed to create a superhydrophilic pattern on a superhydrophobic background, resulting in static water contact angles (WCA) 0°.[100] Neto et al. demonstrated a phase separation method to develop a superhydrophobic polystyrene (PS) surface with WCA ~ 156.2°. After that, it was spatially selectively exposed to UV and ozone to introduce hydrophilic patterns, as shown in Figure 1.11.[101] This patterned wettability, achieved by engineering surfaces with regions of differing hydrophilicity to hydrophobicity, provides a powerful platform for spatial control of cell behaviour in culture systems. Cell culture refers to the process of growing cells in a controlled artificial environment outside their natural environment. This technique involves the rapid deposition of biomaterials or proteins on patterned surfaces, allowing for microlitre-scale characterization of their interactions with cells.[101]

Bai et al. used the spin coating method and selective UV light illumination to develop a superhydrophobic/superhydrophilic patterned interface with the help of hazardous fluorine chemistry.[102] Later, researchers have shown significant interest in utilizing patterned interfaces with contrasting wettability for moisture management in addition to other applications, including microfluidics, guided transportation of liquid and so on.[103-106]

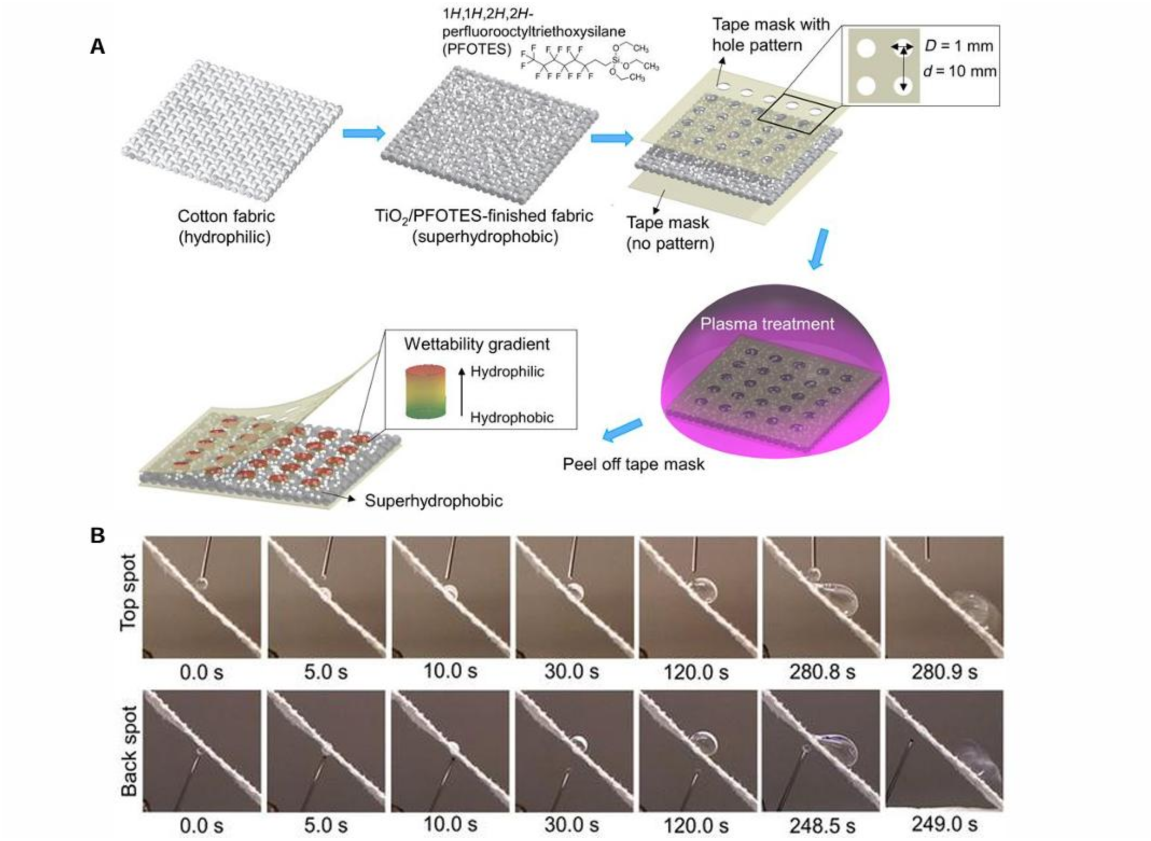

Figure 1.12 A) Schematic representing the fabrication of patterned superhydrophobic fabric for unidirectional water transport. B) Digital images of patterned superhydrophobic fabric, when water droplet was beaded on the plasma-treated top spot, it rolled off, but exposure of water to the back spot areas allows the transfer of water with a flow rate of 10 µl/min at an angle of 45°. This Figure is adapted from ref. 103 with permission from The American Association for the Advancement of Science, Copyright 2020.

Lao et al. developed a patterned superhydrophobic fabric by spray coating technique, where perfluorosilane-coated TiO_2 nanoparticles were subjected to spatially selective plasma treatment to create gradient wettability spot channels for unidirectional water transport for moisture management, as shown in Figure 1.12A.[103] Plasma treatment ensured a reduction in hydrophobicity to different extents, creating a gradient in wettability throughout the thickness of the fabric. The prepared patterned superhydrophobic fabric displayed a unidirectional water transport as well as water repellent property. The patterned superhydrophobic fabric was positioned at a 45° angle, and beaded water was delivered onto the top or back spot regions using a needle connected to a continuous water supply at a flow rate of 10 µl/min. When water was dropped onto the top side of the fabric, the droplet got bigger, by the time the last drop was added at 280.8 seconds, it had grown to about 46 microliters and was large enough to roll off the fabric (Figure 1.12B). Throughout this process, no water passed through the fabric. In the opposite direction, when the first droplet touched the back side of the fabric, it quickly moved through to the top side after 10.0 seconds. As more water collected, it reached a similar size by 248.5 seconds, and the large droplet rolled off again from the top surface (Figure 1.12B). Thus, it displayed a unidirectional water transport property. Subsequently, a few other patterned channels were developed by creating gradient wettability spot channels for moisture management.[104-106]

In the previous literature, mostly noncontact patterning methods (UV-ray, plasma treatment, etc.)[103-106] were spatially and selectively applied to perturb the hydrophobic chemical groups (e.g., fluorinated hydrocarbons) on hydrophobic/superhydrophobic interface to achieve patterned textile; however, controlled and uniform penetration of UV-radiation or plasma across the highly opaque fibrous substrate would be a challenging task to achieve. Thus, it is difficult to introduce a wettability gradient with precision across the selected fibrous substrate.

1.6.4 Solid slippery

The superhydrophobic surface is used to repel water for many different applications, but it fails to repel low-surface-tension organic solvents; rather, it readily infiltrates into the superhydrophobic coating. Researchers have often used complex topographies featuring re-entrant surface curvatures in combination with fluorinated chemical modifications to mitigate the fouling of solid surfaces by low-surface-tension organic solvents.[107-111] Nevertheless, achieving such complex surface architectures on a large scale while ensuring long-term durability remains a huge challenge. To solve this issue, slippery liquid-infused porous substrates have been developed in the past decade to repel all types of liquid irrespective of their surface tension.[42,112] However, long-term durability has always been a concern due to the leaching of lubricant on exposure to probe liquids.

To overcome this problem, another type of slippery coating has been developed, without infusing liquid lubricants, is recognised as a solid slippery coating. It has been prepared by infusing phase-transitioning solid lubricants (paraffin and polymer) in a porous matrix.[113,114] Subsequent methods have been adopted to include layer-by-layer growth of nanoparticles on the surface,[115] direct deposition of nanoparticles,[116] direct to form an assembly of oligomers,[117,118] growth of polymer brushes,[119] attachment of a flexible polymer,[120-121] Such solid slippery surfaces tend to be more durable than liquid-infused ones, as they do not depend on a liquid lubricant that can degrade or leach over time. These surfaces are more resistant to high humidity, extreme temperatures, and harsh physical and chemical exposure. Meng et al. developed a solid slippery surface by infusing phase-transitioning solid paraffin wax (melting temperature of 41 ˚C) into a hydrophobic polystyrene porous network.[113] This slippery surface demonstrated repellency against various liquids with surface tensions ranging from approximately 32 mN/m to 72 mN/m. However, it failed to repel liquids with surface tension values below 32 mN/m, such as ethanol, methanol and similar other solvents with low surface tension. Notably, such coatings exhibited excellent self-healing ability at elevated temperature. This behaviour is attributed to the thermoresponsive nature of paraffin wax. When heated above its melting point, the paraffin melts and flows into the damaged regions, forming a smooth liquid layer. Upon cooling to room temperature, the paraffin solidifies, effectively healing the damaged area and restoring its liquid-repellent properties.

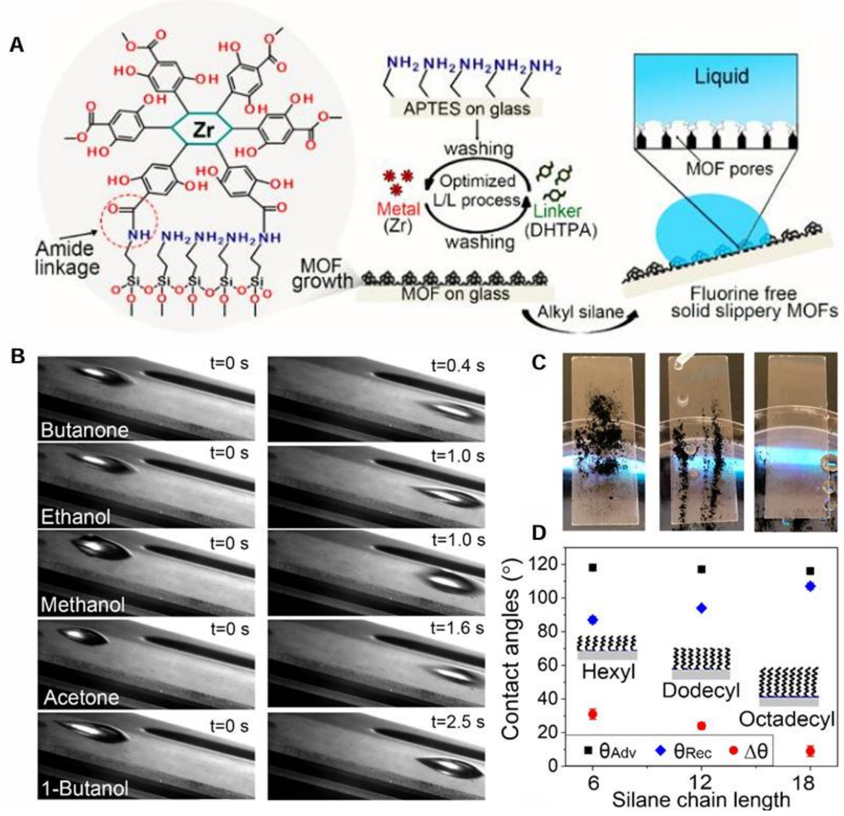

Figure 1.13 A) Schematic depicting the fabrication of MOF-based solid slippery surface by a layer-by-layer approach. B) Digital images illustrating sliding of low-surface-tension liquids at a 15˚ tilting angle. C) Digital images illustrating the self-cleaning process of the solid slippery surface. D) Graph accounting the effect of different chain lengths of alkyl silane on water advancing, receding, and hysteresis angles. This Figure is adapted from ref. 115 with permission from American Chemical Society, Copyright 2021.

In another report, Singh et al. prepared a transparent and robust MOF-based solid slippery amphiphobic surface by a layer-by-layer approach in DMF solvent through postmodication with alkyl silanes, where hydroxyl groups present in the MOF linker reacted with alkyl silane, as shown in Figure 1.13A.[115] This solid slippery surface exhibited repellency against various liquids with surface tensions ranging from approximately 22.1 mN/m to 72 mN/m (Figure

1.13B) and also show self-cleaning property (Figure 1.13C-D). Notably, this surface can sustain thermal stability up to 200 °C, resistance to water jet (up to approximately 35 m/s, with a Weber number exceeding 4×10^4), pencil scratch test, be durable in harsh acidic and alkaline environments, etc. Next, Wang et al. prepared an omniphobic solid slippery surface by acid-catalyzed polycondensation of dimethyldimethoxysilane following the dip coating method in toluene solvent.[120] This coating displayed repellency against various liquids with surface tensions ranging from approximately 18.4 mN/m to 78.2 mN/m and also shows self-cleaning property with thermal stability up to 150 °C.

Most reported solid slippery surfaces have been fabricated in fully or partially organic solvents, which are harmful to our environment, and tedious fabrication restricts to scaleup. So, it is important to develop solid slippery surfaces, which is completely waterborne, substrate-independent, highly transparent, mechanically durable and it should be prepared adopting a facile fabrication process.

1.7 Applications of Functional Liquid Wettability and Related Materials

Wettability-based functional materials and interfaces are gaining significant attention for their diverse applications across multiple disciplines such as oil-water separation,[109,124,134-141] microfluidics,[109,116,142-145] anti-fouling,[148-154] anti-icing,[155-161] water harvesting,[162-169,] etc. Some key applications are discussed below:

1.7.1 Oil-water separation

The contamination of water by oils resulting from oil spill accidents and the discharge of industrial effluents leads to a significant environmental and public health concern.[122-126] Various remediation strategies have been developed to address this issue, including in situ burning, air flotation, chemical and microbiological oxidation and electrocoagulation, etc.[125,126] Among these approaches, the physical separation process has garnered considerable attention due to its dual capability of achieving simultaneous separation and facilitating the straightforward collection of both liquid phases.[91,127-130] A particularly promising approach within the domain of physical separation involves using superhydrophobic interfaces for the separation of oil-water mixtures. These interfaces have inherent ability to repel water while preferentially allowing oil passage, enabling efficient phase separation. The implementation of superhydrophobic coatings on porous substrates displayed substantial potential due to their simplicity, scalability, and high separation efficiency, for mitigating oil-water contamination.

In 2004, Feng et al. first demonstrated that a coated metal mesh embedded with superhydrophobic and superoleophilic properties, allowing for the effective separation of immiscible oil-water mixtures.[128] The fabrication process involved spraying a low surface energy polytetrafluoroethylene (PTFE) emulsion, resulting in a crater-like hierarchical structure on the stainless-steel surface while keeping the mesh's pores unperturbed (Figure 1.14A).

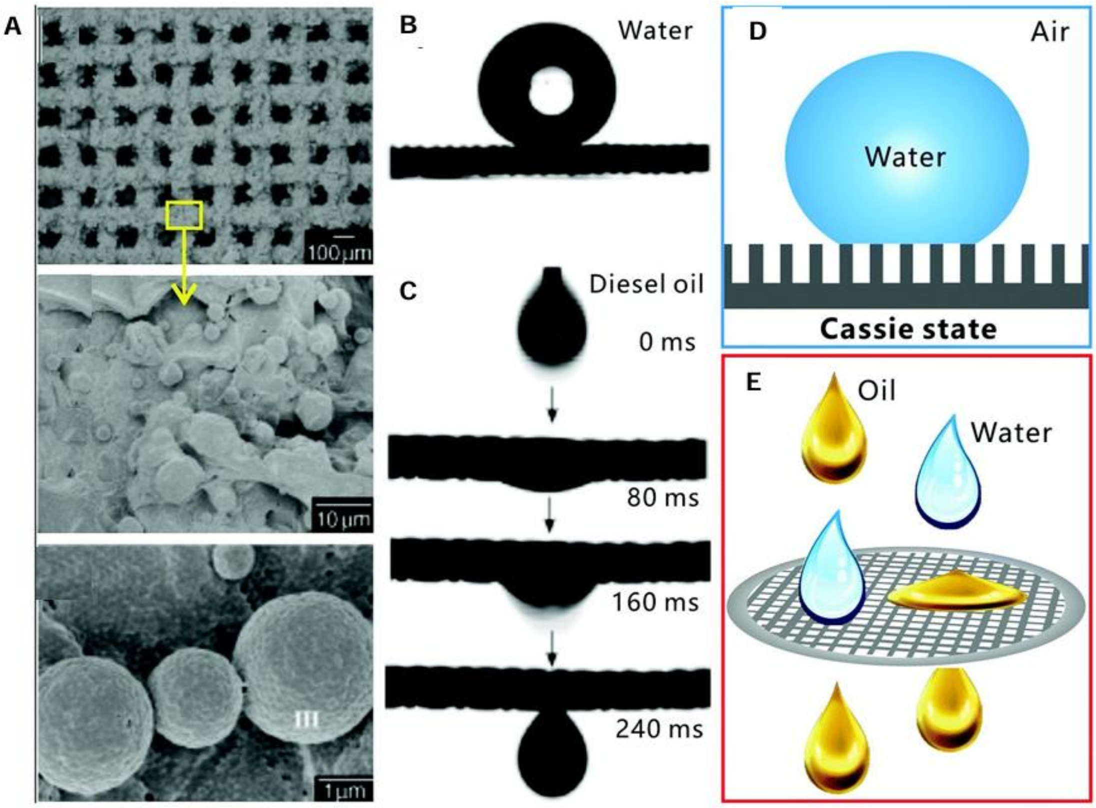

Figure 1.14 A) Scanning electron microscope images of superhydrophobic stainless steel mesh. B, C) Depicting the water repellence behaviour (B), spreading behaviour of diesel oil from the superhydrophobic mesh (C). D, E) schematic representation of superhydrophobic mesh (D) and oil-water separation behaviour (E). This figure is adapted from ref. 129 with permission from The Royal Society of Chemistry, copyright 2018.

This surface modification imparted non-adhesive superhydrophobicity to the mesh, characterized by a water contact angle of more than 150° and a roll-off angle of 4° (Figure 1.14B). In contrast, diesel oil droplets quickly spread and a complete penetration occurred within 240 milliseconds (Figure 1.14C). Thus, the coated mesh exhibited dual functionality of superhydrophobicity and superoleophilicity, allowing for efficient separation of an oil-water mixture with a reported separation efficiency of 95% (Figure 1.14D, E). Sun et al. prepared a metal organic framework (MOF) using metal ($ZrCl_4$) and ligand (2-aminoterephthalic acid) and subsequently modified it with phenyl silane to develop superhydrophobicity. The superhydrophobic MOF was coated physically on stainless mesh, it allowed only organic phase components from the organics/water mixture.[91] The mesh membranes mentioned above are ineffective in separating the oil-in-water emulsion. In another report, Cheng et al. described the creation of a superhydrophobic membrane by combining polyvinylidene fluoride and polydimethylsiloxane-based solutions through a simple electrospinning method.[130] This membrane effectively separated water-in-oil emulsions, achieving a separation efficiency of more than 99.6%.

1.7.2 No-Loss Liquid Transportation

No-loss liquid transportation is the ability to move liquid droplets across a surface without any loss of volume, which means the droplet leaves no residue behind during movement. This is especially important in microfluidics, chemical analysis, or biomedical applications where precise liquid handling is required.[131-132] Superhydrophobic surfaces with extremely high water repellency (contact angle >150°), where water droplets on these surfaces are highly mobile, often rolling off easily due to minimal contact between solid and liquid due to metastable trapped air.

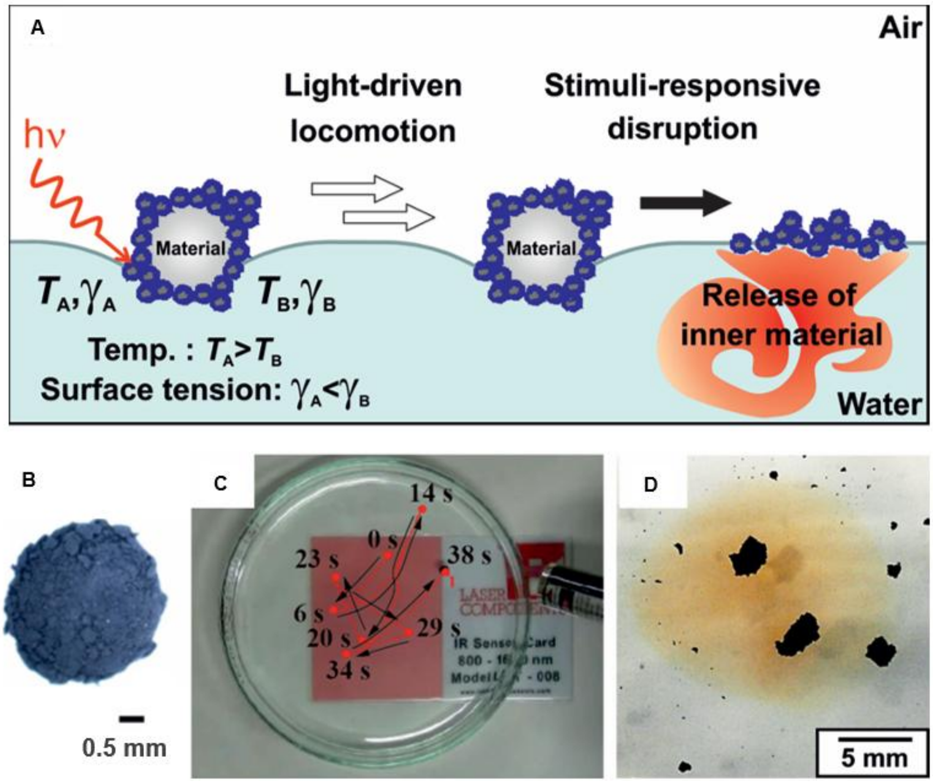

Figure 1.15 A) Scheme representing the NIR laser irradiation-driven motion using functional liquid marbles. B- D) Digital images of liquid marble (B), NIR laser irradiation on liquid marble for stimuli-induced movement (C) and D) disruption of the liquid marble to release its inner material, on the water-air interface. This figure is adapted from ref. 133 with permission from WILEY-VCH Verlag GmbH & Co. KGaA, Weinheim, Copyright 2016.

In addition to superhydrophobic surfaces, slippery surfaces also displayed remarkable no-loss liquid transportation performance due to an extremely smooth surface and almost zero pinning. The techniques are now used engineering, physics, chemistry and biology. Transportation of liquid without adhesion loss is challenging due to the interaction between the two phases. Initiating the motion of a liquid droplet requires significant forces and often leads to the deposition of particles behind the droplet.[131-132] To overcome this problem, LMs were discovered, which consist of encapsulating a liquid droplet with a hydrophobic/superhydrophobic powder.[82] The formed liquid marbles act as a soft solid and exhibit significantly lower adhesion to solid surfaces. Consequently, their movement can be induced by gravitational, electrical, or magnetic forces.[85]Additionally, due to the minimal viscous friction during motion, some researchers have successfully achieved rapid droplet motion without any leakage.[85] In this regard, Paven et. al. reported light-driven actuation of liquid marbles, prepared with polypyrrole and carbon black modified with octadecanoic acid to render hydrophobic material.[133] It was used to transport the liquid with hydrophobic materials encapsulated within the LM, which were then released at a certain place and driven by different external stimuli depending on their encapsulated materials (Figure 1.15A-D). Xue et al. reported a LM that was responsive to magnets. A magnetic LM was synthesized by fluorinated decyl polyhedral oligomeric silsesquioxane (FD-POSS) and hydrophobic magnetic nanoparticles. It acted as an encapsulating agent to construct LMs from both aqueous solution and organic solvent with a wide range of surface tension from 72 to 20.1 dyne cm^{-1}, and it behaves as a universal miniature reactor for chemical reaction, storage, and transportation of liquid.[134] However, LMs have some drawbacks; it is not useful for long-term storage due to metastable trapped air present in superhydrophobic materials, due to loss of evaporation and adhesion of liquid at the solid interface of materials.

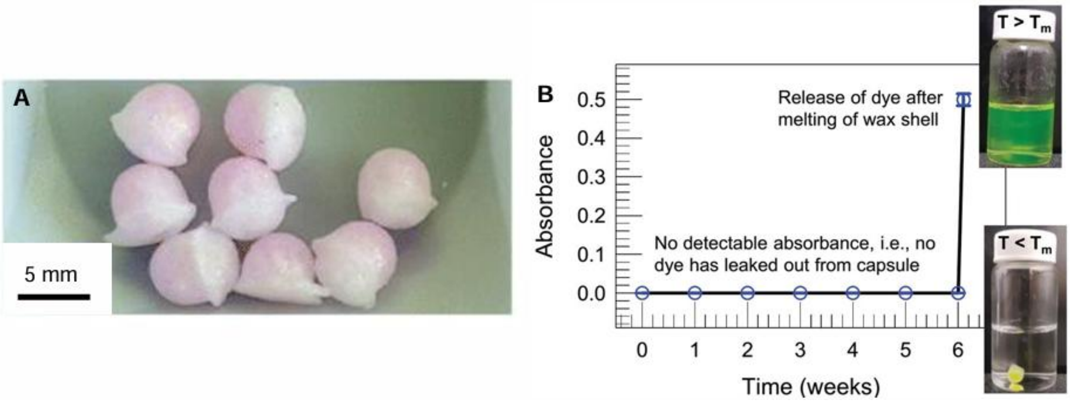

Figure 1.16 A) Photograph of wax-shelled capsules. B) leak-proof wax-shelled capsules over six weeks, and then it was melted by heating above the melting temperature (Tm), where the absorbance in the solution suddenly changes, digital images of a vial before (colorless solution) and after (green color solution) melting the capsule. This figure is adapted from ref. 94 with permission from The Royal Society of Chemistry, copyright 2019.

To overcome this problem, Goertz et. al. reported a capsule, prepared by wax and used for controlled encapsulation and targeted release of chemical reagents at a specific temperature.[94] Wax-shelled capsules allowed for the hermetic encapsulation of small, hydrophilic solutes (Figure 1.16A). Capsules with a paraffin-wax shell were loaded with fluorescein and submerged in water. Over six weeks, the absorbance of the surrounding solution remained at zero, demonstrating that the shell had no leakage during this period. When heated above the melting temperature, the capsules melted, resulting in the absorbance of the solution rising to 0.5. Photographs of the vial taken before and after the melting of the capsules depicted this change (Figure 1.16B).

1.7.3. Anti-biofouling

Antibiofouling is a process to prevent the accumulation of unwanted organisms. Biofilms can foul a broad range of infrastructure, systems and equipment, including plumbing systems, oil refineries, medical implants, food production lines and air conditioning networks. Over time, these biofilms can cause increased drag, structural damage, and reduced fuel efficiency.[135-137] Superhydrophobic and slippery surfaces have received significant attention for creating bioinspired anti-biofouling surfaces due to their liquid repellence and low adhesion, as they also effective in reducing biofouling.[137,138] Pernites et al. introduced a superhydrophobic polymeric surface prepared by deposition of a polystyrene layer followed by electrodeposition of the polythiophene layer. The superhydrophobic polymeric surface showed remarkable resistance towards the adhesion of fibrinogen and E. coli. The anti-wetting property of the polymeric surface hampers bacterial adhesion due to a change in redox properties by a potential switch of conducting material, which can turn the wettability of the material from hydrophilic to superhydrophobic. In contrast, without a potential switch, it exhibited significant bacterial colony growth, demonstrating its lack of anti-bacterial properties.[139] Besides superhydrophobic materials, slippery surfaces showed outstanding anti-fouling performance by minimizing direct contact between bio-organisms and the substrate.[140,141]

In another report, Epstein et al. developed SLIPS by infusing perfluoropolyether (Krytox-103) in a porous superhydrophobic PTFE membrane with an exceptional ability to prevent biofilm attachment (Figure 1.17A). The fabricated SLIPS significantly reduced the P. aeruginosa biofilms after 48 hours of growth on SLIPS (Figure 1.17B) and superhydrophobic PTFE (Figure 1.17C), confirmed by the fluorescence microscopic images. Further, they compared the residue left behind after an evaporation of a P. aeruginosa biofilm culture droplet on SLIPS (Figure 1.17D) and superhydrophobic PTFE (Figure 1.17E). On the SLIPS surface, the weakly adhered biofilm retracts cleanly during evaporation, resulting in a small, easily detachable pellet.

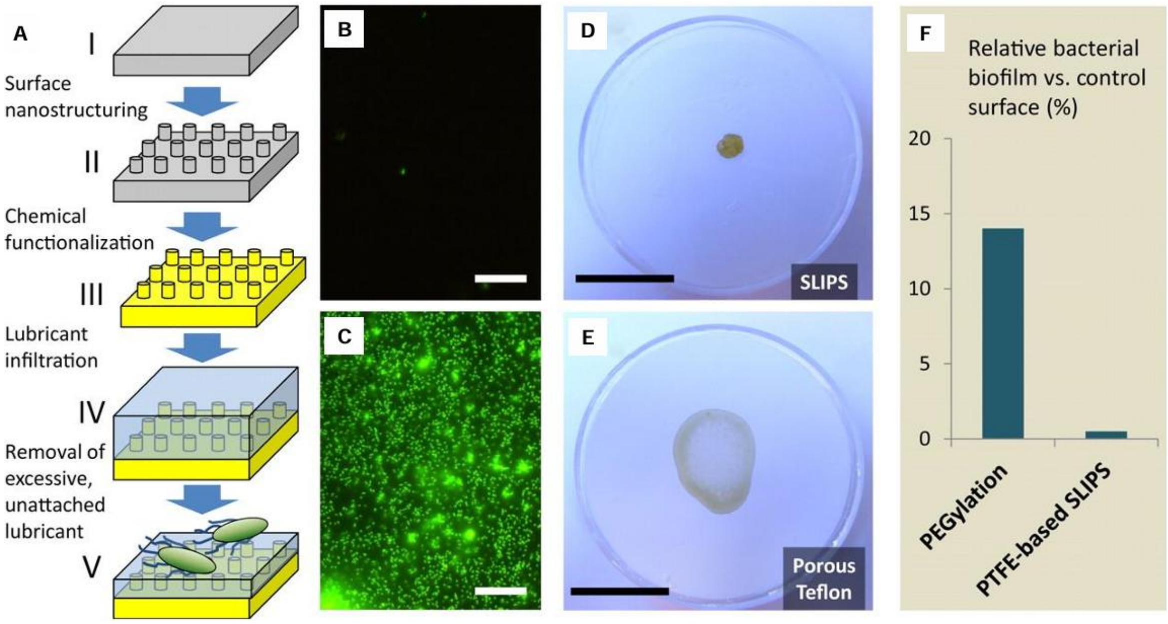

Figure 1.17 A) Schematic depicting the fabrication of SLIPS. B-C) Fluorescence microscopic images show P. aeruginosa biofilms after 48 hours of growth on SLIPS (B) and superhydrophobic PTFE (C) surfaces. Scale bar: 30 µm. D) Residues left behind after evaporation of a P. aeruginosa biofilm culture droplet on SLIPS (D) and on superhydrophobic PTFE (E). Scale bar: 2 cm. F) This plot illustrated the biofilm attachment on SLIPS after 7 days is compared to a PEGylated surface after only 5 hours. This figure is adapted from ref. 140 with permission from National Academy of Sciences, copyright 2012.

In contrast, biofilms grown on porous superhydrophobic PTFE exhibit complete surface wetting and strongly adhered coffee ring-like residue. Further, they compared biofilm attachment on SLIPS after 7 days to a PEGylated surface after only 5 hours. Even under the most favourable assumption that the PEG surface maintains its anti-biofilm performance over 7 days without degradation or surface chemistry changes, the SLIPS platform still shows a > 30-fold improvement, with only 0.4% relative attachment.[140] Tesler et al. introduced a novel approach to create an omniphobic slippery surface by depositing titanium oxide (TO) nanoparticles onto stainless steel via chemical vapor deposition to demonstrate anti-fouling properties. Then substrate was modified with a low surface energy perfluoroalkyl moiety-bearing phosphate group, resulting in a TO-embedded superhydrophobic surface (TO-SHS). Further the infusion with lubricants (perfluoropolyether) produced an omniphobic TO-contain slippery surface, termed TO-SLIPS. The omniphobic TO-SLIPS significantly reduced blood adhesion while retaining its slippery properties, even after prolonged submersion in a filled cuvette with blood. In contrast, TO-SHS lost its superhydrophobic properties upon submersion, leading to an adherence of blood. Thus, the slippery surface remains more effective in inhibiting bacteria and algae growth, indicating its potential for marine applications.[141]

1.7.4. Anti-icing

Icing is a common phenomenon when temperatures drop to freezing temperature. Ice formation can be dangerous for roads, power transmission lines, airplanes and ships.[142,143] It is important to find crucial ways to prevent and remove ice. Traditional methods, like using chemicals or scraping ice, can be complicated and expensive. It also demands external input of energy.[144,145]

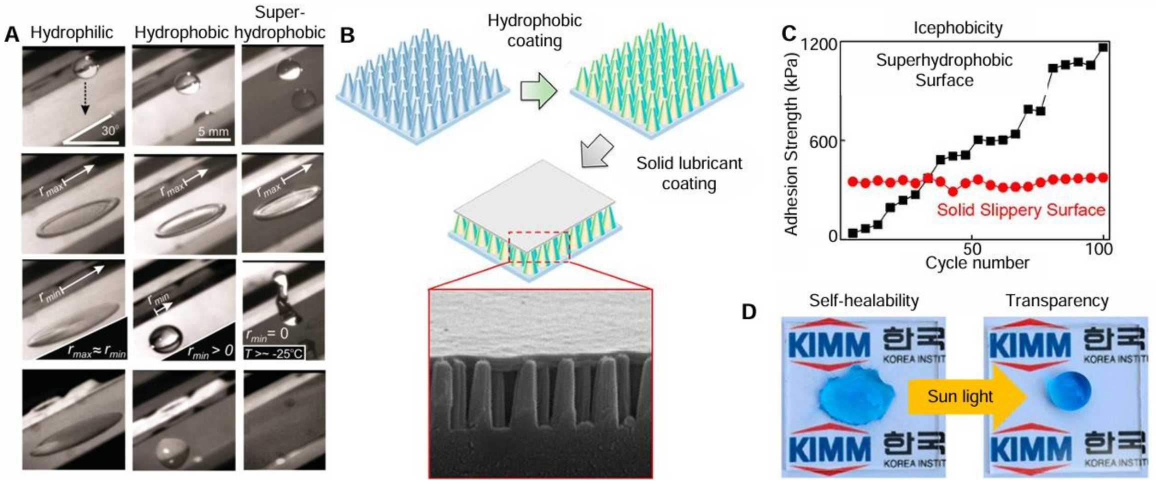

Figure 1.18 A) Digital images comparing the anti-icing properties between hydrophilic, hydrophobic and superhydrophobic surfaces. This Figure is adapted from ref. 147 with permission from American Chemical Society, Copyright 2010. B-D) Schematic representing the fabrication of solid slippery surface (B), graph comparing the anti-icing properties between superhydrophobic and solid slippery surface (C), digital image illustrating the self-healable and transparency of solid slippery surface (D). This Figure is adapted from ref. 148 with permission from American Chemical Society, Copyright 2020.

In contrast to the earlier approach, superhydrophobic and slippery surfaces help to prevent ice formation or adhesion by repelling water.[146] In 2010, Mishchenko et al. demonstrated their ability to accumulate ice over extended periods at freezing temperatures. When a stream of droplet ($T_{\text{droplet}} = 0\ ^{\circ}$C) was released from a height of 10 cm onto the surfaces ($T_{\text{substrate}} = -10\ ^{\circ}$C) tilted at an angle of 30°, the hydrophobic surface exhibited an approx one min delay in ice formation as compared to the hydrophilic surface, On the other hand, superhydrophobic surface, no ice accumulation was seen after 10 minutes of water flow (Figure 1.18A).[147] Thereafter, Han et al. developed an anti-icing, self-healable and highly transparent solid slippery interface. They mimicked the Moth-eye nanopillar structures for porous SLIPS structures and coated them with paraffin wax as a solid lubricant to repel the water droplets (Figure 1.18B-D). It provides a solid, slippery surface to reduce freezing time and adhesion strength of water while also possessing self-healing properties. This coating was applied on the glass cover of solar cells to maintain their unperturbed performance.[148]

1.7.5. Guided Transport of Liquid

Guided transport of liquid involves controlling the movement of liquids in a certain direction.[149-153] In nature, these unique liquid behaviours can be seen on natural surfaces. For example, the peristome surface of the pitcher plant quickly transports water in a certain direction by a slippery surface to trap insects,[151] shorebirds keep their beaks continuously open to drink water,[152] while the semi-open capillary channels on the surface of the Texas horned lizard's skin guide water movement.[153]

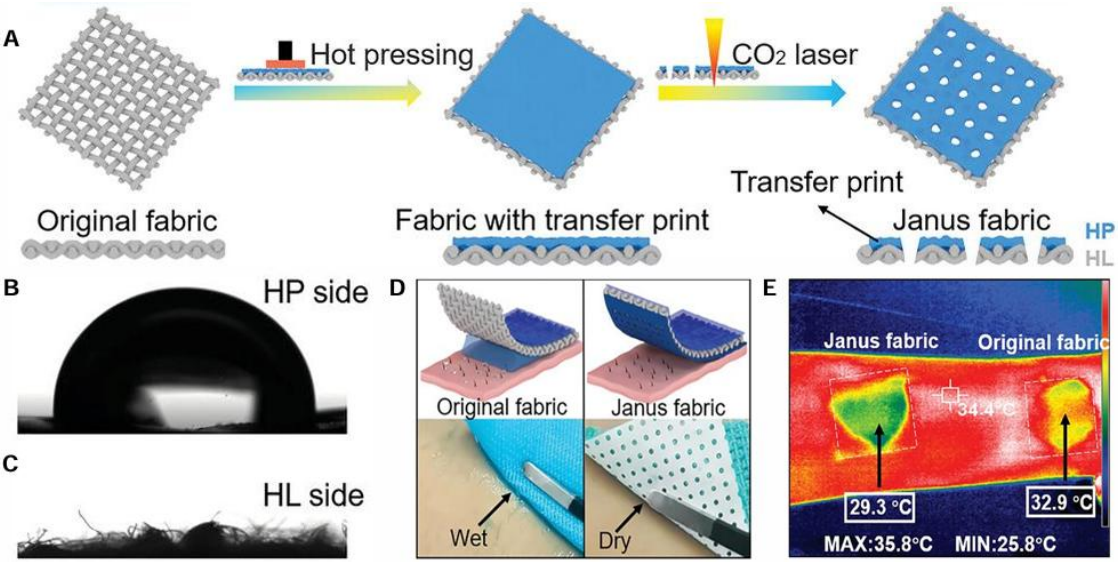

Figure 1.19 A) Schematic representing the fabrication process of the Janus fabric based on the thermal transfer printing followed by the CO_2 laser technique. B, C) Contact angle images of a beaded water droplet placed on both sides of the Janus fabric, hydrophobic side (B) and hydrophilic side (C) respectively. D) Schematic and digital images exhibited the sweat transport performance of Janus fabric and cotton fabric for personal moisture management. E) Infrared camera image displayed thermal management of the Janus fabric and cotton fabric covering over wet skin. This figure is adapted from ref. 156 with permission from WILEY-VCH Verlag GmbH & Co. KGaA, Weinheim, Copyright 2023.

To draw inspiration from these phenomena, researchers have developed special structures by using chemical gradient modifications[154] and anisotropic wettability gradient[155] methods to transport liquid in a specific direction without requiring external energy. This is done by adjusting the surface's energy to guide how the liquid spreads or moves on a solid surface. Zhou et al. developed a Janus fabric by thermally transferring hydrophobic prints onto a highly hydrophilic cotton fabric, forming a conical micropore array on its surface using the CO_2 laser method, as shown in Figure 1.19A.[156] The surface wetting characteristics of the Janus fabric were evaluated using water contact angle (WCA) measurements. The top surface displayed apparent hydrophobicity with WCA~102.1° (Figure 1.19B), while the bottom surface exhibited superhydrophilic with a WCA of 0° (Figure 1.19C), confirming the successful fabrication of a

Janus fabric. Further, they demonstrated the fabric's unidirectional liquid transport capability for personal moisture and thermal management, as shown in Figure 1.19D, E. To mimic human perspiration, they added artificial sweat on human skin and covered it with Janus fabric on wet skin. Sweat directly passes from the skin side (hydrophobic side) to the outer surface (hydrophilic side), which leads to wet skin turning into dry skin (Figure 1.19D). The skin surface temperature under the Janus fabric was approximately 29.3 °C, which is about 3.6 °C cooler than the temperature under the cotton fabric, which was around 32.9 °C (Figure 1.19E). This behaviour confirms that the Janus fabric enables directional liquid transport from its hydrophobic to hydrophilic side. In another report, Wang et al. created a Janus PET fabric by depositing a cation-π hydrophilic agent (CPHA) onto one side of a hydrophobic PET fabric, enabling directional liquid transport through spray coating.[157]

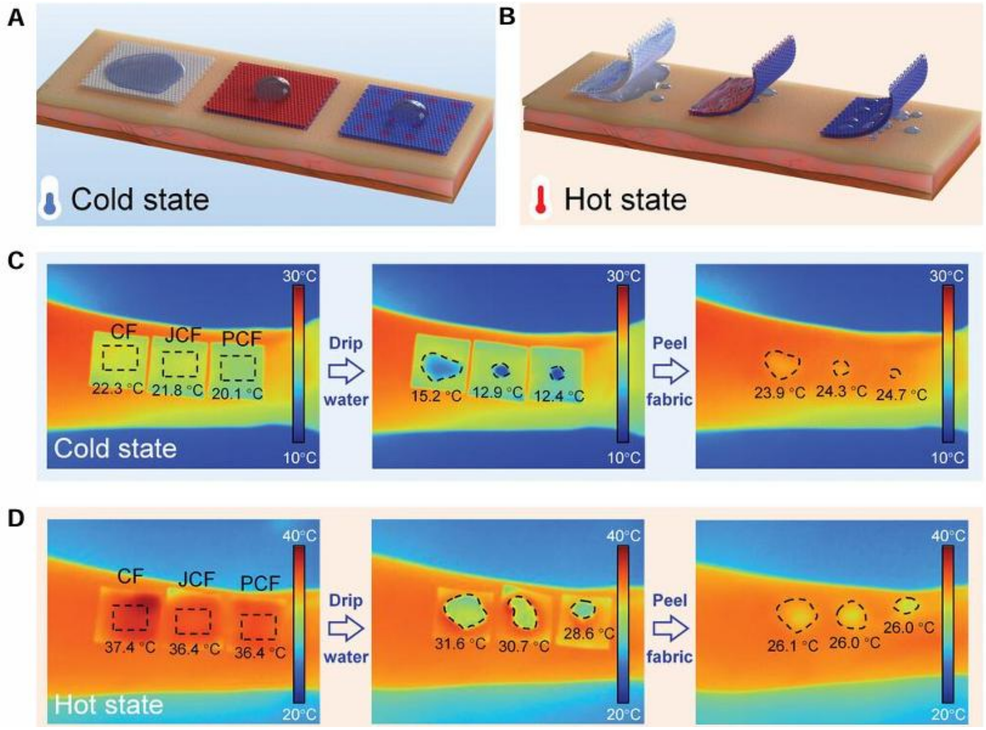

Figure 1.20 A) Schematic representing the thermal management properties of fabrics; A) protects against the invasion of rainwater in the cold state, and B) unidirectional transportation of sweat from inner side fabric to outside fabric in the hot state. Infrared images of the cotton fabric (CF), Janus cotton fabric (JCF), and patterned cotton fabric (PCF) put on the skin in C) cold and D) hot environments. This figure is adapted from ref. 158 with permission from WILEY-VCH Verlag GmbH & Co. KGaA, Weinheim, Copyright 2023.

The Janus PET fabric transports sweat away from the skin side to the outer surface while preventing water from the reverse side, helping to keep the skin dry and clean. However, the previously reported directional liquid transport fabrics can effectively move moisture (such as sweat) from the inner, skin-facing side to the outer surface for evaporation. Their performance declines once the outer layer becomes saturated. At that point, the rate of liquid transport decreases, and the fabrics become heavier and stick to the skin. Moreover, these fabrics are unable to repel liquid contaminants from the external environment.

To address this issue, Li et al developed a fouling-proof patterned Janus fabric that derived from Boron Nitride (BN) particles with a fluorinated polyelectrolyte multilayer was subjected to a spatially selective ultraviolet-triggered strategy to develop wettability gradients for unidirectional liquid transport.[104] Further, they have shown the unidirectional water transport and water repellency. In another report, Lin et al. fabricated a patterned hydrophobic fabric by a spray coating mixture of 3-(trimethoxysilyl)propyl methacrylate and [2-(Methacryloyloxy)ethyl]dimethyl-(3-sulfopropyl), where spatially selective ultraviolet (UV) illumination provided a gradient wettability spot channels for guided water transport.[158] Further, they demonstrated thermal management performance of various fabrics was evaluated under cold and hot conditions (Figure 1.20A-D). In the cold environment, water was dropped onto the outer surface of each fabric placed on the arm to mimic rain (Figure 1.20A). In the hot environment, water was applied between the skin and fabric to mimic sweat (Figure 1.20B). An infrared camera recorded both fabric surface temperatures during water diffusion and skin temperatures after fabric removal. As shown in Figure 1.20C, fabric surface temperatures in the cold conditions were 22.3 °C, 21.8 °C, and 20.1 °C, respectively. Water spread quickly across the surface of CF, while it remained more localized on the other two fabrics. After removal, the skin under PCF was 0.8 °C warmer than under CF. In the hot conditions, water diffused across both surfaces of CF, while in JCF and PCF, it remained on the upper surface, with PCF showing the least spread on the fabric (Figure 1.20D). The average skin temperature after fabric removal was similar across samples; however, the cold sensation area was smallest under PCF. Its antifouling property in cold conditions and one-way water transport in hot conditions effectively regulate the skin's moisture, giving comfort in different environments.

1.7.6. Other applications

Apart from the above-mentioned applications, functional liquid wettability and related materials have many other potential applications, including water harvesting,[159-162] anti-corrosion,[163,164] drug delivery,[165,166] energy harvesting,[167,168] anti-counterfeiting,[169,170] etc.

1.8. Motivation and Objectives

Over the past decade, significant progress has been achieved in fabricating artificial anti-wetting interfaces because of their practical potential applications. Various methodologies and chemical modifications have been explored to enhance the durability and performance of these artificial anti-wettable surfaces. Advanced material engineering strategies, including micro/nano structuring, surface energy modulation and biomimetic design, have been employed to optimize their wettability, mechanical robustness, environmental concern and long-term stability in real-life environments. However, there is still a need for developing anti-wetting coatings as they mainly suffer from mechanical durability, the use of toxic organic solvents, facile synthetic approaches, lack of ability to tailor water wettability and transparency, which restricts their use in practical applications. Though there are some approaches for modulating the liquid wettability, but still a facile approach for modulating liquid wettability across the three-dimensional coating is still a challenge. Mostly, researchers have made a patterned interface through a noncontact-based method, but using sophisticated instruments is still a problem. To prepare responsive liquid marbles (LMs) for on-demand release of the inner liquid in the presence of different stimuli and their stability is still a challenge. Though there are lots of slippery and superhydrophobic coatings but developing completely waterborne, highly scalable and durable coatings remains a challenge.

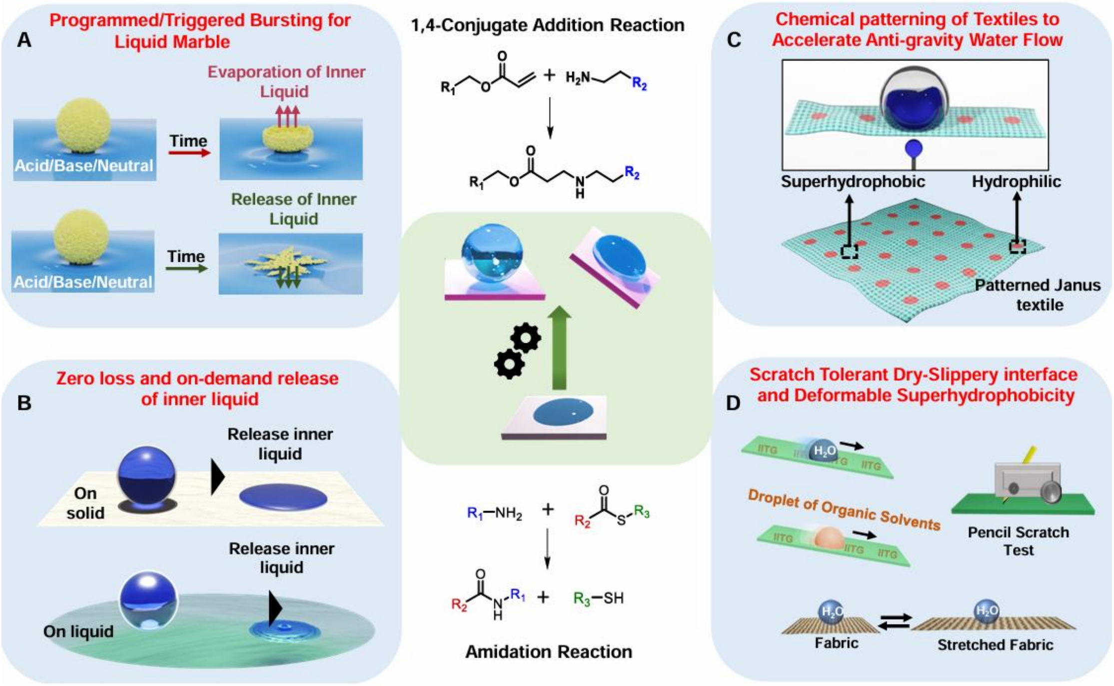

Figure 1.21 A-C) Schematic representation of the utilization of 1,4-conjugate addition reaction and amidation reaction for developing different liquid repellent material/interfaces, consisting; A) adjustable wettability of liquid marble for programmed/triggered bursting on water pool, B) Developing of omniphobic colloidosome for zero-loss and on-demand of release of inner liquid C) water-born, Scratch tolerant, substrate independent dry slippery interface and superhydrophobic surface for self-cleaning application, D) Developing a pattern Janus fabric for unidirectional liquid transport.

To address these current challenges, implementing facile and highly reactive covalent chemistry would be a rational strategy for constructing the requisite surface topography and chemical composition, which is necessary to achieve durable liquid-repellent material/surfaces. In this thesis work, I have used facile and catalyst-free amidation and 1,4-conjugate addition reactions to develop robust, tailored and transparent liquid-repellent functional materials/surfaces.

The objectives of my thesis work are illustrated schematically in Figure 1.21. Briefly, I have exploited the 1,4-conjugate addition reaction to tailor the liquid wettability from hydrophobic to superhydrophobic. It allowed for the development of liquid marble for on-demand and customized release of the inner liquid in the presence of different pH of water pool (Figure 1.21A). Next, I have introduced omniphobic capsules/colloidosomes from crystalline and hydrophobic comb-polymer to prevent loss of inner liquid because of surface adhesion and evaporation of encapsulated volatile liquid (Figure 1.21B). Further, I have fabricated chemically reactive superhydrophobic polymeric coating on a textile to develop a chemically modulated wettability pattern for antigravity water transport (Figure 1.21C). Thereafter, I have developed completely waterborne, highly transparent, abrasion-tolerant and substrate-independent solid slippery and superhydrophobic interface through an amidation reaction between thioester and aminosilane (Figure 1.21D).

1.9. References

1. N. K. Katiyar, G. Goel and S. Hawi, S. Goel, *NPG Asia Mater*, 2021, **13**, 56.
2. R. R. Naik and S. Singamaneni, *Chem. Rev.*, 2017, **117**, 12581-12583.
3. S. Linić, V. Lučanin, S. Živković, M. Raković, S. Ristić, B. Radojković and S. Polić, *J Braz. Soc. Mech. Sci. Eng.*, 2021, **43**, 57.
4. A. K. Geim, S. V. Dubonos, I. V. Grigorieva, K. S. Novoselov, A. Zhukov, A. S. Y. Shapoval, *Nat. Mater.*, 2003, **2**, 461-463.
5. M. Heim, D. Keerl and T. Scheibel, *Angew. Chem. Int. Ed.*, 2009, **48**, 3584-3596.
6. W. Wright and O. Wright, *U. S. Patent*, 1906, **821**, 393.
7. X. Wei, Y. Wang, Y. Liu, K. Ji, K. Li, J. Wang and Z. Gu, *Matter*, 2024, **7**, 826-854.
8. W. Barthlott and C. Neinhuis, *Planta*, 1997, **202**, 1.
9. L. Feng, S. Li, Y. Li, H. Li, L. Zhang, J. Zhai, Y. Song, B. Liu, L. Jiang and D. Zhu, *Adv. Mater.*, 2002, 14, 1857-1860.
10. M. Liu, S. Wang and L. Jiang, *Nat Rev Mater.*, 2017, **2**, 17036.
11. J. D. Smith, R. Dhiman, S. Anand, E. Reza-Garduno, R. E. Cohen, G. H. McKinley and K. K. Varanasi *Soft Matter*, 2013, **9**, 1772.
12. Z.Yu, F. F. Yun, Y. Wang, L. Yao, S. Dou, K. Liu, L. Jiang and X. Wang, *small*, 2017, **13**, 1701403.
13. M. Villegas, Y. Zhang, N. A. Jarad, L. Soleymani and T. F. Didar, *ACS Nano*, 2019, **13**, 8517-8536.
14. S. Zhang, J. Huang, Z. Chen, S. Yang and Y. Lai, *J. Mater. Chem. A*, 2019, **7**, 38.

15 R. J. Archer, B. Becher-Nienhaus, G. J. Dunderdale and A. Hozumi, *Adv. Funct. Mater*., 2020, **30**, 1907772.

16 K. Koch, B. Bhushan, Y. C. Jung and W. Barthlott, *Soft Matter*, 2009, **5**, 1386-1393.

17 R. Nishimura, K. Hyodo, H. Sawaguchi, Y. Yamamoto, Y. Nonomura, H. Mayama, S. Yokojima, S. Nakamura and K. Uchida, *J. Am. Chem. Soc.*, 2016, **138**, 10299.

18 E. Ozkan, C. C. Crick, A. Taylor, E. Alland and I. P. Parkin, *Chem. Sci*.,2016, **7**, 5126-5131.

19 G. B. Hwang, K. Page, A. Patir, S. P. Nair, E. Allan and I. P. Parkin, *ACS Nano*, 2018, **12**, 6050-6058.

20 J. Guo, W. Huang, Z. Guo, and W. Liu, *Nano Lett*., 2022, **22**, 3104-3111.

21 F. Zhang and Z. Guo, *Adv. Mater*., 2020, **1**, 2592-2613.

22 Q. Liu, Y. Wang, X. Liu, Y. Li, E. Yu, Z. Sun, L. Wang, G. Zhuang, J. Yu, and S. Liu, *Adv. Mater*., 2025, **37**, 2410941.

23 M. Mao, J. Wei, B. Li, L. Li, X. Huang and J. Zhang, *Nat Commun*., 2024, **15**, 9610.

24 B. Bhushan, Y. C. Jung, and K. Koch, *Langmuir*, 2009, **25**, 3241-3248.

25 F. Geyer, M. D. Acunzi1, A. Sharifi-Aghili, A. Saal, N. Gao, A. Kaltbeitzel, T.-F. Sloot, R. Berger, H.-J. Butt, D. Vollmer *Sci. Adv*., 2020, **6**, eaaw9727.

26 L. Feng, Y. Zhang, J. Xi, Y. Zhu, N. Wang, F. Xia and L. Jiang, *Langmuir*, 2008, **24**, 4114-4119.

27 B. Bhushan, and E. K. Her, *Langmuir*, 2010, **26**, 8207-8217.

28 X. Gao, X. Yan, X. Yao, L. Xu, K. Zhang, J. Zhang, B. Yang, and Lei Jiang, *Adv. Mater.,* 2007, **19**, 2213-2217.

29 M. Kasahara, S.-i. Akimoto, T. Hariyama, Y. Takaku, S.-i. Yusa, S. Okada, K. Nakajima, T. Hirai, H. Mayama, S. Okada, S. Deguchi, Y. Nakamura and S. Fujii, *Langmuir*, 2019, **35**, 6169.

30 A. R. Parker and C. R. Lawrence, *Nature*, 2001, **414**, 33-34.

31 S. Shibuichi, T. Onda, N. Satoh and K. Tsujii, *J. Phys. Chem*., 1996, **100**, 19512.

32 X.-M. Li, D. Reinhoudt and M. Crego-Calama, *Chem. Soc. Rev*., 2007, **36**, 1350-1368.

33 E. A. Vogler, *Adv. Colloid Interface Sci*., 1998, **74**, 69-117.

34 X. Zhang, F. Shi, J. Niu, Y. Jiang and Z. Wang, *J. Mater. Chem*., 2008, **18**, 621-633.

35 B. Su, Y. Tian, L. Jiang, *J. Am. Chem. Soc*., 2016, **138**, 1727-1748.

36 A. Das, A. Shome and U. Manna, *J. Mater. Chem. A*, 2021, **9**, 824-856.

37 T. Young, *Philos. Trans. R. Soc. London*, 1805, **95**, 65-87.

38 R. N. Wenzel, *Ind. Eng. Chem.*, 1936, **28**, 988-994.

39 A. B. D. Cassie and S. Baxter, *Trans. Faraday Soc.*, 1944, **40**, 546-551.

40 E. Bormashenko, *Colloids Surf. A*, 2009, **345**, 163.

41 H. Chen, P. Zhang, L. Zhang, H. Liu, Y. Jiang, D. Zhang, Z. Han and L. Jiang, *Nature,* 2016, **535**, 85-89.

42 T. S. Wong, S. H. Kang, S. K. Tang, E. J. Smythe, B. D. Hatton, A. Grinthal and J. Aizenberg, *Nature*, 2011, **477**, 443-447.

43 U. Manna and D. M. Lynn, *Adv. Mater*., 2015, **27**, 3007-3012

44 X. Zhou, Y. Sun, and J. Liu, *Adv. Mater. Interfaces*, 2021, **8**, 2100327.

45 W. Liu, R. Pan, M. Cai, X. Luo, C. Chen, G. Jiang, X. Hu, H. Zhang and M. Zhong, *J. Mater. Chem. A*, 2020, **8**, 6647-6660.

46 S. Wang, K. Liu, X. Yao and L. Jiang, *Chem. Rev*., 2015, **115**, 8230-8293.

47 S. Peppou-Chapman, J. K. Hong, A. Waterhouse and C. Neto, *Chem. Soc. Rev.,* 2020, **49**, 3688-3715.

48 A. Shome, A. Das, A. Borbora, M. Dhar and U. Manna, *Chem. Soc. Rev.*, 2022, **51**, 5452-5497.

49 E. M. Kris, S. H. Morgan, N. G. Chris, D. W. Wilkinson and M. O. Riehle, *Nano Lett*., 2005, **5**, 2097-2103.

50 S. Y. Chou, C. Keimel and J. Gu, Nature, 2002, **417**, 835-837.

51 J. Fresnais, L. Benyahia and F. Poncin-Epaillard, *Surf. Interface. Anal*., 2006, **38**, 144-149.

52 D. Oner, and T. J. McCarthy, *Langmuir*, 2000, **16**, 7777-7782.

53 R. Furstner, C. Barthlott, C. Neinhuis, P. Walzel, *Langmuir*, 2005, **21**, 956-961.

54 K. Tsougeni, N. Vourdas, A. Tserepi and E. Gogolides, *Langmuir*, 2009, **25**, 11748-11759.

55 S. Minko, M. Muller, M. Motornov, M. Nitschke, K. Grundke and M. Stamm, *J. Am. Chem. Soc*., 2003, **125**, 3896-3900.

56 E. Celia, E.T. D. Givenchy, S. Amigoni and F. Guittard, *Soft Matter*, 2011, **7**, 10057-10062.

57 E. J. Lee, C.H. Jung, I. T. Hwang, J. H. Choi, S. O. Cho and Y. C. Nho, *ACS Appl. Mater. Interfaces*, 2011, **3**, 2988-2993.

58 J. P. Youngblood and T. J. McCarthy, *Macromolecules*, 1999, **32**, 6800-6806.

59 D. Nandyala, Z. Wang, D. Hwang, T. Cubaud and C. E. Colosqui, *ACS Applied Materials & Interfaces*, 2020, **12**, 45950-45960.

60 Q. Cao, S. Zheng, C.-P. Wong, S. Liu and Q. Peng, *J. Phys. Chem. C.*, 2019, **123**, 30382-30388.

61 P. Fan, R. Pan and M. Zhong, *Langmuir*, 2019, **35**, 16693-16711.

62 B. J. Privett, J. Youn, S. A. Hong, J. Lee, J. Han, J. H. Shin and M. H. Schoenfisch, *Langmuir*, 2011, **27**, 9597-9601.

63 Y. Zhao, J. Fang, H. Wang, X. Wang and T. Lin, *Adv. Mater.*, 2010, **22**, 707-710.

64 J. Fang, H. Wang, Y. Xue, X. Wang and T. Lin, *ACS Appl. Mater. Interfaces*, 2010, **2**, 1449-1455.

65 J. Ji, J. Fu and J. Shen, *Adv. Mater.*, 2006, **18**, 1441-1444.

66 Z. Tang, Y. Wang, P. Podsiadlo and N. A. Kotov, *Adv. Mater*., 2006, **18**, 3203-3224.

67 L. Zhai, F. C. Cebeci, R. E. Cohen and M. F. Rubner, *Nano Lett*., 2004, **4**, 1349-1353.

68 E. Ahn, T. Lee, M. Gu, S. Park, H. Min and B. S. Kim, *Chem. Mater*., 2017, **29**, 69-79.

69 S. W. Lee, B. S. Kim, S. Chen, Y. S. Horn and P. T. Hammond, *J. Am. Chem. Soc*., 2009, **131**, 671-679.

70 D. D. Kulkarni, I. Choi, S. S. Singamaneni and V. V. Tsukruk, *ACS Nano*, 2010, **4**, 4667-4676.

71 K. K. S. Lau, J. Bico, K. B. K. Teo, M. Chhowalla, G. A. J. Amaratunga, W. I. Milne, G. H. McKinley and K. K. Gleason, *Nano Lett*., 2003, **3**, 1701-1705.

72 J. Zimmermann, F. A. Reifler, G. Fortunato, L. C. Gerhardt, S. Seeger, *Adv. Func. Mat*., 2008, **18**, 3662-3669.

73 M. Sun, C. Luo, L. Xu, H. Ji, Q. Ouyang, D. Yu and Y. Chen, *Langmuir*, 2005, **21**, 8978-8981.

74 Z. Wang, L. Scheres, H. Xia and H. Zuilhof, *Adv. Funct. Mater*., 2020, **30**, 1908098.

75 Y. Li, L. Li and J. Sun, *Angew. Chem. Int. Ed*., 2010, **122**, 6265-6269.

76 L. Zhang, A. G. Zhou, B. R. Sun, K. S. Chen and H.-Z. Yu, *Nat. Commun.*, 2021, **12**, 982.

77 L. Xu, R.G. Karunakaran, J. Guo and S, Yan, *ACS Appl. Mater. Interfaces,* 2012, **4**, 1118-1125.

78 D. Wang, Q. Sun, M. J. Hokkanen, C. Zhang, F.-Y. Lin, Q. Liu, S.-P. Zhu, T. Zhou, Q. Chang, B. He, Q. Zhou, L. Chen, Z. Wang, R. H. A. Ras and X. Deng, *Nature*, 2020, **582**, 55-59.

79 A. Baidya, M. A. Ganayee, S. J. Ravindran, K. C. Tam, S. K. Das, R. H. A. Ras and T. Pradeep, *ACS Nano*, 2017, **11**, 11091-11099.

80 J. Zhang, Z. Gao, L. Li, B. Li, and H. Sun, *Adv. Mater. Interfaces,* 2017, **4**, 1700723.

81 Y. Li, B. Li, X. Zhao, N. Tian and J. Zhang, *ACS Appl. Mater. Interfaces*, 2018, **10**, 39391-39399.

82 P. Aussillous and D. Quéré, *Nature*, 2001, **411**, 924-927.

83 P. Aussillous and D. Quéré, *Proc. R. Soc. A*, 2006, **462**, 973-999.

84 G. Mchale and M. I. Newton, *Soft Matter*, 2011, **7**, 5473-5481.

85 M. Tenjimbayashi, T. Mouterde, P. K. Roy and K. Uto, *Nanoscale*, 2023, **15**, 18980-18998.

86 C. H. Ooi, J. Jin, K. R. Sreejith, A. V. Nguyen, G. M. Evans and N.-T. Nguyen, *Lab Chip*, 2018, **18**, 3770-3779.

87 D. Dupin, S. P. Armes and S. Fujii, *J. Am. Chem. Soc*., 2009, **131**, 5386-5387.

88 K. Nakai, S. Fujii, Y. Nakamura and S.-I. Yusa, *Chemistry Letters*, 2015, **44**, 1077-1079.

89 S.-I. Yusa, M. Morihara, K. Nakai, S. Fujii, Y. Nakamura, A. Maruyama and N. Shimada, *Polym J*, 2014, **46**, 145-148.

90 W. Gao, H. K. Lee, J. Hobley, T. Liu, I. Y. Phang and X. Y. Ling, *Angew. Chem. Int. Ed.*, 2015, **54**, 3993.

91 D. Sun, P. R. Adiyala, S.-J. Yim and D.-P. Kim, *Angew. Chem. Int. Ed*., 2019, **58**, 7405-7409.

92 S. Fujii, M. Mochizuki, K. Aono, S. Hamasaki, R. Murakami and Y. Nakamura, *Langmuir*, 2011, **27**, 8067-8074.

93 J. Zhang, Y. Gu, J. Jiang and R. Zheng, *Langmuir*, 2022, **38**, 5702-5707.

94 J. P. Goertz, K. C. DeMella, B. R. Thompson, I. M. White and S. R. Raghavan, *Mater. Horiz.*, 2019, **6**, 1238-1243.

95 S. A Ryu, Y.-H. Hwang, H. Oh, K. Jeon, J. H. Lee, J. Yoon, J. B. Lee and H. Lee, *ACS Appl. Mater. Interfaces*, 2021, **13**, 36380-36387.

96 R. Lathia, S. Nagpal, C. D. Modak, S. Mishra, D. Sharma, B. S. Reddy, P. Nukala, R. Bhat and P. Sen, *Nat. Commun.*, 2023, **14**, 6445.

97 S. Zhao, H. Zhao, X. Zhang, Y. Li and Y. Du, *Lab Chip*, 2013, **13**, 2350.

98 A. K. Gaharwar, A. Arpanaei, T. L. Andresen and A. Dolatshahi-Pirouz, *Adv. Mater.*, 2016, **28**, 771.

99 S. J. Pastine, D. O. Brian, K. M. Rolandi, M. Llorente, A. Zettl and Jean M. J. Fréchet, *J. Am. Chem. Soc.*, 2008, **130**, 4238-4239.

100 D. Zahner, J. Abagat, F. Svec, J. M. Fréchet and P. A. Levkin, *Adv. Mater.*, 2011, **23**, 3030-3034.

101 A. I. Neto, C. A. Custodio, W. Song and J. F. Mano, *Soft Matter*, 2011, **7**, 4147-4151.

102 H. Bai, L. Wang, J. Ju, R. Sun, Y. Zheng and L. Jiang, *Adv. Mater.*, 2014, **26**, 5025-5030.

103 L. Lao, D. Shou, Y. S. Wu, and J. T. Fan, *Sci. Adv.*, 2020, **6**, eaaz0013.

104 F. Li, S. Wang, Z. Wang, K. Jiang, X. Zhao, L. Shao and Y. Pan, *Adv. Funct. Mater.*, 2023, **33**, 2210769.

105 Y. Peng, J. Zhou, Y. Yang, J.-C. Lai, Y. Ye and Y. Cui, *Adv. Mater.*, 2022, **34**, 2204168.

106 F. Li, S. Wang, Z. Wang, K. Jiang, X. Zhao, L. Shao and Y. Pan, *Adv. Funct. Mater.*, 2023, **33**, 2210769.

107 A. Tuteja, W. Choi, M. Ma, J. M. Mabry, S. A. Mazzella, G. C. Rutledge, G. H. McKinley and R. E. Cohen, *Science*, 2007, **318**, 1618-1622.

108 K. Tsujii, T. Yamamoto, T. Onda and S. Shibuichi, *Angew. Chem. Int. Ed.*, 1997, **36**, 1011-1012.

109 A. K. Kota, Y. Li, J. M. Mabry and A. Tuteja, *Adv. Mater.*, 2012, **24**, 5838-5843.

110 L. Yuan, T. Wu, W. Zhang, S. Ling, R. Xiang, X. Gui, Y. Zhu and Z. Tang, *J. Mater. Chem. A*, 2014, **2**, 6952-6959.

111 T. L. Liu and C. J. Kim, *Science*, 2014, **346**, 1096-1100.

112 X. Zhou, Y. Sun, and J. Liu, *Adv. Mater. Interfaces*, 2021, **8**, 2100327.

113 X. Meng, Z. Wang, L. Wang, L. Heng and L. Jiang, *J. Mater. Chem. A*, 2018, **6**, 16355-16360.

114 M. Dhar, A. Das, D. Parbat and U. Manna, *Angew. Chem., Int. Ed.*, 2022, **134**, e202116763.

115 V. Singh, X. Men and M. K. Tiwari, *Nano Lett.*, 2021, **21**, 3480-3486.

116 W. Pan, Q. Wang, J. Ma, W. Xu, J. Sun, X. Liu and J. Song, *Adv. Funct. Mater.*, 2023, **33**, 2302311.

117 K. Zhang, S. Huang, J. Wang and G. Liu, *Angew. Chem. Int. Ed.*, 2019, **58**, 12132-12137.

118 W. Zheng, J. Huang, X. Zang, X. Xu, W. Cai, Z. Lin and Y. Lai, *Adv. Mater.*, 2022, **34**, 2204581

119 M. Rabnawaz and G. Liu, *Angew. Chem., Int. Ed.*, 2015, **54**, 6516-6520.

120 L. Wang and T. J. McCarthy, *Angew. Chem. Int. Ed.*, 2016, **55**, 244-248.

121 W. S. Y. Wong, A. Naga, L. Hauer, P. Baumli, H. Bauer, K. I. Hegner, M. D'Acunzi, A. Kaltbeitzel, H.-J. Butt and D. Vollmer, *Nat. Commun.*, 2021, **12**, 5358.

122 W. Feng, L. Li, X. Du, A. Welle and P. A. Levkin, *Adv. Mater.*, 2016, **28**, 3202-3208.

123 C. H. Peterson, S. D. Rice, J. W. Short, D. Esler, J. L. Bodkin, B. E. Ballachey and D. B. Irons, *Science*, 2003, **302**, 2082-2086.

124 E. Stokstad, *Science*, 2010, **328**, 1618-1619.

125 M. K. McNutt, R. Camilli, T. J. Crone, G. D. Guthrie, P. A. Hsieh, T. B. Ryerson, O. Savas and F. Shaffer, *PNAS*, 2012, **109**, 20260-20267.

126 Z. Ren, Y. Yang, W. Chena and Y. Lina, *Nanoscale*, 2024, **16**, 17248-17275.

127 C. Ruan, K. Ai, X. Li and L. Lu, *Angew. Chem. Int. Ed.*, 2014, **53**, 5556-5560.

128 L. Feng, Z. Zhang, Z. Mai, Y. Ma, B. Liu, L. Jiang and D. Zhu, *Angew. Chem. Int. Ed.*, 2004, **43**, 2012-2014.

129 J. Yong, J. Huo, F. Chen, Q. Yang and X. Hou, *Phys. Chem. Chem. Phys.*, 2018, **20**, 25140-25163.

130 X. Q. Cheng, Y. Jiao, Z. Sun, X. Yang, Z. Cheng, Q. Bai, Y. Zhang, K. Wang and L. Shao, *ACS Nano*, 2021, **15**, 3500-3508.

131 J. K. Nunes and H. A. Stone, *Chem. Rev.*, 2022, **122**, 6919-6920.

132 C. Wang and Z. Guo, *Nanoscale*, 2020, **12**, 22398-22424.

133 M. Paven, H. Mayama, T. Sekido, H.-J. Butt, Y. Nakamura and S. Fujii, *Adv. Funct. Mater.*, 2016, **26**, 3199.

134 Y. Xue, H. Wang, Y. Zhao, L. Dai, L. Feng, X. Wang and T. Lin, *Adv. Mater.*, 2010, **22**, 4814-4818.

135 J. W. Costerton, P. S. Stewart and E. P. Greenberg, *Science*, 1999, **284**, 1318-1322.

136 C. G. Kumar and S. Anand, *Int J Food Microbiol.*, 1998, **42**, 9-27.

137 G. Wena, X. Gao, P. Tian, L. Zhong, Z. Wang and Z. Guo, *Chem. Eng. J.*, 2018, **346**, 94-103.

138 P. Hu, Q. Xie, C. Ma and G. Zhang, *Langmuir*, 2020, **36**, 2170-2183.

139 R. B. Pernites, C. M. Santos, M. Maldonado, R. R. Ponnapati, D. F. Rodrigues, and R. C. Advincula, *Chem. Mater.*, 2012, **24**, 870-880.

140 A. K. Epstein, T. S. Wong, R. A. Belisle, E. M. Boggs and J. Aizenberg, *PNAS*, 2012, **109**, 13182-13187.

141 A. B. Tesler, P. Kim, S. Kolle, C. Howell, O. Ahanotu and J. Aizenberg, *Nat. Commun.*, 2015, **6**, 8649.

142 R. Chatterjee, H. Bararnia and S. Anand, *Adv. Mater*. 2022, **34**, 2109930.

143 J. Huang, D. Li, Z. Peng, B. Zhang, Y. Yao and S. Chen, *ACS Appl. Mater. Interfaces* 2023, **15**, 43026.

144 P. Kim, T. S. Wong, J. Alvarenga, M. J. Kreder, W. E. Adorno-Martinez and J. Aizenberg, *ACS Nano*, 2012, **6**, 6569-6577.

145 L. Cao, A. K. Jones, V. K. Sikka, J. Wu and D. Gao, *Langmuir*, 2009, **25**, 12444-12448.

146 M. J. Kreder, J. Alvarenga, P. Kim and J. Aizenberg, *Nat. Rev. Mater.*, 2016, **1**, 15003.

147 L. Mishchenko, B. Hatton, V. Bahadur, J. A. Taylor, T. Krupenkin and J. Aizenberg, *ACS Nano* 2010, **4**, 7699-7707.

148 G. Han, T.-B. Nguyen, S. Park, Y. Jung, J. Lee and H. Lim, *ACS Nano*, 2020, **14**, 10198.

149 H. Dai, Z. Dong and L. Jiang, *Sci. Adv.*, 2020, **6**, eabb5528.

150 C. Li, B. Kim, J. Yoon, S. Sett and J. Oh, *Adv. Funct. Mater.*, 2024, **34**, 2308265.

151 H. Chen, P. Zhang, L. Zhang, H. Liu, Y. Jiang, D. Zhang, Z. Han and L. Jiang, *Nature*, 2016, **532**, 85-89.

152 M. Prakash, D. Quéré and J. W. Bush, *Science*, 2008, **320**, 931-934.

153 P. Comanns, G. Buchberger, A. Buchsbaum, R. Baumgartner, A. Kogler, S. Bauer and W. Baumgartner, *J. R. Soc. Interface*, 2015, **12**, 20150415.

154 M. K. Chaudhury and G. M. Whitesides, *Science*, 1992, **256**, 1539-1541.

155 K.-H. Chu, R. Xiao and E. N. Wang, *Nat. Mater.*, 2010, **9**, 413-417.

156 W. Zhou, S. Min, T. Zhan, Y. Zhang, D. Pan, Y. Yuan and B. Xu, *Small*, 2023, **19**, 2302512.

157 Y. Wang, G. Xia, H. Yu, B. Qian, Y. H. Cheung, L. H. Wong and J. H. Xin, *Adv. Mater.*, 2021, **33**, 2100140.

158 Y. Lin, N. Cheng, N. Meng, C. Wang, X. Wang, J. Yu and B. Ding, *Adv. Funct. Mater.*, 2023, **33**, 2304109.

159 D. Wu, J.-N. Wang, S.-Z. Wu, Q.-D. Chen, S. Zhao, H. Zhang, H.-B. Sun and L. Jiang, *Adv. Funct. Mater.*, 2011, **21**, 2927-2932.

160 Z. Yu, T. Zhu, J. Zhang, M. Ge, S. Fu and Y. Lai, *Adv. Funct. Mater.*, 2022, **32**, 2200359.

161 Y. Zheng, H. Bai, Z. Huang, X. Tian, F.-Q. Nie, Y. Zhao, J. Zhai and L. Jiang, *Nature*, 2010, **463**, 640-643.

162 Z. Li, L. Tang, H. Wang, S. C. Singh, X. Wei, Z. Yang and C. Guo, *ACS Sustainable Chem. Eng.*, 2023, **11**, 11019-11031.

163 M. Cui, B. Wang and Z. Wang, *Adv. Eng. Mater.*, 2019, **21**, 1801379.

164 J. Zhang, C. Gu and J. Tu, *ACS Appl. Mater. Interfaces*, 2017, **9**, 11247-11257.

165 S. T. Yohe, Y. L. Colson and M. W. Grinstaff, *J. Am. Chem. Soc.*, 2012, **134**, 2016-2019.

166 J. Wang, J. A. Kaplan, Y. L. Colson and M. W. Grinstaff, *Angew. Chem. Int. Ed.*, 2016, **55**, 2796-2800.

167 W. Xu, H. Zheng, Y. Liu, X. Zhou, C. Zhang, Y. Song, X. Deng, M. Leung, Z. Yang, R. X. Xu, Z. L. Wang, X. C. Zeng and Z. Wang, *Nature*, 2020, **578**, 392-396.

168 M. Li, C. Li, B. R. K. Blackman and E. Saiz, *Matter*, 2021, **4**, 3400-3414.

169 S.-H. Cho, P. Joo, C. Zhang, E. A. Lewis, B. D. Vogt and N. S. Zacharia, *ACS Appl. Polym. Mater.*, 2022, **4**, 100-110.

170 M. Dhar, U. I. Kara, S. Das, Y. Xu, S. Mandal, R. L. Dupont, E. C. Boerner, B. Y. Chen, Y. X. Yao, X. G. Wang and U. Manna, *Mater. Horiz.*, 2023, **10**, 2204.

Chapter 2: pH-triggered Adjustable Bursting of Liquid Marbles in Water Pools

Non-sticking millimetric droplets wrapped with micron or submicron-sized liquid-repellent solid particles and aggregates are recognized as liquid marbles (LMs). LMs behave like a non-wetting solid, which enables zero-loss transportation on solid surfaces and liquid pools. The challenge is controlling the liquid-releasing behavior, especially in a liquid pool. For example, releasing the inner liquid of LMs at a specified time in adaptation to liquid pool conditions has not been achieved. In the past, different approaches were introduced to demonstrate the instant release of inner liquid in the presence of a specific stimulus, but reports on controlling the lifetime of floating LMs in the presence of a stimulus are extremely rare in the literature. In this context, an inherently porous and crystalline nanomaterial, i.e., metal organic frameworks (MOFs), is rationally transformed into a chemically reactive nanomaterial for associating both (a) dual pH-responsive hydrophobicity and (b) non-responsive superhydrophobicity via a 1,4-conjugate addition reaction. Further, the Kang-Jacobi wettability model was applied to examine the wettability transition of the modified MOFs at different pH. Hydrophobic MOFs yielded LMs with the ability to automatically release inner liquid at a pre-defined time without requiring external intervention. Furthermore, the strategic association of protonizable amines, labile coordination bonds, and the tailored hydrophobicity attributed to the dual (acidic/alkaline) stimulus-responsive adjustable lifetime of LMs in the water pool. Such LMs were utilized for demonstrating an (1) adjustable drug release, (2) on-demand release of the reactants to perform chemical reactions, and (3) rapid optode detection of NO_2^-.

S. Kumar, N. Barman, A. Borbora, P. Mondal, M. Tenjimbayashi and U. Manna, *J. Mater. Chem. A*, 2024, **12**, 3362-3372.

2.1. Introduction

Liquid marbles (LMs) are liquid droplets wrapped in micron/submicron-sized liquid-repellent solid particles and aggregates.[1] The wrapping layer, comprising mostly liquid-repellent solid particles around the encapsulated liquid droplet, provided an isolated and dry environment, eventually protecting the LMs from contamination.[1-3] The stability of such tiny and dry liquid droplets and their controlled bursting are essential for a wide range of practically relevant applications of LMs.[1-8] In the past, various particles with different shapes and sizes were explored to improve the stability of LMs on both the solid/air and the liquid/air interfaces.[9-13] In a seminal report, Fujii and coworkers introduced a stimulus-responsive LM through the strategic use of an alkaline steric stabilizer chain of a polymer latex particle.[4] The reported stimulus-responsive LM remained stable under alkaline conditions but readily collapsed in both neutral and acidic water pools because of the protonation-induced switching of the wettability of the polymeric latex particle. This work pioneered responsive LMs.[4,7] Inspired by this result, other stimulus-responsive LMs with the ability to immediately release the inner liquid at different monotonic stimuli, including alkaline conditions, UV light, and temperature, were introduced thereafter.[4,5,7,8,14,15] In the recent past, LMs have been successfully applied in various relevant research topics, including miniaturized chemical reactions, loss-less transportation of liquid, tissue engineering, and CO_2 capture.[16-19] However, after significant progress on these research topics, the design of LMs with tunable or even adaptive responsiveness has not been achieved.[4,5,7,8,14,15,20-31] Various types of hydrophobic particles were introduced to demonstrate almost instant bursting of LMs in the presence of specific stimuli, and such earlier reported approaches remained inapplicable to adjust the lifetime of LMs in the presence of respective stimuli. [4,5,7,8,14,15,20-31] Thus, the report of mechanically robust LMs, having the ability to a) automatically release the inner liquid at a precise and pre-defined time without having any external intervention, and b) adjustable triggered bursting of the inner liquid on a water pool in both acidic and alkaline conditions, is yet to be introduced in the literature. Such a principally distinct design would likely to provide an elegant avenue for deriving functional soft materials for different fundamental and applied studies, including adjustable triggered drug release, on-demand chemical reaction and rapid chemical sensing, etc.

In the past, the metal-organic framework (MOF) that was inherently associated with high crystallinity, porosity and surface area was strategically integrated with water-repellence property for improving structural stability and applied successfully in various potential applications related to energy, environment, catalysis, etc.[32-34] Recently, a few water-repellent

MOFs were also explored to construct LMs,[35-38] but with no intention of designing programmable and triggered release of the inner liquid at the water pool.

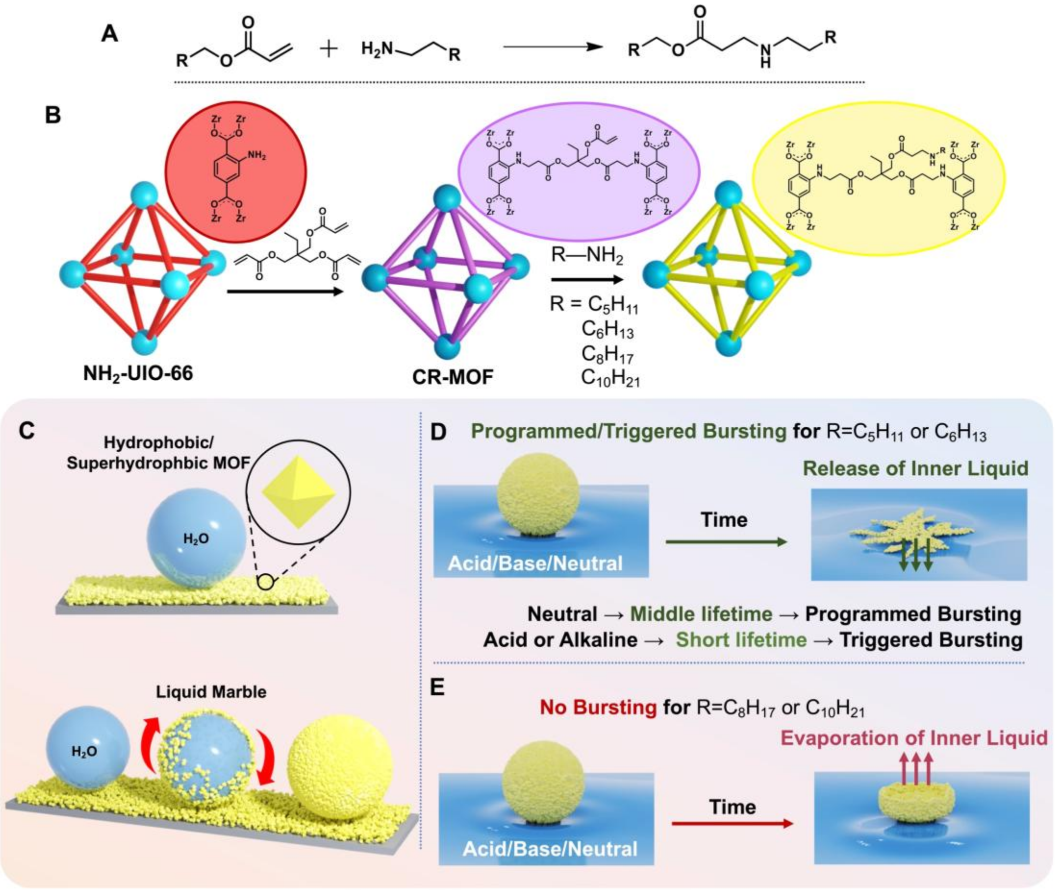

Figure 2.1 A) Illustrating a catalyst-free 1,4-conjugate addition reaction between representative amine and acrylate groups. B) Accounting the conversion of prepared MOF (NH$_2$-UIO-66) into a chemically reactive MOF (CR-MOF) following the covalent modification with 3-Acl through 1,4-conjugate addition reaction. The residual acrylate group in CR-MOF provided a facile basis for post covalent modification with selected alkyl amines at ambient conditions to tailor water wettability (hydrophobicity and superhydrophobicity). C) Depicting the process of forming LMs by rolling the beaded water droplet on the pile of either hydrophobic or superhydrophobic MOFs. D) Schematic depicting the LMs prepared from hydrophobic MOFs displayed both programmed (moderate lifetime of LM) and triggered release of inner liquid at water pool, without having any external intervention at neutral pH and in the presence of acidic/alkaline stimuli, respectively. E) Schematic depicting the LMs derived from superhydropphobic MOFs failed to release inner liquid irrespective of the pH of the water pool, rather encapsulated water evaporated out from the LM.

In the recent past, an amine-containing Zr-based MOF, formally recognized as NH$_2$-UiO-66, was modified by strategically reacting the available amine and Zr-OH groups at harsh and complex chemical reaction conditions.[20,39-43]

In this current design, a strategic association of metal-organic framework and protonizable chemistry, in combination with tailored hydrophobicity, is introduced to develop a LM with stimuli-responsive adjustable "lifetime till breakage" on a water pool. In this context, the prepared NH_2-UiO-66 was subjected to covalently react with trimethylolpropane triacrylate (3-Acl) to achieve a selectively chemically reactive MOF (CR-MOF, Figure 2.1A-B) because of the residual acrylate reactivity of CR-MOF. It allowed for post-modification with selected alkyl amines following a common and facile 1,4-conjugate addition reaction at ambient conditions.[3] I hypothesized that the hydrocarbon tails of selected alkyl amines would modulate water repellence and eventually control the exposure of available amines and labile coordination bond of the modified MOFs at acidic and alkaline conditions, respectively. Depending on the length of hydrocarbon tails in the selected alkyl (i.e., pentyl ($-C_5H_{11}$), hexyl ($-C_6H_{13}$), octyl ($-C_8H_{17}$) and decyl ($-C_{10}H_{21}$)) amine, the modified MOFs provided either dual (acid/alkaline)-responsive (pentyl, hexyl) or non-responsive (octyl, decyl) water repellence (hydrophobicity/superhydrophobicity). Covering the water droplet with such chemically modulated MOF (Figure 2.1C), I aimed to introduce a new class of responsive LMs that provide an automated (at neutral conditions) and adjustable (depending on pH) triggered release of inner liquid at the water pool, as shown in Figure 2.1D. The choice of chemical modulation decides the floating time of the same LM at acidic and alkaline conditions (Figure 2.1D-E).

2.2. Experimental Section

2.2.1. Materials Required

2-Aminoterephthalate (H_2ATA), zirconium chloride ($ZrCl_4$), trimethylolpropane triacrylate (3-Acl; molecular weight: 296.31 g/mol), butyl amine, pentyl amine, hexyl amine, octyl amine, decyl amine, sulfanilamide, aniline, rhodamine B, potassium thiocyanate, iron(III) chloride hexahydrate, sodium dodecyl sulphate (SDS), methylene blue and DMSO-d_6 were purchased from Sigma Aldrich (Bangalore, India). DMF was purchased from Alfa-Aesar, India. Sodium hydroxide, sodium chloride, sodium nitrite, and hydrochloric acid were purchased from Emparta (Merck Specialties Private Limited). Superglue (ethyl cyanoacrylate) was procured from Amazon India. Ethanol and methanol were purchased from Changshu Hongsheng Fine Chemical. Microscopic glass slides were purchased from JSGW (Jain Scientific Glass Works), India. Milli-Q grade water was used for all experiments.

2.2.2. Characterization

The contact angle measurements were performed using KRUSS Drop Shape Analyser-DSA25 instrument with an automatic liquid dispenser at ambient conditions. Static contact angles were measured at four different positions for each sample. Field Emission scanning electron microscope (FESEM) images were taken using Sigma Carl Zeiss scanning electron microscope (a thin layer of gold coating was done on the sample prior to the imaging). UV-Vis spectra for transmittance measurement were recorded using the Perkin-Elmer Lambda 750 (UV/Vis/NIR Spectrometer). The ^{1}H NMR spectra were recorded using Bruker 500 MHz NMR spectrometer. For the ^{1}H NMR analyses of MOFs, 5 mg of sample was dispersed in 10 μL of HF, followed by adding 500 μL of DMSO (d_6) to dissolve the sample under sonication. Transmission electron microscope images were obtained using JEOL-2100F field emission transmission electron microscope (FETEM). The attenuated total reflectance infrared spectra was recorded using a PerkinElmer ATR instrument at ambient conditions in the range of 400-4000 cm^{-1}. Nitrogen adsorption-desorption measurement was carried out by Quantachrome Autosorb-IQ MP gas sorption analyzer at 77 K. X-ray powder diffraction patterns of the samples were recorded by using a Rigaku Smart Lab X-ray diffractometer using Cu-K_{α} ($\lambda = 0.15406$ nm) radiation at 9 kw (50kv, 100 mA) with a 1D detector (scan speed: 0.05 degree/second). The digital images and videos were captured using a Nikon Coolpix B-700 digital camera.

2.2.3. Synthesis of NH_2-UiO-66

NH_2-UiO-66 was synthesized by following the previously reported methods with minor modifications.[20] Sequentially, H_2ATA (0.186 g, 1.029 mmol) and $ZrCl_4$ (0.240 g, 1.029 mmol) were dissolved in 60 mL of anhydrous DMF, followed by the addition of 0.2 mL of deionized water into the solution. The resulting solution was stirred at room temperature for 5 min and then transferred to 100 mL teflon-lined autoclave. The reaction was carried out at 120 °C for 24 h, giving rise to a suspension that was later filtered and washed with DMF and acetone, and dried under vacuum condition to obtain the yellowish product. The product was characterized by ^{1}H NMR. The ^{1}H NMR data for MOF (DMSO-d_6, 500 MHz): $\delta = 7.77$ (d, $J = 8.2$ Hz, 1H), 7.38 (s, 1H), 7.03 (d, $J = 8.2$ Hz, 1H).

2.2.4. Synthesis of Chemically Reactive MOF and Post-modification

NH_2-UiO-66 (117 mg, ca. 0.4 mmol eq. of NH_2) and 3-Acl (477 mg, 1.6 mmol, 4 eq.) were taken in a teflon-lined autoclave containing 10 mL of ethanol. The autoclave was then sealed and heated at 120 °C for 48 h. After cooling to room temperature, the autoclave was opened and the yellow powder was thoroughly rinsed and periodically centrifuged with ethanol (20mL×3). After centrifugation of the resulting mixture, the powder was dried at 80 °C in an oven. For further modification, this powder was activated at 120 °C for 12 h. The product was characterized by ^{1}H NMR. The ^{1}H NMR data for CR-MOF (DMSO-d_6, 500 MHz): $\delta = 7.87$ (d, $J = 8.2$ Hz, 2H), 7.27 (s, 2H), 7.10 (d, $J = 8.2$ Hz, 2H), 6.25 (dd, $J = 17.2$, 1.6 Hz, 1H), 6.07 (dd, $J = 17.2$, 10.3 Hz, 1H), 5.87 (dd, $J = 10.3$, 1.6 Hz, 1H), 3.49 (t, $J = 6.5$ Hz, 2H), 3.45 (t, $J = 6.6$ Hz, 2H), 2.73 – 2.70 (m, 2H), 2.63 (t, $J = 6.4$ Hz, 2H), 2.57 (t, $J = 6.4$ Hz, 2H), 1.17 (t, $J = 7.1$ Hz, 3H).

2.2.5. Post-modification of CR-MOF with Alkyl Amines

Activated CR-MOF (100 mg) and 1 mL of different alkyl amines (butyl amine, pentyl amine, hexyl amine, octyl amine and decyl amine) solutions were taken separately and stirred overnight at ambient conditions. After completion of the reaction, the resultant mixtures were centrifuged 3 times with 20 mL of ethanol each to remove the residual amines. Next, the products were dried in an oven at 80 °C prior to use it in various characterizations and demonstrations. The ^{1}H NMR data for pentyl amine modified CR-MOF: ^{1}H NMR (DMSO-d_6, 500 MHz): δ = 7.87 (d, J = 8.2 Hz, 2H), 7.27 (s, 2H), 7.10 (d, J = 8.2 Hz, 2H), 3.49 (t, J = 6.5 Hz, 2H), 3.45 (t, J = 6.6 Hz, 2H), 3.10 (t, J = 6.3 Hz, 2H), 2.91- 2.87 (m, 2H), 2.74 – 2.69 (m, 2H), 2.63 (t, J = 6.3 Hz, 4H), 2.57 (t, J = 6.3 Hz, 2H), 1.57 – 1.50 (m, 2H), 1.32 – 1.25 (m, 4H), 1.17 (t, J = 7.1 Hz, 3H), 0.87 (t, J = 6.6 Hz, 3H).

2.2.6. LMs Fabrication and Surface Morphology of MOFs Based LMs

A droplet of water was individually beaded on a pile of different amine modified CR-MOF powder. After the droplet was rolled over, chemically modified superhydrophobic/hydrophobic MOF particles spontaneously self-organized to encapsulate the water droplet to form the LM. The surface structure of the selected MOFs based LMs was characterized with FESEM imaging. MOFs based LMs were exposed to ECA vapor at 50 °C to cause anionic polymerization at the air-water interface of the MOFs based LMs.

2.2.7. Lifetime Analysis of MOFs Based LMs on a Water Pool

To study the lifetime of LMs of different amine modified CR-MOF on a water pool, the freshly prepared LMs of DI water (20 µL) were gently placed on a water pool with the help of a metal spatula. Digital images were acquired at regular intervals to study the lifetime of the LMs.

2.2.8. Impact Test for MOFs Based LMs

The impact test was performed by dropping a LM of volume 10 µL from a certain height to study the breakage behavior of the LM.

2.2.9. Compression Test for MOFs Based LMs

The LMs were prepared of different amine modified CR-MOF were subjected to controlled and repetitive compressive strains. In this context, a lab-made setup was built to apply gradual compressive strain on the prepared LMs. Two clean microscopic glass slides were attached on to the upper and lower platforms of a laboratory jack. Then, respective LM was gently placed on the lower glass slide, prior to gradually bringing down the upper glass slide to apply gradual compressive strain on the LMs by rotating the attached screw of the laboratory jack. The compressive strain was calculated by measuring the change in the height of the respective LM before and after its deformation. Further, this experimental setup was utilized to apply compressive strain of 50% repeatedly. Further, the prepared LMs were also compressed with bare finger, where the LM was placed on a finger and pressed repeatedly using the thumb for several times.

2.2.10. Triggered Bursting of LMs in Acid/Alkaline Conditions

The different amine modified LMs were transferred into a petri dish containing 50 mL of water divided superficially into four sections. Then, ~ 400 µL of concentrated HCl was added to the center of the petri dish to make the water solution of pH 1. In another setup, ~ 400 µL of NaOH (0.2 µM) solution was separately added to the center of another petri dish to make the water solution of pH 12. Both in the pH 1 and pH 12, the LM of pentyl amine modified hydrophobic MOF was found to burst, followed by the LM of hexyl amine modified MOF, but the LMs of octyl and decyl amine modified MOF remained intact. See the main text for more details.

2.2.11. Triggered Chemical Reaction on Air/Water Interface

Two different LMs of pentyl amine modified hydrophobic MOF were prepared using aqueous solutions (20 µL) of mutually reactive reactants, i.e., potassium thiocyanate (one equivalent) and iron (III) chloride (nine equivalents, 57 mM) solution. Similarly, another two distinct LMs of decyl amine modified superhydrophobic MOF were to encapsulate above mentioned aqueous solutions of potassium thiocyanate and iron (III) chloride. A petri dish containing 50 mL of water was divided superficially into two parts prior to transfer these LMs, where two LMs of decyl amine modified MOF were placed on the left half of the water pool and other portion of the air/water interface accommodated two LMs of pentyl amine modified MOF. On addition of aqueous droplet of acid to the water pool, the LMs of pentyl amine modified MOF popped out, and the mutually reactive released reactants formed metal complex to give a visually distinguishable red color. However, the LMs of decyl amine modified MOF remained intact to their shape, and failed to release encapsulated reactants at identical settings.

2.2.12. Release of Small Molecules by LM in Acidic, Neutral and Basic conditions

The release of rhodamine-B (model drug molecule) from different LMs that were individually prepared from pentyl amine and hexyl amine modified MOFs were studied by measuring the change in UV-absorption intensity at λ_{max} in the aqueous phase. In this context, rhodamine-B solution (1 mg/mL solution) was prepared in de-ionized water. The pentyl amine and hexyl amine modified CR-MOF were separately used to form respective LM encapsulating the aqueous solution of rhodamine B. The dye loaded LM was subsequently placed on an acidic, neutral and basic water pool to examine the release of rhodamine B by visual inspection and UV spectral analysis. The aqueous aliquot was collected at regular time intervals to obtain the

UV absorption spectra. The UV/Vis absorption of the collected aliquots at regular intervals was recorded with the Perkin-Elmer Lambda 750 UV/Vis/NIR Spectrometer to get the percentage of change in intensity of UV-absorption in the water pool due to the release of rhodamine B in the water pool.

2.2.13. Sensing of Nitrite Ion

A 20µL droplet of solution of sulfanilamide (1 mM), aniline (1 mM) rolled on a pile of pentyl amine modified CR-MOF powder. After the droplet was rolled over, chemically modified hydrophobic MOF particles spontaneously self-organized to encapsulate the solution of sulfanilamide (1 mM), aniline (1 mM) to form the LM. The pentyl amine modified LMs were transferred into a petri dish containing 20 mL of water without and with Nitrite (40 µL) solution. Then, 170 µL of concentrated HCl was added to the corner of the petri dish to alter the pH of water pool to pH 1. After addition of acid the LM of pentyl amine modified hydrophobic MOF was found to burst in both case but water pool containing nitrite ions turned yellow to form diazo dye, however, without nitrite ion, it didn't show any colouration.

2.3. Results and Discussion

2.3.1. Developing Chemically Reactive Metal-Organic Framework

In the recent past, automated bursting of LMs, without demanding any external intervention, was introduced by strategically modifying the halloysite nanoclay with different alkyl acrylates, where the embedded hydrophobicity of the modified nanoclay controls the diffusion length of water vapour across the LM's shell to control the lifetime of floating LMs.[40] Here, a completely distinct approach is adopted to design of chemically reactive MOF for precisely controlling the wettability transition from hydrophobicity to hydrophilicity by, i) triggering the structural instability of MOF in alkaline condition and ii) protonating the available amine moiety in the modified MOF at acidic conditions. This simple principle is extended to achieve both automated (at neutral condition) and adjustable (depending on pH) triggered release of inner liquid from LMs at water pools.

In this relevance, the NH_2-UiO-66 was prepared and characterized with ^1H NMR, powder XRD, FETEM and FESEM studies (Figures 2.2 and 2.5D-F) prior to covalently reacting with trimethylolpropane triacrylate (3-Acl) through the 1,4-conjugate addition reaction. The resultant MOF is embedded with residual acrylate groups which makes it chemically reactive, and such MOF is denoted as CR-MOF. The covalent modification of NH_2-UiO-66 with 3-Acl and the existence of residual acrylate groups were characterized with ^1H NMR study (Figure 2.3). After the mutual reaction between prepared NH_2-UiO-66 and 3-Acl, the ^1H NMR spectrum of the HF/DMSO-d_6-digested product (CR-MOF; Figure 2.2B) displayed peaks at δ= 7.10 (d), 7.27 (s) and 7.87 (d) ppm, corresponding to the aromatic protons of the MOF.

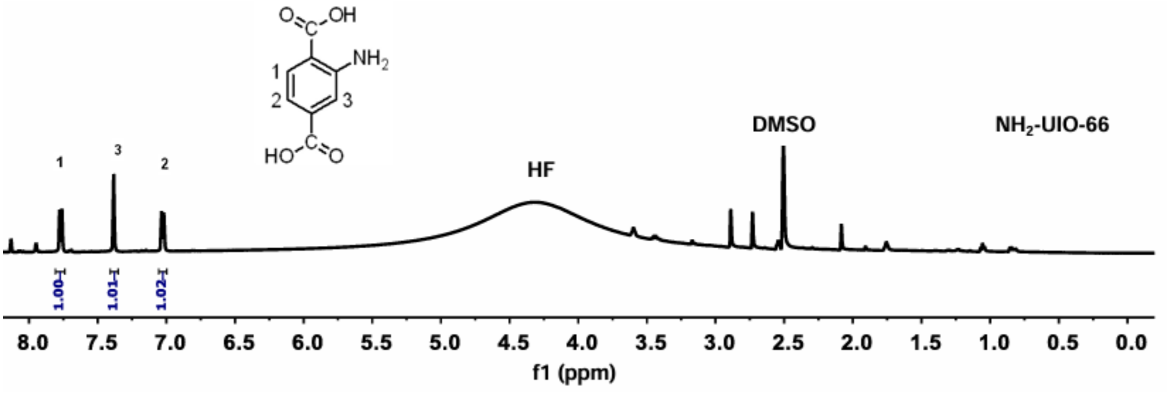

Figure 2.2 ^{1}H NMR spectra of NH$_2$-UiO-66 MOF was digested/ dissolved in HF/ DMSO-*d6* (10 µL + 500 µL).

Furthermore, four sets of triplets at δ= 2.57, 2.63 ppm and δ= 3.45, 3.49 ppm appeared in the aliphatic region, which correspond to the β- and α-protons of the two chemically different secondary amines, respectively. Additionally, the three sets of doublets of doublet at 5.87 (dd, *J* = 10.3, 1.6 Hz, for cis & geminal coupling), 6.25 (dd, *J* = 17.2, 1.6 Hz, for trans & geminal coupling) and 6.07 (dd, *J* = 17.2, 10.3 Hz, for trans & cis coupling) ppm can be found which correspond to the remaining vinylic protons of the 3-Acl. The peaks at 1.17 (t, 3H) and 2.73-2.70 (m, 2H) correspond to the aliphatic ethyl group.

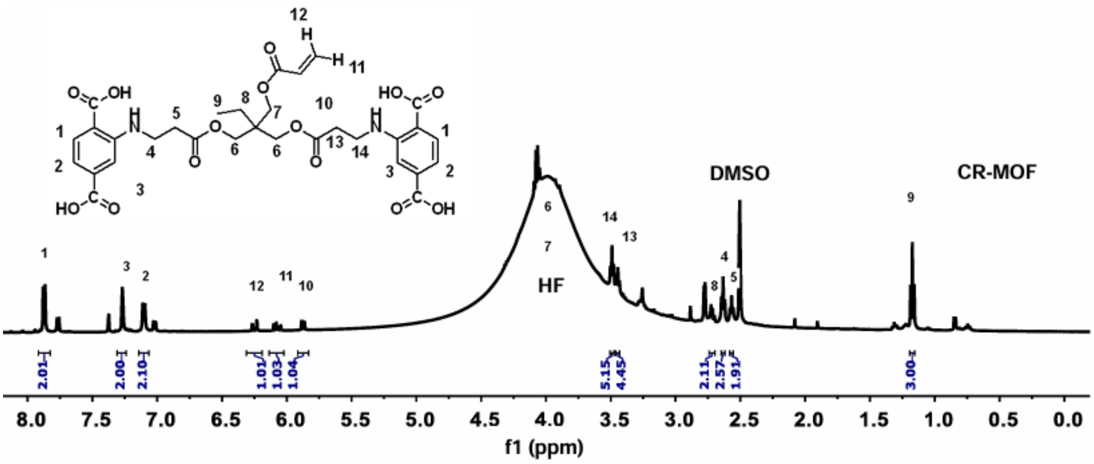

Figure 2.3 ^{1}H NMR spectra of NH$_2$-UiO-66 MOF was digested/ dissolved in HF/ DMSO-*d6* (10 µL + 500 µL).

However, the peaks for three aliphatic -CH_2 groups (assigned by 6 & 7 in the NMR spectrum) at the region 4.0-4.5 ppm are merged with the broad peak arising due to HF used. The integral intensity ratio of aromatic proton to vinyl proton is found to be 2/1 as two-thirds of the acrylate groups of one 3-Acl are mutually reacted with amines of two ligands, i.e., H_2ATA. The third acrylate group of 3Acl remained unreacted to NH_2-UiO-66, likely due to the existence of steric hindrance imposed by the reacted MOF around the 3Acl molecule. Thus, the unreacted acrylate moiety makes the prepared MOF readily chemically reactive at ambient conditions.

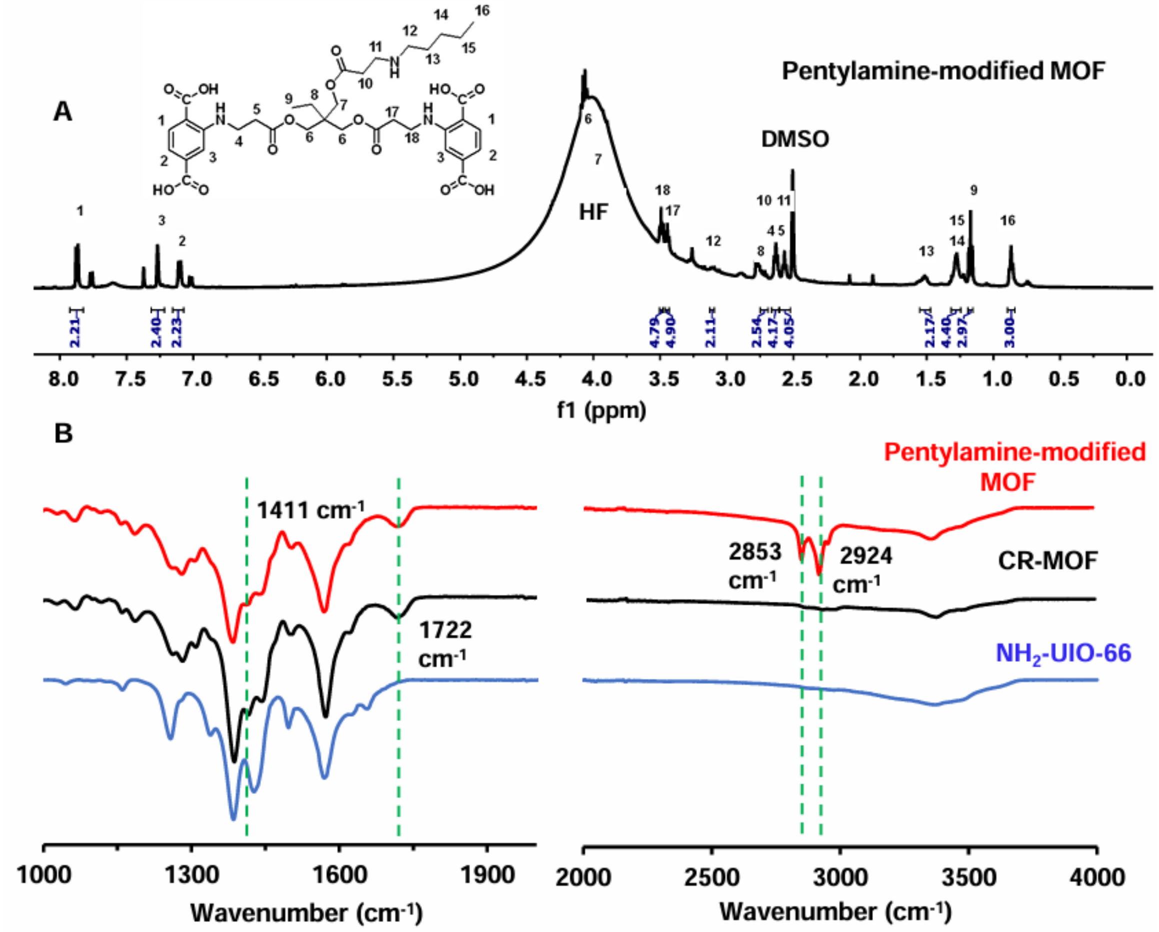

Figure 2.4 A) ^{1}H NMR spectra of pentylamine (PA)-modified MOF was digested/ dissolved in HF/ DMSO-*d6* (10 µL + 500 µL). B) FTIR spectra of NH_2-UiO-66MOF (black) and CR-MOF before (blue) and after (PA@3Acl@NH_2-UiO-66MOF; red) post-modification with pentylamine.

Further, the residual acrylate group present in CR-MOF was exploited to post-modify with the desired amine-containing alkyl chain. In this context, the post-covalent modification of CR-MOF with pentyl amine was successfully characterized with ^{1}H NMR spectral analysis. After the reaction with pentyl amine, the ^{1}H NMR spectrum of the HF/DMSO-d_6-digested product (Figure 2.4A) showed the appearance of new peaks at δ= 0.87 (t, 3H), 1.32-1.25 (m, 4H), 1.57-1.50 (m, 2H) and 2.91- 2.88 (m, 2H) for the aliphatic protons of pentyl group and two new methylene protons (10 & 11 in the NMR spectrum). During this mutual chemical reaction between amine and acrylate, the vinyl moiety is converted into a methylene moiety. Out of these two methylene protons, one is raised separately at 3.10 ppm (t, 2H) and the other is merged with one of the β protons of secondary amine at 2.63 ppm (t, 4H) due to the nearly similar chemical environment of the protons. This is supported by the integral intensity of the peaks at that particular region.

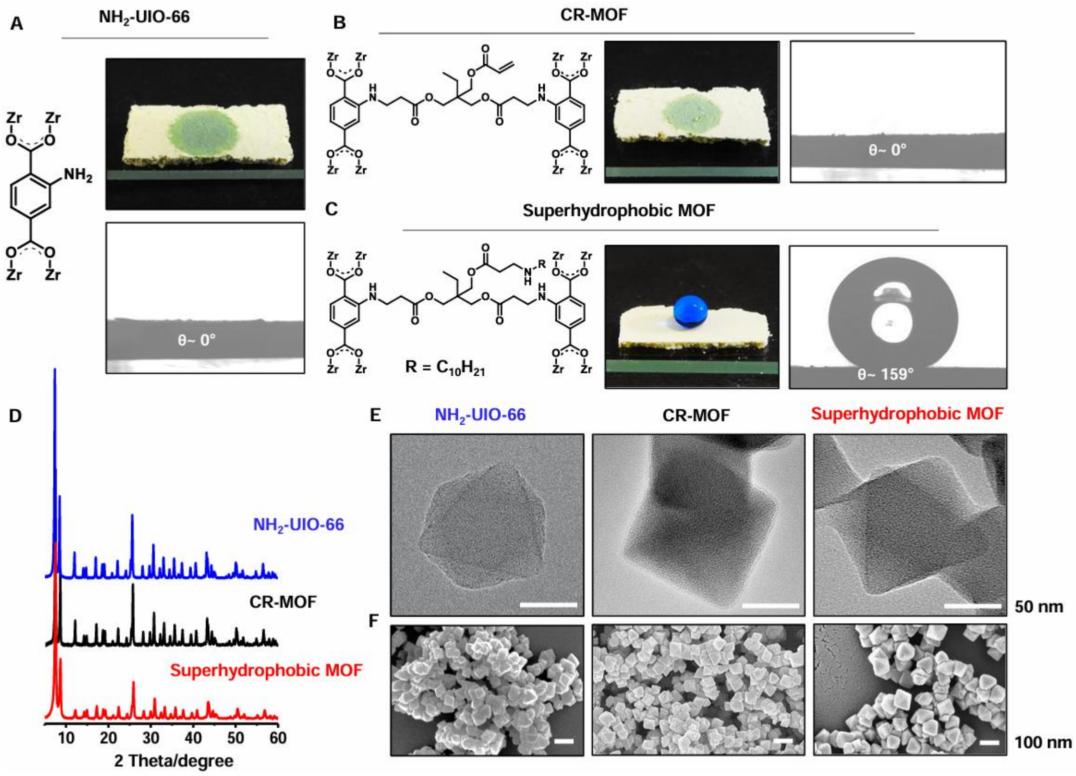

Figure 2.5 (A–C) The digital images and contact angle images accounting for water wettability of NH_2-UiO-66 (A), CR-MOF (B) and super hydrophobic MOF (C). (D) Powder XRD patterns of NH_2-UiO-66 (blue), CR-MOF (black), and superhydrophobic MOF (red). (E, F) Field emission transmission electron microscope (FETEM; E, scale bar, 50 nm) and field emission scanning electron microscope (FESEM; F, scale bar, 100 nm) images of NH_2-UIO-66, CR-MOF and superhydrophobic MOF.

In addition, a significant depletion of the ^{1}H-NMR signal for the residual acrylate group in the range from 6.25 ppm to 5.87 ppm was noted with respect to the aromatic protons (δ= 7.10 (d, 2H), 7.27 (s, 2H) and 7.87 (d, 2H) ppm) as shown in Figure 2.3. This data unambiguously indicated the post-covalent modification of CR-MOF with selected pentylamine. Furthermore, FTIR spectral analysis supported that the mutual reaction between 3-Acl and NH_2-UiO-66 yielded CR-MOF, where IR signatures for carbonyl stretching and C-H deformation of vinyl group appeared at 1722 cm^{-1} and 1411 cm^{-1}, respectively. On treating the CR-MOF with pentylamine, the characteristic IR peak for aliphatic C-H stretching of pentyl moiety was noticed, as shown in Figure 2.4B. Eventually, such a facile chemical modulation strategy allowed for the tailoring of a range of desired water wettability of the prepared MOF (Figure 2.5A-C). For example, the post-covalent modification of the CR-MOF with decyl amine (DA) yielded a superhydrophobic MOF with a water contact angle (WCA) of ~159°, as shown in

Figure 2.5C. The impact of other modifications on the water wettability to achieve degrees of hydrophobicity is discussed later. Importantly, the integration of the residual acrylate group in the NH_2-UiO-66 and the subsequent post-covalent modification of CR-MOF have minimal impact on the structural integrity of the native MOF, as evident from the similarity in the powder XRD pattern of native MOF, CR-MOF and superhydrophobic MOF, as shown in Figure 2.5D. Similarly, the morphology of the native MOF remained unaffected after the association of residual acrylate groups and its post-covalent modification with DA through the 1,4-conjugate addition reaction, as confirmed from both FETEM and FESEM images in Figure 2.5E, F. The octahedral shape was preserved in the highly crystalline FESEM images in Figure 2.5E, F. The octahedral shape was preserved in the highly crystalline MOF, irrespective of associating these distinct chemical modulations.

2.3.2. MOFs with Chemically Tailored and Responsive Water Wettability

For the controlled tailoring of water wettability, the chemically reactive MOF was post-modified with various alkyl amines, i.e., lower analogues of DA, and the hydrophobicity of the MOF was gradually depleted by reducing the length of the hydrocarbon tail of the selected alkyl amine from $C_{10}H_{21}$ (DA) to C_5H_{11} (pentyl amine, PA), as shown in Figure 2.6A-C. While individual modifications of CR-MOF (Figure 2.6A) with octyl amine (OA) and DA provided superhydrophobicity with a WCA > 150°, the modification of the same MOF with hexyl amine (HA) and PA provided only hydrophobicity with WCA of ~133° and ~121°, respectively.

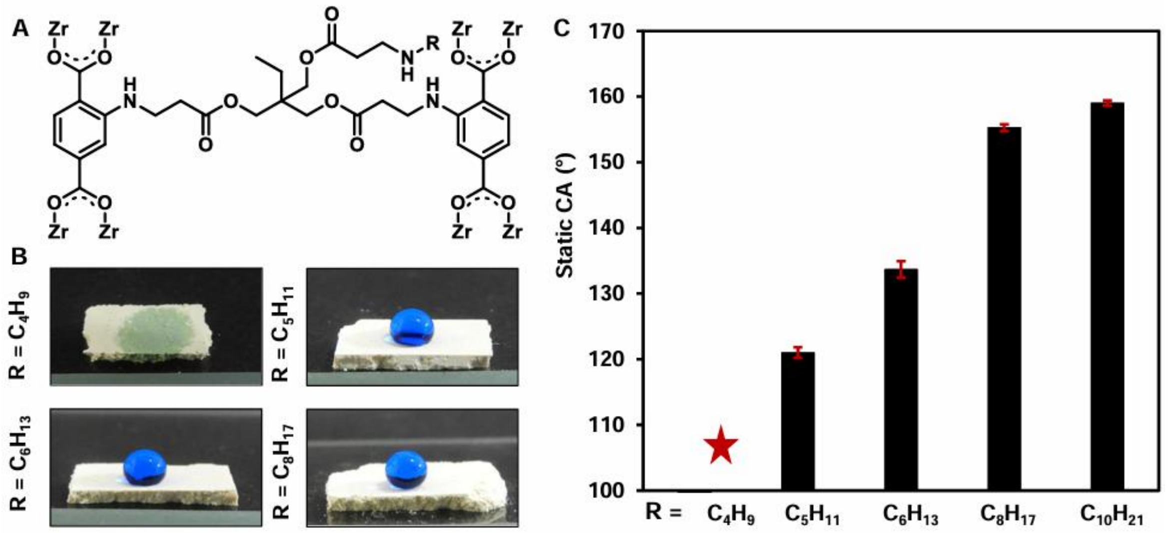

Figure 2.6 A) Chemical structure of CR-MOF. B) Digital images accounting the wettability of beaded water droplet (blue color aids visual inspection) on the prepared MOFs that were individually post-modified with different alkyl amine, including butyl amine, pentyl amine, hexyl amine and octyl amine. C) The plot accounting for the change in water wettability of the modified MOFs depending on the hydrocarbon tail length of selected modifiers, i.e., alkyl amines.

However, the post-covalent modification with butylamine (BA) failed to alter the water wettability, and it remained highly hydrophilic, as shown in Figure 2.6B. Thus, the water wettability of the octahedral-shaped MOF was successfully tailored through the facile and catalyst-free 1,4-conjugate addition reactions with appropriate alkyl amine at ambient conditions. Thereafter, the impact of pH on the chemically modified MOF was examined. Interestingly, the PA ($-C_5H_{11}$) modified hydrophobic MOF displayed a drastic and instant transition in water wettability from hydrophobicity (WCA of 122°) to hydrophilicity (<70°) in both highly acidic (pH 1) and alkaline (pH 12) conditions, however, superhydrophobic MOF (DA-treated) remained non-responsive to the extremes of pH, instead it continued to exhibit unperturbed superhydrophobicity with WCA > 155°, as shown in Figure 2.7A and Figure 2.7B. Thereafter, the water wettability of differently chemically-modulated (PA, HA, OA) hydrophobic and superhydrophobic MOFs were examined in various pH over a range from pH 1 to pH 12, as shown in Figure 2.7C. We observed no instant change in water wettability for the hydrophobic MOFs at the pH range of 4 to 8, however, a significant depletion of the WCA was noted at highly acidic (pH 1 & 2) and alkaline (pH 10 & 12) conditions, as shown in Figure 2.7C. Whereas the superhydrophobic MOFs displayed uninterrupted water repellence with WCA of > 150° over a pH range from 1 to 12. Thus, the same CR-MOF individually post-modified with selected alkyl amine resulted in dual (acidic/alkaline) pH-sensitive hydrophobicity and stable superhydrophobicity. To understand such distinct wettability transitions for hydrophobic and superhydrophobic MOFs in various pH, further experiments were designed.

In the past, the structural instability of NH_2-UiO-66 at alkaline condition was addressed through the association of superhydrophobicity. Similar to the previous report, the currently synthesized superhydrophobic MOF continued to display unperturbed extreme water repellence at extremes of pH, with no change in structural integrity even after exposure to extremes of pH for 6 h as evident from the powder XRD pattern in Figure 2.7F. However, the PA-modified hydrophobic MOF failed to protect the structural integrity of the MOF (Figure 2.7D, E) at the alkaline condition, as evident from the powder XRD pattern (Figure 2.7F). The octahedral shape of the MOF was distorted entirely, and the appearance of random granular domains after the alkaline treatment indicated the damage of the structural integration of hydrophobic MOF as shown in Figure 2.7E. Thus, the structural instability contributed to the transition of water wettability of the PA treated MOF from hydrophobicity to hydrophilicity at alkaline conditions. However, the same hydrophobic MOF that was treated at highly acidic (pH 1) condition, continued to display the octahedral morphology (Figure 2.7G), with unaffected

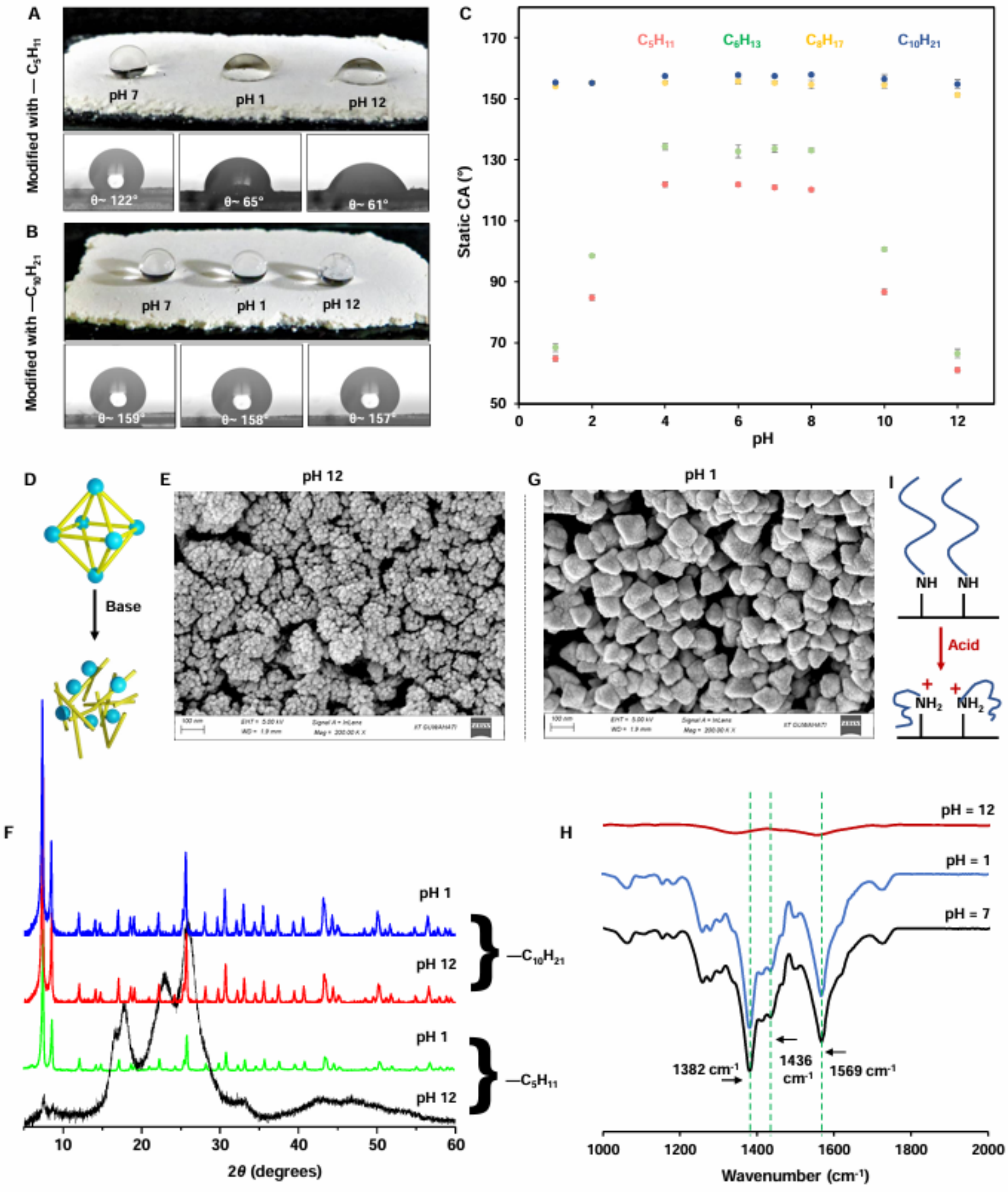

Figure 2.7 (A, B) Digital and contact angle images illustrating the water wettability of hydrophobic (modified with pentyl amine: -C_5H_{11}, A), and superhydrophobic (modified with decyl amine: -$C_{10}H_{21}$, B) MOFs at neutral (pH 7), acidic (pH 1) and alkaline (pH 12) conditions. C) Plot depicting the changes in water wettability of differently modified hydrophobic and superhydrophobic MOFs having distinct hydrocarbon tails (C_5H_{11}, C_6H_{13}, C_8H_{17} and $C_{10}H_{21}$) at various pH (from 1 to 12). D) Schematic depicting the collapse of the structural integrity of hydrophobic MOFs under alkaline conditions. E) FESEM images of PA-modified hydrophobic MOF after exposure to alkaline (pH 12) pH. F) Powder XRD pattern of pentyl amine and decyl amine modified MOF in highly acidic (pH 1; green and blue) and alkaline (pH 12; black and red) conditions. G) FESEM images of PA-modified hydrophobic MOF after exposure to acidic (pH 1) pH. H) FTIR spectra of modified MOF after exposure to alkaline (pH 12, red), acidic (pH1, blue) and neutral (pH 7, black) water. I) Schematic of protonation of available amine in modified hydrophobic MOFs.

crystallinity, as evident from the existence of indistinguishable powder XRD pattern to that of native MOF in Figure 2.7F. On exposure of modified MOF to alkaline condition, the characteristic IR signatures, including $\nu_{asym}[COO^-]$ (1569 cm^{-1}), $\nu_{sym}[COO^-]$ (1382 and 1436 cm^{-1}) were disappeared, whereas these peaks remained intact even after exposure to neutral and acidic condition (Figure 2.7H).

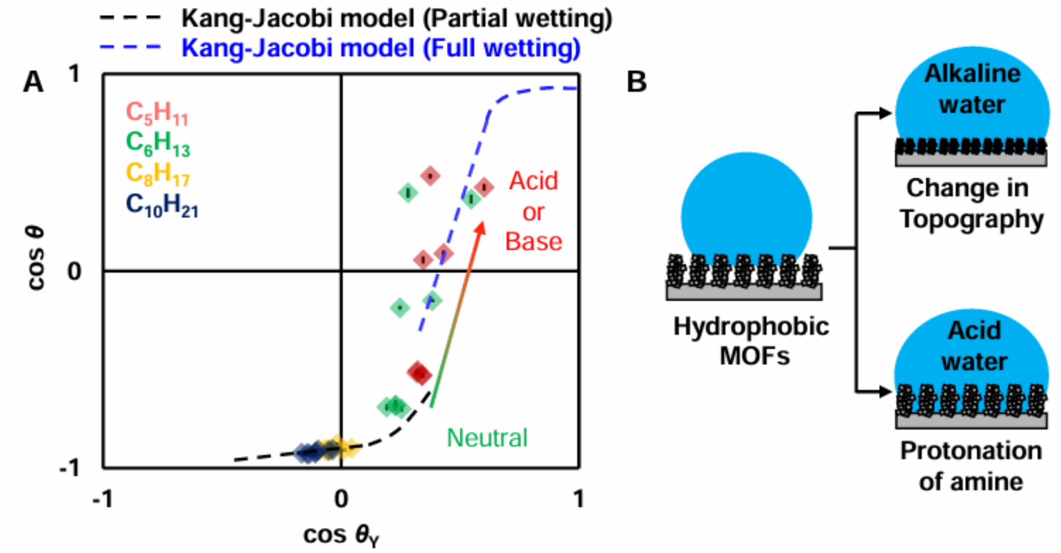

Figure 2.8 (A) Kang-Jacobi wettability model illustrating the wettability transition of both hydrophobic and superhydrophobic MOF at various pH. (B)The schematic depicting the alteration of wettability of hydrophobic MOF in alkaline and acidic conditions through the change in topography and protonation of amine.

This study revalidated the disintegration of modified MOF selectively at alkaline condition. In acidic exposure, the available amine group in the hydrophobic MOF is likely to be protonated, and resulted in the change in wettability from hydrophobic to hydrophilic, as shown in Figure 2.7I. Thereafter, the water wettability of both hydrophobic and superhydrophobic MOFs was investigated at various pH and the obtained data were fitted with the Kang-Jacobi model of wettability, as shown in Figure 2.8A. As expected, the superhydrophobic MOFs followed the partial wetting (i.e., the air layer is entrapped beneath the droplet) of the Kang-Jacobi model, whereas the hydrophobic MOFs displayed a transition from partial wetting to full wetting (i.e., the entrapped air layer diminished) depending on changing the environment from neutral to acidic or alkaline as depicted in Figure 2.8B. Thus, the chemically modulated hydrophobic MOF displayed from both a) the structural instability in alkaline conditions and b) the protonation of available amine in acidic conditions, which eventually provided a facile basis to derive an adaptive LMs with the ability of both automated and adjustable triggered release of inner liquid. However, the superhydrophobic MOFs failed to display such characteristics as the available amine and labile coordination bonds are likely to be buried by the long hydrocarbon tails of the superhydrophobic MOFs.

2.3.3. Deriving Adaptive LMs

Both the dual (acidic/alkaline) pH-responsive hydrophobic and stable superhydrophobic MOFs were explored in preparing LMs by wrapping the water droplet with the respective hydrophobic and superhydrophobic MOFs, as shown in Figure 2.9A-D. In Figure 2.9E-H, the MOF based LMs sit on the hydrophilic glass substrate with an apparent contact angle of >150°, like a superhydrophobic state.

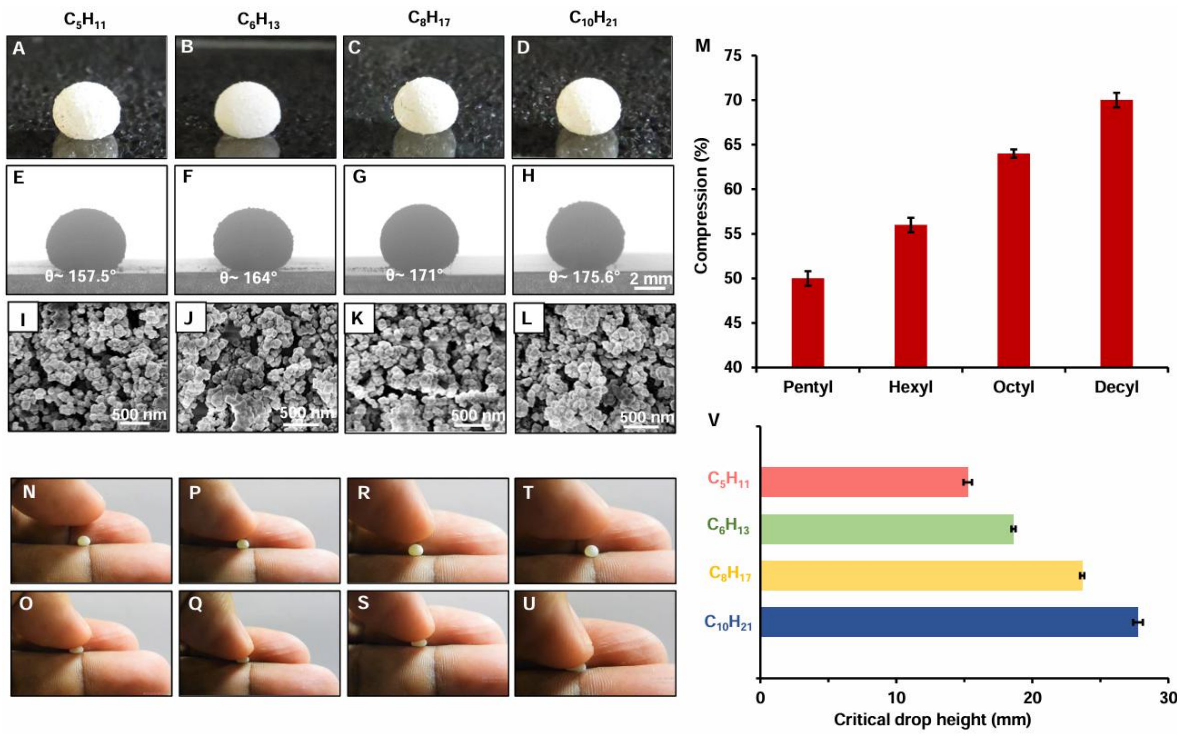

Figure 2.9 Digital images (A-D) and contact angle images (E-H) of LMs that were derived from pentyl amine (A and E), hexyl amine (B and F), octyl amine (C and G), and decyl amine (D and H) modified MOFs. (I-L) FESEM images illustrating the arrangement of MOFs (that were decorated with various alkyl amines (I: pentyl, J: hexyl, K: octyl, and L: decyl)) at the air/water interface, where the superglue (cyanoacrylate) is used to preserve the arrangement of respective MOFs at the air/water interface. (M) The plot compares the limit of tolerance LMs for sustaining the applied compressive strains. (N-U) Digital images of LMs of different alkyl amine modified MOFs [pentyl (N-O), hexyl (P-Q), octyl (R-S), and decyl (T-U)] while compressing with a bare hand. (V) Plot to account for the impact durability of the prepared LMs, where LMs were dropped from a certain height so that they can survive.

The contact angle increases gradually with the increase in chemically modulated hydrophobicity of the modified MOF. The higher contact angle is attributed to the shell tension of the LMs, which resists the deformation caused by the LMs' weight. After that, the surface structures of LMs are obtained by polymerizing their air-water interface[41] and then observed by FESEM (Figure 2.9I-L), where no apparent change in the structure of LM's surface is observed. It is hypothesized that the molecular interaction between MOFs contributes to the change in the LMs tension. The interaction among modified MOFs improved with increasing the length of the hydrocarbon tail. The MOF based LMs exhibit tolerance against mechanical compression (Figure 2.9M) manipulations with bare hands (Figure 2.9N-U) and impact on the solid surface (Figure 2.9V). The mechanical strength and survival under compressive strain improved with the embedded hydrophobicity of modified MOF.

Eventually, the improved hydrophobicity of MOF contributed to resisting the inner liquid spill from the prepared LMs.

Then, these LMs were placed into the water pool to examine their lifetime (Figure 2.10A-D). The lifetime of the LMs drastically changed with the variation in the embedded hydrophobicity. In that, LMs derived from PA ($-C_5H_{11}$) or HA ($-C_6H_{13}$) modified MOF collapsed down with a lifetime of 1.2 or 2.8 hours (Figure 2.10A or 2.10B), whereas LMs prepared out of OA ($-C_8H_{17}$) or DA ($-C_{10}H_{21}$) modified MOF did not collapse until the inner liquid evaporated completely (Figure 2.10C and 2.10D).

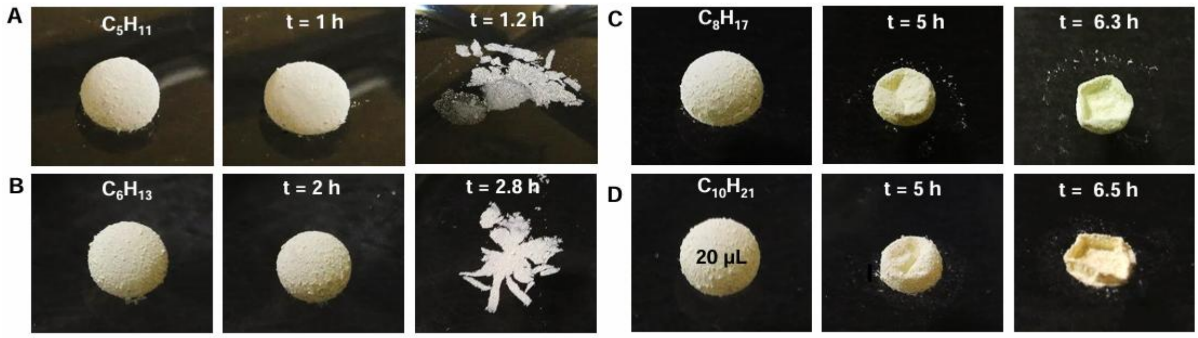

Figure 2.10 (A-D) Digital images illustrating the bursting and buckling of LMs that were prepared from differently modified hydrophobic (A and B) and superhydrophobic (C and D) MOFs.

To understand the stability of LMs that are derived from chemically modulated MOFs, we considered the free energy ΔG required to adsorb a single MOF to the water surface (Figure 2.11A), which yields:

$$\Delta G = -\sqrt{3}/4D^2[1 + \cos\theta_Y]$$

where D is the one side length of the MOF, γ_L is the inner liquid surface tension, and θ_Y is the Young contact angle of the inner liquid droplet on the MOF surface.

Here, θ_Y on the MOF is substituted by the static contact angle on the flat glass substrate coated with the same chemicals used for MOFs' modification (Figure 2.11B). We assume that the one face of the MOF with a surface area of $\sqrt{3}/4D^2$ attach to the water surface, which results in the formation of the MOF-water interface while decreasing the MOF-air and water-air interfaces. Thus, we obtain

$$\Delta G = -\sqrt{3}/4D^2[\gamma_\mathrm{S} + \gamma_\mathrm{L} - \gamma_\mathrm{SL}]$$

where γ_S and γ_SL are MOF-air and MOF-water interfacial energy.

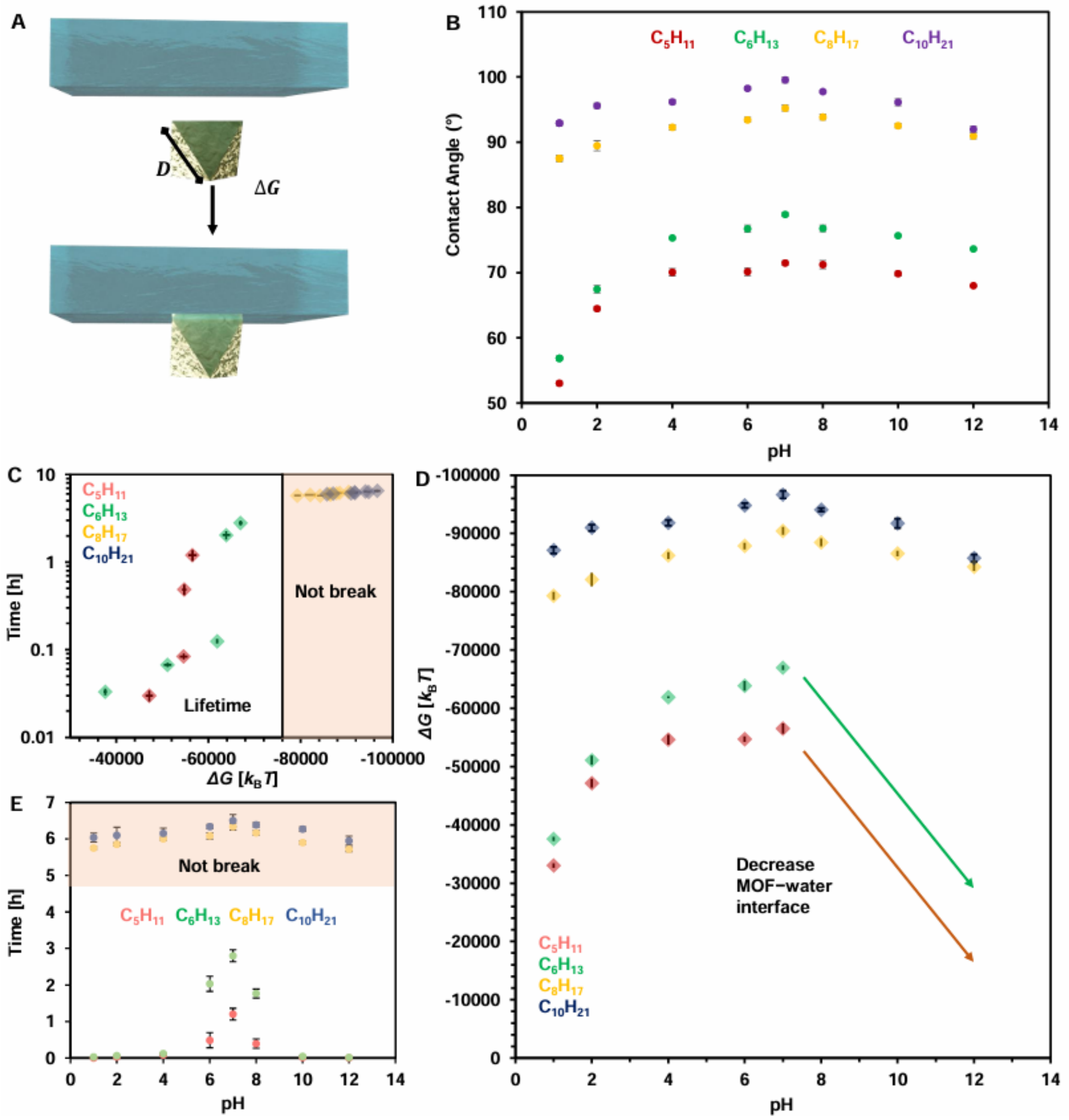

Figure 2.11 (A) Illustrating the energy of adhesion of MOF (B) Plot showing the change in the Young contact angle of a beaded aqueous solution of different pH on different coatings on flat substrates, where 3Acl and different selected alkyl amines were used individually to apply the coating on glass substrate before measuring the contact angle. (C) Accounting the dependence of the lifetime of LMs on the energy of adhesion of chemically-modified MOFs. (D) The plot accounting for the change in adsorption energy of chemically modified MOF to aqueous surface with variation of pH. (E) Accounting for the stability of LMs at various pH values of the water pool.

According to Young's equation, $\gamma_S = \gamma_L \cos\theta_Y + \gamma_{SL}$. By combining these equations, we obtain

$$\Delta G = -\sqrt{3}/4D^2[1+\cos\theta_Y]$$

We observed that the LMs' lifetime was increased with the decrease of the adsorption energy, and the LM with the ΔG smaller than the threshold value was not broken down in this experiment (Figure 2.11C). We noticed that the MOFs' pH responsivity modulates their wettability (Figure 2.7D) and/or size (Figure 2.7I) as well as their ΔG (Figure 2.11D).

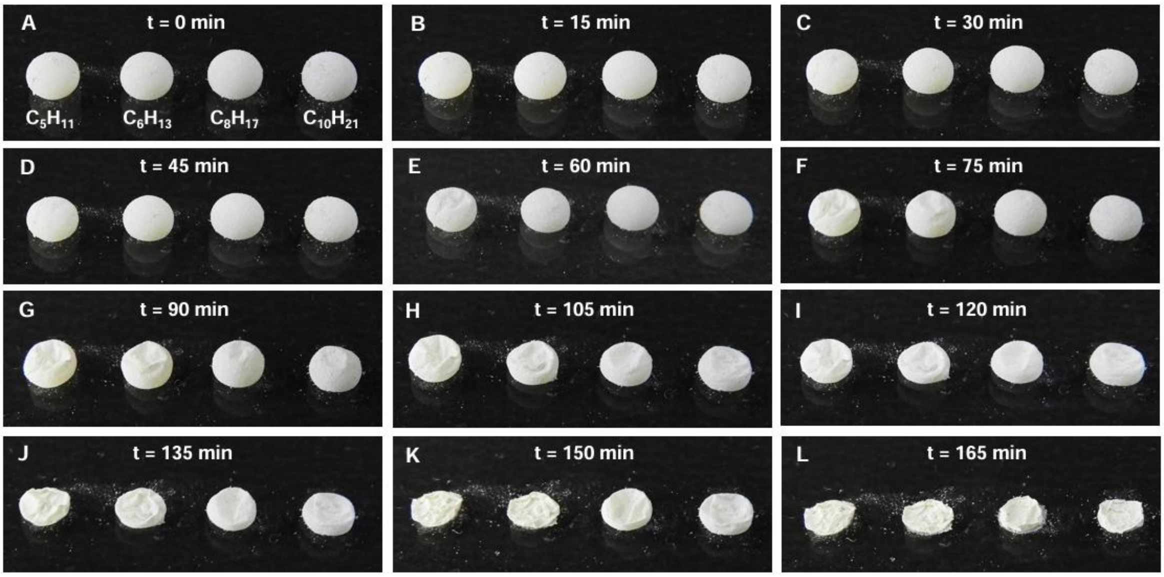

Figure 2.12 (A-L) Digital images accounting for the stability of the LMs (prepared from differently modified MOFs) on solid surface. No release of liquid water was noticed, rather, inner water was evaporated out and resulted in buckling of the LMs over the time.

Thus, the lifetime of the same MOF-based LM is also varied in response to the water pool's pH (Figure 2.11E). However, the lifetime of the LM on water pools mostly depends on the chemical modification of the prepared CR-MOF with selected alkyl amines. On the other side, the LMs prepared from differently modified MOFs did not collapse to release inner liquid on the solid surface; rather, the encapsulated water evaporated over time, which resulted in the buckling of the prepared LMs (Figure 2.12A-L).

2.3.4. Carrier for Adjustable Drug-Release

Taking advantage of the pH-dependent lifetime of the PA and HA-modified MOFs at both acidic and alkaline conditions, I demonstrated the adjustable drug release, where rhodamine B (2 mM) is selected as a model drug molecule (Figure 2.13A-B) for visualizing the inner liquid release, and the concept can be applied to the drug release application. The dissolved model drug molecule is encapsulated in the LMs, and controlled bursting of LMs allows the release of loaded rhodamine B at a specified time, as depicted in Figure 2.13A. At neutral pH (7), the release of the loaded solution of rhodamine B from LMs that were separately prepared using PA and HA-modified MOFs was noticed after 1.2 h and 2.8 h, respectively, as shown in Figure 2.13C-D.

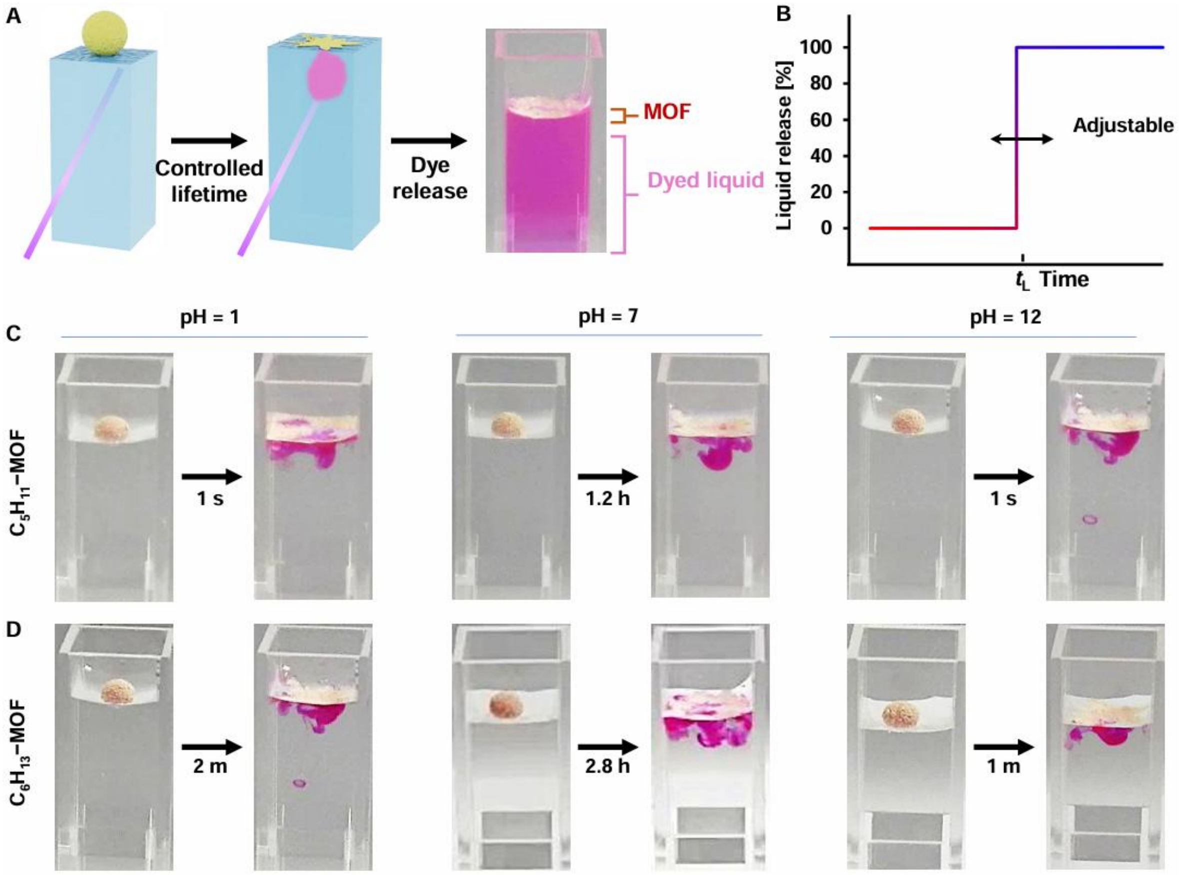

Figure 2.13 (A) Illustrating the release of the loaded dye solution through controlled bursting of LMs. (B) Depicting the adjustable release of the loaded liquid by modulating the life time of the prepared LMs. (C and D) Digital images demonstrating the release of loaded rhodamine B from LMs that were prepared using pentyl (C) and hexyl (D)modified MOF at hour, minutes, and second scales depending on the pH (1, 7, and 12) of the aqueous media.

However, the same LMs rapidly released the loaded solution of dye at both pH 1 and pH 12, and the time scale for releasing the loaded solution of dye was reduced from 1.2 h to 1 second and 2.8 h to 1 or 2 minutes for PA and HA modified MOF based LMs, respectively, as shown in Figure 2.13C-D. Thereafter, the release of loaded dye molecules from the same LMs at various other pH values was monitored by measuring the change in the percentage of absorption intensity over time.

Depending on the pH of the water pool and chemical modification of the MOFs that were used to prepare the respective LMs, it provided an adjustable release of loaded drug molecules from

LMs, as shown in Figure 2.14A, B. The LMs remained efficient in adjusting the triggered release time, depending on the selection of either acidic or alkaline pH of the media. It is because of the alteration of the lifetime of different LMs at various pH of the aqueous pool (Figure 2.14C).

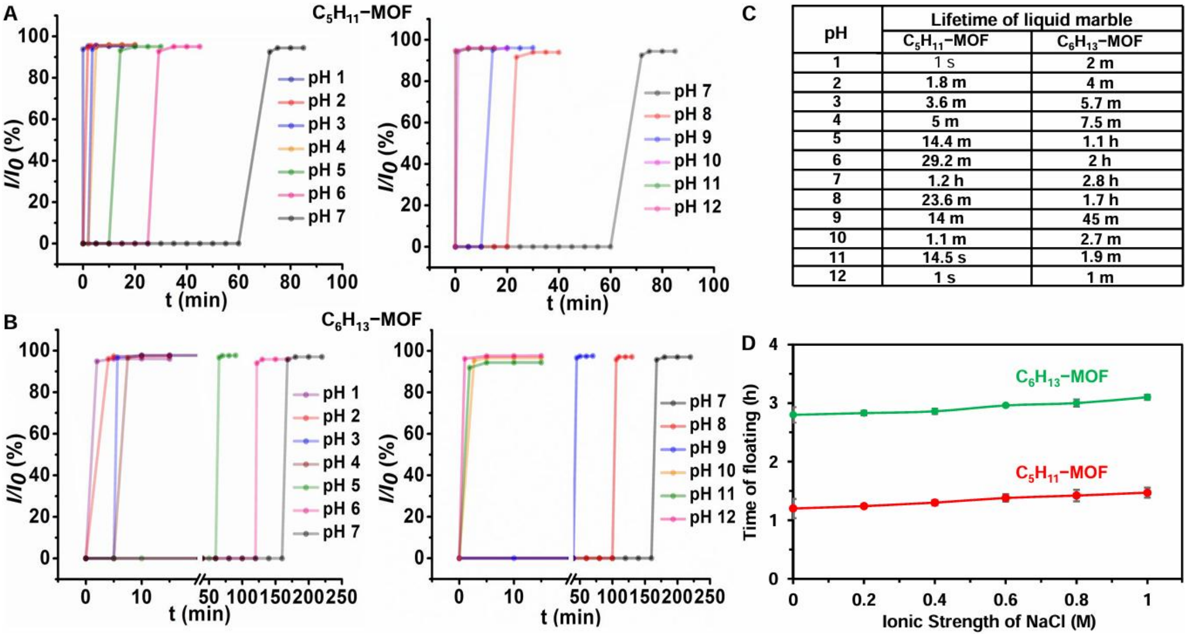

pH	Lifetime of liquid marble	
	C_5H_{11}–MOF	C_6H_{13}–MOF
1	1 s	2 m
2	1.8 m	4 m
3	3.6 m	5.7 m
4	5 m	7.5 m
5	14.4 m	1.1 h
6	29.2 m	2 h
7	1.2 h	2.8 h
8	23.6 m	1.7 h
9	14 m	45 m
10	1.1 m	2.7 m
11	14.5 s	1.9 m
12	1 s	1 m

Figure 2.14 (A and B) The plots accounting the percentage of change in absorption intensity due to the release of the dye from respective LMs (pentyl and hexyl modified MOF-based) in the aqueous phase at different acidic (pH=1,2,3,4,5, and 6) and alkaline (pH=8,9,10,11, and 12) conditions and the adjustment of the release of the dye from the same LMs (either pentyl-modified MOF: A or hexyl-modified MOF: B) are compared with respect to neutral pH conditions. (C) Accounting the life time of different LMs at various pH of the water pool. (D) Accounting a slight improvement in lifetime of LMs (hexyl and pentyl modified MOF based LMs) with increasing the ionic strength of the water pool, where concentration on NaCl was gradually increased to enhance the ionic strength of water pool.

Eventually, such chemically modulated MOF-based LMs can act as a carrier for the time-programmed release of the loaded molecules at different pHs. It is worth mentioning that the lifetime of these LMs is slightly improved by increasing the ionic strength of the water pool by adding salt (NaCl, Figure 2.14D), where the depleted vapour pressure is expected to improve the stability of LMs.

2.3.5. Triggered Chemical Reaction at Water Pool

This section summarizes the behaviour of the MOF-based LMs placed on a water pool as shown in Figure 2.15A-D. The PA ($-C_5H_{11}$) or HA ($-C_6H_{13}$) modified MOF-based LMs broke down in the water pool after a few hours under neutral conditions, and the lifetime could be shortened by the variation in the pH of the water pool (Figure 2.15A and C). Whereas LMs prepared from OA (—C_8H_{17}) or DA (—$C_{10}H_{21}$) modified MOF were not collapsed at any of these pH (Figure 2.15B and D). Such multi-responsivity in LMs on water pools has not yet appeared in the literature. Using the feature of the MOF-based LMs, time-programmed inner liquid release on the water pool was possible under acidic (Figure 2.15E) or alkaline conditions (Figure 2.15F). In the setup, LMs prepared by different hydrophobic MOFs were placed on the water pool, and the concentrated aqueous solution of acid or base was added into the water pool. In both cases, LM derived from hydrophobic MOFs readily broke down to release inner liquid into the water pool.

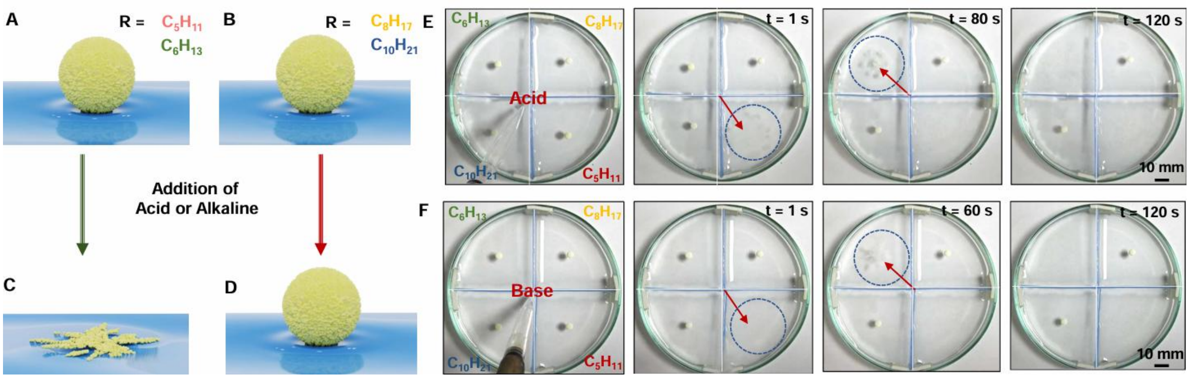

Figure 2.15 (A–D) Schematic illustrating the acid/alkaline-responsive (A and C) and non-responsive (B and D) behaviour of LMs in the water pool. The LMs were prepared from hydrophobic (decorated with C_5H_{11} and C_6H_{13}; A) and superhydrophobic (modified with C_8H_{17} and $C_{10}H_{21}$; B) MOFs. (C) Hydrophobic MOF-based LMs displayed bursting at the water pool at both acidic and alkaline exposures, whereas LMs derived from super hydrophobic MOFs remained unperturbed under both acidic and alkaline water pools (D). (E and F) Digital images demonstrating the spatially selective triggered release of the inner liquid from LMs that were prepared from hydrophobic MOFs under both acidic (E) and alkaline (F) conditions, the LMs that were derived from superhydrophobic MOF failed to burst at identical setups.

As expected, the LM derived from PA (—C_5H_{11}) modified MOF was broken faster (~ 1 minute) than the LM prepared from HA (—C_6H_{13}) modified MOF. These phenomena could be used for demonstrating on-demand chemical reactions at the water pool (Figure 2.16A). For this purpose, the PA (—C_5H_{11}) modified LMs were formed by KSCN (aq.) or $FeCl_3$ (aq.) solutions. In response to the acid added to the water pool, they collapsed to release solutions of mutually reactive reactants. The water gets red colored due to the formation of metal complexes through the mutual reaction between selected metal ions and ligands (Figure 2.16B). During this reaction, the DA(—$C_{10}H_{21}$) modified LMs were not broken down and instead kept floating in the water. The formation of a metal ion complex is characterized by UV-Vis spectral characterization (Figure 2.16C). Moreover, such demonstration of chemical reaction may be extended to other solvent systems and reactants as the modified MOFs allowed to prepare LMs using liquids with different surface tension (Figure 2.16D).

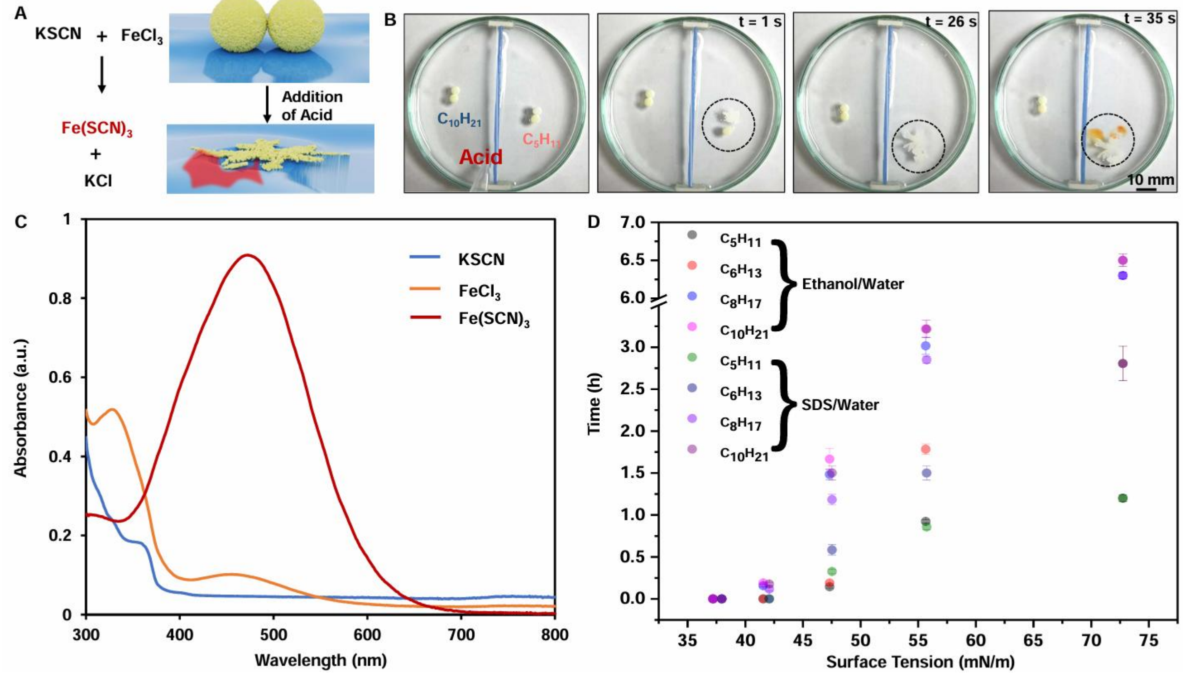

Figure 2.16 (A and B) Demonstrating the triggered chemical reaction on the water pool in the presence of acidic stimuli by individual and triggered release of mutually reactive reactants (ferric chloride and potassium thiocyanate) from the two LM prepared from hydrophobic MOFs. The formation of a ferric thiocyanate complex resulted in the appearance of red colour in the water pool. However, LMs that were prepared from superhydrophobic MOFs failed to release the encapsulated reactants under the identical setup. (C) UV-Vis absorbance spectra of FeCl$_3$ and KSCN and Fe(SCN)$_3$ in HCl (1M) solution. (D) The plot accounting for the lifetime of the prepared LMs on water pool where liquids with different surface tension were used to prepared the LMs.

2.3.6. Optode Detection of Nitrite Ion (NO$_2^-$) in Water

In this section, the acid-triggered bursting behaviour of prepared LM is successfully applied to sense an important and relevant toxic chemical, i.e., nitrite ions (NO$_2^-$). Consumption of NO$_2^-$ contaminated water beyond a certain concentration (65 µM recommended by the World Health Organization (WHO)) is known to have a severe impact on our health.[42-43] Here, the stimuli-responsive LM was utilized to demonstrate optode detection of NO$_2^-$ below its recommended concentration. In this context, reagents for modified Griess reactions,[44] i.e., sulfanilamide and aniline, were loaded in the prepared LM prior to placing it in a water pool contaminated with NO$_2^-$ (40 µM). Upon addition of HCl, the water pool became acidic and the LM collapsed to release the loaded reagents to undergo the Griess reaction in the presence of NO$_2^-$. Immediately, the color of the water poll turned yellow as shown in Figure 2.17A. However, we have not noticed such changes in coloration in the water pool, in the absence of nitrite ions as shown in

Figure 2.17B. The modified Griess reaction between released reagents (sulfanilamide and aniline) from LM and nitrite ions present in the water pool at acidic conditions yielded the yellow colored diazo dye as shown in Figure 2.17C.

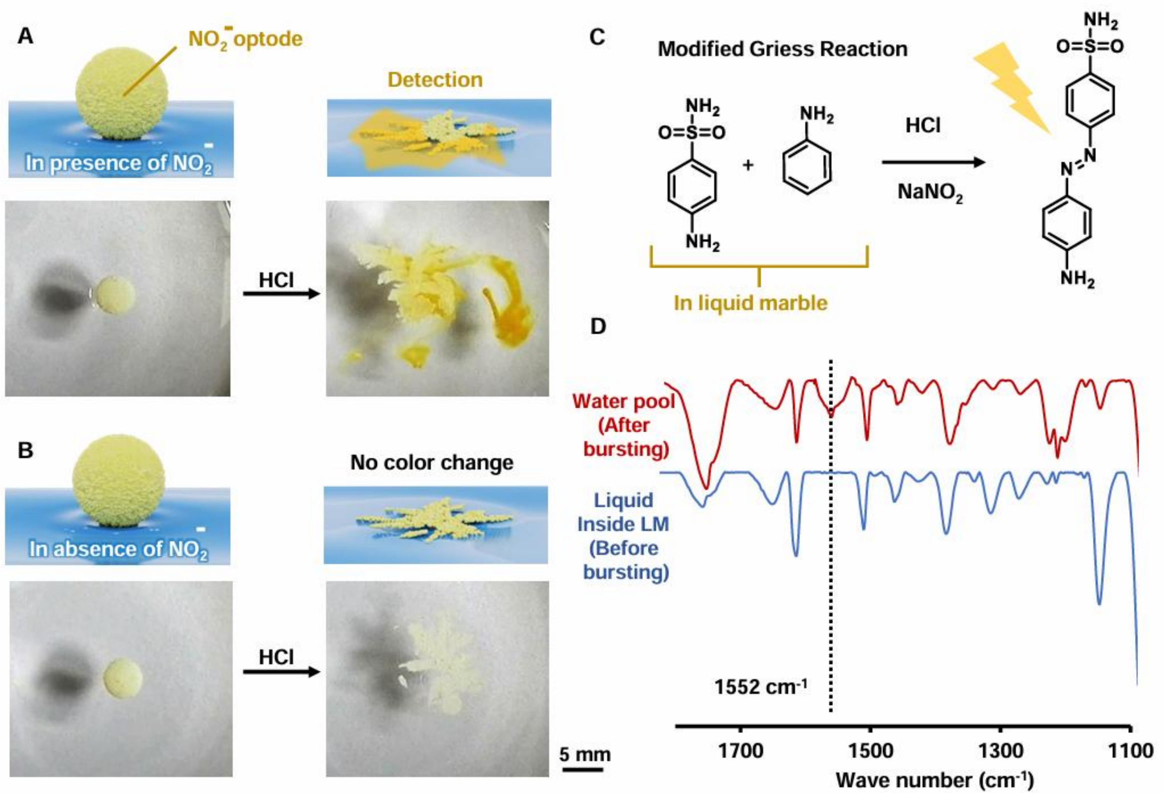

Figure 2.17 (A) Depicting the optode sensing of nitrite ions on acid-triggered bursting of the prepared LM (loaded with sulfanilamide and aniline) in a water pool contaminated with nitrite ions, where the water pool became yellow. (B) No such color change was noted in the absence of nitrite ions in the water pool. (C) Reaction scheme for the modified Griess reaction. (D) FTIR spectra of the loaded aqueous phase in LM (before bursting) and the coloured water pool after bursting of LM.

The appearance of IR peak for N=N stretching at 1552 cm^{-1} revealed the formation diazo compound as shown in Figure 2.17D.[45] Thus, the current strategy is successfully implemented for proof of concept demonstration of the naked eye, fast and facile detection of nitrite ions well below its recommended concentration.

2.4. Conclusion

In conclusion, here, I have introduced a chemically reactive and porous nanomaterial forcontrolled and precise chemical modulation through a 1,4-conjugate addition reaction at ambient conditions to derive mechanically robust LMs with tuneable and adaptive pH sensitivity. While chemically modulated and inherently porous MOFs decorated with longer hydrocarbon tails provided physically and chemically tolerant LMs, the association of shorter hydrocarbon tails yielded LMs for the automated releasing of inner liquid at the water pool at a predefined time (order of hours), without external intervention. The selected chemical modulation of MOF controls the lifetime (from seconds to hours) of LMs at both acidic and alkaline conditions. Such a principle was successfully exploited to demonstrate 1) predetermined automated bursting of inner liquid on a water pool and triggered release of mutually reactive chemicals to perform chemical reaction on demand, 2) adjustable small molecule release and 3) facile and fast chemical sensing.

2.5. References

1 P. Aussillous and D. Quere, *Nature*, 2001, **411**, 924-927.

2 Y. Xue, H. Wang, Y. Zhao, L. Dai, L. Feng, X. Wang and T. Lin, *Adv. Mater.*, 2010, **22**, 4814-4818.

3 C. H. Ooi, R. Vadivelu, J. Jin, K. R. Sreejith, P. Singha, N.-K. Nguyen and N.-T. Nguyen, *Lab Chip*, 2021, **21**, 1199.

4 D. Dupin, S. P. Armes and S. Fujii, *J. Am. Chem. Soc.*, 2009, **131**, 5386-5387.

5 L. Zhang, D. Cha and P. Wang, *Adv. Mater.*, 2012, **24**, 4756-4760.

6 D. Wang, L. Zhu, J.-F. Chen and L. Dai, *Angew. Chem. Int. Ed.*, 2016, **55**, 10795-10799.

7 S. Fujii, S.-I. Yusa and Y. Nakamura, *Adv. Funct. Mater.*, 2016, **26**, 7206-7223.

8 M. Paven, H. Mayama, T. Sekido, H.-J. Butt, Y. Nakamura and S. Fujii, *Adv. Funct. Mater.*, 2016, **26**, 3199.

9 P. S. Bhosale, M.V. Panchagnula and H. A. Stretz, *Appl. Phys. Lett.*, 2008, **93**, 034109.

10 F. Geyer, Y. Asaumi, D. Vollmer, H.-J. Butt, Y. Nakamura and S. Fujii, *Adv. Funct. Mater.*, 2019, **29**, 1808826.

11 Z. Liu, Y. Zhang, C. Chen, T. Yang, J. Wang, L. Guo, P. Liu and T. Kong, *Small*, 2019, **15**, 1804549.

12 Y. Asaumi, M. Rey, K. Oyama, N. Vogel, T. Hirai, Y. Nakamura and S. Fujii, *Langmuir*, 2020, **36**, 13274-13284.

13 M. Tenjimbayashi and S. Fujii, *Small*, 2021, **17**, 2102438.

14 M. Anyfantakis, V. S. R. Jampani, R. Kizhakidathazhath, B. P. Binks and J. P. F. Lagerwall, *Angew. Chem.*, 2020, **132**, 19422-19429.

15 M. Tenjimbayashi, S. Samitsu, Y. Watanabe, Y. Nakamura and M. Naito, *Adv. Funct. Mater.*, 2021, **31**, 2010957.

16 J. Saczek, X. Yao, V. Zivkovic, M. Mamlouk, D. Wang, S. S. Pramana and S. Wang, *Adv. Funct. Mater.*, 2021, **31**, 2011198.

17 Z. Xin and T. Skrydstrup, *Angew. Chem. Int. Ed.*, 2019, **58**, 11952-11954.

18 C. Gabbott, E. Mele, T. Sun, *J. Biotechnol.*, 2020, **323**, 82.

19 X. Rong, R. Ettelaie, S. V. Lishchuk, H. Cheng, N. Zhao, F. Xiao, F. Cheng and H. Yang, *Nat. Commun.*, 2019, **10**, 1854.

20 D. Sun, P. R. Adiyala, S.-J. Yim and D.-P. Kim, *Angew. Chem. Int. Ed.*, 2019, **58**, 7405-7409.

21 D. M. DeChellis, C. M. Ngule and D. T. Genna, *J. Mater. Chem. A*, 2020, **8**, 5848.

22 H. Saini, P. Kallem, A. Schneemann, V. Ranc, M. Otyepka, R. A. Fischer, E. Otyepkova, F. Geyer, F. Banat, R. Zboˇril and K. Jayaramulu, *J. Mater. Chem. A*, 2021, **9**, 23651.

23 M. Inoue, M. Paven, H. Mayama, H.-J. Butt, Y. Nakamura and S. Fujii, *Polym. J.*, 2011, **43**, 778-784.

24 H. Kawashima, S. Fujii, Y. Nakamura, Y. Iwasaki and S.-I. Yusa, *ACS Appl. Mater. Interfaces*, 2017, **9**, 33351-33359.

25 Z. Zhaoa, S. Qina, D. Wanga, Y. Pua, J.-X. Wanga, J. Saczekc, A. Harveyc, C. Lingd, S. Wangd and J.-F. Chen, *Chem. Eng. J.,* 2020, **391**, 123478.

26 M. Uda, H. Kawashima, H. Mayama, T. Hirai, Y. Nakamura and S. Fujii, *Langmuir*, 2021, **37**, 4172-4182.

27 Z. Zhao, X. Yao, W. Zhao, B. Shi, S. Sridhar, Y. Pu, S. Pramana, D. Wang and S. Wang, *Chem. Eng. J.*, 2022, **443**, 136417.

28 Y. Tsumura, K. Oyama, A.-L. Fameau, M. Seike, A. Ohtaka, T. Hirai, Y. Nakamura and S. Fujii, *ACS Appl. Mater. Interfaces*, 2022, **14**, 41618-41628.

29 B. Wang, G.-X. Yan, Y.-J. Cheng, E.-X. Chen, L. He, X. Zhou, Y. Dai, M.-B. Luo and Q. Lin, *Inorg. Chem.*, 2023, **62**, 10054-10058.

30 J. C. Gomez, N. S. Vishnosky, S. T. Kim, S. A. Dinca, E. B. Finkelstein and R. C. Steinhardt, *Adv. Funct. Mater.*, 2023, **33**, 2214893.

31 N. Barman, A. Shome, S. Kumar, P. Mondal, K. Jain, M. Tenjimbayashi and U. Manna, *Adv. Funct. Mater.*, 2023, **33**, 2214840.

32 J. Canivet, A. Fateeva, Y. Guo, B. Coasne and D. Farrusseng, *Chem. Soc. Rev.*, 2014, **43**, 5594.

33 Q. Wang and D. Astruc, *Chem. Rev.*, 2020, **120**, 1438-1511.

34 R. Freund, O. Zaremba, G. Arnauts, R. Ameloot, G. Skorupskii, M. Dinca, A. Bavykina, J. Gascon, A. Ejsmont, J. Goscianska, M. Kalmutzki, U. Lächelt, E. Ploetz, C. S. Diercks and S. Wuttke, *Angew. Chem. Int. Ed.*, 2021, **60**, 23975-24001.

35 L. Feng, S.-H. Lo, K. Tan, S.-L. Wang, K.-L. Lu and H.-C. Zhou, *Matter*, 2020, **2**, 988-999.

36 Y. Zhang, X. Feng, H. Li, Y. Chen, J. Zhao, S. Wang, L. Wang and B. Wang, *Angew. Chem. Int. Ed.*, 2015, **54**, 4259-4263.

37 H. Wang, S. He, X. Qin, C. Li and T. Li, *J. Am. Chem. Soc.*, 2018, **140**, 17203-17210.

38 H. A. Hamzah, T. S. Crickmore, D. Rixson and A. D. Burrows, *Dalton Trans*., 2018, **47**, 14491.

39 S. Wang, C. M. McGuirk, A. d. Aquino, J. A. Mason and C. A. Mirkin, *Adv. Mater.*, 2018, **30**, 1800202.

40 U. Baruah and U. Manna, *Chem. Sci.*, 2021, **12**, 2097.

41 H. A. Hamzah, T. S. Crickmore, D. Rixson and A. D. Burrows, *Dalton Trans*., 2018, **47**, 14491.

42 S. Wang, C. M. McGuirk, A. d. Aquino, J. A. Mason and C. A. Mirkin, *Adv. Mater.*, 2018, **30**, 1800202.

43 WHO (World Health Organization), *Guidelines for Drinking water Quality*, WHO, Geneva, 3rd edn, 2004.

44 J. B. Fox, *Anal. Chem*., 1979, **51**, 1493.

45 P. J. Larkin, *General Outline for IR and Raman Spectral Interpretation, Infrared and Raman Spectroscopy: Principles and Spectral Interpretation*, 2nd edn, 2018, p. 135.

Chapter 3: Droplet Green Chemistry Using Thermally Shape-Reconfigurable Omniphobic Colloidosomes

A high-yield, lossless chemical reaction conducted under ambient conditions is promising for green chemistry. However, owing to the sticky feature of liquids on solid surfaces and the high volatility of useful primary solvents, “droplet chemistry” is far from practical use. Thus, a droplet platform that prevents both droplet evaporation and adhesion losses is promising. Herein, I report a versatile method for droplet encapsulation with poly(octadecylacrylate)(PODAc) based on the colloidosome technique. The PODAc colloidosomes are mechanochemically stable and thermally shape-reconfigurable while maintaining their surface omniphobicity. This feature enabled PODAc colloidosomes to load typical liquids regardless of their surface tension without experiencing evaporation or adhesion loss, transport like solid beads, and release inner liquid on-demand by heating or NIR light irradiation. The colloidosome is mass-producible and recyclable via a simple thermomechanical process. As a proof of concept, different droplet-scale reactions are demonstrated in colloidosomes using a volatile microliter solvent and volatile reactants.

K. Jain,[⊥] S. Kumar,[⊥] M. dhar, H. Ali, D. Sarkar, N. Barman, M. Tenjimbayashi and U. Manna, *Chem. Mater.*, 2024, **36**, 8692-8703.

3.1. Introduction

In 1998, Paul Anastas and John Warner manifested the 12 Principles of green chemistry. Briefly, waste-free, efficient chemical synthesis through catalysis or sustainable sources seems to be essential for the future of the chemical industry without additional energy input. Chemists and chemical engineers endeavored to work on chemical processes with minimal synthesis cost. Ultimately, microliter-scale chemical reactions may minimize the waste generated from such chemical processes and be helpful in the chemical processing of valuable reagents. However, it is known that droplets stick to the contacting media to minimize the total interfacial energy,[1] which results in adhesion loss of reactants, decreasing the reaction efficiency. To address them, designing nonwetting interfaces around the droplet (for example, superhydrophobic,[2] superomniphobic,[3] slippery surfaces,[4,5] or liquid marble (LM)[6]) has been proposed to minimize adhesion loss, which has propelled sustainable chemical synthesis. Since the droplet levitation strategies, by heating, acoustic, or electric field,[7] require high energy input, there has been a notable focus on designing super liquid repellent surfaces, especially in recent decades.[8,9] In Johnson and Dettre's study,[10] droplet sticking decreases with extreme roughening or sensitive smoothening of the interface. Thus, nano-and/or micrometer-scale roughened superhydrophobic or superoleophobic surfaces and nanometrically smooth lubricated[11] or solid-slippery surfaces[12] have been proposed to prevent loss of liquid because of droplets sticking to their contacting substrate. Further functionalizing these surfaces enabled non-sticking droplet movement, and prototype chemical reactions by coalescing reactive droplets have been demonstrated.[13] These works demonstrated that non-sticking surfaces can minimize adhesion loss. Especially, the recent progress has enabled surfaces with non-sticking properties to low-surface tension liquids.[5,14,15]

However, the inherent challenge in droplet chemistry has been ignored: "How to prevent droplets from evaporating?" Primary organic solvents like acetone, ethanol and hexane have high volatility. When the solvent evaporates, the chemical reaction becomes kinetically uncontrollable and the target reaction efficiency suddenly decreases. This is because the solvent mediates the diffusion of reactive chemicals in the droplet. This solvent evaporation process renders droplet chemistry far from practical use. Ironically, the more the reaction volume is reduced toward green chemistry, the more the liquid vaporization effect cannot be ignored. Overall, preventing droplet sticking and evaporation simultaneously by generally applicable methods is critical in droplet green chemistry.

One approach is to encapsulate the liquid droplet inside liquid-repellent materials. The concept of covering the droplet with (super)hydrophobic nanostructure, namely liquid marble (LM), has been reported.[6,16,17] However, the mechanically weak and discontinuous shell of LM (Figure 3.1A) cannot prevent evaporation, as depicted in the last chapter, liquid molecules can escape from the air-exposed area and pores in the nanostructure.[18-30] The other possibility is to cover the droplet with a solid and continuous shell (Figure 3.1B) having solid-slippery properties to prevent loss of liquid because of (1) liquid adhesion to the inner shell of the capsule/colloidosome and (2) evaporation of encapsulated liquid.

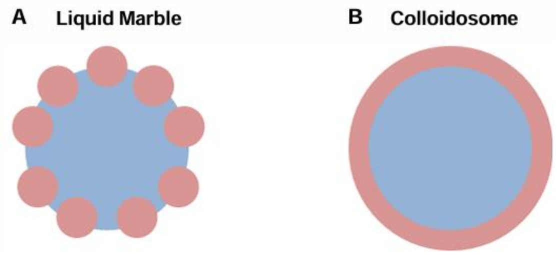

Figure 3.1 A, B) Schematic representing the difference between liquid marble (A) and colloidosome (B). The liquid marble shell is discontinuous and porous, the shell of the colloidosome remains continuous.

In this context, different types of reported capsules or colloidosomes having continuous shells mostly lack the following abilities: (i) repellence to low surface-tension liquids; (ii) preventing evaporation of inner liquid; (iii) on-demand extraction/addition of liquids inside the shell; (iv) reconfigurability of shell; (v) tolerance to mechanical damages; and (vi) triggered release of inner liquid.[31-41] Generally, reported solid-slippery surfaces, formed by covalently grafting flexible polymer brushes or alkyl monolayers on nanometrically smooth surfaces, exhibit omniphobicity.[42,43] It is worth mentioning that the classic omniphobic properties have commonly been achieved by a silane condensation reaction with the assistance of high temperature.[12] It would be extremely challenging to cover droplets of a wide range of volatile/nonvolatile liquids with such a solid-slippery coating following condensing silane oligomers, [18,19] growing the framework materials at elevated temperatures,[44] etc. In this prospect, the challenge is forming a mechanically stable, omniphobic, easily processable, and reconfigurable capsule with an on-demand liquid-insert/release function.

3.2. Experimental Section

3.2.1. Materials Required

Octadecyl acrylate (ODAc), 2-hydroxy-2-methylpropiophenone, glycerol, methylene blue, rose bengal, methyl orange, nile red, propylamine, vanillin, glycidyl methacrylate, bromine, ethylene glycol, poly(vinylpyrrolidone), silver nitrate, NaCl, NaBr, and sodium borohydride were purchased from Sigma Aldrich (Bangalore, India). Tetrahydrofuran (THF) and acetone were purchased from Finar. Perfluoropolyether was purchased from Chemcures. Guaiacol was purchased from Avra Synthesis Pvt. Ltd. Catechol and phenol were purchased from TCI. Dimethyl sulfoxide (DMSO) and hexane were purchased from Alfa-Aesar, India. Apple green food color, raspberry red food color, soldering kit (Techtest 60 W, 220 V) and IR lamp (150 W, 230 V) were procured from Amazon India. The details of the remaining other chemicals used in this work were discussed previously in section 2.2.1 of chapter 2.

3.2.2. Charecterization

Atomic force microscope (AFM) images were acquired using an OXFORD Cypher Atomic Force Microscope. Bright-field and polarized light optical microscopic images were captured using a Zeiss Axio Vert.A1 inverted microscope equipped with crossed polarizers. The transition temperature was measured using a differential scanning calorimeter (Mettler Toledo DSC1) under a nitrogen atmosphere. Mechanical properties were measured using a 5 kN Electromechanical Universal Testing Machine. Number-average molecular weight (M_n) was measured using a high-temperature gel permeation chromatography (HT-GPC) system (Agilent, Model: G7820A). The remaining other instruments used in this chapter for characterization of synthesized materials were the same as discussed previously in section 2.2.2 of chapter 2.

3.2.3. Synthesis of Polyoctadecyl Acrylate

Polyoctadecyl acrylate (PODAc) powder was synthesized following a photopolymerization process.[45] Briefly, 10 g of octadecyl acrylate was dissolved in 15 mL of ethanol, followed by the addition of 50 μL of UV initiator, i.e., 2-hydroxy-2-methylpropiophenone. This prepared solution was kept for photopolymerization under UV irradiation of 365 nm for 30 min, after which the phase-separated polymer was collected and reprecipitated from THF by additions of ethanol three times. I have repeated this process for three times.

3.2.4. Formation of Colloidosome

A 20 μL droplet of glycerol was placed on a bed of superhydrophobic PODAc powder and gently rolled out through the powder. As the droplet was rolled, the superhydrophobic powder spontaneously wrapped around the glycerol droplet, forming a LM. This LM was then placed on a fine powder bed of PODAc on a glass slide, followed by IR light irradiation for ~10 min. The PODAc powder of LM was melted due to IR light irradiation and solidified upon cooling, forming a half-cured colloidosome. Next, the half-cured colloidosome was turned over and positioned so that the remaining uncured powder rested on top. Then, the upper half was cured by using localized heat from a heating solder, forming a fully cured colloidosome.

3.2.5. Refilling of Empty Colloidosome

To exchange the solvent inside the colloidosome, the inside liquid was first decanted. To do so, a surface hole was created in the colloidosome with the help of intense localized heat by using a solder. This broached colloidosome was then placed on a water pool in an orientation such that the hole was in contact with the water pool. Next, the empty colloidosome was individually filled with different liquids, each with a range of surface tension from 72.8 to 17 mN/m. The final step in the process involves closing the surface hole of this liquid-filled colloidosome with a lid made of the same melted PODAc powder. A fine bed of polymer was heated at 70 °C, followed by cooling, which resulted in the formation of a thin film. This thin film was used as a lid and placed on a colloidosome filled with solvent. This lid was then merged with the colloidosome shell by applying localized heat, forming a cured colloidosome packed with the desired solvent.

3.2.6. Tailoring of Colloidosome Shell Thickness

The thickness of the colloidosome shell was tuned by varying the grain size of the PODAc powder. Metal meshes with different predefined pores were used to get PODAc powder with varying size distributions. First, the formed polymer was ground using a mortar and pestle, and the largest particles were obtained with a size distribution around 400-600 µm. These particles are referred to as ST-5. The ground PODAc powder was allowed to pass through a metal mesh with a predefined pore size to obtain particles with different size distributions. The particle size was analyzed under an optical microscope. This microscopic image was then inspected using OpenCV. The pixel-per-metric ratio was defined based on the scale bar provided by the microscopic image. Then, the corresponding contours for different particles in the image were measured. The final particle size reported was the equivalent diameter calculated based on the area and perimeter found from the image detection software. Depending on the size distribution, the PODAc powders are classified as ST-1, ST-2, ST-3, ST-4, and ST-5. The obtained PODAc powder was used to prepare a colloidosome following the above-mentioned procedure.

3.2.7. Impact Test

The impact test was performed by dropping colloidosomes of size 20 µL of different shell thicknesses (ST-5, ST-4, ST-3, ST-2, and ST-1) from various heights (180, 30, 15, 10, and 6 cm) on a hard surface. The physical durability of these was determined by monitoring their rolling behavior on a flat and tilted surface after performing an impact test.

3.2.8. Compression Test

Colloidosomes of size 20 µL were prepared with different shell thicknesses and subjected to gradual compression using a UTM machine with a load capacity of 5 kN.

3.2.9. Measurement of Sliding/Rolling Angle

Sliding and rolling of beaded droplets of selected liquids were observed on coatings embedded with homo- and heterogeneous wettability. In contrast, LM and colloidosomes were rolled on inclined glass surfaces. The rolling angle for LM and colloidosome of 10 μL was carried out by first placing them on a flat glass surface and then gently increasing the tilting angle. A servo motor controlled by an Arduino Uno allows the stage to be tilted at the desired angle. The servo motor was programmed to increase the tilting angle of the stage by 1° every 5 s, and once the stage reached the desired tilting angle, it resulted in rolling off the colloidosome or LM. For super hydrophobic, solid-slippery, and liquid-infused slippery interfaces, sliding/rolling of different solvent droplets of 10 μL was studied on an appropriately tilted interface.

3.2.10. Chemical Reaction in Colloidosome with a Volatile and Low-Surface Tension Medium

Solutions (100 mM) of vanillin and propylamine were separately prepared in ethanol. Thereafter, an empty colloidosome with a capacity of 20 μL is taken and filled with 10 μL each of a solution of vanillin and propylamine. This colloidosome is then packed, as demonstrated earlier, and kept for 1 h to complete the reaction. When mixing transparent solutions of selected reactants, the resultant solution became yellowish, intensifying as the reaction proceeded with time. FTIR analysis was performed by extracting the solution from this colloidosome after 1 h.

3.2.11. Thermoresponsive Reaction with Colloidosome

A highly volatile bromine-water mixture (200 μL/mL) was packed inside a colloidosome of capacity 20 μL. Next, this colloidosome was placed on 20 mL of aqueous solution of phenol (11.4 mM) preheated at 60 °C. Once the colloidosome comes in contact with the aqueous solution of phenol, it releases bromine into the aqueous solution of phenol, forming a white precipitate of tribromophenol. In a controlled study, the same colloidosome loaded with bromine failed to provide such a white residue without phenol in the water pool.

3.2.12. Multifused Colloidosome for the Programmed Reaction

To demonstrate the fusion of colloidosomes, two colloidosomes (capacity of 20 μL) were first broached horizontally to make an interconnection pore. Once connected through this interconnection pore, they were firmly joined together with the help of a PODAc powder, followed by localized heating. This resulted in the formation of fused colloidosomes with an interconnected channel for liquid transport. To demonstrate the flow of liquid across the channel, DI water dyed with methylene blue was placed into one of the colloidosomes with the help of a surface inlet hole. As the liquid volume increased, it reached a stage when the liquid level rose above the interconnection pore and started to flow to the connected colloidosome.

Using the same concept, I demonstrated the fusion of a colloidosome for performing a programmed reaction. A central colloidosome (capacity of 30 µL) was connected to four other colloidosomes (capacity of 20 µL), similar to that explained above. Each of these surface-attached colloidosomes was then filled with different aromatic alcohols including (a) guaiacol (30 mg/mL), (b) catechol (30 mg/mL), (c) phenol (30 mg/mL), and (d) water (for control experiment) such that their level remained below the interconnection pore. A ferric chloride solution (50 mg/mL) was prepared and injected through the central colloidosome, and as its volume increased, it was sequentially distributed to the reaction colloidosomes, yielding (a) a colored oligomer, (b) a colored complex with catechol, and (c) a purple colored complex with phenol. In the control experiment, the fourth colloidosome containing water retained the color of the ferric chloride solution.

3.3. Results and Discussion

3.3.1. Design of Omniphobic Colloidosomes

In this current design of thermally shape-reconfigurable omniphobic colloidosome, a thermoplastic comb-like polymer, PODAc, was synthesized by free-radical polymerization of octadecyl acrylate (ODAc) (Figure 3.2A) following a reported procedure.[21]

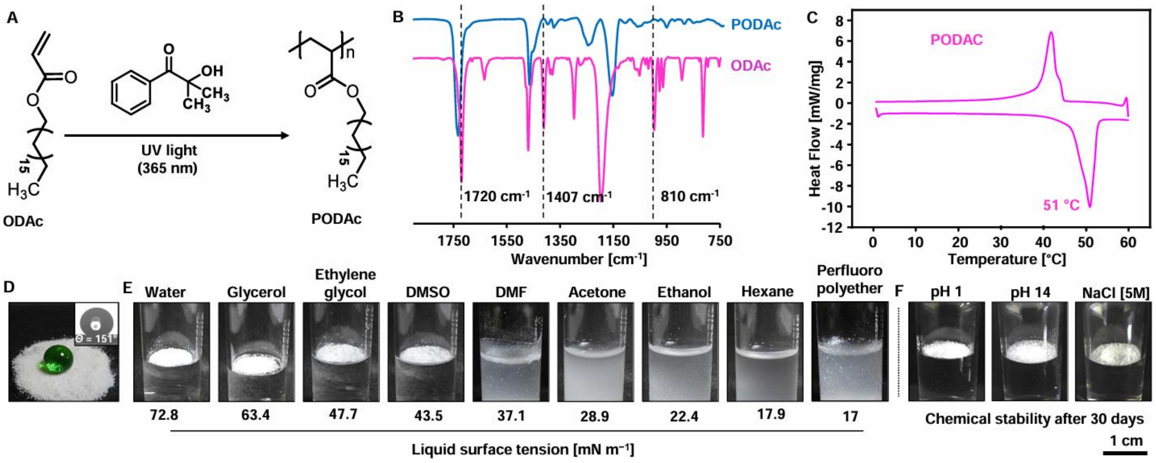

Figure 3.2 A) Reaction scheme representing the synthesis of poly octadecyl acrylate (PODAc) through photopolymerization reaction of octadecyl acrylate (ODAc) in the presence of a photoinitiator. B) Attenuated total reflection-Fourier transform infrared (ATR-FTIR) analysis of PODAc (blue) and ODAc (pink). C) Differential scanning calorimetry (DSC) scan showing the phase transition of PODAc. D) Digital and Static contact angle image (inset) of glycerol on PODAc powder bed. E) Digital images depicting the immiscibility of PODAc powder in different solvents with a wide range of surface tension. F) Digital images showing the stability of PODAc powder after exposure to different chemically contaminated aqueous mediums (pH 1, pH 12, and 5M NaCl) for 30 continuous days.

The conversion of ODAc into PODAc was monitored by ATR FTIR analysis, as shown in Figure 3.2B, where the IR peak for vinylic C-H deformation of the acrylate moiety at 1407 cm^{-1} was significantly compromised with respect to another IR peak for stretching of carbonyl groups at 1720 cm^{-1} after free radical polymerization of ODAc.

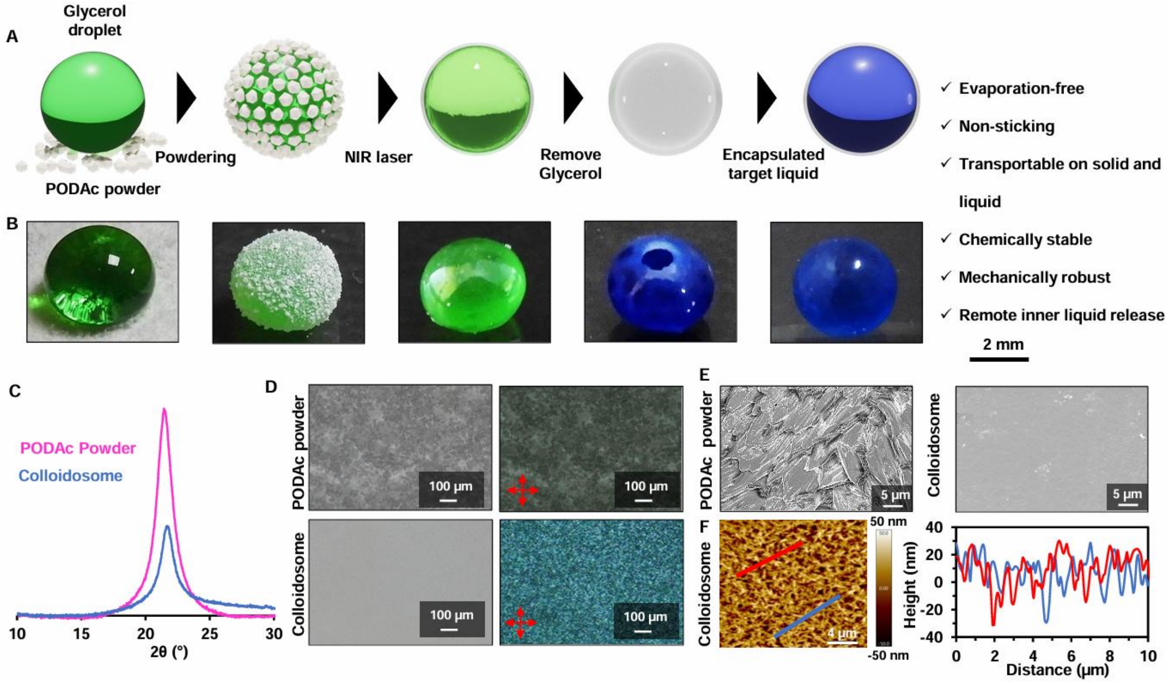

Figure 3.3 A) Schematic representing the steps involved in colloidosome formation. B) Digital images depict the process of preparing a colloidosome (volume = 20 μL). C-E) Powder X-ray diffraction (XRD) spectra (C), bright-field and cross-polarized microscopic images (D), and field emission scanning electron microscope (FESEM; E) image of PODAc powder and colloidosome shell. F) Atomic force microscope (AFM) image and line profiles of colloidosome shell.

This is because only the vinyl group was consumed during the free-radical polymerization of ODAc, while the carbonyl group remained unaffected. After that, the differential scanning calorimetry (DSC) study of PODAc (M_n of 81.7 kDa) revealed the thermoresponsive behavior of the prepared polymer with a phase transition (solid to liquid phase) temperature of 51 °C, as shown in Figure 3.2C. I found the prepared comb-like polymer possessing very low wettability at powder state (contact angle of 151°, Figure 3.2D) to glycerol and remained insoluble in different commonly used organic solvents, having a wide range of surface tensions (72.8-17 mN m^{-1}), as shown in Figure 3.2E. Even the PODAc powder floated on the water pool, whether it was acidic (pH 1), basic (pH 14), or contained dissolved salt, for 1 month, demonstrating its chemical stability (Figure 3.2F). Next, the PODAc capsule was processed based on the "colloidosome" technique, which is depicted in Figure 3.3A, B. First, PODAc is ground to a powder state, possessing very low wettability, adsorbed on the droplet surface, forming a LM instead of being dispersed in the glycerol droplet. Next, the LM was heated locally by using NIR light to melt the PODAc powder around the glycerol droplet to form the PODAc shell. LM, the template for the colloidosome, is typically made of prepared water droplets owing to its high surface tension. However, volatility can decrease the quality of the colloidosome because it includes a thermal process.

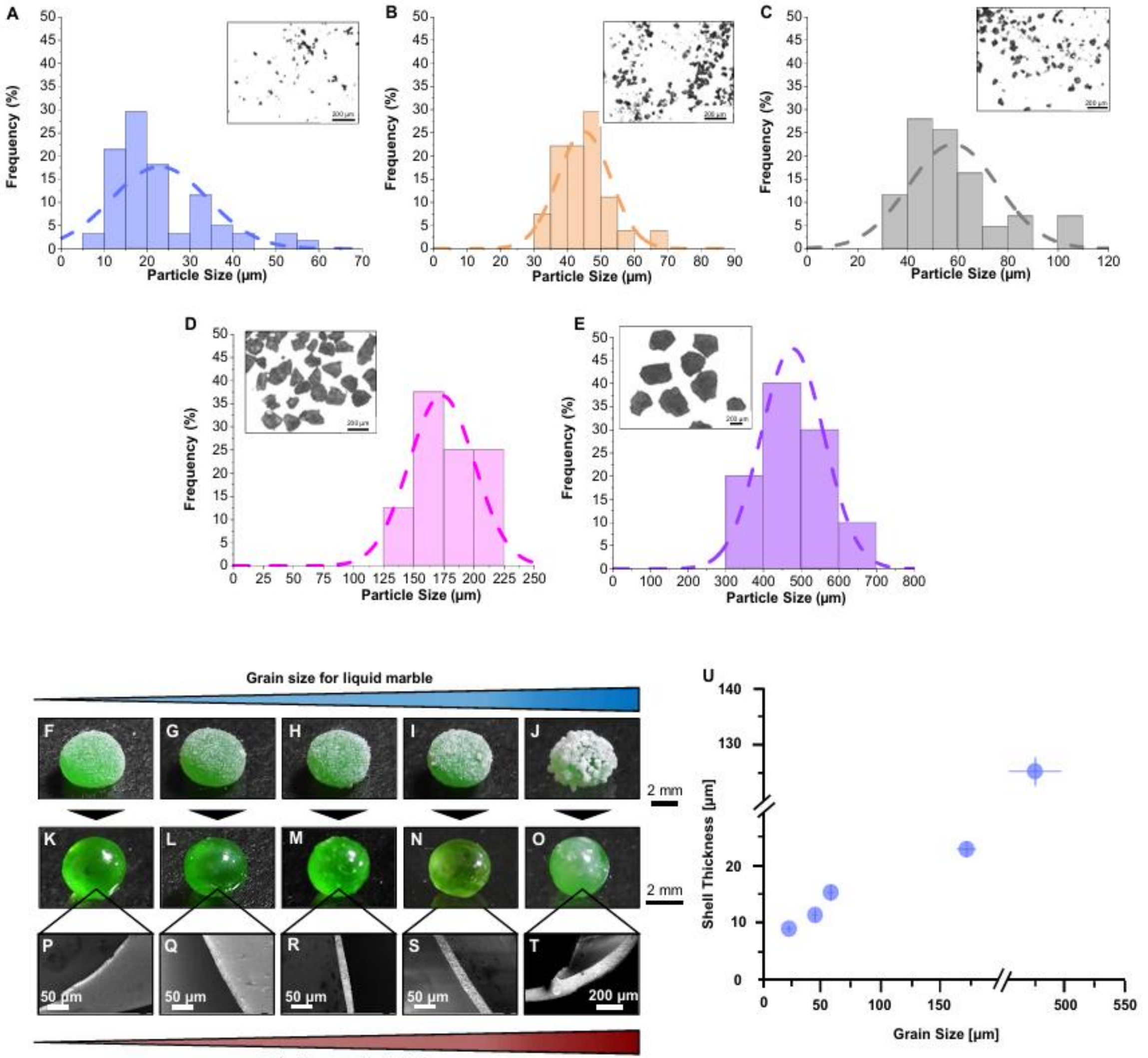

Figure 3.4 A-E) Accounting size distribution of PODAc particles, which was calculated using image analysis of microscopic images (inset). F-J) Digital images of LMs (volume = 20 µL) prepared using PODAc particles of different grain sizes, including 23 ± 1.1 µm (F), 45 ± 1.5 µm (G), 58 ± 2.1 µm (H), 173 ± 7.6 µm (I) and 477 ± 21.8 µm (J). K-O) Digital images of colloidosomes (volume = 20 µL) prepared from the corresponding LMs (F, G, H, I and J). P-T) Field emission scanning electron microscope (FESEM) images showing the different shell thicknesses of 8.7 ± 0.5 µm (P), 11.1 ± 1 µm (Q), 15 ± 1.3 µm (R), 22.5 ± 1.3 µm (S), 125.1 ± 2.4 µm (T) of the prepared colloidosomes. U) Graph accounting for the change in shell thickness of colloidosome based on the grain size of PODAc powder.

Thus, I have selected glycerol to transform the PODAc LM into a colloidosome due to its lower volatility and high surface tension. After that, the thermoresponsive property of the PODAc was strategically utilized to remove encapsulated glycerol from the PODAc shell by thermal poring. The glycerol was completely removed from the capsule due to its liquid-repellent feature. Then, target chemicals or solvents were filled into the empty PODAc capsule, which I term the PODAc colloidosome. It can be utilized successfully as a versatile droplet green chemistry platform, and the proof of concept is shown in the application section.

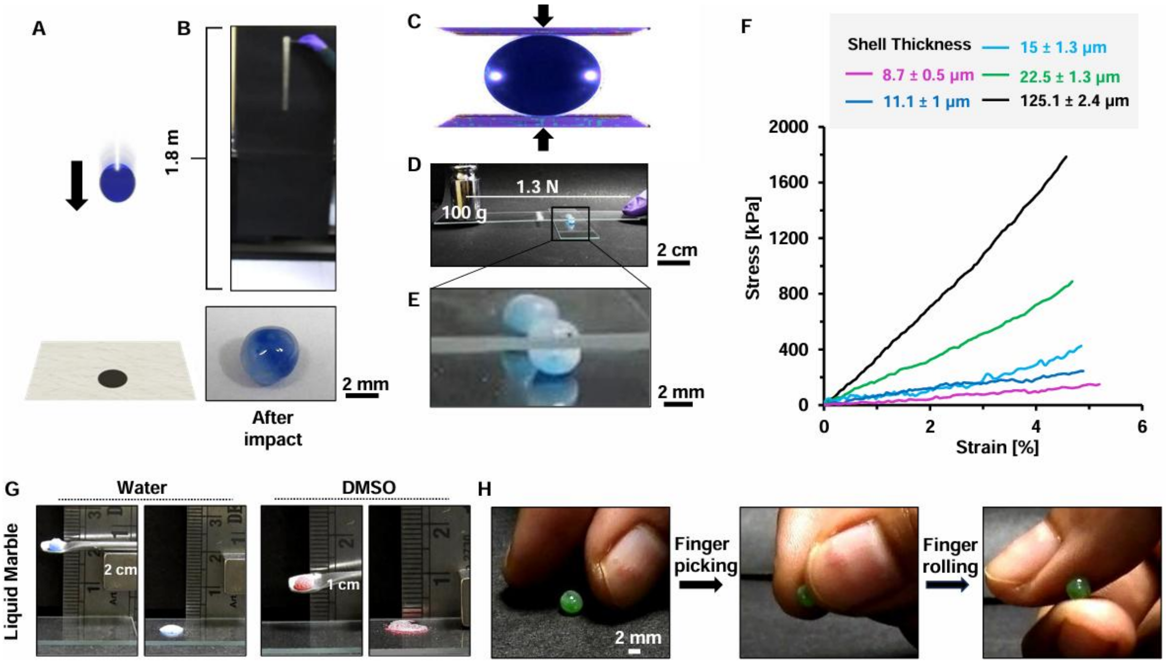

Figure 3.5 (A) Schematic representation of impact test followed to check the mechanical stability of colloidosome. (B) Digital images showing the stability of colloidosome (volume = 20 μL) with a shell thickness of 125.1 ± 2.4 μm when dropped from a height of 180 cm. (C) Schematic illustration of compression test followed to check the mechanical stability of colloidosome. (D, E) Digital images showing the stability of colloidosome (volume = 20 μL) with shell thickness 125.1 ± 2.4 μm after the compression test with 1.3 N load. Zoomed-in digital image showing stable colloidosome after the compression test. (F) Compressive stress-strain plot of colloidosomes (volume = 20 μL) with different shell thicknesses. (G) LMs of water and DMSO derived from PODAc was found to be immediately collapsed on falling from a height of 2 cm and 1 cm, respectively. (H) Digital images exhibiting the picking and rolling of colloidosomes (capacity of 20 μL) with fingers.

The crystalline packing of PODAc is confirmed by X-ray diffraction (XRD) analysis (Figure 3.3C). The XRD peak at 21.6° revealed hexagonal packing of the octadecyl group of PODAc in its powder and colloidosome form. However, in contrast to the PODAc powder, the colloidosome shell comprises a continuous crystalline network. After converting powdered PODAc into the colloidosome shell, a smooth and featureless topography is noted in the optical bright-field microscope image (Figure 3.3D). This smooth polymeric film displayed an intense birefringence of cross-polar light, which was attributed to the existence of the crystalline network of the thermoplastic polymer (Figure 3.3C). The nanometrically smooth surface is required for PODAc to display omniphobicity. The colloidosome's inner shell has nanometric smoothness, as confirmed by the images of the field emission scanning electron microscope (FESEM) and atomic force microscope (AFM) (Figure 3.3E, F). The fibril domains appear due to the crystalline network in the colloidosome shell. While, most of the LMs are fragile and easily break down under mechanical stimuli,[18-30] the mechanical robustness of the prepared colloidosome can be tuned over a wide range from fragile to extremely robust depending on the shell thickness, for that powder size can be tuned with the grinding of the PODAc, and LMs are formed with PODAc powders of different grain sizes from 23 ± 1.1 μm to 477 ± 21.8 μm (Figure 3.4A-E). Further, these different grain size PODAc LMs transform into colloidosomes with different shell thickness, increasing from 8.7 ± 0.5 μm to 125.1 ± 2.4 μm (Figure 3.4F-U). In this work, the shell thickness ranges from 8.7 to 125.1 μm. Landau and Lifshitz's theory can explain increased mechanical durability with thickness. Fragile colloidosomes can be used for the mechanical release of inner liquid, while tough colloidosomes can be used for thermal release. The most robust PODAc colloidosome with a size of ~ 3.2 mm and 125.1 μm shell thickness remains intact even after a fall from a height of 1.8 m under gravity (Figure 3.5A, B). I also confirmed that the colloidosome is not cracked even after compression with a 1.3 N force (Figure 3.5 C-E). Figure 3.5F quantifies the change in stress-strain properties of the prepared colloidosome with different shell thicknesses. However, LM prepared from the highest grain size PODAc powder cannot sustain an impact of falling from a distance of 2 cm, as shown in Figure 3.5G. As a result, the colloidosome with the thick shell can be picked up and rolled with bare fingers, as depicted in Figure 3.5H.

3.3.2. Study of the Droplet Sticking Property

The PODAc shell is chemically stable to any commonly used solvent, which enables the encapsulation of various chemicals for a long time without any spillage (Figure 3.6A). The colloidosome retains its spherical shape even after decanting any target liquids, regardless of their volatility or surface tension (γ_{LV} = 17-72.8 mN m^{-1}). The sphericity of the PODAc is quantified with static contact angle Θ (Figure 3.6B). Owing to the rigid PODAc shell, the colloidosomes exhibited $\Theta > 170^{\circ}$ regardless of liquid surface tension, while conventional liquid-repellent interfaces (superhydrophobic, lubricated slippery, or solid slippery surfaces, and LM) exhibit surface tension dependent Θ evolution (Figure 3.6C). The sphericity (~ contact angle) difference between LM and colloidosome is attributed to the surface tension effect and the continuous crystalline network of the colloidosome. The sphericity depends on the balance of the surface tension over gravity for LM.

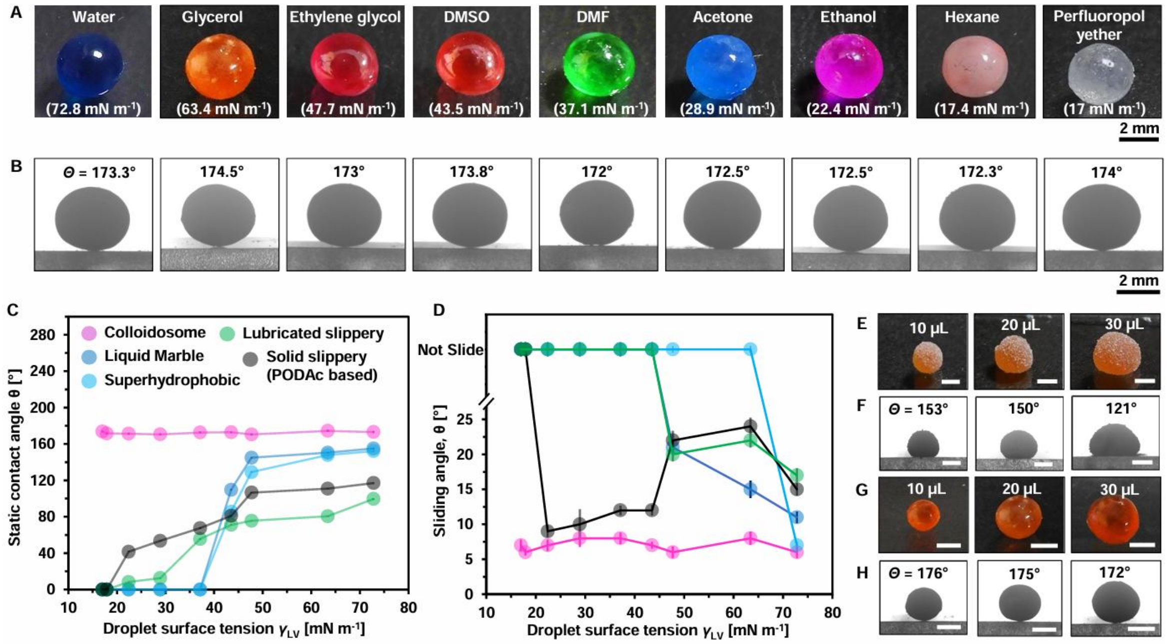

Figure 3.6 A-B) Digital (A) and static contact angle (B) images of colloidosomes (volume = 20 µL) filled with different solvents having a wide range of surface tensions. C) Graph showing the static contact angle values of different solvents used in encapsulating inside colloidosome on different interfaces including PODAc-based slippery coating, lubricated slippery surface, superhydrophobic interface, colloidosome and LM. D) Graph depicting the sliding angles of colloidosome filled with different solvents (volume of 10 µL) and liquid droplets (volume of 10 µL) of the corresponding solvents on a wide variety of selected interfaces. E-H) Digital (E, G) and static contact angle (F, H) images of LMs (E-F) and colloidosome (G-H) of different volumes (10 µL, 20 µL and 30 µL) of glycerol. Results are presented as mean ± SD, where sample size, n = 3.

The PODAc layer is discontinuous and delicate for a LM, and the surface tension varies depending on the inner liquid's properties. Thus, the sphericity decreases with the surface tension for LM, as I confirmed experimentally. For a colloidosome, the melting of PODAc yielded a continuous and rigid shell because of the formation of the crystalline network, which outperformed the surface tension effect observed in LM. Thus, the sphericity is not dependent on the surface tension of the inner liquid for the prepared colloidosome. For instance, a superhydrophobic surface repels high γ_{LV} liquids like water or glycerol with high Θ; however, it fails to repel low γ_{LV} liquids with low Θ. Similarly, the superhydrophobic PODAc powder ($\Theta = 155^{\circ}$ for water) failed to form LMs with low surface-tension liquids (Figure 3.6C). The Θ decreased with the γ_{LV} on perfluoropolyether-lubricated liquid slippery or PODAc-based solid-slippery surfaces (Figure 3.6C). After that, I examined the adhesion force of colloidosomes filled with different liquids (range of surface tension from 72.8 to 17 mN m^{-1}) on a bare glass slide, quantified by the sliding angle α of 10 μL droplets.[48] The colloidosomes exhibit a sliding angle of $\alpha \approx 6\text{-}8^{\circ}$, regardless of the liquid surface tension (Figure 3.6D), while other liquid-repellent surfaces partially failed in liquid repellency. The omniphobicity of the PODAc shell inner wall is critical to repeatedly replacing inner liquids from the PODAc colloidosome without fouling. The shell omniphobicity is estimated from the sliding angle on the PODAc solid-slippery surface in Figure 3.6D, which shows that all the probe liquids having $\gamma_{LV} > 20$ mN m^{-1} can be easily removed. In this context, superhydrophobic and liquid-infused slippery interfaces repel only a few probe liquids with $\gamma_{LV} > 50$ mN m^{-1}, as illustrated in Figure 3.6D. Moreover, the surface tension of encapsulated liquid in LM derived from superhydrophobic PODAc powder displayed a change in the sliding angle because of the alteration in the contact angle of LMs on the solid surface. Despite the existing limitation of other bioinspired interfaces, the currently developed colloidosome enables the no-loss transfer of a broader range of liquids compared to other liquid-repellent materials. It was noticed that the shape and contact angle of the colloidosomes merely altered on changing the volume of the inner liquid; however, powder displayed a deformed shape and depleted contact angle on increasing the volume of the encapsulated liquid, as shown in Figure 3.6E-H. It is important to note that the thermal melting of deposited superhydrophobic PODAc powder on the encapsulated liquid has not only provided a crystalline network but also elevated the contact angle significantly at different volumes of encapsulated liquid. When the inner liquid volume is 30 μL, LM is deformed by gravity, while colloidosomes have high sphericity (Figure 3.6G, H). It means that the thermal melting of the PODAc significantly elevated the contact angle. This encapsulation of different

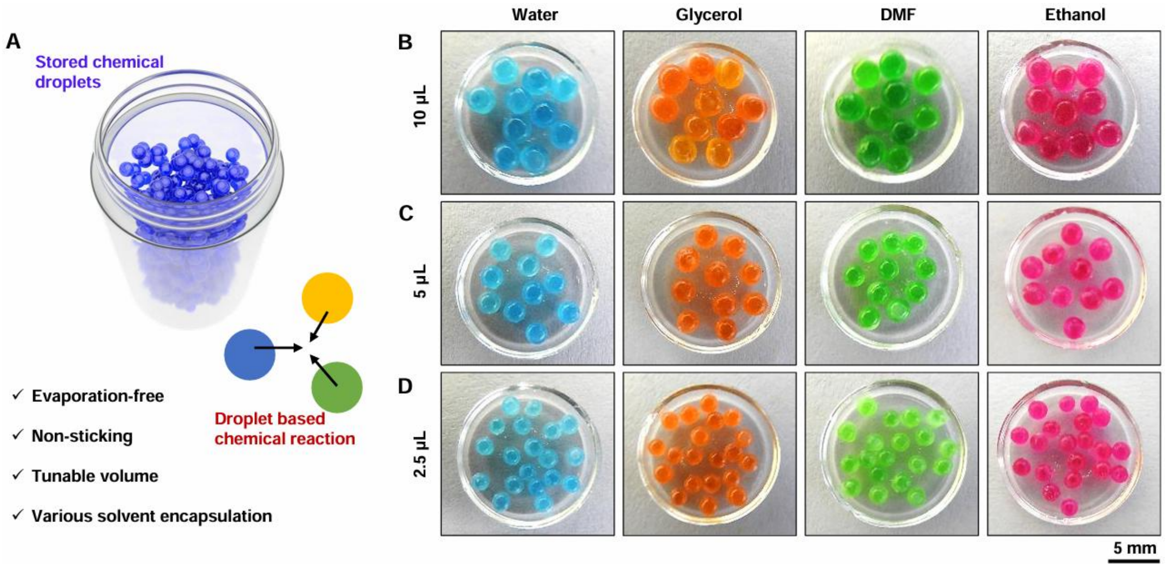

Figure 3.7 A) Schematic representation of colloidosomes storage. B-D) Storing of colloidosomes of different volumes (10 μL, 5 μL and 2.5 μL) packed with different solvents.

liquid types and volumes enabled a simple basis to encapsulate and store volatile/nonvolatile chemicals in predefined volumes-without having any mass loss (Figure 3.7A). In this context, I can handle microliter liquids such as solid beads in containers without sticking or evaporation (discussed later), which would change the protocols of chemical synthesis.

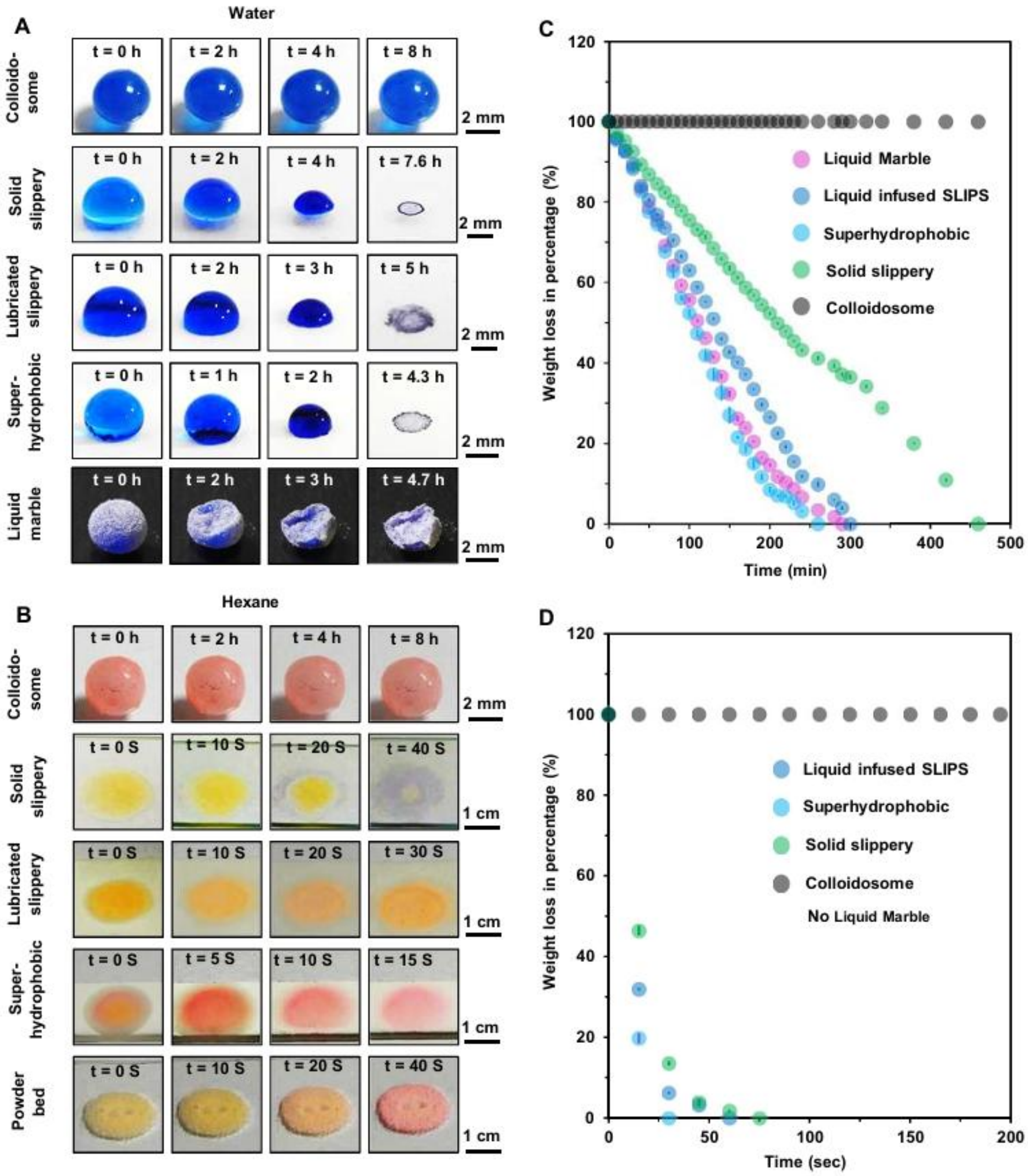

Figure 3.8 A, B) Digital images comparing the evaporation of water (A) and hexane (B) droplets (volume = 20 µL) from different surfaces (solid slippery, liquid-infused SLIPS and superhydrophobic surfaces), LM and colloidosome. C, D) Graphical representation depicting the change in weight percentage of water (C) and hexane (D) droplets with time for different surfaces (solid slippery, liquid-infused SLIPS and superhydrophobic surfaces), LM and colloidosome. Results are presented as mean ± SD, with a sample size of n = 3.

As a prototype demonstration, colloidosomes with different loading capabilities (2.5 to 10 μL) were successfully prepared by encapsulating various volatile and nonvolatile liquids-including water, glycerol, DMF, and ethanol (Figure 3.7B-D). Such a non-sticking platform can handle tiny, volatile and non-volatile liquids and promote highly efficient droplet-based chemical reactions.

3.3.3. Study of the Droplet Evaporation

The PODAc colloidosomes can prevent inner volatile solvents from evaporation (Figure 3.8A, B). I selected water and hexane as probe volatile, polar and nonpolar liquids. The test liquid volumes are 20 μL, and the water and hexane are dyed with methylene blue and Nile red, respectively. Time-lapse images of these liquid droplets in colloidosome compared with other liquid-repellent interfaces, including superhydrophobic, liquid-infused slippery, solid-slippery surfaces, and LMs, are presented in Figure 3.8A, B.

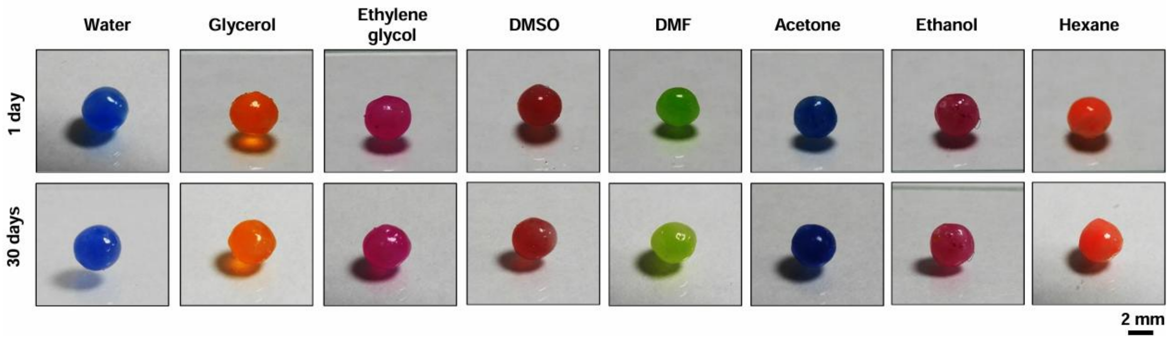

Figure 3.9 Digital images depicting the stability of colloidosome (capacity of 20 μL) on a solid surface with different solvents after 30 days.

No changes in the PODAc colloidosome loaded with water and hexane are observed even after 8 h. In contrast, other liquid–repellent interfaces show droplet evaporation after a shorter duration. Even the shape and weight of water marble derived from powdered PODAc were observed to alter with time. To quantify the evaporation speed, I measured the weight change of the water and hexane droplets, depicted in Figure 3.8C, D. There is no significant weight change with time for the colloidosomes loaded with water or hexane droplets.

Moreover, the water and hexane-encapsulated colloidosomes of crystalline shell displayed no change in shape and weight over 8 h, unambiguously suggesting no mass loss of volatile solvent from the prepared colloidosome. This perfect blocking property of inner liquid evaporation is due to the highly packed crystalline shell of the colloidosome. Irrespective of the nature of the encapsulated liquids, no noticeable change in shape and mass was observed for colloidosomes even after storing the colloidosomes for a month, as shown in Figure 3.9. The encapsulation of the droplet within the PODAc shell lost the liquid diffusion property with respect to the contacted media. However, taking advantage of the thermoresponsive behavior of PODAc, I successfully demonstrated the on-demand extraction of the inner liquid and the addition of external liquids into the prepared colloidosome. The localized temperature-assisted formation of holes in the prepared colloidosome allowed the extraction of an inner liquid and the addition of an external liquid, respectively.

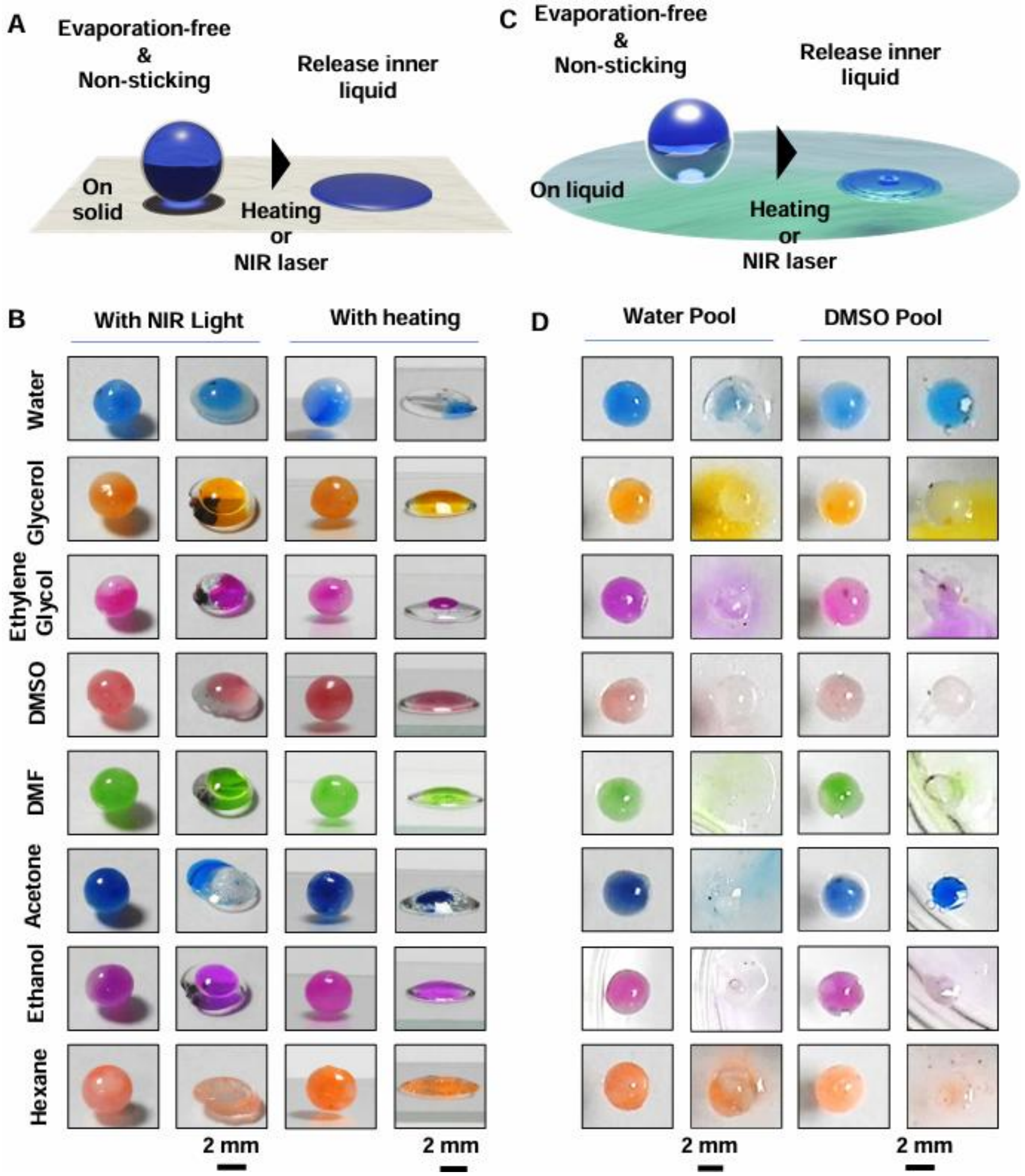

Figure 3.10 A) Scheme depicting the release of inner liquid from colloidosome on a solid surface upon heating. B) Digital images showing the release of different solvents from colloidosome (volume = 20 μL) induced by heating with near-infrared (NIR) light and hot plate. C) Schematic showing the release of inner liquid on a liquid pool upon heating. D) Digital images representing the release of different solvents from colloidosome (volume = 20 μL) on water and DMSO pool induced by heating.

Thus, while the closeness of the capsule prevents adhesion and evaporation, the reconfigurability of the same capsule shell allows on-demand addition and extraction of liquids. Moreover, the release of encapsulated liquids from the colloidosome is successfully depicted in Figures 3.10. In Figure 3.10A, the colloidosome was heated on a hot plate above 51 °C or irradiated with NIR light. I confirmed the release of water, glycerol, ethylene glycol, DMSO, DMF, acetone, ethanol, and hexane liquids, as shown in Figure 3.10A, B. A similar outcome was observed in water or DMSO pools, as shown in Figure 3.10C, D.

When the PODAc shell is heated above 51 °C, the crystalline packing of PODAc is compromised. The PODAc shell rapidly melted, releasing the encapsulated inner liquid into liquid pools. The release of the inner liquid to the solid surface is driven by capillary force, while diffusion guides the release of the inner liquid to the liquid pools. As a consequence, the released liquid accumulated on top of the solid surface, and rapid mixing of the encapsulated liquid was noticed in the liquid pool. Such on-demand, heat-triggered release of the inner liquid from the colloidosome would help to depict various on-demand chemical reactions. Further, the thermoresponsive character of the PODAc allowed the recycling of the PODAc shell to another fresh colloidosome. After melting and releasing the inner liquid, I obtained the solid blocks of the PODAc. The block was processed into superhydrophobic powder by grinding, which enables the formation of the fresh colloidosome by repeating the same formation process. Thus, the current approach of preparing colloidosomes is also recyclable, as shown in Figure 3.11.

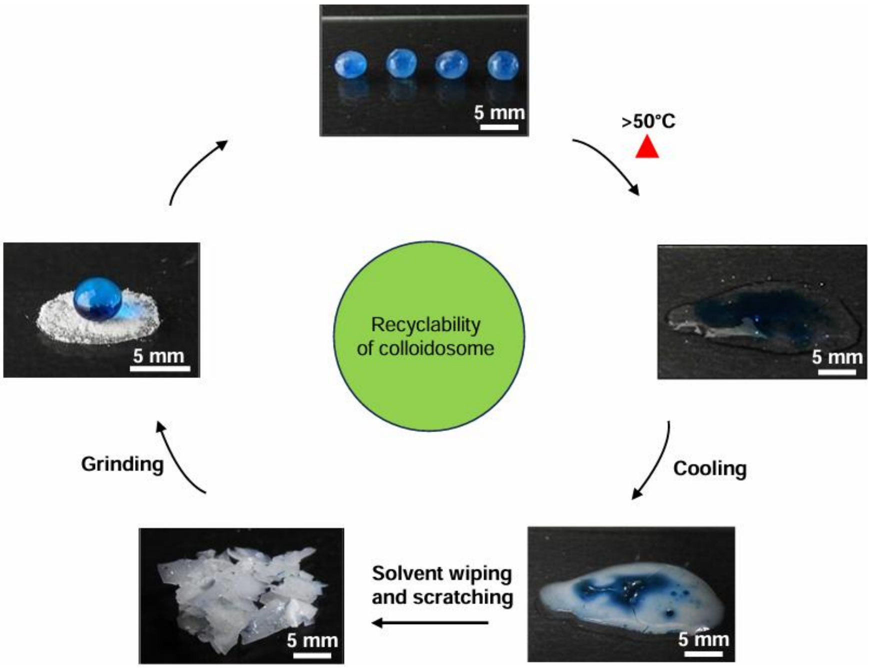

Figure 3.11 Digital images illustrating the recyclability of colloidosomes.

3.3.4. Zero-Loss Microreactor

In the history of droplet chemistry, LMs were promising as a non-sticking platform for miniaturizing chemical reactions in microliter volume, where mostly nonvolatile solvents (e.g., DMSO, DMF) are used as reaction medium.[19,49] However, the use of volatile organic solvents is rarely observed as the rapid loss of volatile solvents through unavoidable evaporation becomes exceedingly challenging. In this context, the prepared colloidosome that allowed evaporation-free, non-sticking encapsulation of various liquids with tunable volume has been successfully applied as a zero-loss microreactor to perform Schiff base reaction with a standard volatile organic solvent, i.e., ethanol in microliter volume over a relatively longer duration (Figure 3.12A, B).

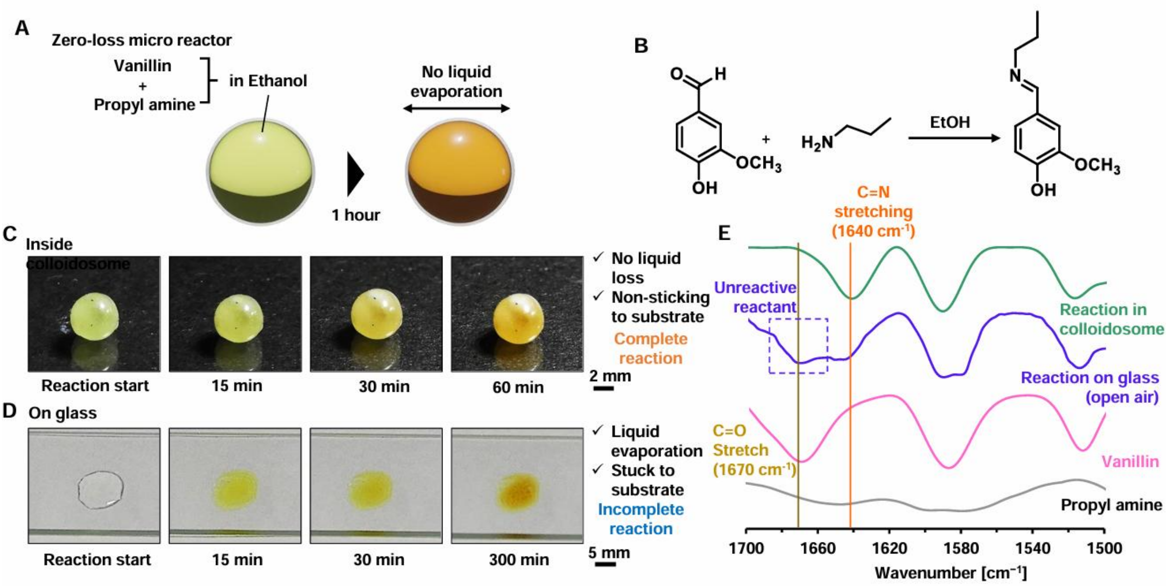

Figure 3.12 A-B) Schematic illustration of miniature Schiff-base reaction between vanillin and propyl amine in a volatile organic solvent (ethanol). C) Digital images showing the complete reaction of vanillin and propyl amine inside a packed colloidosome (volume = 20 µL). D) Digital images showing the incomplete reaction between vanillin and propyl amine performed on an open glass substrate (volume = 20 µL). E) Attenuated total reflection-Fourier transform infrared (ATR-FTIR) spectra of vanillin (pink), propyl amine (grey), reaction mixture inside colloidosome (green) and on a glass substrate in open air (purple).

As a proof-of-concept demonstration, the prepared colloidosome was filled with an equimolar (0.1 M) amount of propylamine and vanillin in 20 µL of ethanol, as demonstrated in Figure 3.12C. As the reaction proceeded, the reactants mutually reacted to form a Schiff base. Eventually, an intense yellow color was observed after a period of 1 h. The ATR-FTIR study of the reaction mixture encapsulated in colloidosome confirmed a complete con version of reactants into the desired product, where the characteristic absorption peak of carbonyl (corresponding to aldehyde moiety of vanillin) at 1670 cm^{-1} was completely depleted, instead, a new absorption peak has appeared for imine stretching at 1640 cm^{-1} as shown in Figure 3.12E. Whereas in a controlled study, when the same reaction mixture was placed on a clean glass surface, a gradual loss of solvent was noted with time. Eventually, a dry and yellow residue was found to be stuck on the glass slide, as shown in Figure 3.12D. Further, the ATR-FTIR analysis of the solid residue on a glass substrate supports the incomplete reaction of the same reaction mixture. The characteristic absorption peaks for carbonyl and imine stretching were noticed at 1670 and 1640 cm^{-1}, respectively (Figure 3.12E), suggesting partial conversion of the used reactants. The rapid evaporation of reaction media prior to the completion of the reaction is responsible for such incomplete chemical reactions. Thus, the prepared colloidosome can be successfully applied as a zero-loss microreactor, where the loss of solvent due to evaporation and the loss of product due to sticking on the solid surface can be avoided.

3.3.5. On-Demand Chemical Reaction

The on-demand chemical reaction is fascinating, as the chemical reaction can be programmed as needed. However, the encapsulation and subsequent storage of volatile reactants for a prolonged duration before their on-demand release to perform desired chemical reactions is challenging. In this context, bromine liquid, known to be a toxic chemical, was encapsulated in a prepared colloidosome and stored for 30 days, as shown in Figure 3.13A. No mass loss was noticed as the continuous crystalline network of the prepared colloidosome is inherently capable of preventing the evaporation of the volatile solvent and reactant. The thermoresponsive behavior of the prepared colloidosome that allowed the release of inner liquid at elevated temperatures (>51 °C) was utilized to depict the on-demand interfacial reaction between phenol and bromine to form tribromophenol, as shown in Figure 3.13B, C. The encapsulated colloidosome was placed in an aqueous pool of phenol. Once the temperature of the aqueous pool was elevated above 51 °C, the shell of the colloidosome melted, and the brown bromine solution was released into the aqueous solution of phenol to rapidly form a white precipitate of tribromophenol, as shown in Figure 3.13D. ^{1}H NMR peak for ortho and para hydrogen at 6.8 and 7.2 ppm of phenol diminished completely after the reaction. Additionally, the peak appearance and position for nonreactive meta-hydrogen changes from a triplet (6.9 ppm) to a singlet (7.5 ppm), confirming the successful bromination at the ortho and para positions of phenol, as shown in Figure 3.13E. However, such an appearance of white precipitate was not observed on the release of the same bromine solution on a phenol-free water pool (Figure 3.13F). Hence, the current approach is capable of storing volatile reactants for a prolonged duration and the thermoresponsive nature of the prepared colloidosome enables the on-demand release of encapsulated volatile reagents to execute chemical reactions. Thus, the prepared colloidosome provided a much safer and greener platform for chemical reactions, even with toxic and volatile reagents.

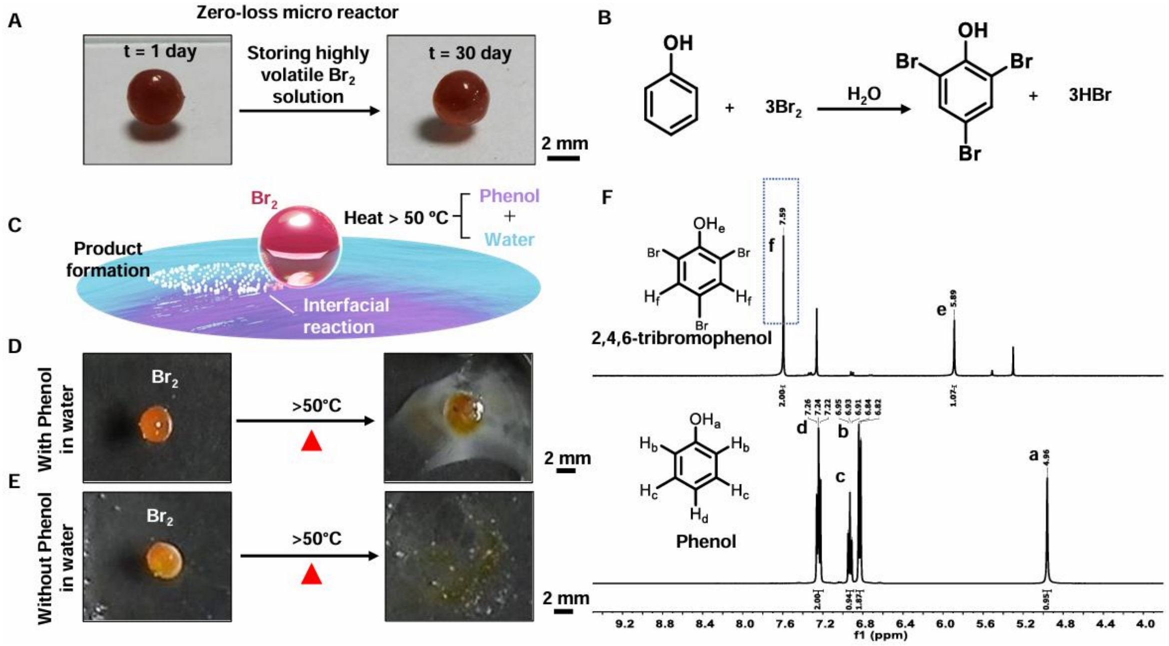

Figure 3.13 A) Digital images depicting the storage of highly volatile bromine–water solution in colloidosome over 30 days. B) Depicting the Bromination of phenol to form 2,4,6-tribromophenol. C) Scheme representing the heat-induced release of bromine from colloidosome into aqueous solution of phenol resulting in the formation of 2,4,6-tribromophenol. D) Digital images showing the release of bromine from colloidosome upon heating (volume = 20 μL) into an aqueous solution of phenol resulting in the formation of white-colored sediment. E) H^1 NMR spectra of while sediment and phenol. F) In the absence of phenol, no such changes were noticed even after the release of bromine from colloidosome (volume = 20 μL) upon heating into the water pool.

Thereafter, an on-demand photopolymerization is demonstrated without releasing the inner reagents; instead, all the essential reactants were placed inside the colloidosome, and under external stimuli, e.g., the chemical reaction is triggered by UV light. In this context, the UV light transmittance (at a wavelength of 365 nm) of the PODAc shell was noticed to be increased by reducing its thickness, as shown in Figure 3.14A. The colloidosome with a shell thickness of 8.7 μm exhibited high UV transmittance (66%) and was used to encapsulate the monomer and initiator together to demonstrate on-demand photopolymerization through the UV irradiation process, as shown in Figure 3.14B, C. The photoreactive initiator (2-hydroxy-2-methylpropiophenone) provided reactive species to initiate the polymerization of glycidyl methacrylate (GMA) and an epoxy group-containing chemically reactive poly glycidyl methacrylate PGMA. Reaction mixtures of monomer with different concentrations were loaded inside the colloidosome and exposed to UV light for 2 h to allow the polymerization reaction. In the end, the colloidosome was mechanically ruptured to get the resultant polymer, as shown in Figure 3.14E-G. Depending on the concentration of (0.75, 1.1, and 1.5 M) monomer, the molecular weight and the appearance of the resultant polymer in terms of its opacity and softness were altered.

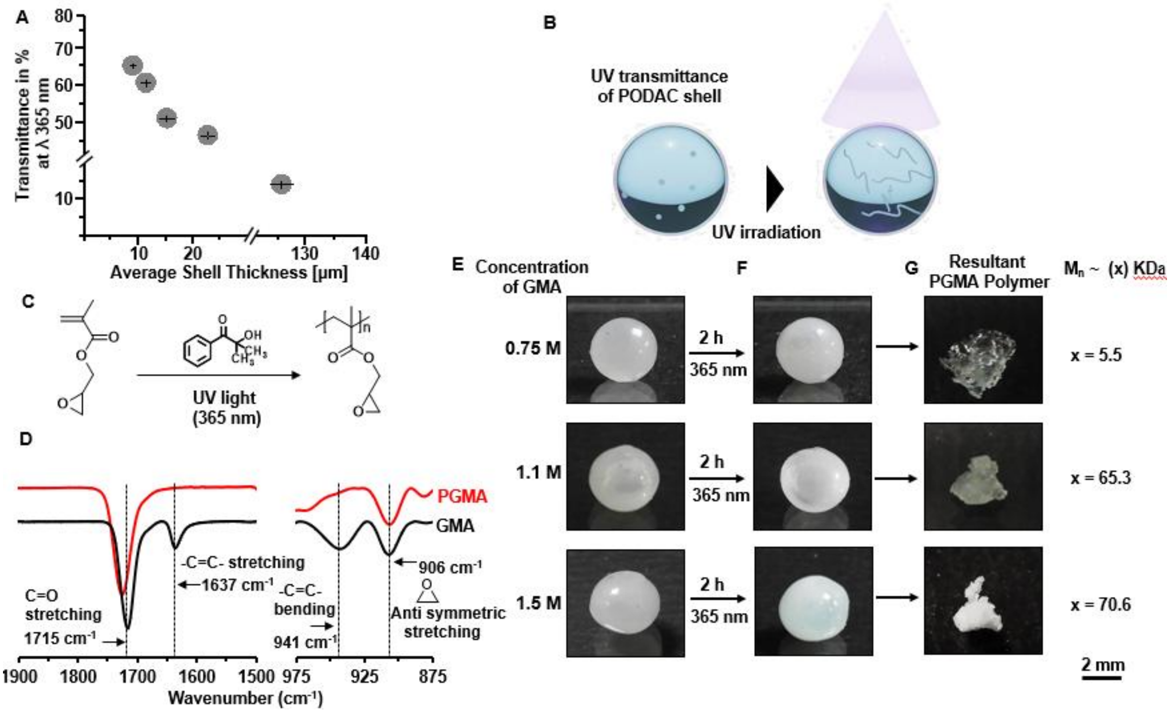

Figure 3.14 A) Graph representing the change in transmittance of colloidosome shell at 365 nm wavelength with increasing shell thickness. B) Schematic illustration of UV light-induced on-demand photopolymerization inside colloidosome. C) Reaction scheme depicting the synthesis of poly glycidyl methacrylate (PGMA) through photopolymerization of glycidyl methacrylate (GMA) in the presence of a radical initiator. D) Attenuated total reflection-Fourier transform infrared (ATR-FTIR) spectra of PGMA and GMA. E, F) Digital images showing the formation of PGMA inside colloidosome (F) packed with different concentrations of GMA in ethanol (E). G) Digital images of resultant PGMA polymers formed inside colloidosomes.

A brittle and solid polymer with an M_n value of 37.9 kDa was obtained at 1.5 M monomer concentration. In contrast, a semisolid transparent (M_n 27.7 kDa) and opaque (M_n 16.5 kDa) polymer was obtained at 1.1 M and 0.75 M, respectively. The complete polymerization of the monomer inside the prepared colloidosome was characterized by ATR-FTIR analysis, where the absorption peak for stretching of a vinyl moiety at 1637 cm^{-1} was diminished after polymerization, as shown in Figure 3.14D. As expected, the IR signatures of the epoxy group were noticed at 907 cm^{-1}. Thus, the current approach allowed the on-demand synthesis of the chemically reactive polymer in an isolated and confined environment.

3.3.6. Chemical Reaction Using Multifused PODAc Colloidosome

The spot melting of the PODAc shell enabled the interconnection of multiple colloidosomes, which made the chemical reaction more systematic. In this section, I have demonstrated the utilization of an interconnected network of colloidosomes for mixing solvents and chemicals.

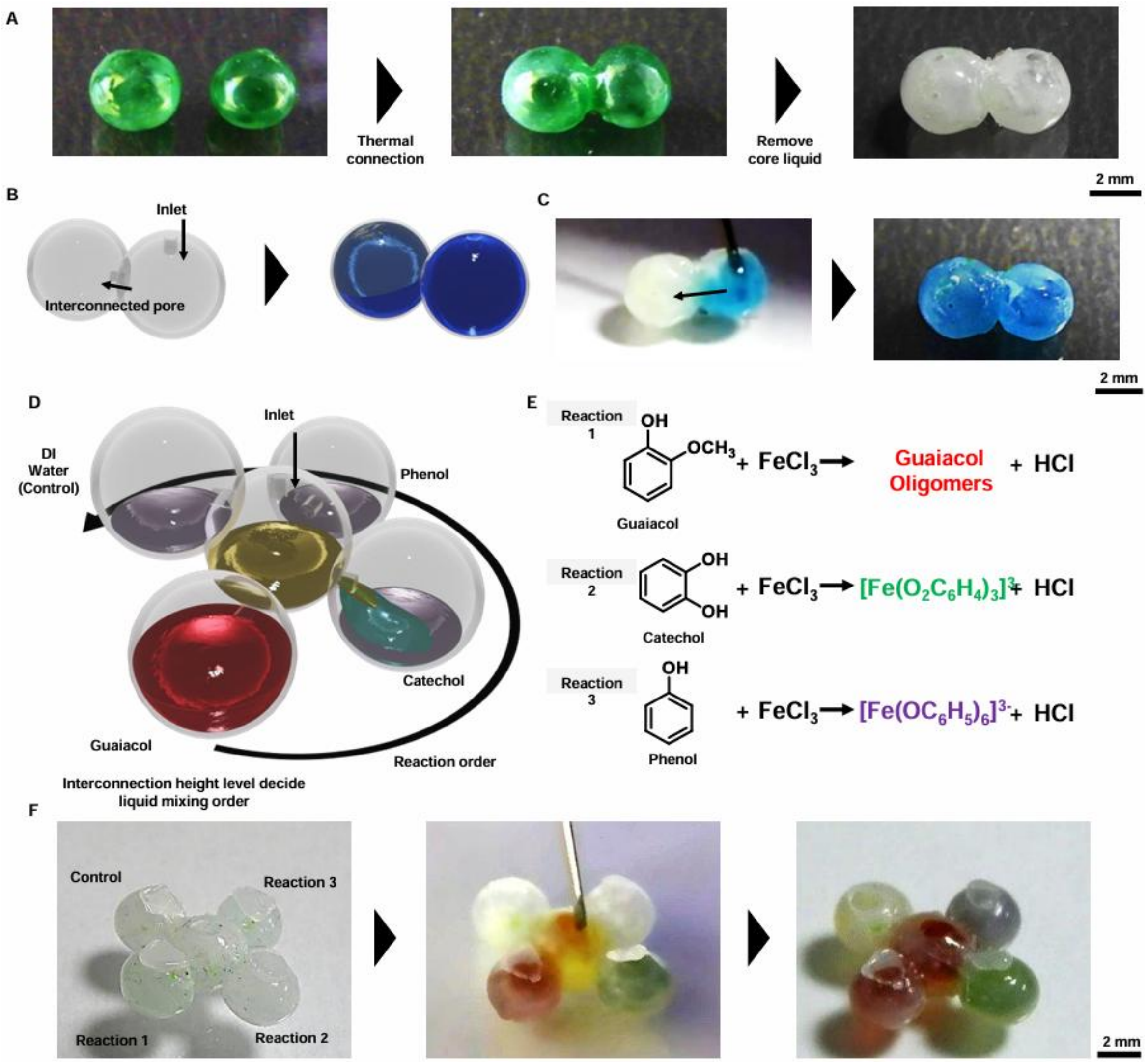

Figure 3.15 A) Digital images depicting the steps involved in preparing a thermally fused empty colloidosome connected through a channel by joining two distinct colloidosomes filled with glycerol (volume = 20 µl), followed by decanting the glycerol from the fused state. B-C) Schematic and digital images illustrating liquid (water dyed with methylene blue) flow from one colloidosome to another connected through a channel. D) Schematic depicting the flow of ferric chloride solution from one colloidosome to four others connected colloidosomes containing hydroquinone, catechol, phenol, and distilled water. E) Reactions of ferric chloride with different aromatic alcohols, including hydroquinone, catechol, and phenol, resulted in the formation of different complexes. F) Digital images showing the flow of ferric chloride solution from one colloidosome to four others connected colloidosomes containing hydroquinone, catechol, phenol, distilled water, and the color change observed due to the formation of different complexes and oligomer.

This is useful in depicting a programmed reaction where multiple colloidosomes were connected through an inner hole to pass liquids. In the simplest model, two colloidosomes were fused thermally to achieve an interconnected passage for demonstrating liquid flow across colloidosomes, as shown in Figure 3.15A, B. Initially, the methylene blue-dyed liquid was introduced through the surface hole of one colloidosome, and this liquid flowed into the other connected colloidosome when the liquid level rose above the interconnected passage (Figure 3.15C). I utilized this principle for the programmed reaction as schematically represented in Figure 3.15D, where four colloidosomes were interconnected with a central colloidosome. After that, these four colloidosomes were prefilled with different aromatic alcohols, including guaiacol, catechol, phenol, and waters, so their level remains below the interconnection pore to avoid backflow to the central colloidosome. Once the ferric chloride solution was passed through the inlet hole of the central colloidosome, it sequentially flowed to each of the connected colloidosomes via the interconnected pore, resulting in a change in the color of respective alcohols because of the formation of respective ferric complexes with aromatic alcohols or oligomers (Figure 3.15E, F). This concept opened the possibility of systematic miniature chemical reactions. Recently, a complex fluidic device has been proposed based on complex geometric regulation of the liquid flow.[50,51] Recently, a high-resolution thermal patterning technique has also been reported.[52] Since the PODAc geometry is controllable with local heating, high-resolution thermal management may help to make the processing of PODAc colloidosomes more and more flexible. In the recent past, different and unique strategies, including spontaneous liquid flow reactors and cellular fluidics, were introduced to achieve rapid and controlled transport of liquids; however, these approaches have limited ability to prevent evaporation of volatile liquids.[53-55] In comparison, the current approach provided a facile basis for guided transport of a wide range of liquids without adhesion- or evaporation-based mass loss. Owing to its facile processability and chemical stability, the PODAc colloidosome would be a powerful tool to customize droplet chemistry more efficiently and systematically.

3.4. Conclusion

In addition to the sticky feature of liquids (for example, sticking to a container), the high volatility of useful primary organic solvents restricts “droplet chemistry” from reaching its promising practical utilities. The dilemma is that the with lower volume of reaction mixture, the vaporization effect of the liquid would be none. Here, I designed a thermally shape-reconfigurable omniphobic colloidosome that prevents both adhesion and evaporation losses of liquids, thus acting as a powerful tool for droplet green chemistry. The novel feature of our approach is the molecular feature of PODAc's comb polymer structure: PODAc assembles to form a hexagonally packed hydrocarbon chain surface exhibiting omniphobicity, providing a phase transition at a moderate temperature for shape reconfigurability. These features also help the easy and recyclable capsule shaping of PODAc by adopting the colloidosome process. Our strategy is advantageous to classical omniphobic surfaces because of the broader range of surface tension of the repelling liquid, the minimization of the liquid evaporation loss, and the controlled release of the inner liquid. As a proof of concept, I show three types of chemical reactions in colloidosomes with a volume of 20 μL solution of reactants: (i) long-time chemical reaction using volatile microliter solvent, (ii) on-demand release of volatile reactants to initiate a chemical reaction, and (iii) on-demand photo polymerization in a confined space. The demonstration covers the typical prototype chemistry of molecular, polymer and particle in a droplet scale, which will be developed for more complex reactions using two or more PODAc colloidosomes using complex liquids. These applications prove that the PODAc colloidosome is inherently efficient for high-yield chemical reactions with valuable reagents and minimized waste. Higher-level processing, such as interconnected fused colloidosome capsules, would make chemical reactions more complex. As a laboratory glass instrument used for complex chemical reactions, the PODAc "vessel" processing would not be limited to the capsule shape for high-level green chemistry. However, the temperature-assisted chemical reaction inside the colloidosome is challenging to achieve because of its melting at high temperatures. However, the melting temperature of the colloidosome can be tailored based on the selection of appropriate polymers.

3.5. References

46 T. Young, *Phil. Trans. R. Soc.*, 1805, **95**, 65-87.

47 T. Onda, S. Shibuichi, N. Satoh and K. Tsujii, Langmuir, 1996, **12**, 2125–2127.

48 A. Tuteja, W. Choi, J. M. Mabry, G. H. Mckinley and R. E. Cohen, *Proc. Natl. Acad. Sci. U.S.A,* 2008, **105**, 18200-18205

49 T.-S. Wong, S. H. Kang, S. K. Y. Tang, E. J. Smythe, B. D. Hatton, A. Grinthal and J. Aizenberg, *Nature*, 2011, **477**, 443-447.

50 A. Lafuma and D. Quéré, *EPL*, 2011, **96**, 56001.

51 P. Aussillous and D. Quéré, *Nature*, 2001, **411**, 924-927.

52 V. S. Ajaev and O. A. Kabov, *Annu. Rev. Fluid Mech.*, 2021, **53**, 203-225.

53 A. Dhyani, J. Wang, A. K. Halvey, B. Macdonald, G. Mehta and A. Tuteja, *Science*, 2021, **373**, eaba5010.

54 M. Liu, S. Wang and L. Jiang, *Nat. Rev. Mater.*, 2017, **2**, 17036.

55 R. E. Johnson and R. H. Dettre, *J. Phys. Chem.*, 1964, **68**, 1744-1750.

56 D. Daniel, J. V. I. Timonen, R. Li, S. J. Velling and J. Aizenberg, *Nat. Phys.*, 2017, **13**, 1020-1025.

57 L. Chen, S. Huang, R. H. A. Ras and X. Tian, *Nat. Rev. Chem.* 2023, **7**, 123–137.

58 R. Seemann, M. Brinkmann, T. Pfohl and S. Herminghaus, *Rep. Prog. Phys.*, 2011, **75**, 016601.

59 J. Li, X. Han, W. Li, L. Yang, X. Li and L. Wang, *Prog. Mater. Sci.*, 2022, **133**, 101064.

60 T. L. Liu, C.-J. CJ Kim, *Science*, 2014, **346**, 1096-1100.

61 P. Aussillous and D. Quéré, *Proc. R. Soc. A: Math. Phys. Eng. Sci.*, 2006, **462**, 973–999.

62 A. Gallo, F. Tavares, R. Das and H. Mishra, *Soft Mater.*, 2021, **17**, 7628-7644.

63 P. S. Bhosale, M. V. Panchagnula and H. A. Stretz, *Appl. Phys. Lett.*, 2008, **93**, 034109.

64 B. Y. Xue, H. Wang, Y. Zhao, L. Dai, L. Feng, X. Wang and T. Lin, *Adv. Mater*., 2010, **22**, 4814-4818.

65 D. Zang, K. Lin, W. Wang, Y. Gu, Y. Zhang, X. Geng and B. P. Binks, *Soft Matter*, 2014, **10**, 1309.

66 E. Bormashenko, R. Balter, H. Aharoni and D. Aurbach, *J. Colloid Interface Sci.*, 2014, **417**, 206-209.

67 S. Yusa, M Morihara, K. Nakai, S. Fujii, Y Nakamura and A. Maruyama, *Polym. J.*, 2014, **46**, 145–14.

68 E. Bormashenko, Y. Bormashenko, R. Grynyov, H. Aharoni, G. Whyman and B. P. Binks, *J. Phys. Chem. C*, 2015, **119**, 9910−9915.

69 Z. Liu, X Fu, B.P. Binks and H.C. Shum, *Langmuir*, 2015, **31**, 11236−11242.

70 F. Geyer, Y. Asaumi, D. Vollmer and H.-J. Butt, Y. Nakamura and S. Fujii, *Adv. Funct. Mater.*, 2019, **29**, 1808826.

71 X. Rong, R. Ettelaie, S.V. Lishchuk, H. Cheng, N. Zhao, F. Xiao and F. Cheng, H. Yang, *Nat. Commun.*, 2019, **10**, 1854.

72 Z. Xin and T. Skrydstrup, *Angew. Chem. Int. Ed.*, 2019, **58**, 11952–11954.

73 H. Shi and X. Li, *Adv. Mater. Interfaces*, 2020, **7**, 2001081.

74 N. Barman, A. Shome, S. Kumar, P. Mondal, K. Jain, M. Tenjimbayashi and U. Manna, *Adv. Funct. Mater.*, 2023, **33**, 2214840.

75 J. C. Gomez, S. Vishnosky, S. T. Kim, S. A. Dinca, E. B. Finkelstein and R. C. Steinhard, *Adv. Funct. Mater.*, 2023, **33**, 2214893.

76 H. Wu, X. Du, X. Meng, D. Qiu and Y. Qiao, *Nat. Commun.*, 2021, **12**, 6113.

77 J. Jiang, A. T. Poortinga, Y. Liao, T. Kamperman, C. H. Venner and C. W. Visser, *Adv. Mater.*, 2023, **35**, 2208894.

78 S. E. Reinhold, K.-G. H. Desai, L. Zhang, K. F. Olsen and S. P. Schwendeman*, Angew. Chem. Int.* Ed., 2012, **51**, 10800.

79 Y. Yang, H. Liu, M. Han, B. Sun and J. Li, *Angew. Chem. Int. Ed.*, 2016, **55**, 13470.

80 L. Zhang, L. H. Cai, P. S. Lienemann, T. Rossow, I. Polenz, Q. V. Martin, M. Ehrbar, H. Na, D. J. Monney and D. A. Weitz, *Angew. Chem. Int. Ed.*, 2016, **55**, 13538.

81 B. C. Zarket and S. R. Raghavan, *Nat. Commun.*, 2017, **8**, 193.

82 X. Guo, K. S. Gonzale and D. M. Lynn, *Chem. Mater.*, 2019, **31**, 7443.

83 R. Lathia, S. Nagpal, C. D. Modak, S. Mishra, D. Sharma, B. S. Reddy, P. N. R. Bhat, P. Sen, *Nat. Commun.*, 2023, **14**, 6445.

84 J. P. Goertz, S. R. Raghavan, K. C. DeMella, B. R. Thompson and I. M. White, *Mater. Horiz.*, 2019, **6**, 1238.

85 A. C. Sather, H. G. Lee, R. Colombe, A. Zhang and S. L. Buchwald, *Nature*, 2015, **524**, 208.

86 S. A. Ryu, Y.-H. Hwang, H. Oh, K. Jeon, J. H. Lee, J. Yoon, J. B. Lee and H. Lee, *ACS Appl. Mater. Interfaces*, 2021, **13**, 36380.

87 L. Wang and T. J. Mccarthy, *Angew. Chem. Int. Ed.*, 2016, **55**, 244-248.

88 J. Liu, Y. Sun, X. Zhou, X. Li, M. Kappl, W. Steffen and H.-J. But *Adv. Mater.*, 2021, **33**, 2100237.

89 V. Singh, X. Men and M.K. Tiwari, *Nano Lett.*, 2021, **21**, 3480–3486.

90 M. Dhar, A. Das, D. Parbat and U Manna, *Angew. Chem. Int. Ed.*, 2022, **134**, e202116763.

91 M. Tenjimbayashi and S. Fujii, *Small*, 2021, **17**, 2102438.

92 L. D. Landau and E. M. Lifshitz, *Cour. Theor. Phys.*, 1986, **109**, 3.

93 C. G. L. Furmidge, *J. Colloid Sci.*, 1962, **17**, 309-324.

94 N.-K. Nguyen, C. H. Ooi, P. Singha, J. Jin, K. R. Sreejith, H.-P. Phan and N.-T. Nguyen *Processes*, 2020, **8**, 793.

95 M. Yafia, O. Ymbern, A. O. Olanrewaju, A. Parandakh, A. S. Kashani, J. Renault, Z. Jin, G. Kim, A. Ng and D. Juncker, *Nature*, 2022, **605**, 464-469.

96 C. Zeng, M. W. Faaborg, A. Sherif, M. J. Falk, R. Hajian, M. Xiao, K. Hartig, Y. Bar-Sinai, M. P. Brenner and V. N. Manoharan, *Nature*, 2022, **611**, 68-73.

97 L. Durdevic, H. M. L. Robert, B. Wattellier, S. Monneret and G. Bafou, *Sci. Rep.*, 2019, **9**, 4644.

98 M. Cao, Y. Qiu, H. Bai, Y. Tian, Y. Wu and L. Jiang, *Matter*, 2024, **7**, 3053-3068.

99 N. A. Dudukovic, E. J. Fong, H. B. Gemeda, J. R. Deotte, M. R. Cerón, B. D. Moran, J. T. Davis, S. E. Baker and E. B. Duoss, *Nature*, 2021, **595**, 58-65.

100 U. Manna and D. Lynn, *ACS Appl. Mater. Interfaces*, 2013, **5**, 7731-7736.

Chapter 4: Controlled Chemical-patterning of Textile to Accelerate Anti-gravity Water Flow

Bio-inspired unidirectional flow of tiny aqueous droplets across the fibrous substrate paved the way for the emergence of various advanced materials. In the past, textiles decorated with noncontact-based wettability-patterns enabled unidirectional water flow, without flooding the top surface by the transferred water. However, such approaches mostly suffer from a low (≈0.176 µL mm^{-2} s^{-1}) flow rate and are likely to delay the overall liquid ejection process. Here, a chemically reactive coating capable of tailoring water wettability ($121.3^{\circ} \pm 2.4^{\circ}$ to $153.3^{\circ} \pm 1.8^{\circ}$) is introduced on commercially available textiles to develop chemically modulated wettability-pattern for achieving a rapid (2.57 ± 0.28 µL mm^{-2} s^{-1}) flow rate of water against the gravity with an ability to roll the accumulated liquids on the top surface. The spatially selected and controlled chemical modification with hydrophilic and hydrophobic small molecules through a 1,4-conjugate addition reaction yielded a 3D channel with a customized wettability gradient. The pinning and depinning of invaded water through such chemically decorated channels enabled unidirectional and fast penetration of liquid, where the water penetration resistance largely depends on the water penetration direction and dimension of the chemically modulated channels.

S. Kumar, A. Borbora, P. Chakraborty, H. Sarma, A. Bose, M. Tenjimbayashi and U. Manna, *Adv. Funct. Mater.*, 2024, **34**, 2410955.

4.1. Introduction

In nature, many living objects adopted different strategies for the unidirectional liquid flow for their survival. For example, asymmetric spines in cacti,[1,2] periodic spindle knots in spider silk,[3,4] bird beaks,[5,6] and peristome surface structure of pitcher plants[7-10] inherently display a unidirectional flow of water. Inspired by these naturally existing interfaces, various macroscopic and microscopic asymmetric structures of naturally existing interfaces were mimicked artificially to achieve unidirectional liquid transportation—which finds diverse potential applications, including water harvesting,[2,11] oil/water separation,[12,13] heterogeneous catalysis,[14,15] smart textile,[16,17] etc. In contrast to asymmetric bio-inspired structures, Whitesides and coworkers introduced a gradient of wettability to achieve another type of unidirectional water transport, where water droplets run "up the hill" without requiring any external energy.[18] Since then, few other approaches, including water column-assisted coalescence of tiny water droplets across a superhydrophobic barrier,[19] patterned channel with wettability gradient,[16,17,20–23] and Janus wettability across a fibrous substrate[24–29] were introduced for liquid transport against gravity. Among these, the approach of patterned channels with a liquid repellent background not only provides a facile basis for the anti-gravity transport of water but also prevents the flooding of the top surface by the transferred liquid. Moreover, such a design allows the rolling of transferred water droplets to keep the top interface dry. Transportation of secreted body waste found in the form of tiny aqueous droplets on the skin (widely recognized as sweat) is of great challenge, as the flooding of commonly used hydrophilic textiles by sweat leads to prolonged exposure to an unhealthy and uncomfortable environment.[30] An average person is known to produce sweat at a rate of ≈1 Kg m^{-2} h^{-1} under a condition of moderate exercise,[31] whereas the water-repellent commercially available fabrics remained capable of rejecting sweat at a much lower rate, i.e., ≈0.46 Kg m^{-2} h^{-1}.[32,33] Recently, to achieve better management of personal moisture, the principle of anti-gravity transport of liquid has been successfully applied in designing a "skin-like" fabric to eject sweat from the body surface to keep the body skin dry and relatively cool with respect to its surroundings.[21] In a seminal report, a superhydrophobic background derived from perfluorosilane-coated TiO_2 nanoparticles was subjected to spatially selective plasma treatment to develop gradient wettability spot channels for unidirectional water transport.[16] Thereafter, various other patterned channels were introduced by strategic modulation of the pore and wettability of the used fibrous substrates.[17,20,22,23] However, the use of environmentally toxic fluorinated chemistry in the superhydrophobic backgrounds and the low flow rate of water transfer (<0.2 μL mm^{-2} s^{-1}) demand further design of material for rapid ejection of relevant liquids (e.g., bio-fluids, sweat and so on) across the selected fibrous substrate for its more realistic and prospective applications in the efficient management of personal moisture, wound healing, design of liquid diode etc.

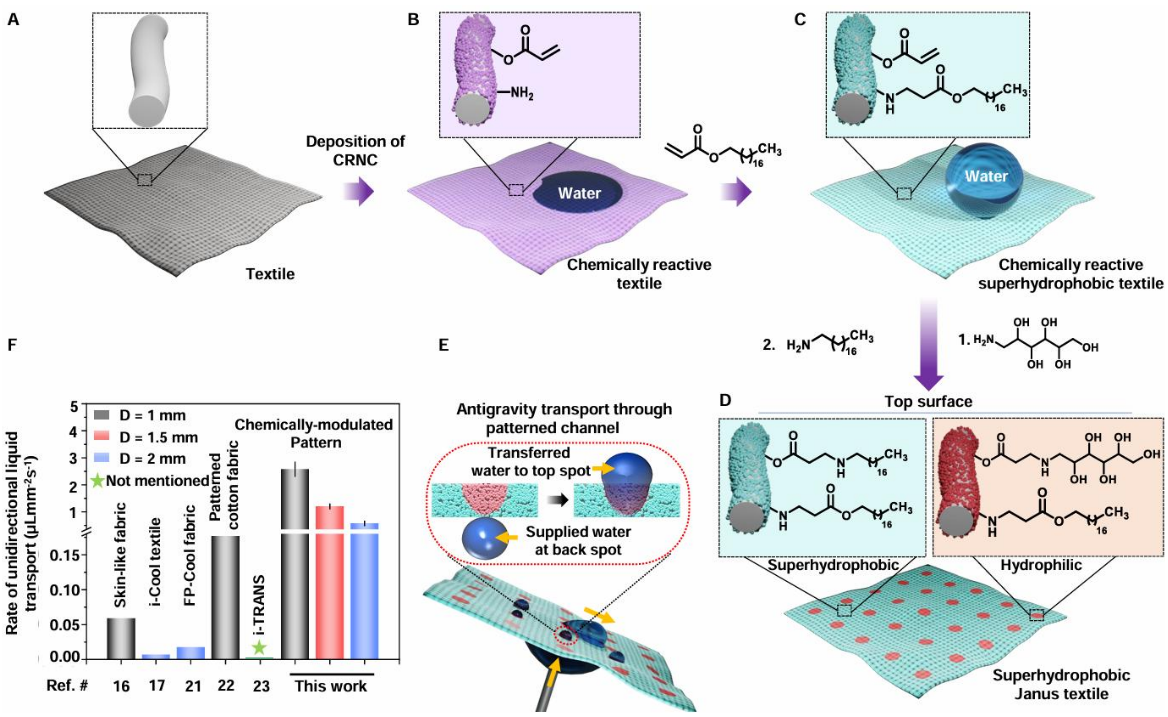

Figure 4.1 (A-D) In situ, deposition of chemically reactive nano complex (CRNC) derived from a reaction mixture of 5Acl and BPEI on a selected textile (A) following the dip coating process yielded chemically reactive textile (B). Its post-chemical modifications with octadecylacrylate conferred superhydrophobicity and denoted as a chemically reactive superhydrophobic textile (C). The spatially selective modification of chemically reactive superhydrophobic textile with glucamine followed by octadecylamine provided Janus channels on a chemically inert superhydrophobic background. E) Schematic illustrating the unidirectional transport of beaded droplets through patterned textiles against gravity. F) The plot comparing the rate of unidirectional transport against the gravity of current work with reported literature.

Various natural or synthetic fabrics have complex geometries and tend to rapidly absorb water and other liquids, leading to arbitrary spillage. This made contact-based controlled chemical patterning on fabric challenging in the past. In the previous literatures, mostly non-contact patterning methods (UV-ray, plasma treatment, etc.) were spatially selectively applied to perturb the hydrophobic chemical groups (e.g., fluorinated hydrocarbons) on the hydrophobic/superhydrophobic interface;[16-23] however, controlled and uniform penetration of UV-radiation or plasma across the highly opaque fibrous substrate would be a challenging task to achieve. On the other side, a liquid repellent and chemically reactive coating on fabric is essential to restrict the arbitrary absorption of water or other solvents during spatially selective chemical modification. To the best of my knowledge, examples of chemically reactive superhydrophobic coating on fabric are rare in the literature. While the residual reactivity allowed a controlled chemical modification, the embedded water repellency restricts arbitrary spillage of modifying solution during wet chemistry on fabric, ensuring a controlled and spatially selective patterned wettability across its thickness as depicted in Figure 4.1. As the current method is substrate-independent, I can successfully develop a wettability pattern on a wide range of natural and synthetic fabrics at ambient conditions without requiring any instrument.

In this chapter, chemically reactive nanocomplex (CRNC) was dip-coated on a selected fibrous substrate for direct and spatially selective modulation of wettability through adopting a 1,4-conjugate addition reaction in aqueous medium at ambient conditions, referred to as "wet-chemistry" using selected small molecules, i.e., glucamine, as depicted in Figure 4.1A-D. In the current approach, no sophisticated instrumental setup is required; rather, the diameter and depth of the patterned spot can be regulated easily just by controlling the contact area between the textile and aqueous droplet of glucamine and the duration of the wet chemistry. The hydrophilic moiety is installed without perturbing the hydrophobic moiety (e.g., hydrocarbon) to spatially selectively modulate the water wettability on the water-repellent interface (Figure 4.1E). The prepared patterns provided superior anti-gravity transport of water irrespective of the channel diameters (D) that were commonly adopted in the reported literature on patterned textiles, as shown in Figure 4.1F. This is likely due to the chemically controlled optimization of pattern dimension with a gradient of wettability on a water-repellent background (Figure 4.1E). In the current strategy, chemically modified hydrophobic and hydrophilic moieties present in the patterned channel contribute to a unidirectional pinning and depinning process to transport the beaded water droplet against the gravity, where both water friction force of transported water and breakthrough pressure varies depending on the channel size and hydrophobicity of background of the prepared channel. Such material remained successful in the rapid ejection of accumulated sweat from the skin to provide a dry and non-sticky environment. Moreover, the rapid anti-gravity transport of artificial sweat ensured a temperature depletion of 4.2 $^{\circ}$C in a relevant and hot (40 $^{\circ}$C) outdoor condition, where the improvement in controlling body temperature performance was found to be 40% compared to the best available performance of patterned textiles in the literature.[16-23] In addition, such a strategy would be useful in intravenous therapy, where unidirectional transport of saline and medicine would be possible with an added feature for preventing blood backflow.

4.2. Experimental Section

4.2.1. Material Required

Branched poly(ethyleneimine) (BPEI, M_W ~ 800 Da), dipentaerythritolpenta-acrylate (5-Acl, M_W ~ 524.21 g mol^{-1}), octadecyl amine (ODA), lauryl acrylate (LAc), octyl acrylate (OAc), hexyl acrylate (HAc), butyl acrylate (BAc), acetic acid, lactic acid, tertramethylrhodamine cadaverine (TMRC) and fluorescein isothiocyanate (FITC) were purchased from Sigma-Aldrich, Bangalore, India. D-glucamine (> 95 %) was obtained from TCI (Tokyo Chemical Industry). Magnesium chloride, ammonium hydroxide, calcium chloride and magnesium sulphate were purchased from Emparta (Merck Specialties Private Limited). Dimethyl sulfoxide (DMSO) was procured from Finar, India. High glucose DMEM (Gibco, United States of America), fetal bovine serum (FBS), phalloidin-488 solution, hoechst-33342 were purchased from Thermofisher (USA). Antibiotic antimycotic solution was purchased from HiMedia Laboratories, India. Thiazolyl blue tetrazolium bromide (MTT), neutral buffer formalin (NBF), Triton X-100, bovine serum albumin (BSA), tween-20 were procured from Sigma-Aldrich. UV cabinet used for continuous exposure to UV radiation was purchased from Relitech (Bengaluru, India). Sandpaper (grit no. 400) was purchased from Amazon, India. Polyurethane textile, cotton textile, wool textile, polyester textile and lycra textile were procured from a local shop in Guwahati (Assam, India). The details of the remaining other chemicals used in this work were provided in the previous chapters.

4.2.2. Charecterization

Depth of D-glucamine modification in reactive superhydrophobic textile was performed by electron dispersive X-ray spectroscopy. The samples were coated with a thin layer of gold by sputtering for 90 seconds before measurements. The X-ray photoelectron spectroscopy (XPS) was performed in PHI5000 VersaProbe III (Φ ULVAC-PHI, INC.) with a monochromated Al Kα X-ray source. All fluorescence microscopic images were captured using a ZEISS Axio Vert.A1 inverted microscope with a 5X objective. The surface temperature of the patterned textile and bare textile was measured with a thermal infrared camera (Testo 05608721). The remaining other instruments used in this chapter for characterization of synthesized materials were the same, as discussed previously in section 2.2.2 of chapter 2.

4.2.3. Fabrication of Dual Chemically Reactive Textiles

Dual chemically reactive textiles were prepared following a dip coating procedure. In this context, I have selected a plain weave of polyurethane fabric with a twill pattern (180 g m^{-2}) and a thickness of ~ 456 µm. In brief, a reaction mixture was prepared by mixing 6 mL BPEI solution (0.105 M in ethanol) into 20 mL 5Acl solution (0.252 M in ethanol). Then, a piece of textile (10 × 10 cm^2) was dipped into the reaction mixture. After 30 minutes, when the reaction mixture started to appear milky-turbid because of the formation of reactive nanocomplex, the textile was removed and kept for air drying overnight. Thereafter, it was thoroughly washed with ethanol, followed by air drying to obtain the dual chemically reactive textile.

4.2.4. Developing Chemically Reactive Superhydrophobic Textiles

The chemically reactive superhydrophobic textile was prepared through the post-covalent modification of dual chemically reactive textiles with ODAc, where residual amine groups of dual chemically reactive textiles readily reacted with the acrylate groups of ODAc through 1,4-conjugate addition reaction at ambient condition. In this context, the dual chemically reactive textile was dipped into an ethanol solution of ODAc (5 mg mL^{-1}) for 12 h, followed by washing the coated substrate thoroughly with fresh ethanol multiple times to remove excess and loosely deposited ODAc molecules. Finally, the ODAc-modified textile was kept for air drying to obtain the chemically reactive superhydrophobic textile. A similar protocol was followed for OAc and LAc modification to tailor water wettability.

4.2.5. Fabrication of Janus Textiles

The chemically reactive superhydrophobic textile was kept on a planar substrate, and all four edges of the textile were covered with adhesive tape to restrict the spreading of the aqueous solution of D-glucamine (0.275 M) to the backside of the textile. The textile was submerged in D-glucamine solution to allow the reaction with residual acrylate of reactive superhydrophobic textiles for different durations. Thereafter, the treated textile was washed thoroughly with water multiple times to remove excess and loosely deposited D-glucamine moiety. The wettability on both sides (top and bottom) of the textiles was investigated by visual inspection and contact angle measurements. Textiles with contrast wettability at two sides are denoted as Janus textile.

4.2.6. Fabrication of Patterned Textiles

To create patterned textiles with spatially selective chemical modification using glucamine, the chemically reactive superhydrophobic textile was placed on a flat substrate. Arrays of spatially selective regions were then exposed to 5 µL of the D-glucamine solution for different durations. Followed by washing thoroughly with water multiple times to obtain patterned hydrophilic channels on a superhydrophobic background. Additionally, the volume of the beaded droplets of D-glucamine solution on reactive superhydrophobic textiles was varied to modulate the dimension of hydrophilic spots in the patterned textiles. Finally, the patterned textile was treated with octadecyl amine (concentration of 5 mg mL^{-1}) to consume available acrylate groups in the superhydrophobic background and then washed with ethanol.

4.2.7. Water Vapour Transmission Test

Both patterned and bare textiles were separately wrapped around the opening of a centrifuge tube (50 ml, diameter 3 cm, pre-filled with 40 ml of distilled water) by thread. The water inside the centrifuge tubes was allowed to evaporate out at room temperature with a relative humidity of 50 ± 5%. The weight of the centrifuge tube was measured at regular time intervals. The water vapor transmission was measured by dividing the reduced mass of water by the exposed area of the textiles placed on top of the centrifuge tubes.

4.2.8. Estimation of Water Breakthrough Pressure

A patterned textile was fixed to a hollow glass tube, which has a bottom opening of diameter (2r) of 1cm. Then, water was poured into the tube till the water spilled from the bottom fabric. Here, the critical height of the water in the tube is proportional to the breakthrough pressure.

4.2.9. Chemical Durability Tests

Patterned textiles were immersed in different chemically harsh conditions, such as artificial seawater (Prepared by mixing NaCl (2.673g), $MgSO_4$ (0.325g), $MgCl_2$ (0.226g), and $CaCl_2$ (0.112g) in 100 ml of deionized water), deionized water, river water, alkaline solution (pH 12), acidic solutions (pH 1), surfactant solutions: DTAB (1mM), and SDS (1 mM) and UV irradiation (254 nm and 365 nm) for 6 weeks. Thereafter, the unidirectional and anti-gravity water transport property was examined visually and the extreme water repellence of beaded droplets was measured by contact angle instruments.

4.2.10. Physical Durability Tests

The prepared coatings were subjected to various practically relevant and physically abrasive exposures widely accepted in the literature. The details of each abrasive and challenging exposure are mentioned below-

4.2.10.1. Sand Paper Abrasion

An abrasive sandpaper 400 grit (1 cm × 2 cm) was individually applied on the patterned textiles (5 cm × 1 cm) for 5000 cm distance by rubbing with back-and-forth motion across the patterning top spot side coating with an applied pressure of 25 kPa. After that, the unidirectional water transport property of superhydrophobic Janus channel textiles was examined with visual inspection. On the other hand, the water repellence of beaded droplets was measured using contact angle instruments.

4.2.10.2. Adhesive Tape Peeling Test

A freshly peeled adhesive tape was exposed to the patterned textiles with an externally applied load of 500 g for 1 minute. Thereafter, the adhesive tape was peeled off manually from the surface of the textile. This procedure was repeated for 500 times on the coating. The treated interface remained efficient for unidirectional water transport and the embedded water repellence remained intact, as confirmed with contact angle instruments.

4.2.10.3. Sand Drop Test

A freshly prepared patterned textile was adhered to a glass slide inclined at a 45° tilting angle, and then 300 g of sand grains were poured from a height of 40 cm through a funnel towards the patterning top spot side of the coated textile. After that, the exposed interface was cleaned by blowing air on it. Thereafter, the unidirectional and anti-gravity water transport property through the patterned textiles was characterized and the water repellence of beaded droplets was measured by contact angle instruments.

4.2.10.4. Tensile Deformation Test

The patterned textile was exposed repetitively to a tensile strain of up to 125% for 1000 cycles. Afterwards, the unidirectional water transport performance by treated textiles was examined visually, and the repellence of beaded droplets was measured by contact angle instruments.

4.2.10.5. Laundry Test:

The washing durability was investigated by following a standard procedure (AATCC Test Method 61-2006 test No 2A), where the patterned textile was laundered at 40 $^{\circ}$C for 45 min in the presence of 0.37 wt% SDS surfactant. This procedure was repeated for 500 times. The water wettability of the coated textiles was examined by measuring the contact angle at regular intervals, and the unidirectional water transport property was measured through visual inspection.

4.2.10.6. Cellular Compatibility Studies

The various fabric samples were sterilized using ethanol exposure (70 % v/v, 20 min) followed by exposure to ultraviolet radiation (365 nm, 1000 mW cm^{-2}, 20 min). Thereafter, individual fabric groups of size 45 mm x 45 mm were incubated in complete cell culture medium (CCM), comprising high-glucose DMEM supplemented with 10% fetal bovine serum (FBS) and 1% antibiotic-antimycotic solution (HiMedia Laboratories, India), at room temperature. The fabrics were incubated for 24 h and the subsequent leachate medium (LM) was collected for further experiments of Cellular compatibility using human dermal fibroblast (HDF) cells.[34-36]

4.2.10.6.1. Cell viability evaluation

HDF (passage 4-8) were used for the evaluation of biological compatibility, cellular viability and cell morphological studies. HDF were cultured in CCM within an incubator (37 $^{\circ}$C, 5% CO_2) until they reached 70 % confluence. The confluent cells were dissociated using trypsin, neutralized using CCM and centrifuged thereafter to obtain a cell pellet. The cells were resuspended in CCM and counted for further seeding.

4.2.10.6.2. MTT Assay

HDFs were seeded into a 48-well plate (n = 3 per group) at a density of 2 x 10^4 cells/well for MTT assay. The cells were grown for 24 h in CCM within the well plate. This was followed by removal of CCM and addition of LM which was used for culturing the attached HDFs for 48 h. These conditioned cells were incubated with thiazolyl blue tetrazolium bromide (MTT) reagent as per the previously used protocol for determining cell viability.[36] Briefly, a 10x diluted solution of 5 mg mL^{-1} MTT was prepared in phosphate-buffered saline (PBS). This diluted MTT solution was used for incubation with the LM-treated and untreated HDFs for 4 h. This was followed by the removal of MTT solution. 100 µL DMSO was added to each well for dissolution of the formazan crystals formed by the viable cells. Further, the dissolved formazan-DMSO solution was collected for measurement of absorbance at 570 nm wavelength using a Multiskan Sky Spectrophotometer. The cellular viability was evaluated by normalizing the absorbance from all the fabric LM-treated cells with the untreated TCP-seeded HDF cells taken as a positive control.

4.2.10.6.3. Cellular morphology evaluation

HDFs were seeded onto poly-l-lysine coated glass cover slips (n = 3) at a density of 2 x 10^4 cells for phalloidin staining to determine changes in cellular morphology. The HDFs were grown for 24 h on cover slips with CCM followed by a treatment of fabric LM of various groups for 48 h. Untreated HDFs on glass cover slips were taken as controls. Further phalloidin-hoechst 33342 staining was performed after 48 h of treatment as per the defined protocol.[36] Briefly, the HDF seeded cover slips were washed gently with PBS, followed by fixation using 10 % neutral buffer formalin for 30 min. The fixed cells were permeabilized for 10 min using 0.1 % Triton X-100. Post-permeabilization, samples were blocked using 5% bovine serum albumin solution in 0.01 % Tween-20 for 30 min. After blocking, the cells were incubated in phalloidin-488 solution using the manufacturer's recommended concentration for 30 min at room temperature in the dark. These stained cells were then counterstained using Hoechst-33342 nuclear stain briefly for 5 minutes using the manufacturer's recommended concentrations in the dark. The stained cells were then washed with PBS gently and observed using an inverted fluorescence microscope (Axio Observer, Zeiss, Germany). Cell samples were washed between each step of permeabilization, blocking and staining gently using PBS.

4.3. Results and Discussion

4.3.1. Reactive Superhydrophobic Textile

In the recent past, branched polyethylenimine (BPEI) and dipentaerythritol pentaacrylate (5Acl) were mutually reacted through a 1,4-conjugate addition reaction to prepare chemically

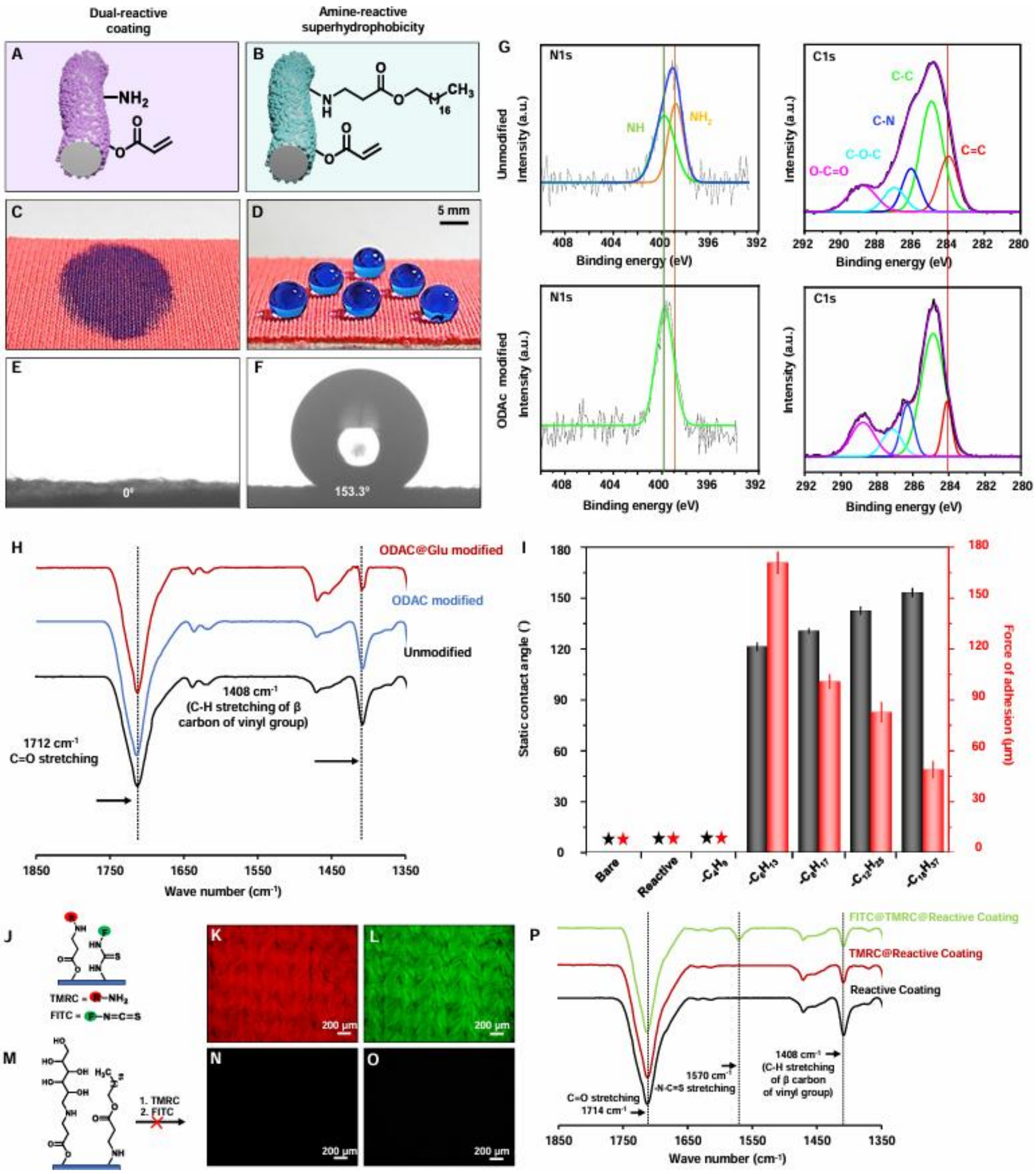

Figure 4.2 A-F) Schematic representations (A and B), digital images (C and D), and contact angle images (E and F) of a dual reactive coating before and after octadecylacrylate (ODAc) modification. G) High-resolution XPS spectra with deconvolution for N 1s (left panel) and C 1s (right panel) before and after chemical modifications of dual reactive coating with ODAc. H) FTIR spectra of dual reactive coating before and after modification with ODAc followed by glucamine. I) Plots illustrating the static contact angle and adhesive force of dual reactive coating after modifying with different alkyl acrylate. J-L) Schematic illustration (J) and corresponding fluorescence images (K, L) of the dual chemically reactive coatings after sequential treatments with TMRC and FITC. M-O) Schematic illustration (M) and corresponding fluorescence images (N, O) of D-glucamine/ODAc-modified reactive coatings after sequential modification with TMRC and FITC. P) FTIR spectra before (black) and after TMRC modification (red) and FITC/TMRC modification (green) of the reactive coating.

reactive nanocomplex (CRNC) and its porous coatings on planar substrates provided a facile basis to independently tailor liquid (oil/water) wettability and adhesion property for anti-counterfeiting and naked-eye chemical sensing applications.[37,38] Inspired by these results, here, CRNC is deposited on an inherently hydrophilic and stretchable fibrous substrate (polyurethane (PU) fabric) to prepare orthogonally reactive polymeric coating (Figure 4.2A-F) to demonstrate anti-gravity flow of water without flooding the top surface of textile through introducing chemically-modulated patterned channels on a an extremely water-repellent background. The existence of residual chemical reactivities (i.e., amine and acrylate) was characterized with X-ray photoelectron spectroscopy (XPS) and Fourier transform infrared spectroscopy (FTIR) analysis, as shown in Figure 4.2G, H. The deconvoluted XPS signatures at a binding energy of 399.8 eV revealed the presence of a residual primary amine group. That diminished after mutual reaction with octadecyl acrylate (ODAc) through 1, 4-conjugate addition reaction, as shown in Figure 1G. Consequently, the ODAc-modified coating displayed a significant rise in water contact angle (WCA) from 0° to 153° as shown in Figure 4.2C-F. Notably, the association of superhydrophobicity through ODAc modification was achieved without affecting the residual acrylate groups in the prepared coating as evident from the existence of the characteristic XPS peak for vinyl moiety at 284.1 eV as shown in Figure 4.2G. Similarly, the characteristic IR signature for C-H deformation of β carbon of the vinyl group at 1408 cm^{-1} remained intact with respect to an internal reference, i.e., IR peak for carbonyl stretching at 1712 cm^{-1} (Figure 4.2H). Further, the orthogonal reactivity of available functional chemical moieties (i.e., amine and acrylate), for mutual reaction with selected small molecules, was separately validated with an optical fluorescence microscopic study and FTIR, as depicted in Figure 4.2 J-P. The dual reactive textile was sequentially post-modified with reactive dyes, i.e., TMRC and FITC, to independently validate the presence of acrylate and amine groups through fluorescence microscopic analysis in Figure 4.2 J-L. Eventually, the selected dye-modified coating provided fluorescence images. However, the coating that was pre-treated with non-fluorinated small molecules (glucamine and octadecyl acrylate) before treatment with TMRC and FITC failed to provide such a fluorescence signal (Figure 4.2M-O), likely due to the lack of covalent bonding with TMRC and FITC. The residual acrylate groups in the reactive coating mutually reacted with TMRC through 1,4-conjugate addition, and the amine moiety of the same coating remained capable of reacting with FITC through the formation of thio-urea bond as characterized by FTIR analysis in Fig. 4.2P. In addition to superhydrophobicity, the modification of reactive coating with ODAc provided a relatively low (48.8 μN) force of water adhesion as shown in Figure 4.2I. Both water wetability and force of water adhesion on the prepared coating majorly depends on the length of hydrocarbon tails of selected alkyl acrylates (i.e., butyl acrylate (BAc), hexyl acrylate (HAc), octyl acrylate (OAc), lauryl acrylate (LAc), and ODAc), as shown in Figure 4.2I. Thereafter, the topography of the selected fibrous substrate (PU fabric) with and without polymeric coatings and after their post-covalent modifications with selected alkyl acrylates, was characterized with FESEM; Figure 4.3A-F. The smooth and featureless fibers (Figure 4.3A, B) of PU fabric were decorated with globular domains due to the deposition of CRNC; however, no distinguishable change in globular domains was observed after modifying the reactive coating with selected alkyl acrylates (Figure 4.3C-F).

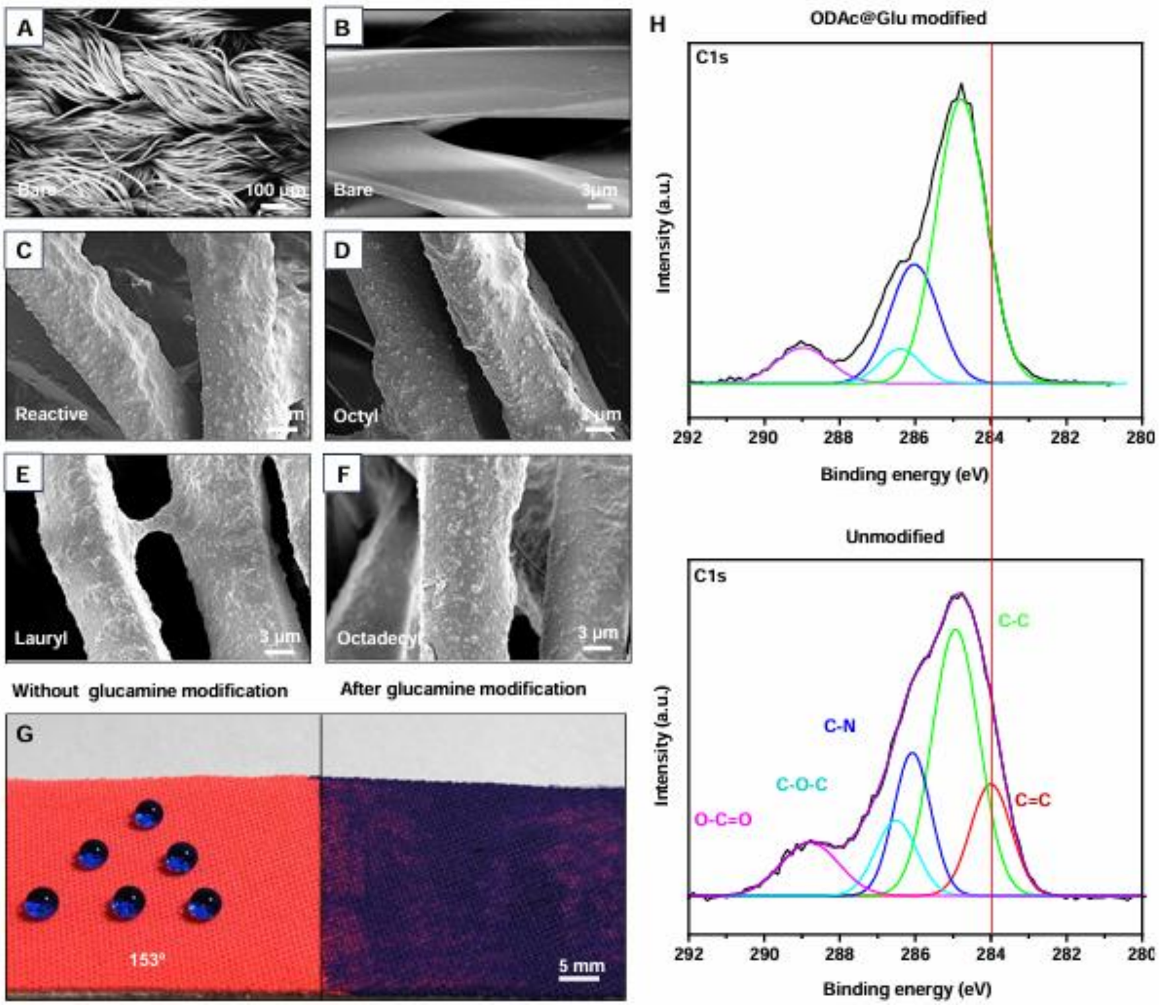

Figure 4.3 A-F) FESEM images of bare (A, B) and dual chemically reactive coated textile before (C) and after octyl (D), lauryl (E), and ODAc (F) modifications. G) Digital image of a chemically reactive superhydrophobic interface after modifying half (right side) of it with glucamine. (H) High-resolution XPS spectra with deconvolution for C1s before and after chemical modifications of dual reactive coating with ODAc followed by glucamine.

Hence, the post-chemical modification does not change the topology of the fabrics, and the alkyl chain length in the selected modifiers remained the experimental variable to modulate water wettability in this current design. Such coated textiles with tailored hydrophobicity remained chemically reactive because of the existence of a residual acrylate group. To independently validate the existence of chemical reactivity of the prepared superhydrophobic textile, a portion of it was subjected to modification with selected hydrophilic small molecules, i.e., glucamine, which resulted in alteration of WCA from 153° to 0° (Figure 4.3G). The depletion of the characteristic IR signature of vinylic C-H deformation at 1408 cm^{-1} (Fig. 4.2H) with respect to another invariable IR signature, i.e., carbonyl stretching at 1712 cm^{-1} supported the 1,4-conjugate addition reaction between amine of glucamine and residual acrylate of superhydrophobic coating. Further, the XPS study independently revealed the disappearance of the characteristic peaks for vinyl moiety at 284.1 eV as shown in Figure 4.3H. Thus, an amine-reactive superhydrophobic coating is successfully developed on the selected fibrous substrate.

4.3.2. Wet-Chemistry Based Patterned Textile

In this section, the chemically reactive superhydrophobic coating applied on the fibrous substrate was subjected to chemical modification with selected hydrophilic molecules in wet conditions to prepare a Janus membrane, where one face of the coated fabric was selectively exposed to aqueous (concentration of 0.275 M) solution of glucamine for different durations. The surface of the prepared superhydrophobic textile that was directly exposed to an aqueous solution of glucamine is denoted as the top side, and the other surface of the textile is referred to as the backside. The gradual ingression of glucamine solution allowed to modify the chemically reactive superhydrophobic coating on the textile through a 1,4-conjugate addition, where an apparent change in WCA of beaded water droplets was noticed, as shown in Figure 4.4A. However, the trends for change in WCA on the top and backsides of the same fabric were distinct. Till 45 min of glucamine treatment, the WCA on the topside was gradually depleted from 153° to 110°, whereas the back side remained extremely water repellent with a static WCA of >150°. After the exposure of the glucamine solution for 60 min, the top surface became hydrophilic with WCA ≈ 41° and remained wet. However, the back side of the same fabric immediately soaked a beaded water droplet with an apparent WCA of 0° without leaving any trace of it on the backside. Eventually, this process yielded a Janus textile, where flooding of liquid was only observed on the top side and the back side remained dry as shown in Figure 4.4B. Thereafter, the penetration of the beaded aqueous phase across the coated and chemically-modified textile was examined, where the mutual reaction duration between the selected modifier (i.e., glucamine) and the reactive superhydrophobic interface was gradually increased to 90 min. In this context, an aqueous solution of calcium salt was beaded on the modified textile to trace it's spreading and soaking into the chemically modified coated textile, where alteration of water wettability from superhydrophobicity to hydrophilicity because of glucamine modification enabled the immediate infiltration of the aqueous phase in the modified textile.

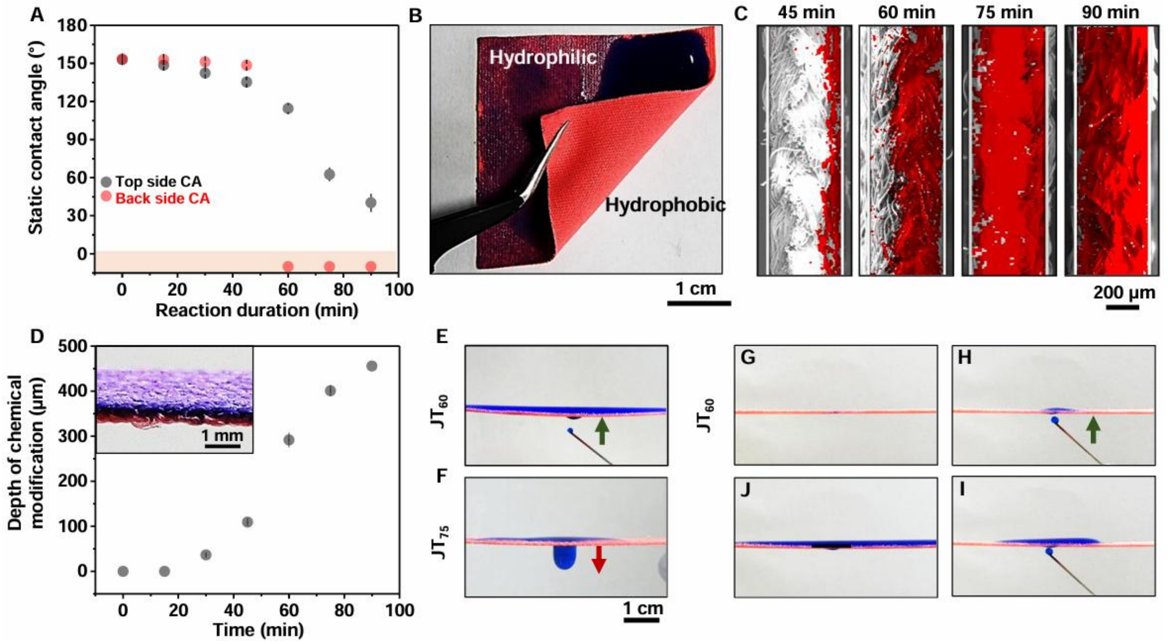

Figure 4.4 A) The plot illustrating static WCAs of beaded water on the top and back sides of the chemically reactive superhydrophobic textile after glucamine treatment for different durations. B) Digital images of modified textile with Janus wettability, where beaded water (blue colored) droplets spread on the top surface, and the bottom surface remained dry. C) Energy-dispersive X-ray (EDX) mapping of calcium metal ions across the chemically reactive superhydrophobic textiles with different time modifications of D-glucamine. D) Plot illustrates the depth of chemical modification of textiles with the progress of reaction time with glucamine and digital image (inset) of a cross-sectional view of the Janus wettability textile. E, F) Digital images depicting anti-gravity transport of blue colored water droplets across the Janus textiles derived through modifying reactive superhydrophobic textile with glucamine for different durations, i.e., E) 60 min (denoted as JT$_{60}$) and F) 75 min (JT$_{75}$). (G-J) Digital images of JT$_{60}$ display anti-gravity transfer of water in the absence of beaded water droplet on top. Results are presented as mean ± SD, where sample size, n = 3.

This process allowed the wetting of the hydrophilic portion by a beaded aqueous solution of calcium. Thus, the EDX mapping of selected metal ions in the textile provided a basis to track the penetration of aqueous solution of calcium ions in the modified textile, and so the thickness of chemical modification across the superhydrophobic textile with glucamine (Figure 4.4D). It is worth mentioning that the glucamine present in its aqueous solution gets exposed to the reactive superhydrophobic textile to react with residual acrylate groups at the contact area between the reactive textile and the beaded aqueous solution of glucamine. The contact area becomes partially hydrophilic and an aqueous solution of glucamine wets the area and gradually penetrates the reactive textile. On further chemical reaction, the interior of the reactive fabric became selectively hydrophilic. Hence, the penetration of calcium ions in the bulk of the textile (thickness of 456 ± 8μm) was improved from 36.5 ± 4.2 to 456 ± 8 μm with increasing the exposure time of reactive superhydrophobic textile to an aqueous solution of glucamine, as shown in Figure 4.4D. Following this process, two distinct Janus textiles were obtained, where the chemically reactive superhydrophobic textile was individually exposed to aqueous solution of glucamine for 60 and 75 min, where both of them displayed soaking of beaded water at back-side of Janus textiles (denoted as JT_{60} and JT_{75}, respectively) with apparent WCA of 0° (Figure 4.4E, F), but having differences in thickness of chemical modification, i.e., 291.8 ± 6.4 and 401.2 ± 6.8 μm (Figure 4.4E, F). These two Janus textiles displayed distinct abilities toward unidirectional and anti-gravity transfer of aqueous phase under an identical experimental set-up. As expected, beaded droplets of water (200 μL) on the top side of both Janus textiles failed to filtrate into the back side under gravity. However, tiny droplets of blue-colored water (because of added methylene blue dye) readily passed through the membrane against gravity to reach the beaded droplet of water on the top side of both Janus textiles (Figure 4.4E). However, JT_{75} remained capable of unidirectional and anti-gravity transfer of only 460 μL of aqueous phase; beyond this volume, the transferred water flowed back to the back side of the textile (Figure 4.4F). In contrast, JT_{60} remained efficient in transferring a relatively larger volume (1.5 mL) of water against gravity, without having any reverse flow to its bottom side (Figure 4.4E). The thickness of chemical modification in these Janus textiles is likely to contribute to distinct ability towards unidirectional and anti-gravity transfer of aqueous droplets. The prepared JT_{60} remained efficient in displaying the anti-gravity transfer of water in the absence of beaded water droplets on top; however, transferred water readily spread on the top side because of the embedded hydrophilicity, as shown in Figure 4.4G. Such a phenomenon is common for other Janus textiles as well. However, to restrict such arbitrary spreading and spilling of transferred water on top of the Janus textile, a patterned textile with Janus channels on a superhydrophobic background is developed by following spatially selective chemical modification of a chemically reactive superhydrophobic textile. In this current strategy, the beading of tiny droplets of aqueous solution of glucamine allowed mutual and spatially selective reaction with residual acrylate groups present in the chemically reactive superhydrophobic textile through 1,4-conjugate addition reaction at the contact of textile and aqueous droplet, where the embedded superhydrophobicity restricts the random spreading of aqueous solution of glucamine on the fabric.

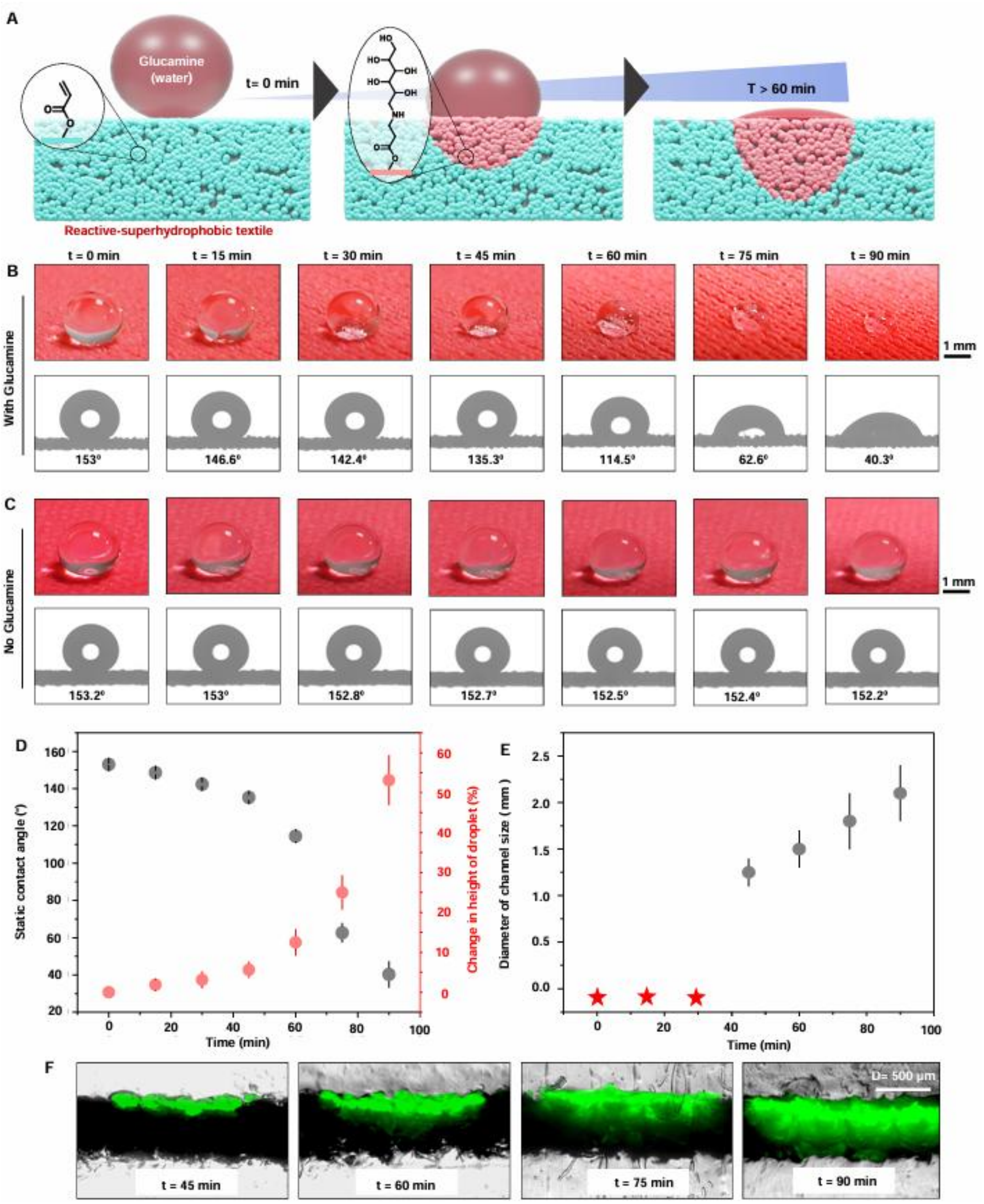

Figure 4.5 A) This schematic illustrates the spatially selective glucamine modification on reactive-superhydrophobic textile through gradual infiltration of beaded aqueous droplets of glucamine. B-C) Digital images and contact angle images accounting the beading of water droplets with (B) and without (C) modifier (i.e., glucamine) on chemically reactive and water-repellent textile with time. This experiment was performed in humid conditions to prevent water evaporation. D) Accounting the change in contact angle and % change in height of the beaded droplet of glucamine solution with time. E) Illustrated the change in the diameter of the pattern spot at the top surface of the chemically reactive superhydrophobic textile with time. The star sign indicates an inability to measure the diameter of the channel. F) The merged microscopic images (fluorescent: green and brightfield: black) of the cross-section of the patterned spot accounting the depth of chemical modification with time. Results are presented as mean ± SD, where sample size, n = 3.

absorbed by the reactive superhydrophobic coating over time, without leading to any arbitrary spillage (Figure 4.5A, B). Further, the gradual change in the percentage of the height of the beaded droplet and the depletion of water contact angle (Figure 4.5D) suggested the 1,4-conjugate addition reaction between amine of glucamine and residual acrylate of reactive superhydrophobic textile at the place of contact between the beaded water droplet and reactive superhydrophobic coating. In the absence of glucamine molecules, the beaded droplet of DI water on the reactive superhydrophobic textile failed to display such a drastic change in water contact angle, as shown in Figure 4.5C. Moreover, the diameter and depth of the chemically modulated pattern on the superhydrophobic background gradually increased with time, as shown in Figure 4.5E, F.

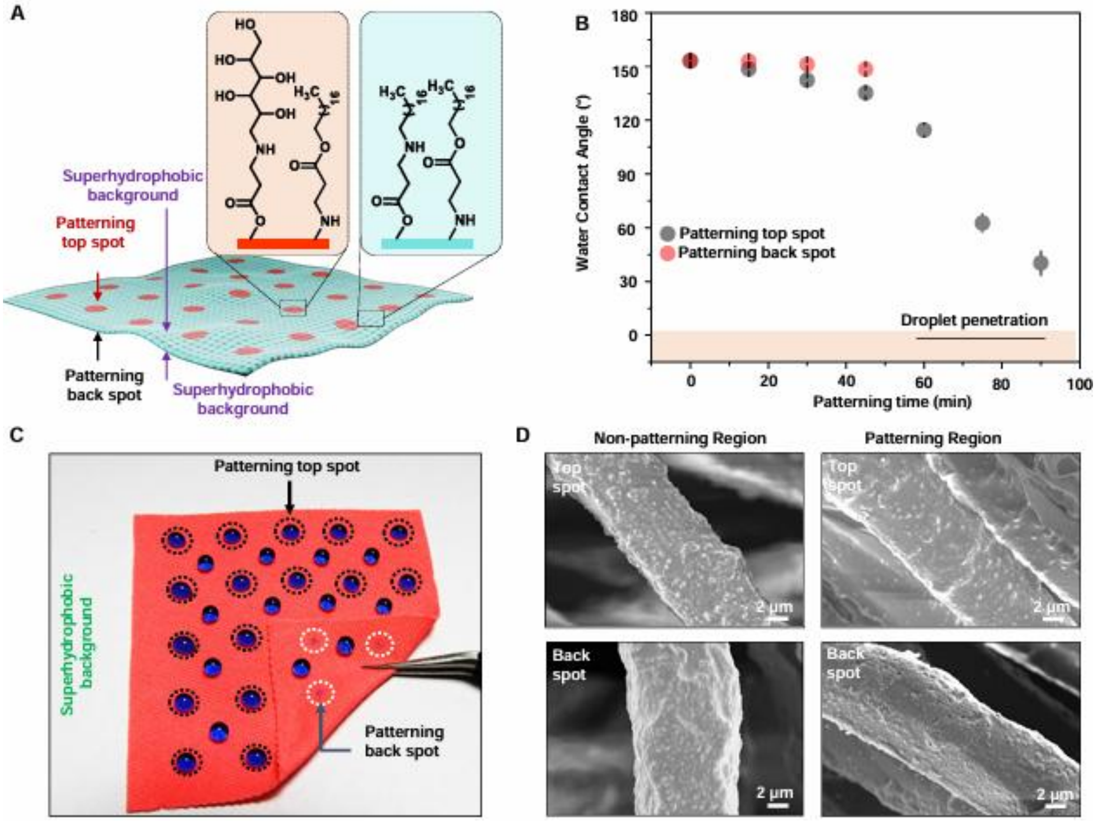

Figure 4.6 A) Schematic of a chemically patterned superhydrophobic interface, where hydrophilic spots, denoted by red colors, were achieved on a superhydrophobic background via spatially selective chemical modifications. B) Accounting the water contact angle change on both top and bottom pattern surfaces with patterning/chemical modification time. C) Digital images depicting the difference in wetting of beaded water droplets on patterning top-spots (indicated with dotted black circle), and patterning back-spots (depicted with dotted white circle). While the beaded water displayed a low contact angle on the patterning top spot, the droplet readily soaked on placing into the patterning back spot. The background on both surfaces repelled the beaded water extremely, causing it to appear spherical. D) FESEM images on patterning and non-patterning regions at the top and back sides of the patterned textile.

Thus, the current approach provided a basis to tune the dimension of the patterned channel through a direct chemical modification at ambient conditions. Eventually, a patterned textile with a Janus channel on a superhydrophobic background was achieved following contact-based selective "wet chemistry". As expected, a distinct change in water wettability was observed on both patterning top-spot and patterning back-spot because of this chemical modification with time, as shown in Figure 4.6B. While the channel is decorated with hydrophilic and hydrophobic moieties, the covalently attached octadecyl moiety contributed to the background superhydrophobicity, as depicted in Figure 4.6A. After that, the prepared patterned textile was partially inverted at its bottom right corner to display the beading behavior of the water droplets on its top and bottom surfaces. Water droplets beaded at the patterning top-spot (denoted with a black dotted circle in Figure 4.6C) with low WCA, while the patterned back-spot readily soaked the beaded blue-colored water droplets, as indicated by the white dotted circles in Figure 4.6C. As expected, the background of the patterned channel displayed extreme water repellence, as shown in Figure 4.6C. Thereafter, the morphology of the patterned textile was examined. No significant change in topography was observed between the top and back sides of the textile, irrespective of patterning and background regions, as shown in Figure 4.6D. Such a change in the wettability of beaded water droplets is attributed to the spatially selective chemical modification of reactive superhydrophobic textiles with glucamine. Thereafter, a droplet of water was placed on the patterned top spot of a patterned textile prepared by exposing it to glucamine solution spatially selectively for 60 and 75 min, denoted as PT_{60} and PT_{75}, respectively. On exposing a tiny droplet of dyed water (blue color) on the patterning back spot, an immediate anti-gravity transfer of the water was noticed without having any arbitrary spreading of transferred water on the top surface, as illustrated in Figure 4.7A. However, distinct results toward anti-gravity water transfer were noticed for patterned textiles, i.e., PT_{60} and PT_{75}, after transferring the water droplets beyond a certain volume (70 µL). A 50 µL droplet of water was individually placed on the patterning top-spot of both PT_{60} and PT_{75}, where the water droplet beaded with different apparent contact angles due to the different infiltration of water into the patterned textiles, as shown in Figure 4.7B. Initially, an instant anti-gravity transfer of water was observed for both patterned textiles, but the backflow of the transferred liquid to the bottom surface of PT_{75} (Figure 4.7B) was noticed just after transferring 70 µL of water through back-spot. However, PT_{60} remained successful in transferring water more than twice (i.e., at least 150 µL; Figure 4.7B) against gravity, without failure at an identical experimental condition.

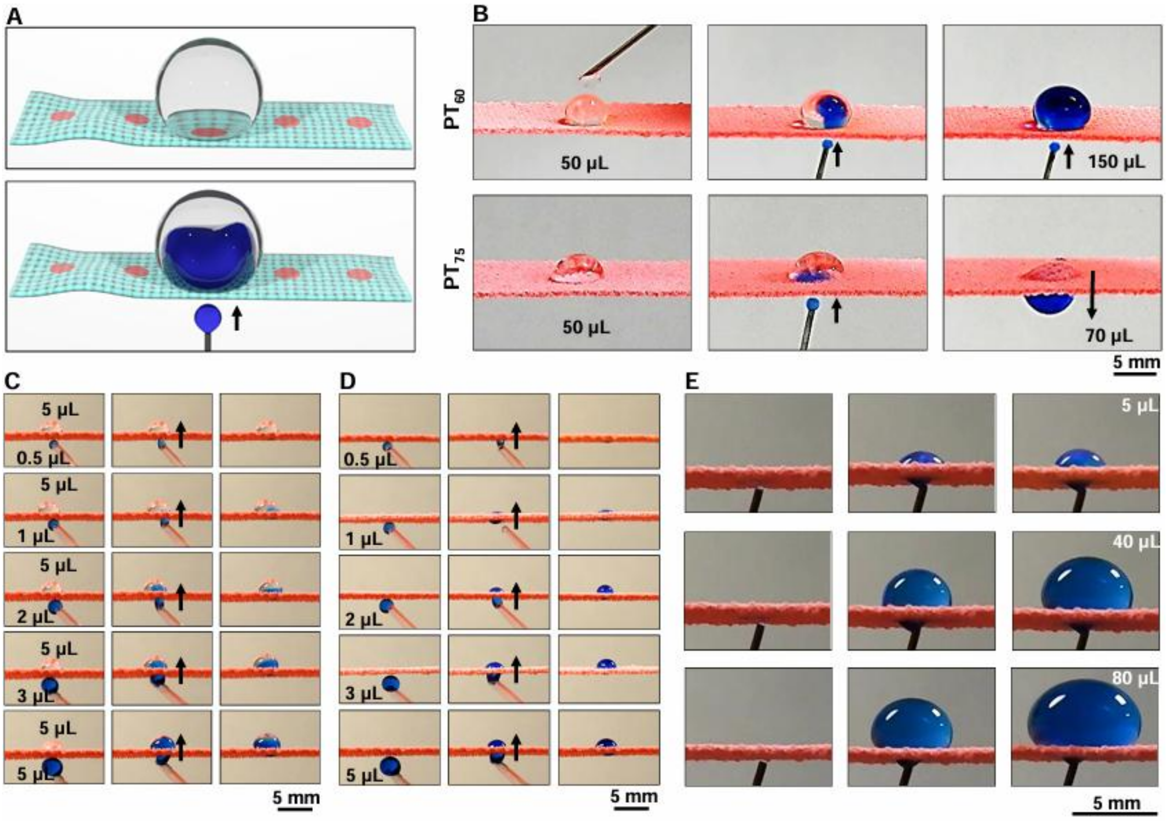

Figure 4.7 A) This schematic depicts the unidirectional transport of blue-colored water against gravity to the beaded droplet on the top of the patterned textile. B) Digital images account for the ability of two distinct patterned textiles (PT$_{60}$ and PT$_{75}$) toward anti-gravity water transportation. C) Digital images demonstrating the anti-gravity transfer of water droplets of various volumes from 0.5 µL to 5 µL, where the volume of beaded water droplets on top was 5 µL. D) Digital images demonstrating the anti-gravity transfer of water droplet of various volume from 0.5 µL to 5 µL in absence of water droplet on top surface of the patterned textile. E) Digital images illustrating the anti-gravity transfer of large amounts of water without causing arbitrary spillage on the top surface of the patterned textile.

It is likely due to the decrease in the breakthrough pressure, which resists the backflow of transferred water under gravity. The alteration of breakthrough pressure, on such a pattern interface is discussed later in detail. Thereafter, to examine the impact of the relative volumes of beaded and tiny droplets on anti-gravity water transport behavior through this patterned textile, volumes of water droplets exposed at the back side of the patterned textile were gradually varied from 0.5 to 5 µL, keeping the beaded water droplet volume (i.e., 5 µL) constant on the top side of same prepared textile (Figure 4.7C). The patterned fabric successfully transported water droplets against gravity, irrespective of the volume ratio of water placed on top and back sides of the patterned textile (Figure 4.7C). In fact, without a beaded water droplet on the top side, the water droplets were successfully transported against gravity, irrespective of their volume, as shown in Figure 4.7D Thus, the prepared patterned textile works regardless of the volume of water droplets, and it continues to perform both in the presence and absence of beaded water droplets on the top of the patterned textile. Moreover, the continuous exposure of water droplets at the back spot allowed for rapid transport against gravity. It accumulated at the top spot of the patterned textile without causing spreading (Figure 4.7E), unlike Janus membranes (Figure 4.4G-J).

4.3.3. Mechanism of Unidirectional Water Transportation

In this section, I first study the mechanics of water adhesion on the textile. The optimized patterned textile was applied to demonstrate an anti-gravity transfer of water in the absence of a beaded droplet on its top-side without flooding the top surface of the patterned on its top-side without flooding the top surface of the patterned material; rather, the transferred water rolls on inclined patterned interface as shown in Figure 4.8A. The pattern interface is capable of rolling both directly beaded droplets on the patterned top-spot and transferring water from the patterned back-spot, with a low difference in the volume of rolling droplets of water. The rolling of transferred water primarily depends on the water friction force. In this context, the water friction forces acting on the top side vary depending on the direction of water supply, either from the top side or the bottom side of the textiles. In case of supplying water from the top side, the water friction force is estimated following the given equation in Equation (1).

$$F_{c\,(\mathrm{Top})} = [\rho U t_c g - \pi d \gamma] \sin\alpha \qquad (1)$$

where ρ: water density ≈ 997 kg m^{-3}, U: feed water flow rate, t_c: critical flow time for droplet sliding, g: gravitational acceleration constant ≈ 9.80065 m s^{-2}, d: syringe diameter ≈ 0.48 mm, γ: water surface tension ≈ 72.8 mN m^{-1}, α: textile tilting ≈ 45° (Figure 4.8B).

On the other hand, when the water was supplied from the bottom side (Figure 4.8C), the friction force was estimated using Equation (2).

$$F_{c\,(\mathrm{Bottom})} = \rho U t_c g \sin\alpha \qquad (2)$$

Figures 4.8D and 4.8E systematically studied the water friction forces, indicating that the force increased with the hydrophilic channel size $2r$ in variation of water-supplying sides and hydrophobic modifications on the background (Figures 4.8D, E).

Here, I hypothesized that the water friction force variation is owing to the pinning of the water contact line at the hydrophilic channel (Figure 4.8F).[39] In this model, the water friction is estimated by integrating the local pinning force $\sim 2r\gamma$ with the hydrophilic spot number near the contact line n, which yields $F_c \sim cn\gamma r$ where c is a constant that should be influenced by the energy dissipation at the superhydrophobic area F_{SHPO}. Figure 4.8G shows the channel size dependence on $F_{c\,(\mathrm{Top})}$ to a log-log plot, in which the slope explains the power law of r on F_c, and the section value decreases with the increase of textile hydrophobicity.

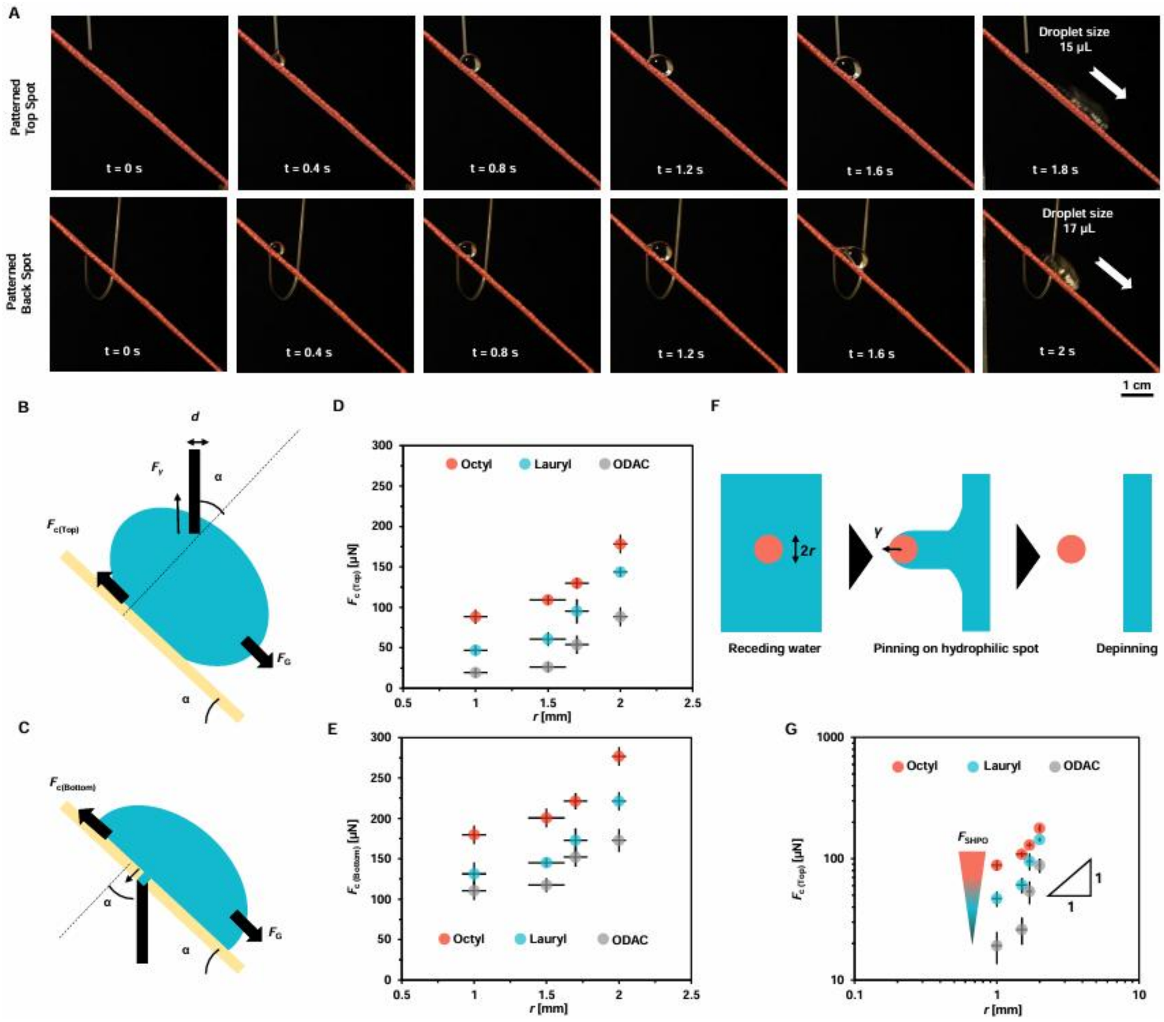

Figure 4.8 A) Digital images accounting for the rolling of beaded (from the top side) and transported water droplets (from the back side) on patterned textile that was kept inclined at an angle of 45°. B, C) Side view schemes of adhesion mechanics of water fed from B) top-side or C) back-side of the textile. D, E) Water friction force as a function of channel size. D) Water is fed from the top side or E) the back side. F) Top-view scheme of the contact line-depinning behavior of the water on the superhydrophobic textile with hydrophilic spot. G) Log-log plot of water adhesion force as a function of channel size in case of water supplied from the top side. Results are presented as mean ± SD, where sample size, n = 3.

Thereafter, I study the dynamics of water penetration through the textile (Figure 4.9A). When the feed water from the syringe contacts the superhydrophobic surface of the textile, the Laplace pressure P_{Lap} works to the water surface, depending on the curvature of the invading water surface. Here, the role of Laplace pressure is $P_{\text{Lap}} > 0$ for resisting or $P_{\text{Lap}} < 0$ for inducing water penetration.[40] In Figure 4.9B, the textile fiber diameter $D \approx 10$ µm and inter-fiber interval W feature the textile geometry. The geometrical angle Φ features the water invasion degree between the fibers. Θ is the water contact angle on the fiber.[41] From this model, the water surface curvature ε can be approximated to be $\varepsilon \approx 2\cos(\Theta - \Phi) / [W + D(1 - \sin\Phi)]$ in the case of the $\Theta - \Phi > 0$. This estimation is applicable in the case of $\Theta - \Phi < 0$ by reversing the water-air phase. Thus, I obtain the Laplace pressure $P_{\mathrm{Lap}} \approx \gamma\varepsilon \approx 2\gamma \cos(\Theta - \Phi) / [W + D(1 - \sin\Phi)]$, where I estimated that the water curvature parallel to the fiber direction ≈ 0. While this, the water feed pressure is estimated to be $4F_{\mathrm{feed}}/[\pi d^2]$, where F_{feed} is the hydrodynamic force in supplying water. Thus, the condition for the water penetration is $4F_{\mathrm{feed}}/[\pi d^2] > P_{\mathrm{Lap}}$ and vice versa.

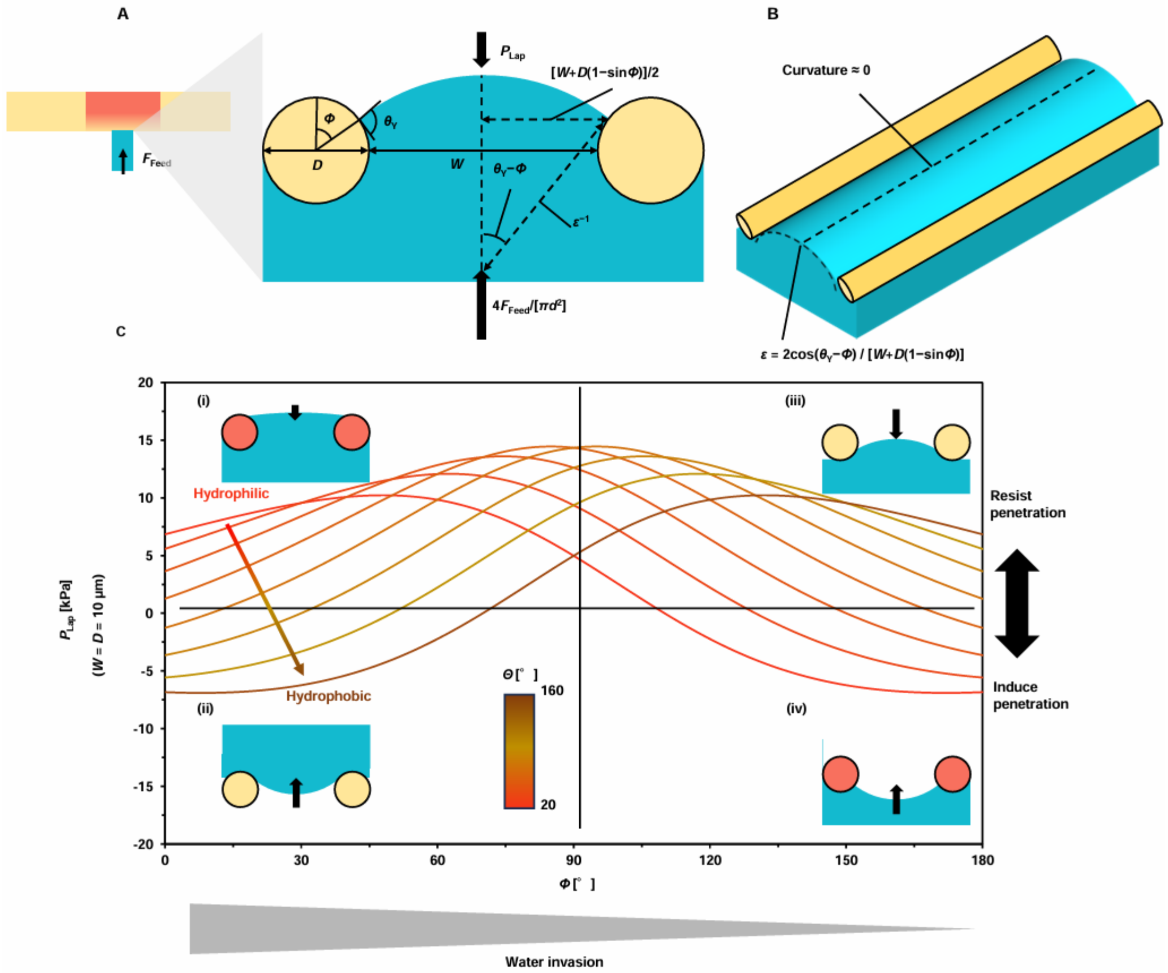

Figure 4.9 (A, B) Scheme of feed water penetrating behavior between modified textiles. The textile fiber diameter D and inter-fiber interval W feature the textile geometry. The geometrical angle Φ features the water invasion degree between the fibers. Θ is the water contact angle on the fiber. C) Estimating the Laplace pressure P_{Lap} with different fiber wettability (that is Θ ranging from 20° to 160°) and water invasion Φ in case of W = D = 10 μm.

In Figure 4.9C, I simulated the change in Laplace pressure when the textile wettability (Θ) and water invasion (Φ) were varied. This simulation explains how wettability variation and water invasion behavior change the mechanics of water penetration. For the simple estimation, I assumed $W \approx D$. I divided the water invasion state into four types depending on the plus/minus of P_{Lap} and $\Phi < 90^\circ$ or $> 90^\circ$: (i) Laplace pressure works to resist water penetration in water penetrating more than half of the hydrophilic fiber; (ii) Laplace pressure works to induce water penetration in water penetrating more than half of the hydrophobic fiber; (iii) Laplace pressure works to resist water penetration with small water invasion between hydrophobic fibers, and (iv) Laplace pressure works to induce water penetration in the early stage of water invasion between hydrophilic fibers. In cases (i), (iii), and (iv), I use Θ with advancing contact angles. In case (ii), I use Θ with a receding contact angle. When the water contacts the hydrophilic fiber (Φ = 180°), the negative Laplace pressure induces wetting in a (iv) state, and water invasion proceeds (Φ gradually decreases). Then, Laplace pressure transitions from negative to positive with the decrease of Φ, and water penetration is resisted in a (i) state. Thus, hydrophilic textile induces the trapping of water between the fibers. In contrast, when the water contacts the hydrophobic fiber (Φ = 180°), the positive Laplace pressure resists water penetration in a (iii) state despite the large Φ. However, when water invasion is proceeded by significant water feed pressure, Laplace pressure transitions to negative with the decrease of Φ, and water is detached from the fiber in a (ii) state. Thus, water does not remain inside the fibers of hydrophobic textiles. After that, to investigate the flow rate of unidirectional transport of water against gravity, the patterned textile was kept tilted at 45° (Figure 4.8A bottom panel) prior to feeding water to the back-spot of the patterned textile, maintaining a continuous flow rate of 10 μL s^{-1}. Within 2 s, the supplied water transferred to the top side of the PT_{60} and rapidly grew to a volume of 17 μL and immediately rolled off from the top surface due to the low water frictional force. Eventually, this experimental setup allowed us to measure the flow rate of the unidirectional transport of water against gravity, i.e., 8.5 μL s^{-1}. It is interesting to note that an elevation in the flow rate of transferred water was noticed on increasing the hydrocarbon chain length of selected alkyl modifications (octyl, lauryl, and octadecyl), as shown in Figure 4.10A. On the other hand, the patterning channel with a larger diameter affected the transfer of liquid and its subsequent rolling on the top surface. This experiment indicates the need for precise control over channel dimension and chemical modulation to achieve a high flow rate for transporting water against gravity. While a high flow rate is desired to ensure immediate transport of water, an elevated breakthrough pressure prevents the backflow of accumulated water across the patterned textile. Figure 4.10A shows the experimental setup, in which I feed the water flow of 10 μL s^{-1} to the pattern interface having a difference in the diameter of channel size, and define the critical height for the feed water penetration H_c. I assume the critical pressure for the water penetration is concentrated in the channel area, which yields $H_c \sim r^{-2}$. Figure 4.10B shows the experimental results of the H_c with different r, where the slope of the plot validates the power law between H_c and r. Figure 4.10B estimates the macroscopic water penetration resistance of the textiles with channels. The hydrophilic channel size and water penetration direction (top or bottom sides) are changed here. Moreover, I find that the water penetration resistance was largely influenced by the water penetration direction, where the background chemical modification had minimal influence.

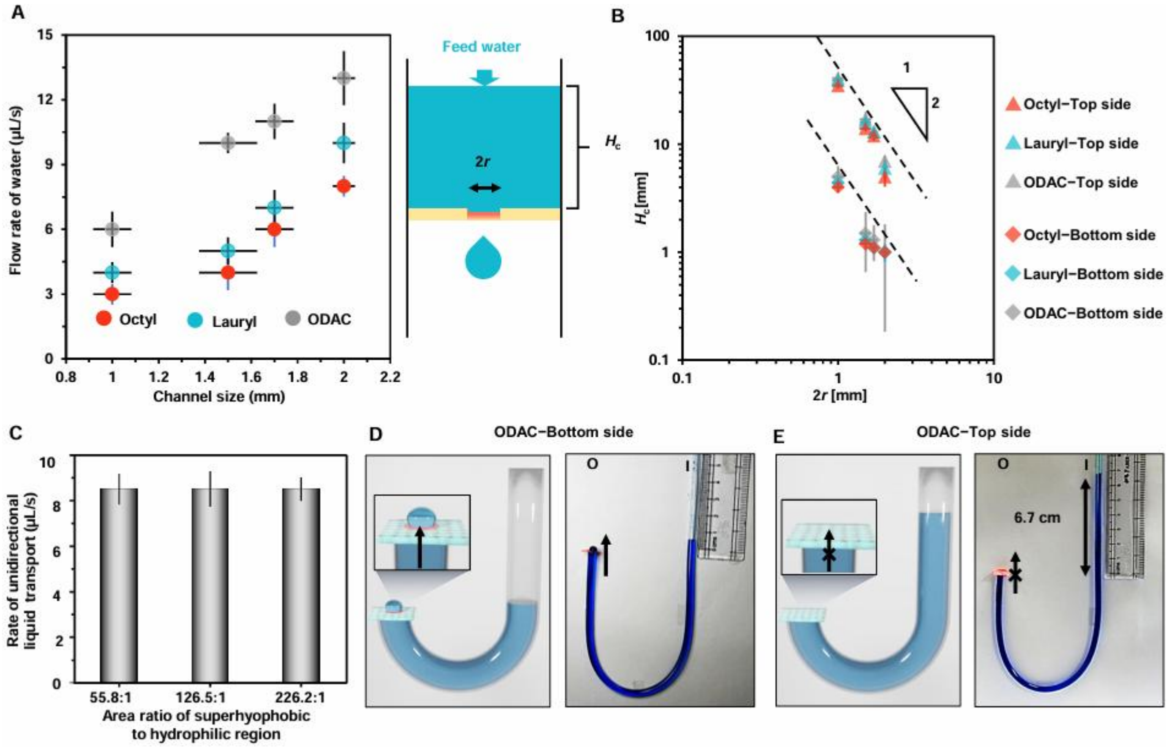

Figure 4.10 A) Plot illustrating the change in water flow rate with a variation of channel dimensions and chemical modification in the background. B) The plot accounting for the change in water penetration resistance on the variation of the dimension of channels and chemical modifications at the background of the channel, and the scheme displays the experimental setup. C) Accounting for the influence of the change in area ratio of superhydrophobic to hydrophilic region on the prepared pattern surface's top surface on the water's anti-gravity flow rate. D, E) Depicting the patterned textile as a “liquid diode”, where one end of the intravenous transfusion tube was covered with patterned textile, keeping the patterning spot inverted. The penetration of water was noticed from the back side when the water level on the other side of the tube was slightly elevated (D); however, such transportation of water was not observed even though the difference in the water columns on the left and right side of the tube was kept at 6.7 cm as the patterned textile was kept inverted to exposed the patterning side toward the interior of the tube (E). Results are presented as mean ± SD, where sample size, n = 3.

It is worth mentioning that the change in a relative area between superhydrophobic to hydrophilic regions on the top surface of the prepared pattern barely affects the anti-gravity flow rate of water, as shown in Figure 4.10C. Thereafter, prepared pattern textile was utilized as a ‘liquid diode’, where readily penetration of water was noticed in a single direction of the patterned textile as shown in Figure 4.10D, i.e., from back-spot to top-spot. However, the flow of water in the reverse direction was completely restricted even at relatively high pressure created by a water column of 6.7 cm in a commercially available intravenous transfusion tube, as depicted in Figure 4.10E. Often, the venous pressure in the body leads to uncontrolled blood backflow into the infusion tube, which causes blood clots and other related unwanted medical complications. Such a 'liquid diode' would be useful in achieving a unidirectional and intravenous delivery of nutrition and medications without causing backflow of blood during and after the intravenous transfusion process. The inherently high breakthrough pressure on the top-spot of the patterned textile would be capable of avoiding backflow of blood during such medical procedures. Moreover, this 'liquid-diode' would be further utilized in the guided transport of liquid following an anti-gravitational pathway.

4.3.4. Durability and Performance of Patterned Coating

The prospective application of such patterned textiles in outdoor conditions is only possible if they remain tolerant to various abrasive physical and chemical exposures. In this context, widely accepted and standard physical abrasion tests were adopted to examine the stability of the embedded superhydrophobicity of the coated textile.[42] First, the superhydrophobic textile was subjected to tensile deformation with 125% repetitive strain for 1000 cycles without compromising the embedded extreme water repellence (Figure 4.11A). Thereafter, an abrasive sandpaper (400 grit (1 × 2 cm)) was rubbed with back-and-forth motion on the coated textile with an applied external pressure of 25 kPa, and water wettability was examined at regular intervals of abrasion distance. The coated textile remained superhydrophobic with a WCA of ≈150° even after incurring sandpaper abrasion at a distance of 5000 cm (Figure 4.11B). Thereafter, to examine the chemical durability of the embedded superhydrophobicity, the coated textile was separately exposed to different chemically complex conditions, including seawater, river water, surfactant contaminated water, and UV irradiation for 6 weeks, prior to examining the water wettability (Figure 4.11C). The treated textile continued to display extreme water repellence, likely due to covalent modification of the reactive coating with selected hydrocarbons (i.e., octadecylamine and ODAc) through robust β aminoester type linkage. The prepared coating remained efficient in tolerating various and relevant physical manipulations including bending, creasing, and twisting without compromising the embedded superhydrophobicity (Figure 4.11D-I). Next, the patterned textile was subjected to tensile deformation with 125% strain, prior to sequentially exposing water droplets on top-spot and then on the back-spot. While the beaded water droplet on the top-spot failed to filtrate through the patterned textile under gravity, the blue-colored water droplet readily transported from the back-spot to the top-spot against the gravity with and without the applied strain of 125% tensile deformation as depicted in Figure 4.11J-M.

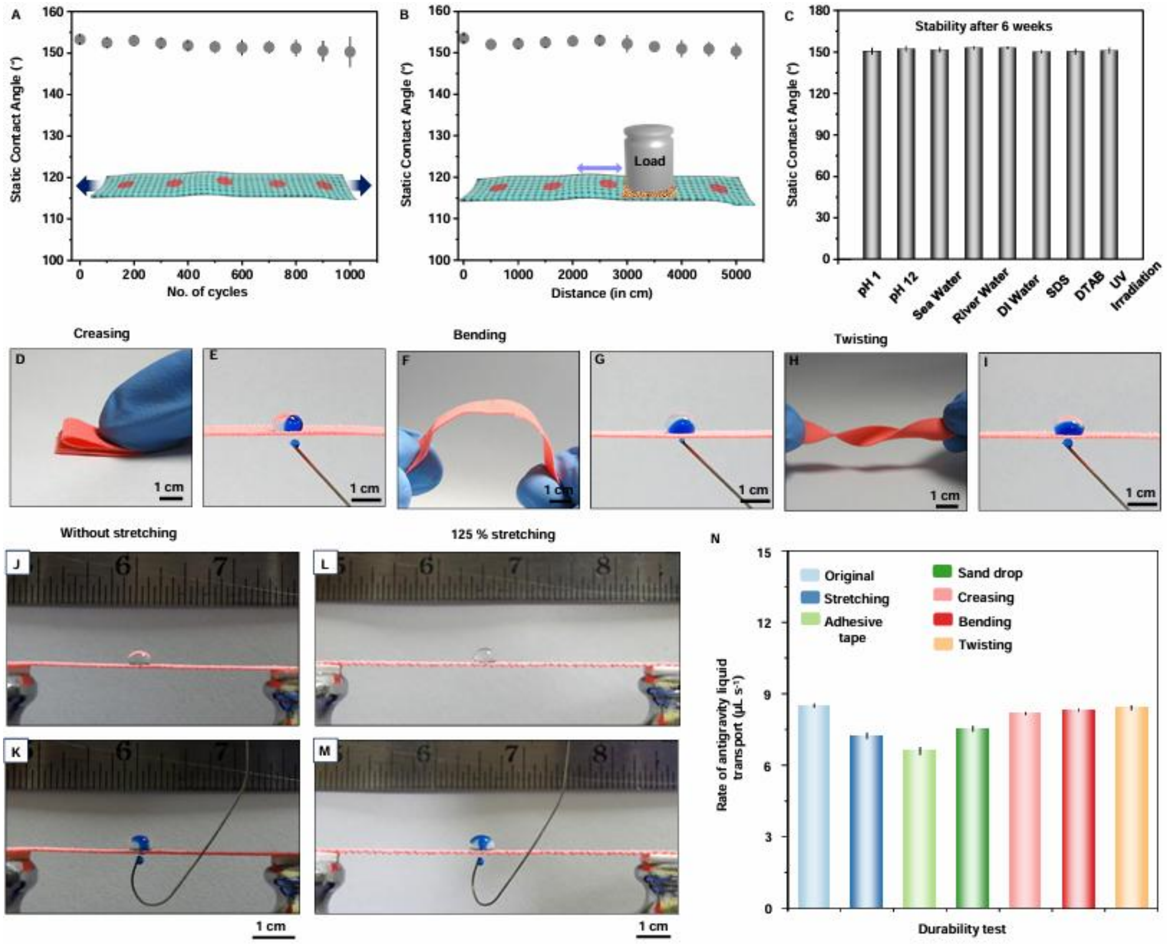

Figure 4.11 A, B) Plot illustrating the change in static contact angle of a beaded water droplet on patterned textiles after repetitive (1000 cycles) tensile deformation, (A) and sandpaper abrasion up to 5000 cm (B). C) Plots accounting the impact of practically relevant various harsh exposures on the patterned coating including highly acidic (pH 1) & alkaline (pH 12) media, artificial-sea water, river water, DI water, surfactant contaminated aqueous phase (SDS, DTAB; 2 mM) and UV irradiation (at λ_{max} = 254 and 365 nm) for 6 weeks. (D-I) Digital images depicting the various physical manipulations and anti-gravity transfer of water, including creasing (D, E), bending (F, G) and twisting (H, I) on the patterned coating. (J-M) Digital images illustrating the unidirectional and anti-gravity transport of water through the patterned textile in the absence (J, K) and presence (L, M) of 125% tensile deformation. (N) Plot accounting for the rate of anti-gravity transport of water through patterned textiles after performing different types of physical abrasion tests. Results are presented as mean ± SD, where sample size, n = 3.

Moreover, the ability to unidirectionally transport beaded water on the patterned textile remained unaffected even after performing the adhesive tape peeling and sand drop tests. While in a standard adhesive tape peeling test, a freshly exposed adhesive tape was applied on the patterned textile with an external load of 1 kg and peeled off; 300 g of sand was dropped on the prepared material from a distance of 40 cm prior to demonstrating the unidirectional transport of water droplet as depicted in Figure 4.11N. The anti-gravity flow rate of the water across the patterned textile that was subjected to various physical abrasions or manipulations remained nearly unperturbed only except for patterned textiles that were exposed to adhesive tape peeling test or tensile deformations (Figure 4.11N).

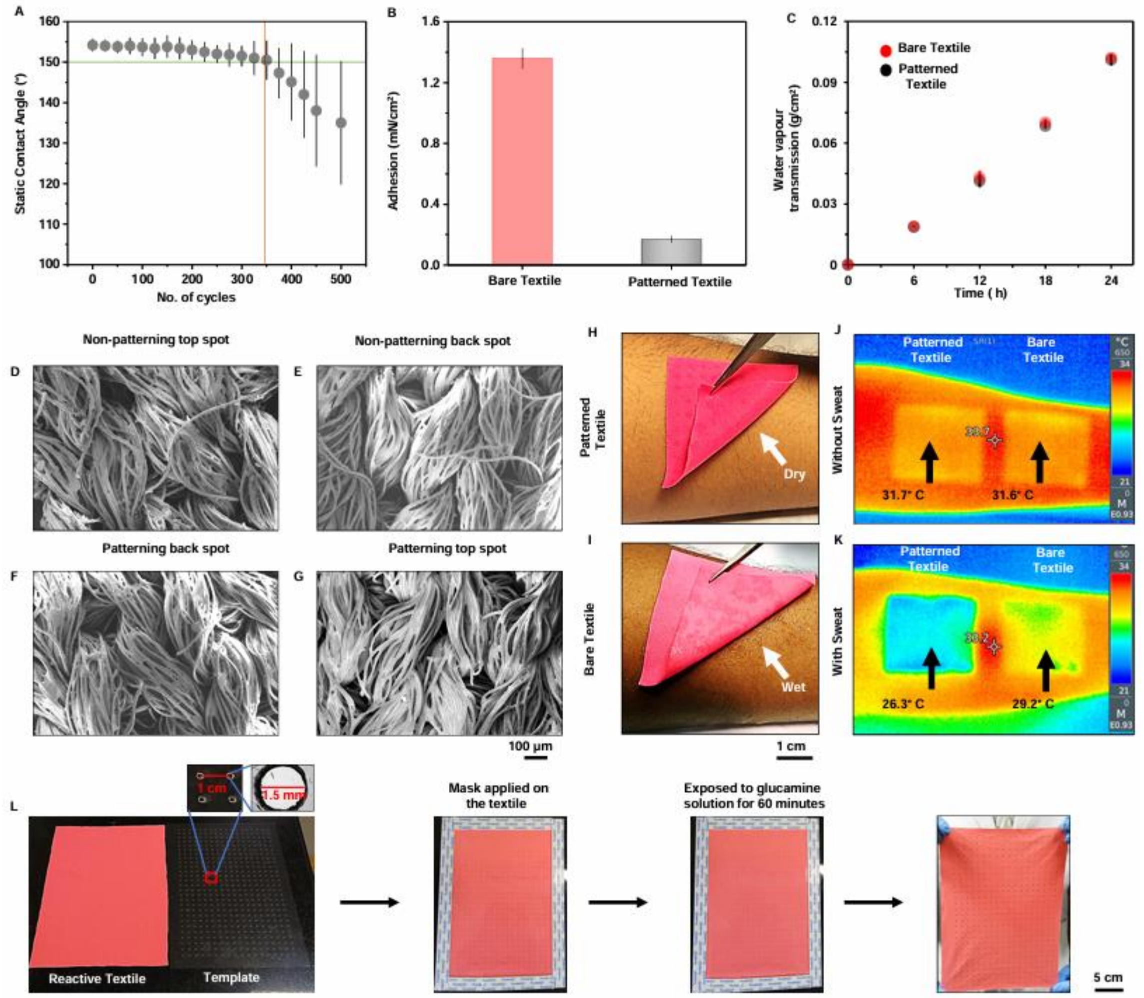

Figure 4.12 A) Plot illustrating the change in static contact angle of a beaded water droplet on patterned textiles after repetitive (500 cycles) washing (red; the red dotted line referring to the limit of performance, i.e., 350 cycles). B) Adhesion forces of bare and patterned textiles on wet surfaces. C) Accounting water vapor transmission rates through the bare and patterned textiles. D-G) Field emission scanning electron microscope (FESEM) of coated textile at non-patterning top spot (D), non-patterning back spot (E), patterning back spot (F), and patterning top spot (G). H, I) Digital images depict artificial sweat transport by H) patterned and I) bare textiles. J, K) Infrared camera images of the patterned and bare textiles applied on the skin in artificial sweat's J) absence and K) presence, recorded outdoors at a surrounding temperature of 40 °C. L) Accounting the process of large-scale fabrication of patterned textile following spatially selected chemical modification at ambient conditions, where an acrylic sheet with an array of holes (diameter of 1.5 mm) with a spacing of 1 cm was applied on the reactive textile as a mask, prior to poured the aqueous solution of glucamine on top of the mask. The spatially selective chemical modification provided patterned textile at ambient conditions.

In such scenarios, the porosity and arrangement of fiber in the patterned textile are expected to be altered, which is likely to contribute to a slight depletion of the flow rate of transferred water. The embedded superhydrophobicity of the fabric remained unperturbed even after undergoing the standard washing test for 350 cycles (Figure 4.12A). The above results are attributed to the durability of the patterned interface, which makes it more appropriate for its realistic application. In general, a wet native textile is found to be sticky on wet skin. Hence, the force of adhesion of patterned textile was estimated and compared with respect to native textile under identical experimental conditions using a force tensiometer. In this context, both patterned and bare textiles were individually and similarly brought in contact with the wet interface, and the force of adhesion was measured to detach bare and patterned textiles from the wet surface. The force of adhesion of the patterned textile is observed to be approximately eight times less than that of the native textile, as shown in Figure 4.12B. The depleted force of adhesion of the patterned textile certainly indicates the existence of non-sticky features in wet conditions, because of the unidirectional transport of water, which provided a dry interface. Next, another important property, i.e., the breathability of textile, which helps to maintain health and hygiene of the skin, was examined by studying the water vapor transmission rate (WVTR) as shown in Figure 4.12C. The WVTR of the patterned textile remained very similar to the native fibrous substrates, as the deposition of reactive coating is less likely to affect the inherent pores of the fibrous substrate, as revealed from the microscopic images (Figure 4 .12D-G). Thereafter, the water elimination performance by the patterned interface was demonstrated directly on the skin of a volunteer, prewetted with artificial sweat, prior to exposing the back side of the prepared pattern-textile. The Janus channel of the patterned textile ensured the unidirectional transport of artificial sweat from the skin of a volunteer, as depicted in Figure 4.12H. Thus, the moist skin turned dry. On the contrary, bare textile failed to display such unidirectional and anti-gravity transport of artificial sweat; rather, some traces of artificial sweat remained even after the similar exposure of bare textile to the pre-wetted (with artificial sweat) skin, as demonstrated in Figure 4.12I. Thereafter, both bare and patterned textiles were placed on the prewetted skin of a volunteer, prior to recording the body surface temperature using an infrared camera. The temperature difference was noticed to be 4.2 $^{\circ}$C. The ability of unidirectional transport of artificial sweat resulted in better cooling (31.5 vs 35.7 $^{\circ}$C) of the patterned textile in comparison to bare textile, where the temperature of skin was recorded to be 36.9 $^{\circ}$C. This is likely due to faster evaporation of ejected artificial sweat by the patterned textile (Figure 4.12J), which is not possible to achieve with bare textile. However, such efficient cooling was not observed in the absence of artificial sweat, and barely any temperature difference was noticed between bare and patterned textiles (Figure 4.12K) and body temperature remained nearly similar, i.e., ≈37.1 $^{\circ}$C. After that, I fabricated a large-scale pattern fabric with a dimension of A4 size printing paper (29.7 × 21 cm) in the laboratory without demanding any equipment, following the same principle of spatially selective chemical modification. In this context, a plastic mask with holes of specific dimensions (diameter of 1.5 mm) and arrangements (spacing of 1 cm) was placed on top of the chemically reactive superhydrophobic fabric before exposing it to glucamine solution, as depicted in Figure 4.12L (Supporting Information). The holes in the plastic mask allowed for spatially selective exposure of glucamine solution to chemically reactive superhydrophobic coating, enabling post-covalent modification at ambient conditions. Consequently, I derived a well-ordered patterned fabric of a dimension of A4-sized printing paper (29.7 × 21 cm), as shown in Figure 4.12L. Next, to demonstrate the versatility of the current coating and patterning approach, various other fibrous substrates- including lycra, polyester, cotton, and wool were successfully coated following the same approach to attain a superhydrophobic state, maintaining residual chemical reactivity (Figure 4.13A).

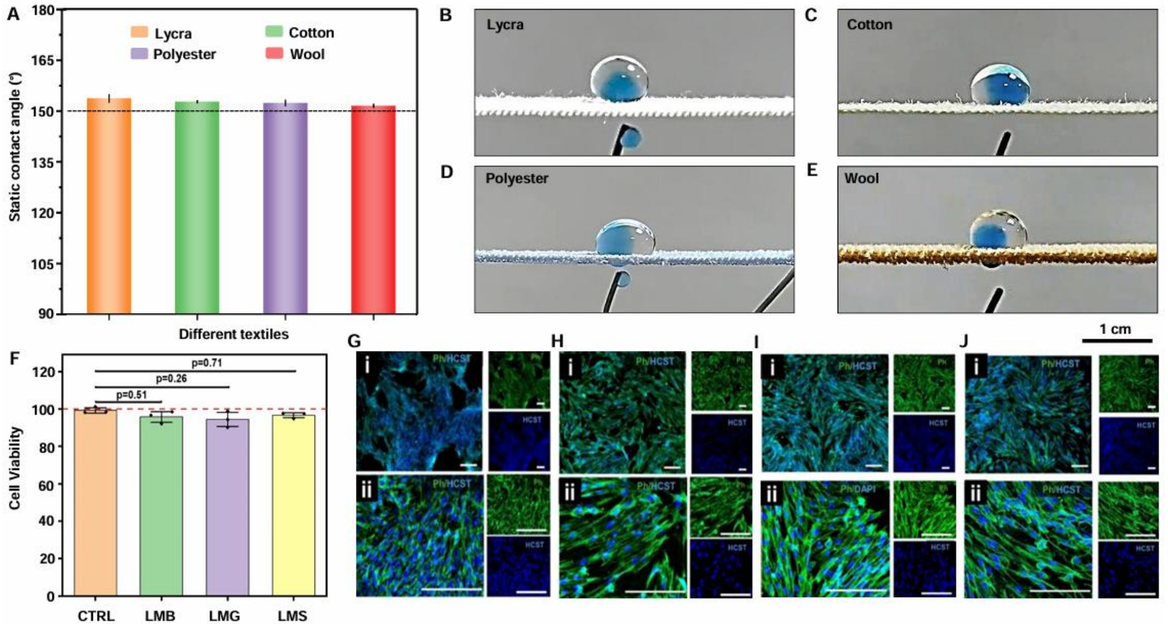

Figure 4.13 A) Illustrates the fabrication of water repellent coating on different textiles. B-E) Illustrating the unidirectional water transport ability of the patterned interfaces developed on various fibrous substrates, including B) lycra, C) cotton, D) polyester, and E) wool. F) Cell viability assessment of HDFs treated with leachate medium (LMB: leachate medium of bare fabric, LMS: leachate medium of patterned superhydrophobic fabric and LMG: leachate medium of glucamine modified fabric) from various fabric groups plotted as percentage after normalization with the viability of untreated HDFs after 48 h. Red dotted line marks 100% viability, CTRL denotes TCP control. G-J) Representative micrographs of phalloidin-488 (green) and hoechst-33342 (blue) staining of (G) untreated, (H) bare fabric LM treated, (I) patterned fabric LM treated and (J) glucamine modified fabric LM treated cells after 48 h. Micrographs were taken at (i) lower (5x) magnification and (ii) higher (20x) magnification, Ph: phalloidin-488, HCST: Hoechst 33342. Scale bar: 200μm.

Further, spatially selective chemical modification provided patterns on such reactive superhydrophobic coating deposited on various fibrous substrates to depict the anti-gravity transfer of water as shown in Figure 4.13B-E. Thus, our current approach of direct chemical modulation provided a general basis to develop Janus patterned coating, irrespective of the nature of the selected textile. Finally, the cell viability study was performed on pattern fabric, and the result was compared with respect to the bare, glucamine-modified fabric and tissue culture plate (TCP). The selected textiles of dimension 4.5 × 4.5 cm were incubated in a cell culture medium for 24 h prior to performing MTT assessment on human dermal fibroblast (HDF) cells. The study revealed a minimal change in the cellular viability between the various fabric leachate mediums (LM) and positive control (i.e., TCP) after 48 h (Figure 4.13F). Moreover, morphologies of the seeded HDFs were observed using the phalloidin-hoechst 33342 staining after 48 h of treatment with LM from various fabric groups and compared with the untreated control and representative micrographs have been shown in Figure 4.13G-J. The cellular morphologies of HDFs treated with LM from bare fabric (Figure 4.13H), patterned fabric (Figure 4.13I), and glucamine-treated fabric (Figure 4.13J) demonstrated minimal deviations from the cellular morphology observed for untreated HDFs (Figure 4.13G). Thus, the prepared pattern textiles remained compatible with potential interaction and/or exposure to skin tissue. Further, the ability of prepared patterned textile in fast removal of aqueous phase against gravity is likely to be useful in relevant bio-medical applications, including wound healing, where the prepared patterned textile would help in keeping the wound dry and clean by removing the excess biofluid from the site of the wound.

4.4. Conclusion

In summary, the current approach of preparing a chemically reactive superhydrophobic coating on the fibrous substrate provided a facile basis to develop Janus patterns of chemically modulated wettability with an extremely water-repellent background through spatially selective 1,4-conjugate addition reaction with hydrophilic small molecules, i.e., glucamine. The prepared Janus pattern remained efficient for anti-gravity transporting the water droplets, with a record high flow rate with respect to the relevant reported literature. The fast flow of liquid is attributed to the favorable pinning and depinning mechanism of invaded water through such chemically decorated patterns on selected fibrous substrates. Further, rational choice of other hydrophilic small molecules is likely to provide a scope to improve the versatility and functionality of such pattern interfaces. In contrast to the reported Janus textile, the design of Janus patterns on a superhydrophobic background prevents the flooding of the top surface of the patterned textile; rather, transported water rolled off easily on the tilted interface because of the embedded low frictional force. The prepared Janus pattern of wettability with the ability of unidirectional anti-gravity transfer of tiny and relevant aqueous droplets across the fibrous substrates demonstrated efficient ejection of artificial sweat and management of temperature. Further, the fast and unidirectional anti-gravity flow of liquid with high breakthrough pressure would be useful in achieving accelerated wound healing, developing a liquid diode, etc. Importantly, the prepared Janus pattern remained efficient in tolerating exposure to various and severe physical (i.e., physical manipulations, tensile deformation, adhesive tape peeling, sandpaper abrasion) and chemical exposures (e.g., seawater, river water, UV light, repetitive washing, etc.). Furthermore, the current approach of depositing reactive superhydrophobic coating and followed by spatially selective chemical patterning through 1,4-conjugate addition reaction with primary amine containing small molecules at ambient conditions can be successfully applied to various types of textiles. The current design is not restricted to a specific type of textile; hence, it would be more appropriate for multiple prospective applications in diverse and realistic conditions.

4.5. References

1 J. Ju, H. Bai, Y. Zheng, T. Zhao, R. Fang and L. Jiang, *Nat. Commun.*, 2012, **3**, 1247.

2 S. Zhang, M. Chi, J. Mo, T. Liu, Y. Liu, Q. Fu, J. Wang, B. Luo, Y. Qin, S. Wang and S. Nie, *Nat Commun.*, 2022, **13**, 4168.

3 Y. Zheng, H. Bai, Z. Huang, X. Tian, Fu-Q. Nie, Y. Zhao, J. Zhai and L. Jiang, *Nature*, 2010, **463**, 640-643.

4 J. Chen, A. Tsuchida, A. D. Malay, K. Tsuchiya, H. Masunaga, Y. Tsuji, M. Kuzumoto, K. Urayama, H. Shintaku and K. Numata, *Nat. Commun.*, 2024, **15**, 527.

5 M. Prakash, D. Quere and J. W. M. Bush, *Science*, 2008, **320**, 931-934.

6 S. Martin and B. Bhushan, *Phil. Trans. R. Soc. A.*, 2016, **374**, *20160134*.

7 TS. Wong, S. H. Kang, S. K. Y. Tang, E. J. Smythe, B. D. Hatton, A. Grinthal and J. Aizenberg, *Nature*, 2011, **477**, 443-447.

8 S. Anand, A. T. Paxson, R. Dhiman, J. D. Smith and K. K. Varanasi, *ACS Nano*, 2012, **6**, 10122-10129.

9 H. Chen, P. Zhang, L. Zhang, H. Liu, Y. Jiang, D. Zhang, Z. Han and L. Jiang, *Nature* 2016, **532**, 85-89.

10 X. Dai, N. Sun, S. O. Nielsen, B. B. Stogin, J. Wang, S. Yang and T.-S. Wong, *Sci. Adv.* 2018, **4**, eaaq0919.

11 H. Bai, X. Wang, Z. Li, H. Wen, Y. Yang, M. Li and M. Cao, *Adv. Mater.*, 2023, **35**, 2211596.

12 Z. Liu, Z. Zhan, T. Shen, N. Li, C. Zhang, C. Yu, C. Li, Y. Si, L. Jiang and Z. Dong, *Nat. Commun.*, 2023, **14**, 4128.

13 C. Yang, M. Long, C. Ding, R. Zhang, S. Zhang, J. Yuan, K. Zhi, Z. Yin, Y. Zheng, Y. Liu, H. Wu and Z. Jiang, *Nat. Commun.*, 2022, **13**, 7334.

14 D. Wakerley, S. Lamaison, F. Ozanam, N. Menguy, D. Mercier, P. Marcus, M. Fontecave and V. Mougel, *Nat. Mater.,* 2022, **13**, 7334.

15 T.-H. Shen, L. Spillane and J. Peng, *Nat. Catal*, 2022, **5**, 30-36.

16 L. Lao, D. Shou, Y. S. Wu and J. T. Fan, *Sci. Adv.*, 2020, **6**, eaaz0013.

17 Y. Peng, W. Li, B. Liu, W. Jin, J. Schaadt, J. Tang, G. Zhou, G. Wang, J. Zhou, C. Zhang, Y. Zhu, W. Huang, T. Wu, K. E. Goodson, C. Dames, R. Prasher, S. Fan and Y. Cui, *Nat. Commun.*, 2021, **12**, 6122.

18 A. Ainla, M. M. Hamedi, F. Güder and G. M. Whitesides, *Adv. Mater.*, 2017, **29**, 1702894.

19 Z. Zhao, Y. Ning, S. Ben, X. Zhang, Q. Li, C. Yu, X. Jin, K. Liu and L. Jiang, *Adv. Sci.* 2022, **9**, 2103765.

20 B. Dai, K. Li, L. Shi, X. Wan, X. Liu, F. Zhang, L. Jiang and S. Wang, *Adv. Mater.,* 2019, **31**, 1904113.

21 F. Li, S. Wang, Z. Wang, K. Jiang, X. Zhao, L. Shao and Y. Pan, *Adv. Funct. Mater.*, 2023, **33**, 2210769.

22 Y. Lin, N. Cheng, N. Meng, C. Wang, X. Wang, J. Yu and B. Ding, *Adv. Funct. Mater.*, 2023, **33**, 2304109.

23 Y. Peng, J. Zhou, Y. Yang, J.-C. Lai, Y. Ye and Y. Cui, *Adv. Mater.*, 2022, **34**, 2204168.

24 W. Zhou, S. Min, T. Zhan, Y. Zhang, D. Pan, Y. Yuan and B. Xu, *Small,* 2023, **19**, 2302512.

25 W. Shi, H. Bai, M. Cao, X. Wang, Y. Ning, Z. Li, K. Liu and L. Jiang, *Adv. Sci.*, 2023, **10**, 2301421.

26 Y. Wang, X. Liang, H. Zhu, J. H. Xin, Q. Zhang and S. Zhu, *Adv. Funct. Mater.*, 2020, **30**, 1907851.

27 Y. Wang, G. Xia, H. Yu, B. Qian, Y. H. Cheung, L. H. Wong and J. H. Xin, *Adv. Mater.*, 2021, **33**, 2100140.

28 B. Gu, Q. Xu, H. Wang, H. Pan and D. Zhao, *ACS Nano*, 2023, **17**, 18308-18317.

29 W. Fan, G. Zhang, X. Zhang, K. Dong, X. Liang, W. Chen, L. Yu, and Y. Zhang, *Small*, 2022, **18**, 2107150.

30 H. Murota, K. Yamaga, E. Ono, N. Murayama, H. Yokozeki, and I. Katayama, *Exp Dermatol.*, 2019, **28** 1416-1421.

31 J. Fan and Y. S. Chen, *Meas. Sci. Technol.*, 2002, **13**, 1115-1123.

32 D. J. Gohlke and J. C. Tanner, *J. Coated Fabrics*, 1976, **6**, 28-38.

33 A. Mukhopadhyay and V. K. Midha, *J. Ind. Text.*, 2008, **38**, 17-41.

34 S. Morang, A. Bandyopadhyay, N. Borah, A. Kar, B.B. Mandal and N. Karak, *ACS Appl. Bio Mater.*, 2024, **7**, 1910-1924.

35 S. Morang, A. Bandyopadhyay, B.B. Mandal and N. Karak, *ACS Appl. Bio Mater.*, 2023, **6**, 2771-2784.

36 S. Morang, A. Bandyopadhyay, J.H. Rajput, B.B. Mandal, A. Poundarik and N. Karak, *ACS Appl. Polym. Mater.*, 2023, **5**, 8518-8532.

37 A. Borbora, R. L. Dupont, Y. Xu, X. Wang and U. Manna, *Mater. Horiz.*, 2022, **9**, 991-1001.

38 M. Dhar, U. I. Kara, S. Das, Y. Xu, S. Mandal, R. L. Dupont, E. C. Boerner, B. Y. Chen, Y. X. Yao, X. G. Wang and U. Manna, *Mater. Horiz.*, 2023, **10**, 2204-2214.

39 P.-G. de Gennes, F. Brochard-Wyart and D. Quéré, in *Capillarity and Wetting Phenomena: Drops, Bubbles, Pearls, Waves* (Eds: P.-G. Gennes, F. Brochard-Wyart, D. Quéré), Springer, New York, 2004, p. 153-190.

40 G. Zhang, M. A. Quetzeri-Santiago, C. A. Stone, L. Botto and J. R. Castrejón-Pita, *Soft Matter*, 2018, **14**, 8182-8190.

41 A. Tuteja, W. Choi, J. M. Mabry, G. H. McKinley and R. E. Cohen, *Proc. Natl. Acad. Sci. USA*, 2008, **105**, 18200.

42 X. Tian, T. Verho and R. H. A. Ras, *Science*, 2016, **352**, 142.

Chapter 5: Amidation Reaction to Derive Waterborne, Tolerant, and Optically Transparent Solid Slippery and Superhydrophobic Coatings

Separate and lubrication-free association of low surface energy with hierarchically featured and highly smooth interfaces yields two distinct and prospective bio-inspired wettability superhydrophobicity and solid slippery properties, respectively. However, the derivation of such bio-inspired wettability with high optical transparency, following a simple, completely waterborne, non-fluorinated and scalable fabrication approach is an extremely challenging task to achieve. Here, a simple amidation reaction between thioester and amine groups is rationally extended for aqueous processing of strategically selected small molecules to attain desired outputs through the formation of nanoparticles. An aqueous reaction mixture of selected non-fluorinated small molecules provided a stable (for 30 days) dispersion of nanoparticles (size ~ 210 nm). While the 'in-situ' deposition of the reaction mixture yielded completely waterborne, optically transparent, physically and chemically durable, lubrication-free solid slippery coating on a planar substrate, a highly deformable superhydrophobic coating on porous and fibrous substrates was obtained following a rapid and facile post-deposition of the prepared nanoparticles. The prepared solid slippery coating remained efficient in sliding the beaded droplets of various (e.g., polar and non-polar) liquids having a wide range (70.2 mN/m to 22.3 mN/m) of surface tension. The synthesized superhydrophobic coating on porous and fibrous substrates remained efficient in sustaining repetitive and large physical deformations and other relevant abrasive exposures.

S. Kumar, M. dhar, B. M. Prusty, D. Sarkar, A. Das, D. Manna and U. Manna, *Chemical Engineering Journal*, 2023, **465**, 142776.

5.1. Introduction

Bio-inspired hierarchically rough superhydrophobic interface and the ultra-smooth slippery surface are widely recognized for extreme water repellence and effortless sliding of beaded liquids (polar/nonpolar organic solvents and water), respectively.[1-12] Such bio-inspired wettability has emerged as an elegant basis to develop various prospective materials for relevant applications in health, energy and environmental pollution. [1-12] In the past, distinct approaches were adopted to individually achieve the hierarchically featured and ultra-smooth interfaces optimized with appropriate low surface energy moieties (long hydrocarbon tails or their fluorinated analogues) for conferring superhydrophobicity and lubrication-free solid slippery properties, respectively.[13-32] As the requirements for deriving these two bio-inspired wettability are completely distinct, the adaptation of a common synthetic strategy remains extremely challenging.[13-32] Hence, further design is essential to derive both hierarchically featured and lubrication-free ultrasmooth coatings following a common synthetic procedure.

In the past, mainly two distinct approaches were adopted to develop ultrasmooth solid slippery coating; where a) either a porous and featured coating are lubricated with polymers, and paraffin.[20,28,30-31] or b) PDMS brushes and flexible polymers are grown or attached on the glass substrate to prepare quasi solid slippery coatings.[13,17,25] Very recently, Tiwari and co-workers derived a solid slippery coating from small molecules, where a layer-by-layer construction of metal−organic frameworks was developed on a modified glass substrate through a repetitive and laborious reaction between metal ions and ligands using an organic solvent (e.g., dimethyl formamide) at an elevated temperature (120°) for achieve lubrication-free solid slippery coating with high optical transparency.[26] Even after significant progress in this relevant research topic, a few designs remained successful in providing durable lubrication-free bio-inspired coatings, where mostly different polymers and nanomaterials were strategically associated. But, such earlier reported approaches suffer from either the complex fabrication process and (or) associated with the uses of environmentally hazardous fluorinated components and volatile organic solvents, etc.[13-35] In contrast to conventional liquid infused slippery interface, a few approaches on designing the quasi-liquid slippery surfaces were introduced adopting solvent-free deposition process.[17,36-37] However, reports of waterborne solid slippery interface are extremely rare due to the difficulty in bringing the low surface energy agent in the aqueous phase for co-optimization of essential topography and low surface energy. Here, I introduced thioesters to achieve a water-borne solid slippery coating and physically deformable superhydrophobic coatings.

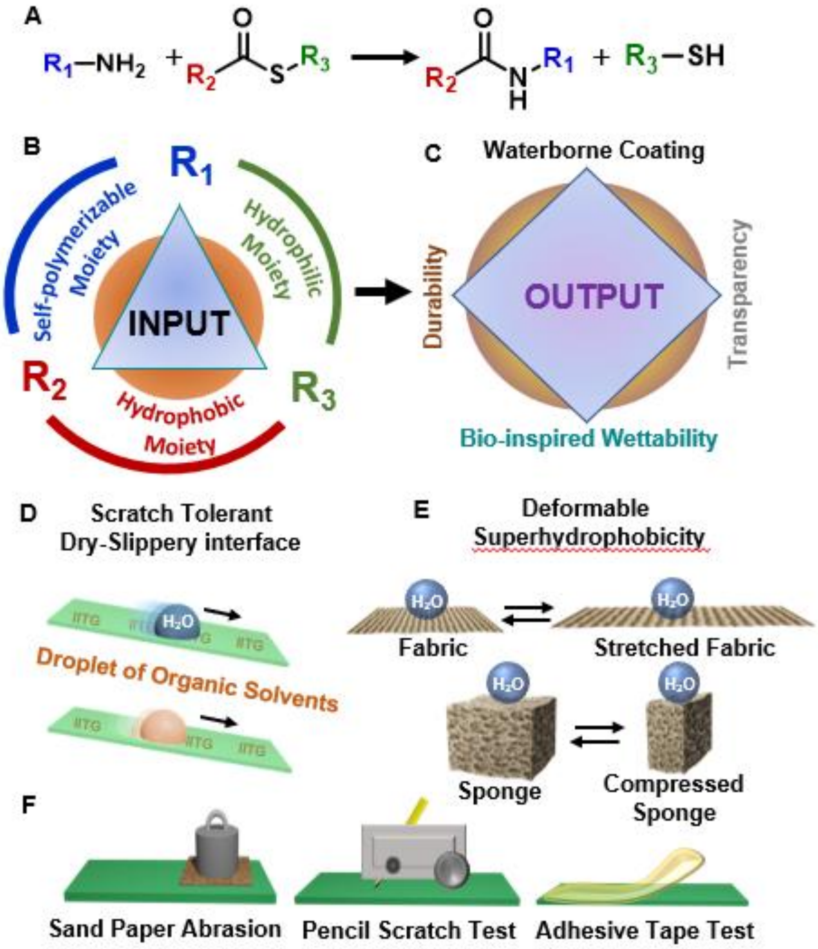

Figure 5.1 A-C) Schematic presentation of the designing principle of 'Processor-Input-Output', where the aqueous processing of small molecules having strategically selected chemical 'inputs' (i.e. self-polymerizable, hydrophilic, and hydrophobic moieties) through an amidation reaction (processor) between amine and thioester groups provided desired 'outputs', including bio-inspired wettability, waterborne process, durable and optically transparent coating. D) Depicting the slippery behaviour of beaded droplets of different liquids on a prepared solid slippery coating. E) Illustrating the physical (tensile and compressive) deformations of fibrous and porous substrates that are embedded with superhydrophobic coating. F) Schematic presenting tolerance of prepared coating towards some relevant and widely accepted abrasive exposures.

In the recent past, strategically designed thioesters are successfully extended in developing various relevant functional materials for triggered releasing of DNA, preparing covalent adaptable networks, hydrogel assisted wound closure, reactive amphiphile, proto-peptide and so on.[39-46] Inspired from such strategic and successful applications of thioesters, in this report, unprecedentedly extended an inherently amine reactive thioester molecule [45] to report abrasion tolerant and optically transparent two distinct bio-inspired wettability, i.e., lubrication-free slippery and superhydrophobic coatings. This current synthetic approach involved a simple aqueous and covalent processing of appropriately selected chemical functional groups (hydrophilic, hydrophobic and self-polymerizable moieties) considered as important 'Inputs' through a mutual chemical reaction between primary amine and thioester groups to achieve desired 'Outputs' (i.e., waterborne coating with durability, transparency and bioinspired wettability), as shown in Figure 5.1A-C. In this waterborne chemical approach, the selectively reactive thioester group provided a simple way to integrate both the hydrophobic and polymerizable moieties on releasing the hydrophilic moiety during the amide bond formation process. Eventually, this chemical approach allowed to prepare a stable dispersion of nanoparticle for co-optimization of essential topography and chemistry to confer both slippery property and superhydrophobicity, where the choice of substrates (fibrous/porous or flat/featureless interfaces) played an important role for associating the desired liquid wettability, as shown in Figure 5.1D, E. The prepared waterborne, optically transparent (~ 88 %) coatings embedded with bio-inspired wettability remained highly tolerant in various challenging and abrasive conditions, as shown in Figure 5.1F. The lubrication-free slippery coating remained efficient in sliding beaded droplets of various polar and non-polar solvents having a wide range of surface tension (22.3 mN/m to 70.2 mN/m) and successfully sustained pencil (applied load of 1 kg) hardness test, knife scratch test, sandpaper abrasion test, exposure of boiling water, extremes of pH, seawater, etc. without having any noticeable physical damages and any change in slippery property. Moreover, the prepared superhydrophobic coating on selected fibrous and porous substrates remained highly efficient in tolerating repetitive (3000 and 2500 times) physical (compressive and tensile) deformations, sandpaper abrasion (of 3000 cm), adhesive tape peeling test (375 times) and complex and prolonged (30 days) aqueous (extremes of pH, sea water, river water etc.) exposures. Such waterborne, non-fluorinated and small molecules derived robust coating embedded with desired physical properties would likely open up various possibilities for various potential and relevant applications.

5.2. Experimental Section

5.2.1. Materials Required

Stearic acid, 4-(dimethylamino)pyridine (DMAP), 1-(3-dimethylaminopropyl)3-ethylcarbodiimide hydrochloride (EDC), sodium 3-mercapto-1-propanesulfonate, (3-aminopropyl)triethoxysilane, triton x-114, diiodomethane, and Nile red were purchased from Sigma Aldrich (Bangalore, India). DCM, CH_3CN, o-xylene, and toluene were purchased from Alfa-Aesar, India. Polyurethane fabric was procured from Amazon India. The average pore size of polyurethane is approximately 50 µm, as measured using ImageJ software on FESEM images of a selected polyurethane fabric. The plane weave of selected polyurethane fabric is twill patterned (112 g m^{-2}), and the thickness of the selected fabric is ~285 mm. The selected melamine sponge, having a density of 7.5 kg/m^3, was purchased from AR Acoustics LLP, Maharashtra. Adhesive tape, sand paper, knife, wool fabric, polyester fabric, cotton fabric, lycra fabric, and jute fabric were procured from a local shop in Guwahati city (Assam, India). Permanent marker (Luxor OHP/CD/DVD) ink was procured from Amazon India. The details of the remaining other chemicals used in this work were discussed previously in section 2.2.1 of chapter 2.

5.2.2. Charecterization

The ^{13}C NMR were recorded at 600 MHz and 151 MHz with Varian AS400 spectrometer and Brucker spectrometer respectively. High-resolution mass spectra (HRMS) were recorded at Agilent Q-TOF mass spectrometer with a Z-spray source using built-in software for analysis of the recorded data. Thermal stability was checked by Autoclave Selfa (model no- 7431SELFA). The remaining other instruments used in this chapter for characterization of synthesized materials were the same as discussed previously in section 2.2.2 of chapter 2.

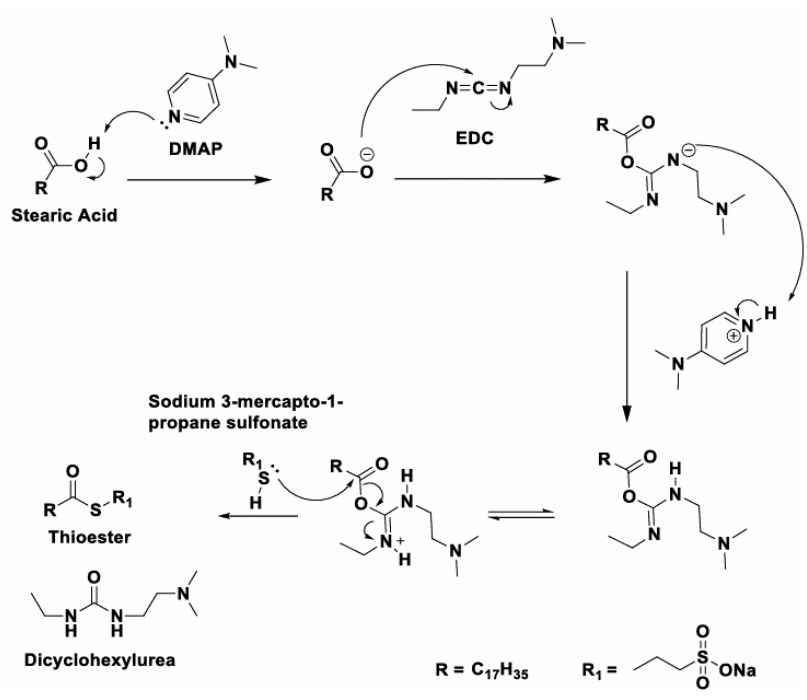

Figure 5.2 Plausible reaction mechanism for the synthesis of 3-(steartoylthio)propane-1-sulfonate.

5.2.3. Procedure for the Synthesis of Alkyl Thioesters

In order to prepare the desired thioester, following reactants, i.e. 4-(dimethylamino) pyridine (DMAP, 0.1 mmol) and 1-(3-dimethylaminopropyl)3-ethylcarbodiimide hydrochloride (EDC) (1 mmol) were successively added into a stirring solution of stearic acid (1 mmol) in CH_2Cl_2

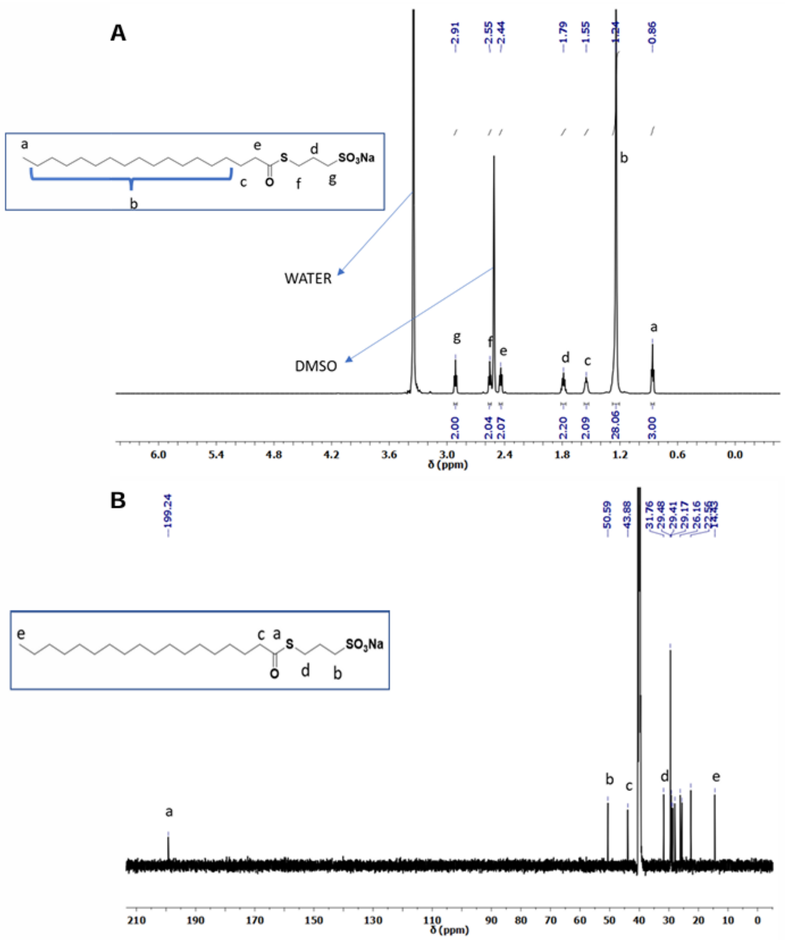

Figure 5.3 A, B) ^{1}H NMR (A) and ^{13}C NMR (B) spectra of 3-(steartoylthio)propane-1-sulfonate.

(5 mL). Entire reaction mixture was kept under stirring condition for 10 minutes at room temperature. Thereafter, sodium-3-mercaptopropanesulfonate (1 mmol) was added to the reaction mixture. The reaction mixture was stirred for 5 h at room temperature. Next, brine solution was added into the reaction mixture and the organic phase was extracted with ethyl acetate (3 × 20 mL). The collected residue was washed with CH_3CN (3 × 10 mL) and dried under reduced pressure to obtain thioester as a white solid compound with 75% yield. The roles of used chemicals are illustrated through reaction mechanism in Figure 5.2. The product was characterized by the ^{1}H NMR, ^{13}C NMR (Figure 5.3A, B) and HRMS (Figure 5.4) analyses. ^{1}H NMR (600 MHz, DMSO-d_6) δ_{ppm} 2.91 (t, $J = 6$ Hz, 2H), 2.55 (t, $J = 9$ Hz, 2H), 2.45 – 2.43 (m, 2H), 1.81 – 1.76 (m, 2H), 1.57 – 1.53 (m, 2H), 1.29 – 1.24 (m, 28H), 0.86 (t, $J = 6$ Hz, 3H). ^{13}C NMR (150 MHz, DMSO-d_6) δ_{ppm} 199.2, 50.6, 43.8, 31.7, 29.5, 29.4, 29.2, 29.1, 28.6, 27.9, 26.1, 25.5, 22.5, 14.4. HRMS (ESI) calcd. for $C_{21}H_{41}NaO_4S_2$ $[(M-Na)]^-$: 421.2446, found: 421.2446.

5.2.4. Fabrication of Transparent Solid Slippery Coating

At first, the glass slide was thoroughly rinsed with methanol and acetone to remove the dust molecules and then dried at room temperature. Further, this glass slide was placed in the aqueous reaction mixture of thioester (7.5 mM) and APTES (7.5 mM), kept at an elevated temperature of 80 °C for 8 h. During this course of experiment, a stable and milky dispersion of nanoparticles appeared (see main text for more details). Finally, the glass slide was thoroughly washed with methanol and H_2O. Even the coated substrate was sonicated for 5 minutes in DI-water to remove the unreacted reactants (if any) and dried at room temperature minutes to get a transparent solid slippery coating.

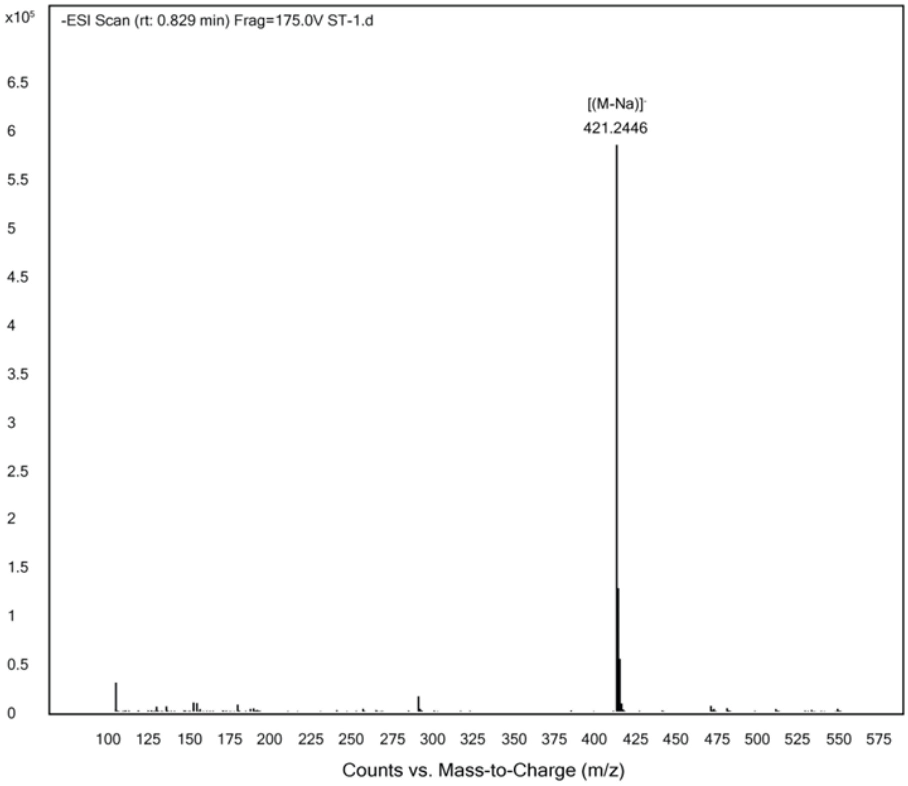

Figure 5.4 HRMS spectra of 3-(steartoylthio)propane-1-sulfonate.

5.2.5. Fabrication of Superhydrophobic Fabric and Sponge

Polyurethane (PU) fabric and melamine formaldehyde (MF) sponge were washed with acetone prior to deposit nanoparticles following dip coating process. A reaction mixture was prepared by mixing of thioester (7.5 mM) and APTES (7.5 mM) in DI-water, and then this solution was kept at 80 °C for 8 h to achieve stable dispersion of nanoparticles. Next, the selected substrates (i.e., polyurethane fabric and melamine sponge) were dipped into the reaction mixture and kept for 5 min. Thereafter, the selected substrate was brought out from the dipping solution and kept hanging in air for 1 min to remove excess deposition solution under gravity without incurring any manual deformation. Next, the sponge was kept for drying in an oven at 80 °C for 6 hours to obtain superhydrophobicity.

5.2.6. Chemical Durability Tests

The optically transparent slippery coating, superhydrophobic coatings on fibrous and spongy substrates were exposed to several harsh chemical exposures, such as artificial seawater (where $MgSO_4$ (0.325 g), $MgCl_2$ (0.226 g), NaCl (2.673 g), and $CaCl_2$ (0.112 g) were dissolved in 100 ml of deionized water), river water, deionized water, extremes of pH (1 and 12), surfactant (DTAB solution,1mM), (SDS solution (1 mM), Triton-X solution(1 mM)) contaminated aqueous phase and UV irradiation (254 nm and 365 nm) 15 days for slippery coating and 30 days for superhydrophobic coating. Thereafter, the sliding of beaded liquids and extreme water repellence were characterized by measuring the sliding angle, contact angle and contact angle hysteresis.

5.2.7. Physical Durability Tests

Various practically relevant and widely accepted physically abrasive exposures were applied on the prepared coatings to examine the durability of the associated liquid wettability. The details of each abrasive and challenging exposures are provided here;

5.2.7.1 Sand Paper Abrasion: An abrasive sandpaper 400 grit (1 cm × 2 cm) was individually applied on both the solid slippery coating and superhydrophobic coating by rubbing with back-and forth motion across the solid slippery and superhydrophobic coating with an applied pressure of 25 kPa. Both the slippery property and extreme water repellence were separately monitored at regular interval of the abrasion distance. While the slippery property of the solid slippery coating was investigated by measuring the sliding angle of beaded droplets of water and diiodomethane, the superhydrophobicity was examined by measuring the contact angle and contact angle hysteresis of beaded water droplet.

5.2.7.2 Pencil Hardness Test

A standard pencil hardness test was performed following a standard procedure (ASTM D 3363) in attempt to incur scratches on the prepared solid slippery coating using a pencil hardness tester (Amittari Instrument, AS-120P), where a 6H (hardest in available series of 6B-6H) pencil having 5 mm of exposed core was applied on the prepared slippery coating at 45° inclination with applied load of 1 kg. The average speed of the pencil tip movement was ~ 10 cm/s. Further, the slippery property of the coating was investigated by measuring the sliding angle with droplets of two distinct types of liquids, i.e., water (polar) and diiodomethane (non-polar).

5.2.7.3 Adhesive Tape Peeling Test

An adhesive tape was separately applied to the solid slippery coating and superhydrophobic coating with an external applied load of 500 g for 5 min. Then, the adhesive tape was removed from the surface of the coating by adopting the manual peeling process. This procedure was repeatedly applied on both solid slippery and superhydrophobic coatings. The slippery property of the coating was investigated by measuring the sliding angle of beaded droplets of water (polar) and diiodomethane (nonpolar) at regular intervals. On the other side, the water wettability of superhydrophobic coating was investigated by studying the water contact angle and contact angle hysteresis of beaded water droplet at regular intervals.

5.2.7.4 Knife Scratch Test

In this abrasive exposure, solid slippery and superhydrophobic coatings were randomly and manually exposed to a sharp metal knife for several times in attempt to incur physical damages. While, the superhydrophobic coated substrates were severely affected as evident from the visual inspection, no noticeable damages were observed for lubrication-free solid slippery coating.

5.2.7.5 Tensile Deformation Test

To perform this durability test, the superhydrophobic coating on stretchable fibrous substrate was repetitively subjected to a tensile strain up to 150% for 2500 cycles. On the other side, another superhydrophobic coating on spongy substrate was exposed to compressive deformation up to 70%, repetitively (3000 cycles). After that, the water contact angles and contact angle hysteresis were measured at different intervals for examining the impact of such physical deformations on the embedded wettability.

5.2.7.6 Laundering and Ironing Test

The durability against the repetitive washing was investigated by following a standard procedure (AATCC Test Method 61–2006 test No 2A), where the superhydrophobic coating on a fibrous substrate was laundered at 40 $^{\circ}$C for 45 min in the presence of 0.37 wt% SDS surfactant. This procedure was repeated for 200 times. The superhydrophobic fabric was repetitively ironed around 180 $^{\circ}$C for 275 times. The water wettability of the coated fabric was examined by measuring the contact angle at regular intervals.

5.2.7.7 Autoclave Test

In this abrasive test, a solid slippery coating was kept in autoclave condition (temperature of 120 $^{\circ}$C, pressure of 103.4 kPa) for 4 h. Further, the slippery property of the coating was investigated by measuring the sliding angle of two distinct liquids, i.e., water and diiodomethane.

5.2.7.8 Sand Drop Test

The sand drop test was conducted following a widely accepted procedure in the literature. Firstly, a solid slippery coated interface was kept at 45° tilting angle attached with a glass slide and then 250 g of sand grains were dropped from a distance of 40 cm. Further, slippery property was examined by measuring the sliding angle of water and diiodomethane solvent.

5.3. Results and Discussion

5.3.1. Design of Optically Transparent and Lubrication-free Solid Slippery Coating

In our design, two distinct bio-inspired coatings were directly derived from selected water-soluble and non-fluorinated small molecules, following a scalable and facile fabrication process. In this context, stearic acid and sodium 3-mercapto-1-propane-1-sulfonate were mutually reacted following an earlier reported protocol[41] for bringing a long hydrocarbon tail (responsible for providing essential low surface energy) in the aqueous phase. Its subsequent covalent reaction with another selected reactant in aqueous phase at ambient conditions allowed to form a stable dispersion of nanoparticles (NP). In this design, the heptadecyl group is linked to a highly water-compatible sulfonate moiety through a dynamic and selectively reactive thioester bond. The primary amine group of another selected small molecule readily reacted with thioester group to form an amide linkage, and simultaneously, the sulfonate moiety released in the deionized (DI) water at ambient conditions, as shown in Figure 5.1A and Figure 5.5A. The successful synthesis of sodium 3-(steartoylthio)propane-1-sulfonate (labelled as R-1) was characterized by ^{1}H NMR, ^{13}C NMR and HRMS spectral analysis, as shown in Figure 5.3 and Figure 5.4. Next, the synthesized R-1 was reacted with a self-polymerizable small molecule, i.e. (3-aminopropyl)triethoxysilane (APTES, denoted as R-2) with 1:1 molar ratio in DI water at 80 $^{\circ}$C. Over time, the transparent reaction mixture (RM) of selected reactants (R-1 and R-2) transformed into a turbid and milky dispersion, due to the formation of NP, as shown in Figure 5.5B. The growth of the NPs was found to be rapid in initial 30 min, and the size of nanoparticles changed from 50 ± 5 nm to 157 ± 6 nm. Thereafter, the growth of NPs was found to be slower, and the size of NPs was enhanced to 209 ± 7 nm after 8 h (Figure 5.5C-E). The same dispersion of the nanoparticles remained stable in water for 30 days, as shown in Figure 5.5F. During the course of the mutual reaction between the selected reactants (R-1 and R-2), the thioester group of R-1 selectively reacted with the primary amine of R-2 to form a robust amide bond, as evident from the ATR-FTIR analysis in Figure 5.6A. The IR signature of carbonyl stretching of the thioester group of R-1 at 1689 cm^{-1} was gradually reduced with the progress of the reaction, and completely disappeared after 8 h of mixing of the selected reactants, as shown in Figure 5.6A. As expected, additional IR signatures appeared at 1644 cm^{-1} and 1547 cm^{-1}, corresponding to amide-I and amide-II bands, respectively. The intensity of these IR peaks was gradually enhanced with time, as shown in Figure 5.6B. These simple experiments validated the formation of amide bonds in the mutual reaction between R-1 and R-2. Thus, the self-polymerizable triethoxysilane moiety of R-2 and hydrophobic hydrocarbon tail is covalently integrated in the aqueous phase.

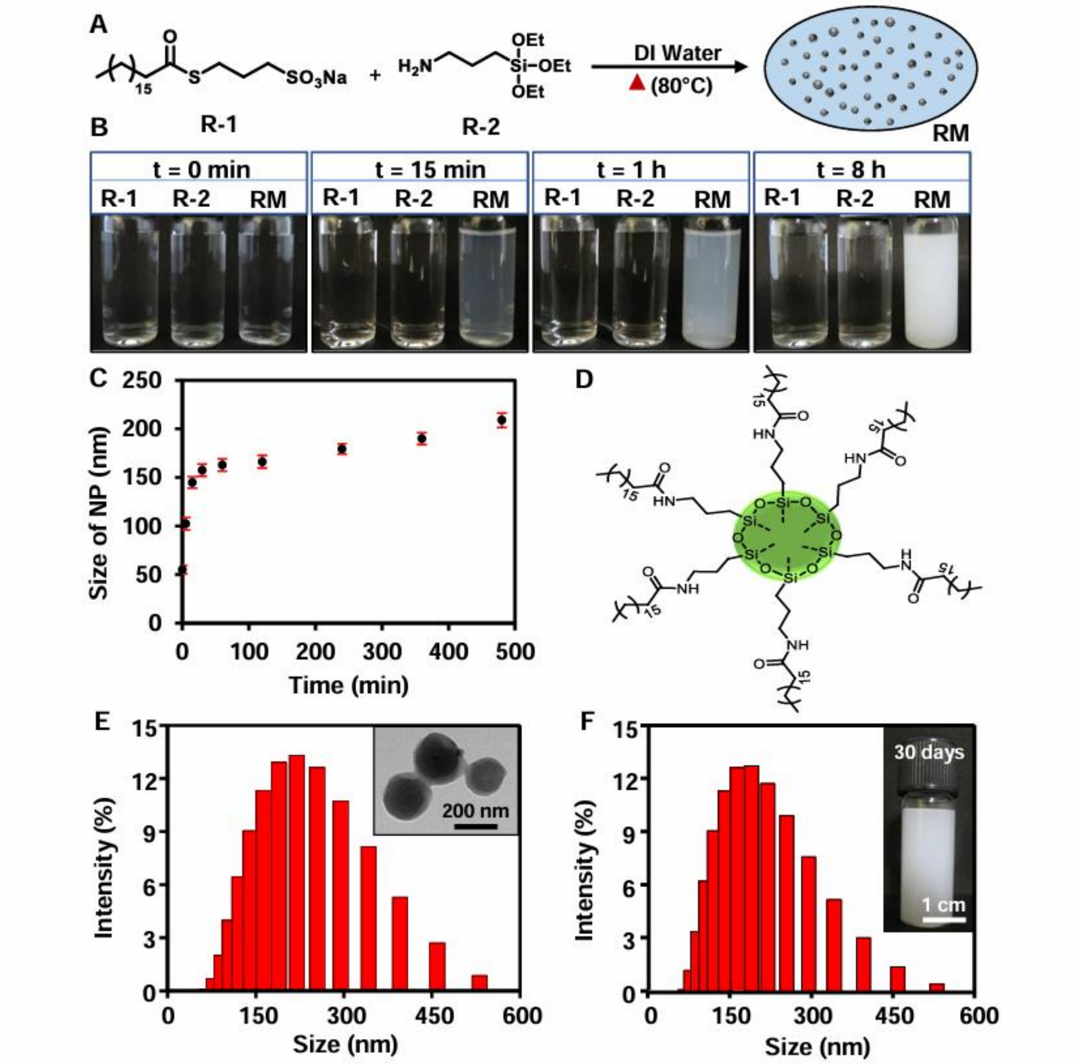

Figure 5.5 A) Illustrating the amidation reaction between selected reactants (i.e. 3-(steartoylthio)propane-1-sulfonate (labeled as R-1) and (3-Aminopropyl)triethoxysilane (APTES, denoted as R-2)), where the reaction mixture of R-1 and R-2 in DI water at 80 ˚C provided a stable dispersion of nanoparticle (NP). B) Digital images accounting the gradual conversion of transparent reaction mixture (RM) of selected reactants (R-1 and R-2) into a turbid and milky dispersion due to the formation of NP. C-D) Illustrating the growth (size) of the NP (C) and schematic of possible chemical representation of developed nanoparticles (D). E-F) Dynamic light scattering (DLS) accounting size distribution of prepared NPs in the DI-water with an inset providing the TEM image of the prepared NPs (E) and size distribution of the prepared nanoparticles after storing for 30 days in DI water with an Inset image illustrating the stable aqueous dispersion of prepared NPs.

In this process, the hydrophilic sulphonate moiety is released and the self-polymerization of the triethoxysilane moiety and followed by phase separation, resulted an aqueous dispersion of

NPs. Thereafter, this aqueous reaction mixture (RM) of selected reactants (R-1 and R-2) was strategically extended to develop both the lubrication-free solid slippery interface and superhydrophobic interfaces, separately.

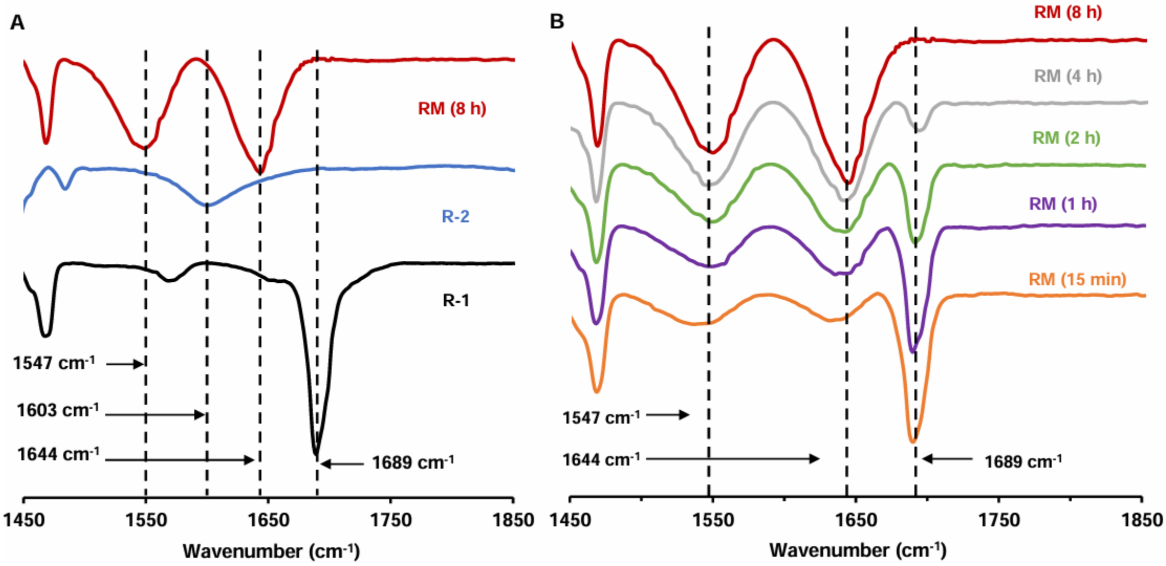

Figure 5.6 A) FTIR-ATR spectra for the individual reactants, i.e. 3-(steartoylthio)propane-1-sulfonate (labelled as R-1, black), (3-Aminopropyl)triethoxysilane (APTES, labelled as R-2), blue) and reaction mixtures (1:1) of R-1 and R-2 after 8 h, (labelled as RM (8 h)). The IR peaks at 1689 cm^{-1}, 1603 cm^{-1}, 1644 cm^{-1} and 1547 cm^{-1} correspond to the carbonyl stretching of the thioester group of R-1, N–H bending of the primary amine group, amide-I and amide-II bands, respectively. The carbonyl stretching of the thioester group is completely disappeared after 8 h of the mutual reaction between amine and thioester moieties. B) FTIR-ATR spectra of the reaction mixtures (1:1) of R-1 and R-2 at different time intervals.

The optimization of the synthesized superhydrophobic coating and its durability will be discussed later in detail. To achieve the lubrication-free slippery coating, a microscopic glass slide was submerged in the aqueous reaction mixture for 8 h, where the RM was prepared by maintaining a fixed molar ratio (i.e. 1:1) of the selected reactants. Thereafter, the water contact angle (WCA) and sliding angle (SA) were measured on the coated glass substrate. On increasing the concentration of the selected reactants in the reaction mixture from 1 mM to 7.5 mM, both the static contact angle and the sliding angle for the beaded water droplets were gradually improved, as shown in Figure 5.7A. However, no significant improvement was noted beyond the concentration of 7.5 mM. This is likely due to no further improvement on the surface coverage of the planar substrate with the deposited nanoparticles. A droplet of water (15 μL) was beaded on the coated substrate with a static water contact angle of ~ 102° and the beaded droplet started sliding on tilting the coated substrates at 15°, as shown in Figure 5.7C-F, without involving any additional lubrication process. The prepared lubrication-free slippery coating remained highly optically transparent and the logo of our institute (Indian Institute of Technology, Guwahati) wasvisible through this coated glass, as shown in Figure 5.7G-H.

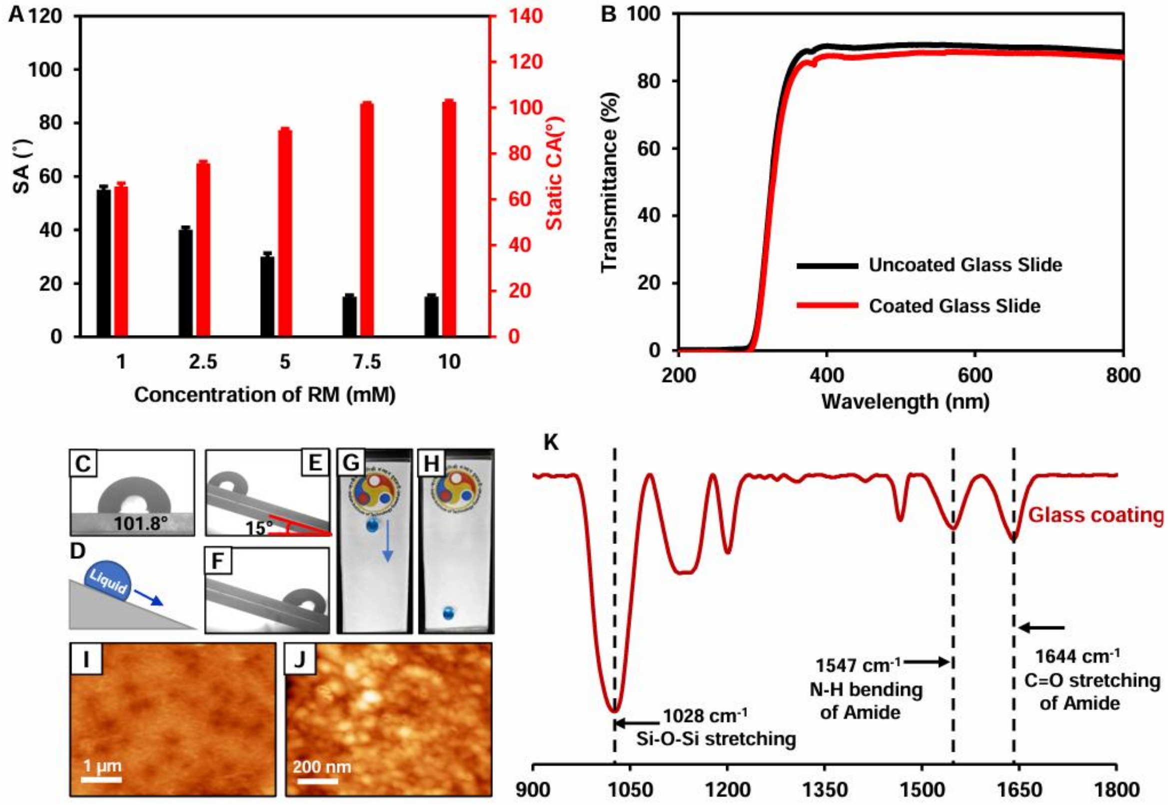

Figure 5.7 A) Plot illustrating the changes in static contact angle (CA) and sliding angle (SA) of a beaded droplet of water on the synthesized coatings that were prepared by changing different molar concentrations of selected reactants, where the molar ratio of selected reactants was kept at 1:1. B) Depicting Optical transmittance (normalized with respect to bare glass) of the coated glass (red). C-H) Static contact angle images (C) of a beaded droplet (5 µL) of water on coated glass, schematic diagram (D) illustrating the sliding of a beaded water droplet on a slippery interface. E-F) sliding angle (E and F) and digital images (G and H) of coated glass depicting the sliding of a beaded water droplet. I-J) AFM images of coated glass under lower (I) and higher (J) magnifications. K) FTIR-ATR spectra of the prepared slippery coating.

Further, the optical transparency was compared with bare glass and the coated glass, which displayed nearly similar (~ 88%) optical transparency, as shown in Figure 5.7B. Thereafter, the morphology of the coating was examined with atomic force microscope (AFM) imaging, which confirmed the existence of a very smooth coating with a root means square (RMS) roughness of ~ 5 nm, as shown in Figure 5.7I-J. Further, the magnified AFM image revealed the presence of aggregated globular domains in the prepared coating, which was derived through the mutual reaction between the selected reactants in DI water. Furthermore, the FTIR spectra of the prepared coating revealed the existence of amide linkages and polymerization of the silane moiety. While the IR signatures at 1644 and 1547 cm^{-1} indicated the presence of an amide bond, the appearance of another IR signature at 1028 cm^{-1} revealed the formation of Si-O-Si bond, as shown in Figure 5.7K. As expected, the characteristic IR signature of the thioester at 1689 cm^{-1} is not observed for the prepared coating.

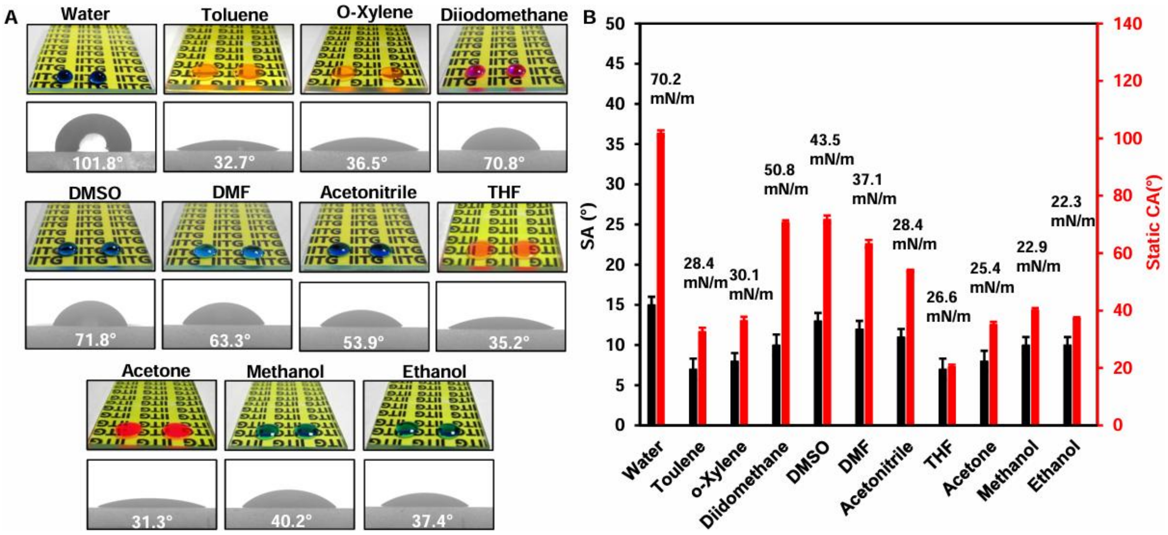

Figure 5.8 A) Digital images and contact angle images of beaded droplets of different liquids having a wide range of surface tension on the lubrication-free slippery coating. B) Bar diagram accounting the static contact angle (CA) and sliding angles (SA) of various non-polar and polar liquids with a wide range of surface tension on the prepared slippery coating.

In addition to water, the prepared coating displayed the ability to slide various other polar (dimethyl sulfoxide, dimethylformamide, acetonitrile, tetrahydrofuran, acetone, ethanol and methanol) and non-polar (toluene, o-xylene and diiodomethane) organic solvents, having a wide range of surface tensions (from 50.8 mN/m to 22.3 mN/m), as shown in Figure 5.8. The beaded droplet of different organic solvents having different static contact angles readily slides on tilting the coated interface, mostly below 15°, as shown in Figure 5.8A and Figure 5.8B. Thus, an optically transparent and waterborne coating embedded with solid slippery property was successfully developed through covalent and aqueous processing of selected small molecules in a single step, without demanding any additional lubrication process.

5.3.2. Tolerance of Lubrication-free Slippery Coating

In the past relevant literature, the lubrication-free slippery coating was often prepared using organic solvents, following a complex fabrication process, and the sustenance of the earlier reported slippery coating under various chemically and physically abrasive conditions was commonly demonstrated for a few cycles and that too with a low (i.e., mostly below 10 kPa) applied pressure.[13-35] While some earlier reported coatings displayed relatively promising physical durability, the instability of such coatings in acidic or alkaline conditions and/or at elevated temperatures (beyond 50 $^{\circ}$C) remained a concern.[13-35] The waterborne and small molecules based slippery coating was exposed to various standard and widely accepted relevant physically and chemically challenging settings, including sandpaper abrasion, knife scratch test, adhesive tape test, pencil hardness test, boiling (~ 100 °C) water, cold (~ 5 °C) water, autoclave test (120 °C, 103.4 kPa) and sand drop test, as shown in Figure 5.9A-U. First of all, an abrasive sandpaper (400 grit abrasive sandpaper (having a dimension of 1 cm × 2 cm)) was repetitively applied to the freshly prepared slippery coating with a to-and-fro motion having an average speed of 15 cm s^{-1} under an external pressure of 25 KPa, which is significantly higher than the relevant reported literature.[13-35] The slippery property of the beaded droplets of polar (water) and non-polar (diiodomethane) liquids was monitored at regular intervals after incurring the sandpaper abrasive distance and the sliding angle remained very similar, as shown in Figure 5.10A.

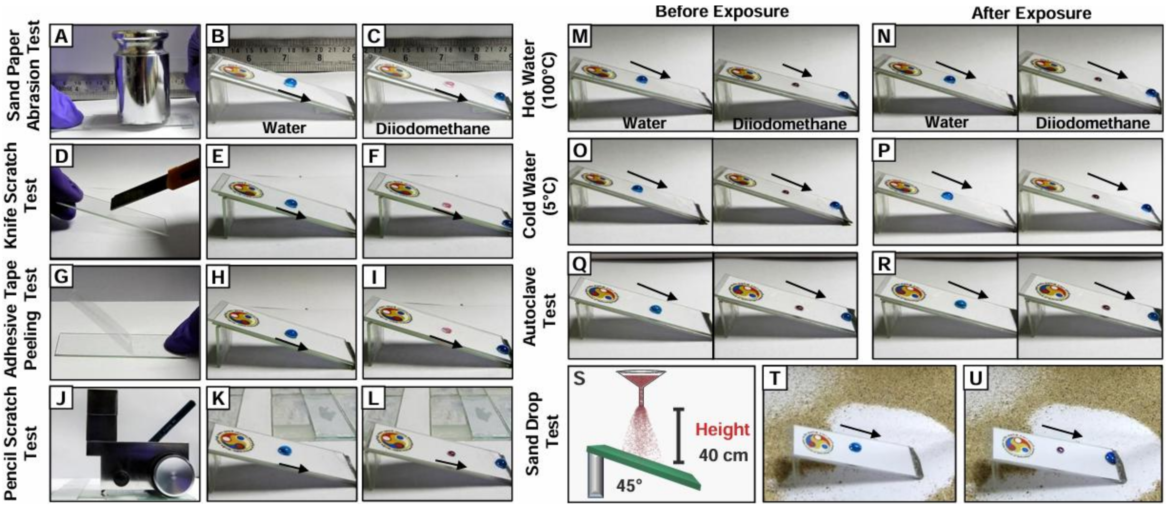

Figure 5.9 A-L) Digital images illustrating the sand paper abrasion test (A), knife scratch test (D), adhesive tape peeling test (G) and pencil scratch test (J) on coated glass and thereafter the sliding behaviour of beaded droplets of water (B, E, H and K) and diiodomethane (C, F, I and L) was examined on the coated interface that was exposed to these different and standard physical abrasions. M-R) Digital images depicted the sliding of beaded droplets of water and diiodomethane (M, Q, R) before and after (N, P, R) submerging the prepared slippery coating in boiling water (100 °C), cold water (5 °C) for 6 h, and standard autoclave treatment of the prepared coating. S-U) Schematic illustration of sand drop test on lubrication-free slippery coating (S) and digital images showing the sliding of water (T) and diiodomethane (U) on the lubrication-free slippery coating after performing the sand drop test.

Even after the exposure of the synthesized slippery coating to such abrasive conditions for 500 cm distance, the tilted interface remained efficient in sliding both beaded droplets of water (polar liquid) and diiodomethane (non-polar liquid), as shown in Figure 5.9A-C. Further, the AFM images revealed the existence of the prepared slippery coating even after performing the sandpaper abrasion test, as shown in Figure 5.10B-E. Thereafter, the prepared coating was exposed to a sharp-edged knife multiple times in arbitrary directions in an attempt to incur scratches on the prepared interface, as shown in Figure 5.9D. But, during the course of this abrasive exposure, any physical damages (scratches) were not noted under visual inspection and the treated interface continued to slide the beaded droplet of water and diiodomethane effortlessly, as shown in Figure 5.9E-F. Moreover, such coating was exposed to another widely accepted physical abrasion test, i.e., adhesive tape peeling test, where a freshly exposed adhesive tape was applied on the slippery coating with an external load of 500 g for 5 minutes, prior to peeling off the tape from the surface (Figure 5.9G). This adhesive tape peeling test was repetitively applied on the same interface, and the slippery property was examined at regular intervals, as shown in Figure 5.10F. The prepared coating sustained such adhesive tape peeling test successfully for 500 times, without compromising the embedded slippery property, where both the droplets of water and diiodomethane were effortlessly moved away, without leaving any trace of the liquid, as shown in Figure 5.9H-I. To understand the existence of such robust and abrasion tolerance of the embedded slippery property of the coating, a standard pencil hardness test was performed on the prepared coating using a pencil hardness tester, where a 6H pencil (considered as one of the hardest pencils) was applied with an external load of 1 Kg (Figure 5.9J). Few flakes of the eroded pencil were noted on the coating; this debris was readily and completely removed by gently rubbing the same interface with tissue paper. Noticeable scratches were not observed after performing the pencil hardness test (Figure 5.10 G-I). Further, the interface that was exposed to the pencil hardness test repetitively remained highly efficient to display unperturbed slippery property, and both the beaded droplets of water and diiodomethane readily slide on tilting the interface (Figure 5.9K-L). In the past, a few self-healable slippery coatings were introduced where physical damages were recovered on application of elevated temperature. While such an approach is promising to heal physical damages, the inconsistent performance over a wide range of temperatures could lead to inconvenience for practically relevant applications. The prepared coating was noticed to be efficient for sliding both droplets of boiling (~ 100 $^{\circ}$C) and cold (~ 5 $^{\circ}$C) water. Thereafter, the prepared coating was submerged in boiling water and exposed to freezing cold environment overnight, but the slippery property remained unaffected, as shown in Figure 5.9M-P. Even such coating survived another severe exposure to standard autoclaving condition (120 $^{\circ}$C, 103.4 kPa) often performed for sterilization of bio-medically relevant materials/interfaces. The coating that was exposed to autoclaving condition for 4 h remained appropriate to display unperturbed slippery property, as shown in Figure 5.9Q-R. The prepared slippery coating was also exposed to a standard sand drop test, where 100 g of sand particles were dropped on the slippery coating from a distance of 40 cm, as shown in Figure 5.9S-U. But the slippery property of the coated interface remained unaffected. These simple demonstrations validated that the prepared coating inherently remained hard enough to survive various severe abrasive exposures. Even some earlier reported slippery coatings that displayed improved physical durability failed to sustain extremes of pH for a prolonged duration.

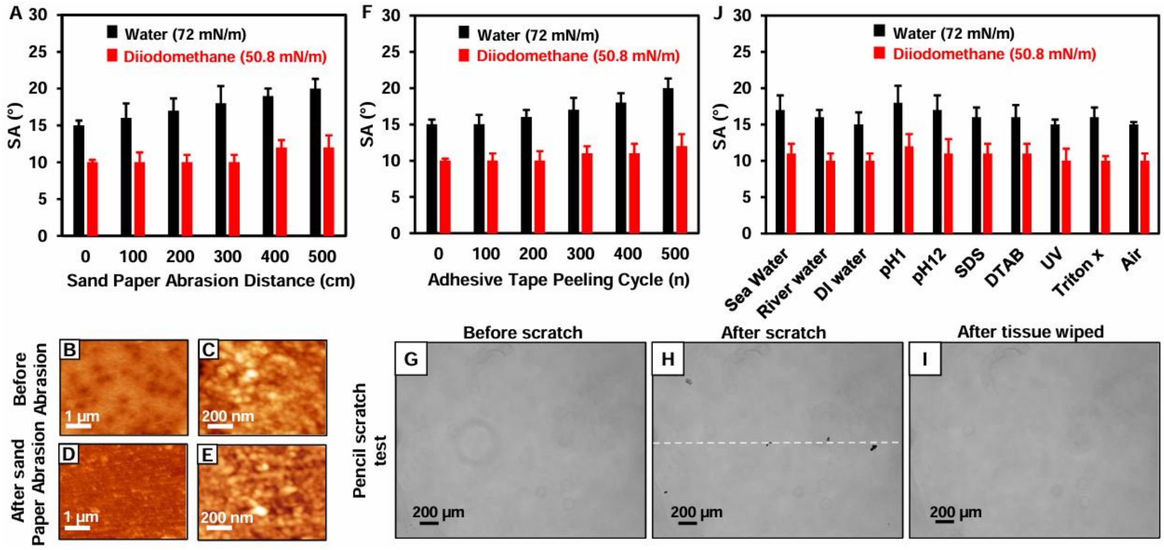

Figure 5.10 A) Bar graph showing variation of sliding angle for beaded droplets of water (black) and diiodo methane (red) on increasing the sand paper abrasion distance. B-E) AFM images of solid slippery coating before (B, C) and after performing sand paper abrasion (D, E) in low (B, D) and high (C, E) magnifications. F) Bar graph accounting the sliding angle of beaded droplets of water (black) and diiodomethane (red) on coated glass after repetitively performing the adhesive tape peeling test. G-I) Bright field microscopic images of a coated glass slide before (G) and after (H) performing the pencil scratch test, and after the tissue wiping (I) of the same coated interface. J) Bar graph illustrating of sliding angles (SA) of a beaded droplet of water (black), and diiodomethane (red) on coated glass after exposure to various harsh chemical environments for 30 days.

The currently developed slippery coating was exposed to various other harsh and extreme of conditions, including extremes of pH, sea water, UV-light, etc., to evaluate the performance of the embedded slippery property. Next, small molecules based slippery coating was exposed to extremes of pH (1 and 12), artificial sea water, river water, surfactants (SDS, DTAB, triton-x; 1 mM) contaminated aqueous phases and UV (at short range: 254 nm and long range: 365 nm) irradiation for 15 days prior to examining the embedded slippery property, as shown in Figure 5.10J. The prepared coating remained appropriate to withstand such a diverse range of prolonged exposures, and the beaded droplets of polar (water) and nonpolar (diiodomethane) liquids readily slipped off without leaving any trace of beaded liquid. Thus, the prepared coating displayed impeccable tolerance to various types of chemical and physical abrasions, without affecting the embedded slippery property. I hypothesize that the amidation reaction between selected reactants, i.e. (3-aminopropyl)triethoxysilane and thioester, followed by self-polymerization of modified aminosilane through Si-O-Si bond formation attributes to the physical and chemical durability of the prepared coating. Further, I have successfully deposited such transparent solid slippery coating on other relavent planar substrates, including PMMA and PC films, as shown in Figure 5.11A-L.

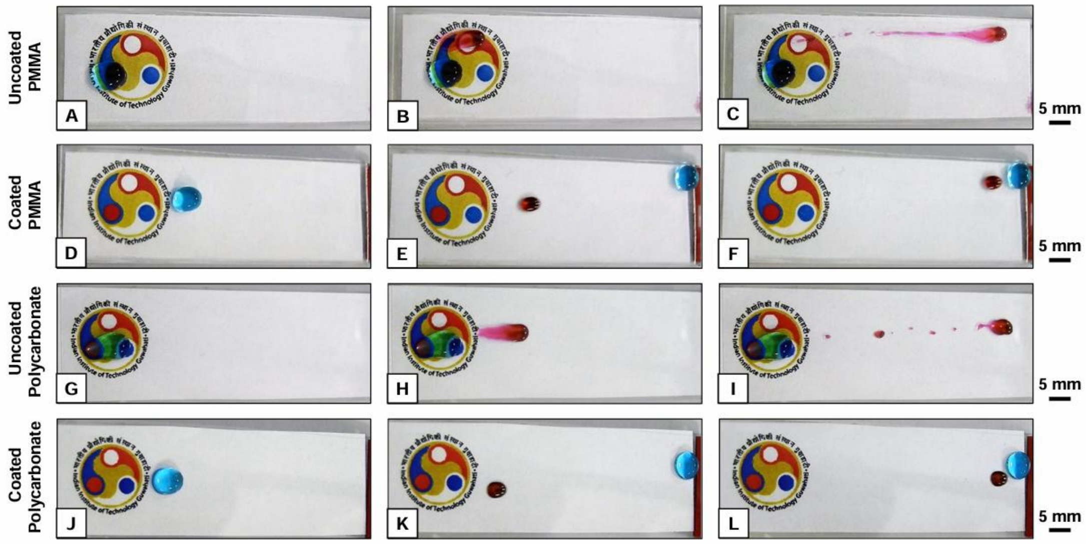

Figure 5.11 A-F) Digital images showing sliding behaviour of beaded droplets of water (blue) and diiodomethane (red) on uncoated (A-C, G-I) and coated (D-F, J-L) poly(methyl methacrylate) sheet (A-F) and polycarbonate (G-L) sheet.

5.3.3. Deformation and Abrasion Tolerant Extremely Water Repellent Coating

In the past, completely distinct approaches were adopted to prepare ultra-smooth solid-slippery and hierarchically-featured superhydrophobic coatings. In the current design, the same chemical approach was successfully extended to achieve even deformable superhydrophobicity on fibrous and porous substrates. The dip-coating process was adopted to deposit the small molecules derived NPs that were prepared by reacting the selected reactants (R-1 and R-2) with 1:1 molar ratio at 80 $^{\circ}$C for 8 h on an inherently hydrophilic (Figure 5.12 A-F) and stretchable polyurethane based fibrous substrate to modulate the water wettability. On increasing the concentrations of selected reactants in the reaction mixture that provided the dispersion of NPs allowed the gradual elevation of the water wettability, as shown in Figure 5.12G-O. Eventually, at the concentration of 7.5 mM, the coated fibrous substrate displayed superhydrophobicity with a water contact angle (WCA) of 155° and contact angle hysteresis of ~ 3°, as shown in Figure 5.13A. Further, the deposition of NPs was confirmed with FESEM imaging where the granular morphology (Figure 5.13B-C) appeared on the featureless fiber (Figure 5.12E) of the selected substrate.

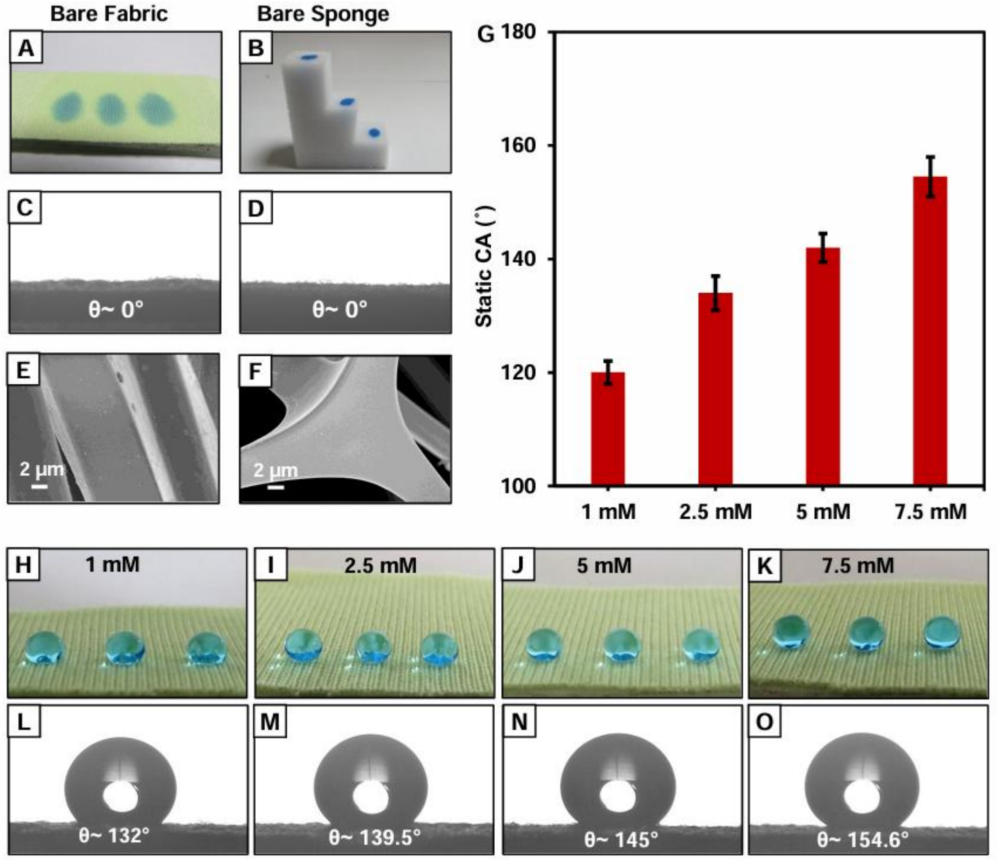

Figure 5.12 A-D) Digital images (A, B) and contact angle images (C, D) of beaded water droplets on the bare fibrous (A, C) and spongy (B, D) substrates. E, F) FESEM images of uncoated fibrous (E) and spongy (F) substrates. G) Bar diagram illustrating the changes in static contact angle of beaded water droplet on the coated fabric on increasing the molar concentrations of reactants (R1 and R2) while maintaining a 1:1 molar ratio. H-O) Digital images (H-K) and static contact angle images (L-O) of beaded water droplet on the coated fibrous, where the coatings were derived from the reaction mixtures of different molar concentrations.

Such integration of NPs covalently associated with the hydrophobic heptadecyl moiety, provided essential topography and chemistry to confer superhydrophobicity on the selected stretchable fibrous substrates, as shown in Figure 5.13A. This approach remained absolutely efficient in successfully decorating various other inherently hydrophilic natural (e.g. jute, wool, cotton, silk) and synthetic (e.g. lycra, polyester) fibrous substrates with extremes of water wettability (WCA above 150°), as shown in Figure 5.13E-P. As the dispersion of NPs remained stable for 30 days (Figure 5.5F), a solution of NPs that was kept at ambient lab-condition for 30 days was utilized for dip-coating a fibrous substrate to achieve non-adhesive superhydrophobicity with WCA of 153°, as shown in Figure 5.13D.

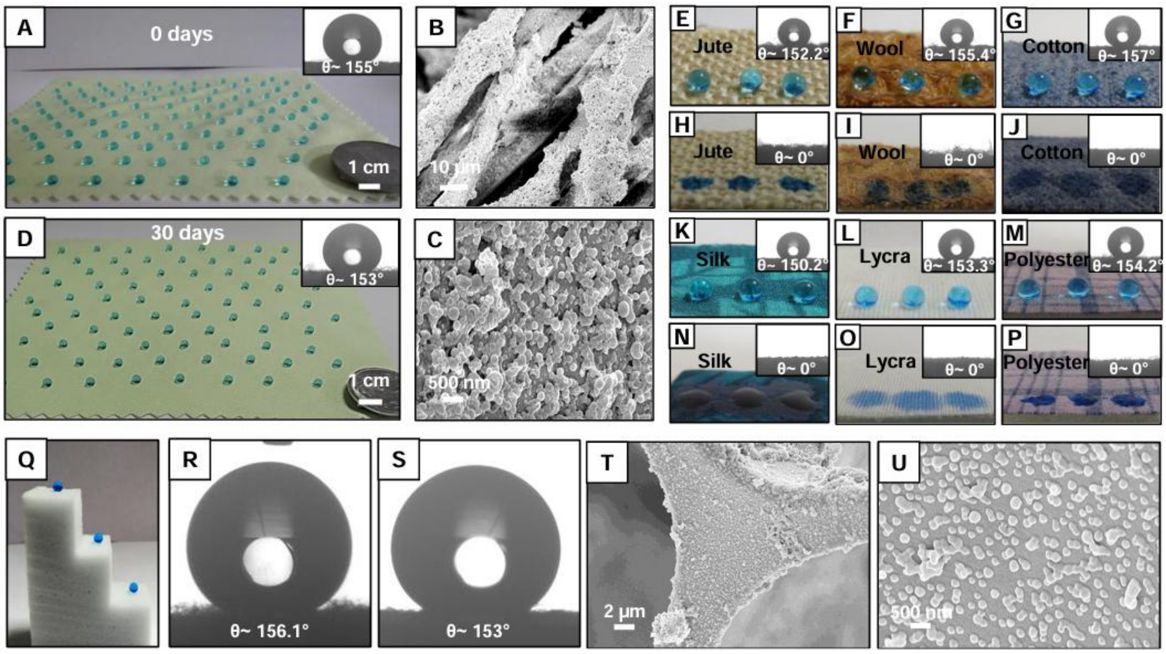

Figure 5.13 A, B) Digital images and contact angle images (inset) of beaded water droplets on the coated fibrous substrate, where fibrous substrate was dip coated with the reaction mixture of selected small molecules that was aged for 8 h (A) and 30 days (B). C, D) FESEM images of coated fibrous substrate under lower (C) and higher (D) magnifications. E-I) Digital image (E) and contact angle images of exterior (F) and interiors (G) of the coated melamine formaldehyde (MF) sponge. H-I) FESEM images of coated MF sponge under lower (H) and higher (I) magnifications. J-U) Digital and static contact angle images (inset) of beaded water droplets on different natural and synthetic fibrous substrates including jute (J and P), wool (K and Q), cotton (L and R), silk (M and S) and lycra (N and T), polyester (J and L) before (P-U) and after (J-O) application of the superhydrophobic coating.

Thereafter, a highly compressible porous melamine formaldehyde (MF) sponge was dip-coated with prepared NPs (concentration of reactants = 7.5 mM) to associate superhydrophobicity with WCA of ~ 156°. The superhydrophobic sponge was further sliced with the shape of a 'step' to expose the interiors for examining the water wettability in the bulk of the porous material. Both exterior and interiors of the coated MF sponge were found to be embedded with superhydrophobicity with WCA well above 150°, as shown in Figure 5.13Q-S. Furthermore, the morphology of the coating was investigated with FESEM imaging. The appearance of granular morphology on the featureless segments of MF sponge (Figure 5.12F) validated the successful deposition of NPs that is essential to associate bio-inspired superhydrophobicity, as shown in Figure 5.13T-U. The tolerance of embedded extreme water repellence in the prepared coating to repetitive physical deformation was investigated in detail. Even after dip-coating, coated substrates (i.e., PU fabric and MF sponge) remained highly stretchable and compressible. First of all, the stretchable fibrous substrate was exposed to a 150 % of tensile strain, and the physically deformed interface continued to display unperturbed superhydrophobicity with WCA of 151°, as shown in Figure 5.14A.

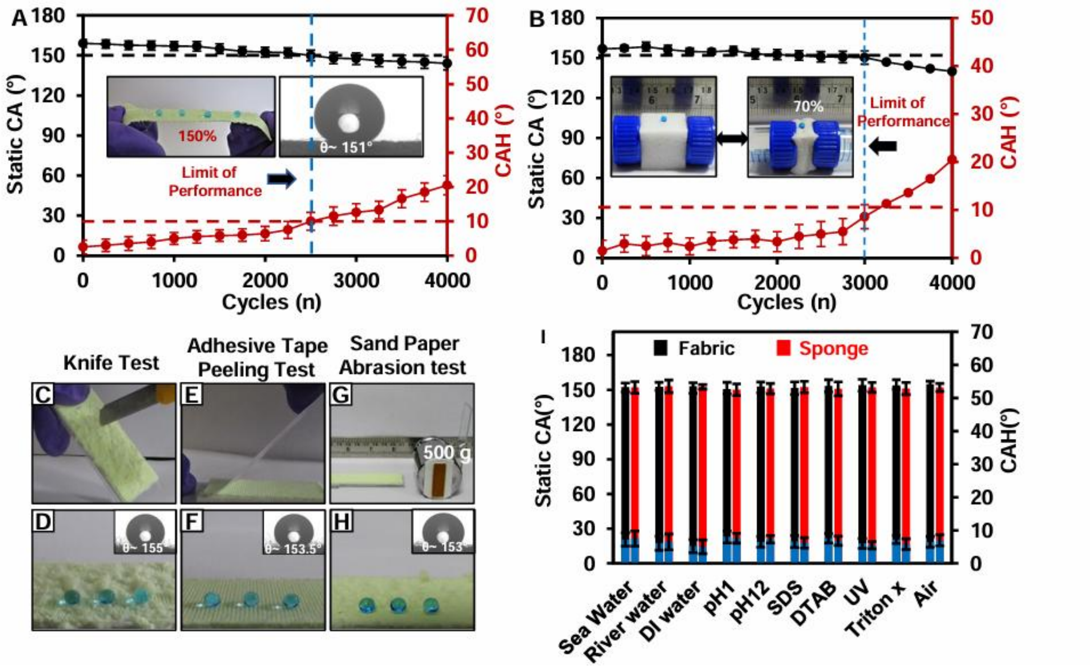

Figure 5.14 A) Plot showing the change in static contact angle (black) and contact angle hysteresis (red) of beaded water droplet on the superhydrophobic coating during the repetitive (4000 cycles; the red dotted line indicating the limit of performance, i.e.2500 times), tensile (150%) deformation process, and the inset showing the digital image & static contact angle image of beaded water droplets on the superhydrophobic coating after application of repetitive external tensile strain of 150%. B) Plot showing the change in static contact angle (black) and contact angle hysteresis (red) of beaded water droplet on the superhydrophobic MF sponge during its repetitive (4000 cycles; the red dotted line indicating the limit of performance, i.e. 3000 times) physical compression (70%). The inset showing the digital image of beaded water droplets on the superhydrophobic coating after application of repetitive compressive strain of 70%. C-H) Digital images of the experimental setups for knife test (C), adhesive tape peeling test (E), sand paper abrasion test (G) and Digital images and contact angle images (inset) of the beaded water droplets after performing knife test (D), adhesive tape peeling test (F) and sand paper abrasion test (H). I) Plot illustrating the impact of various chemical harsh exposures including artificial seawater, river water, DI-water, pH 1, pH 12, SDS, DTAB, UV irradiation (at λ max = 254 and 365 nm), triton x and ambient air (at 25 °C) for 15 days on the water wettability of coated fabric (black) and sponge (red).

Such large amount of physical deformation was repetitively applied and the water wettability of the coated interface was examined at regular interval. Even after incurring 150 % of tensile deformation for 2250 cycles, the prepared coating remained non-adhesive superhydrophobic with WCA above 150° and contact angle hysteresis below 10°, as shown in Figure 5.14A. Thus, the limit of performance was observed to be 2250 cycles and the superhydrophobicity was compromised on further increasing the tensile deformation cycles. Similarly, the prepared superhydrophobic sponge was compressed with 70 % compressive strain and the embedded water repellence remained unaffected, as shown in Figure 5.14B. The droplet of water beaded on the compressed interface with WCA of ~152°. The prepared compressible supehydrophobic material has the ability to sustain the repetitive compressive strain (70 %) for 3000 cycles without losing the nonadhesive superhydrophobicity (WCA above 150° and contact angle hysteresis below 10°), as shown in Figure 5.14B. The same coated fibrous substrate was also exposed to other widely accepted physically abrasive exposures, including knife scratching, adhesive tape peeling and abrasive sand paper test, as shown in Figure 5.14C-H.

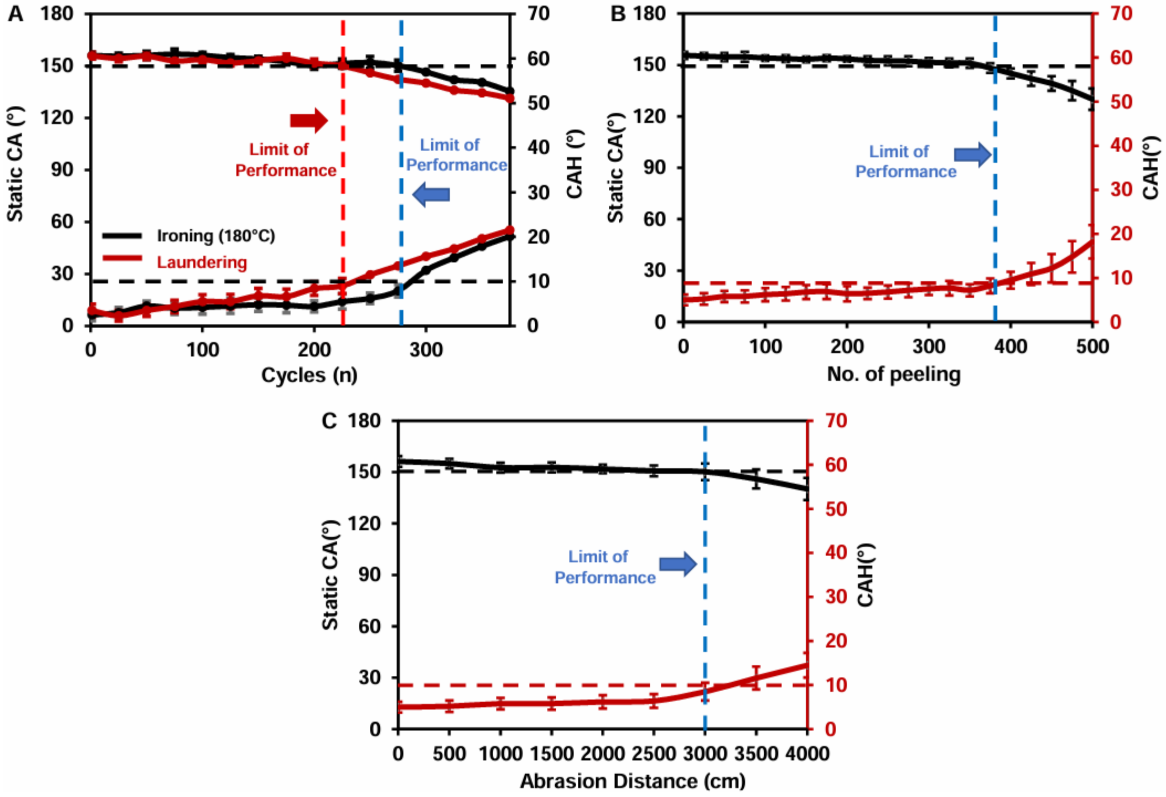

Figure 5.15 A) Plot illustrating the change in static contact angle and contact angle hysteresis of beaded water droplet on superhydrophobic fabric after repeatedly (400 cycles) washing (maroon; the red dotted line referring the limit of performance, i.e., 225 cycles) and ironing (black; the blue dotted line referring to the limit of performance, i.e., 275 cycles) the coated fibrous substrate. B) Plots showing the change in static contact angle and contact angle hysteresis of beaded water droplets on superhydrophobic fabric on repetitive application of adhesive tape peeling test (the blue dotted line referring the limit of performance, i.e., 375 cycles). C) Plots showing the change in static contact angle hysteresis of beaded water droplets on superhydrophobic fabric during the sand paper abrasion test for 4000 cm (the blue dotted line indicating the limit of performance, i.e., 3000 cm).

The repetitive exposures of knife scratching on the superhydrophobic fibrous substrate led to severe physical damages, as noted by the visual inspection (Figure 5.14C-H), but the embedded superhydrophobicity remained unaltered with WCA of 155°. Moreover, both coated fabrics and sponges were exposed to various and complex aqueous phases, including sea water, river water, di water, acidic water (pH 1), alkaline water (pH 12), water contaminated with surfactants (SDS, DTAB, Triton X), UV irradiation (at $\lambda_{max} = 254$ and 365 nm) and in air for 30 days. However, the coated interfaces were efficient in successfully tolerating the exposure to these different chemicals and displayed extreme water repellency (WCAs above 150° and contact angle hysteresis below 10°), as shown in Figure 5.14I. Thereafter, the superhydrophobic stretchable fabric was repetitively exposed to both the standard laundering test and ironing test and the coated interface sustained the laundering and ironing tests for 225 and 275 cycles, respectively, without compromising non-adhesive superhydrophobicity, as shown in Figure 5.15A. Then, the stretchable superhydrophobic coating was exposed to adhesive tape peeling test, where a freshly exposed adhesive interface was applied on the small molecules derived coating for 5 min with an external load of 500 g, prior to peeling off from the coated interface. The external load facilitated the contact between adhesive interface and the coating. The coating survived such repetitive exposure for 300 times without losing the non-adhesive superhydrophobicity, as shown in Figure 5.14E-F and Figure 5.15B. Furthermore, such coating was exposed to another practically relevant severe setting, where an abrasive sand paper was applied with back and forth motion under an external load of 500 g. The water wettability of the coating was monitored with increasing the sand paper abrasion distance, as shown in Figure 5.15C. The prepared coating was appropriate to tolerate a sand paper abrasion distance of 3000 cm without compromising the nonadhesive superhydrophobicity. Although noticeable physical damages appeared during the course of the study as evident from visual inspection (Figure 5.14G-H), but the damaged interface remained efficient to display extreme water repellence with WCA of 153°. Thus, the small molecules based superhydrophobic coating that was processed in the aqueous phase through the mutual covalent reaction between amine and thioester provided chemically and physically robust superhydrophobicity. In the past, various strategies were introduced to achieve a mechanically robust superhydrophobic coating.[47-49] Here, I have introduced a simple chemical approach to address this important durability challenge.

5.3.4. Self-cleaning and Antifouling Performance of Solid Slippery and Superhydrophobic Coatings

The prepared slippery coating that sustained various and severe physical abrasive exposures, as extended to demonstrate the instant and repetitive erasing of an intentionally deposited commercially available permanent marker (Luxor OHP/CD/DVD) ink from the slippery interface, just by the application of gentle rubbing with tissue paper. First of all, the spreading of such ink on the coated glass was noticed to be poor in comparison to bare glass, as shown in Figure 5.16A, B, likely due to the association of bio-inspired wettability.

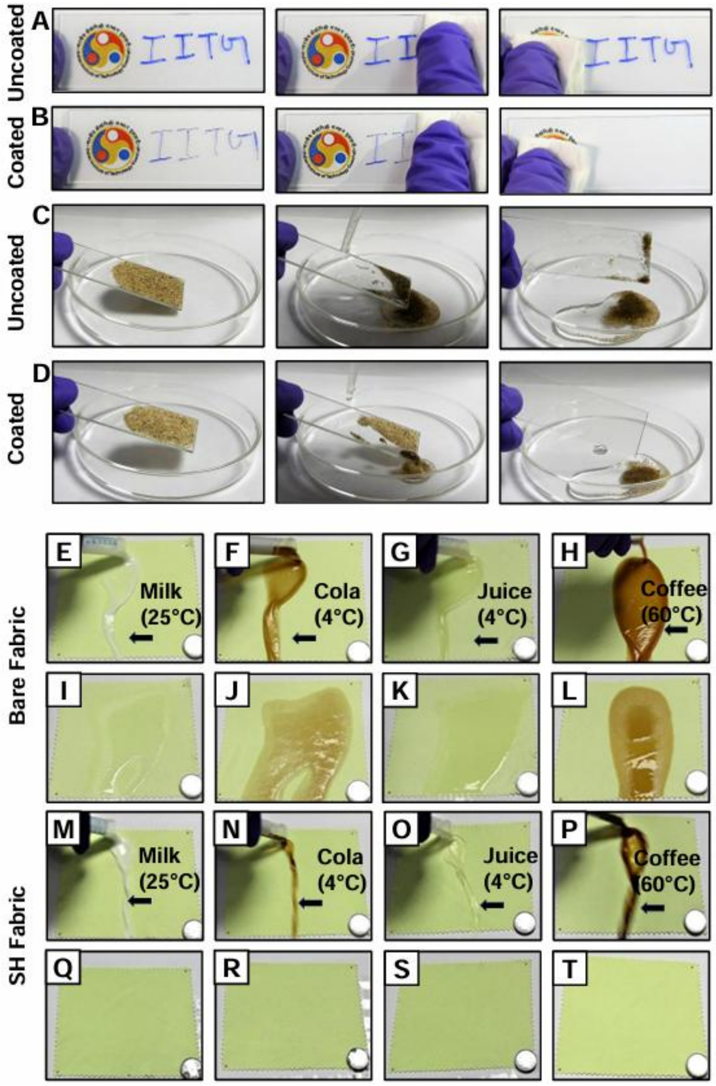

Figure 5.16 A-B) Digital images illustrating the attempts of erasing the manually deposited commercially available permanent marker ink from bare glass (A) and coated slippery interface (B) by gentle rubbing with tissue paper. C-D) Digital images demonstrating the self-cleaning ability of deposited sand particles on both uncoated (C) and coated (D) glass slide with stream of tap water. E-T) Digital images showing the fouling and antifouling behaviour of bare and superhydrophobic fabric with the stream of cow milk (E, I, and M, Q), cold (4 °C) cola (F, J and N, R), cold (4 °C) juice (G, K and O, S), hot (60 °C) coffee (H, L and P, T).

The deposited ink that air-dried on the slippery coating was completely removed on application of a gentle wiping with tissue paper, without having any trace of the permanent marker.

However, as expected, the hand-writing (i.e. IITG) with the same permanent marker on the bare glass remained utterly inerasable even after successive application of gentle and harsh wiping with tissue paper, as shown in Figure 5.16A, B. Thus, the prepared coating has the ability to protect the interface from unwanted exposure of even a permanent marker ink. In the past, superhydrophobic interfaces were extensively extended to demonstrate self-cleaning performance.[50-55] Inspired by earlier reports, here, the prepared solid slippery coating was successfully used to demonstrate the self-cleaning ability, where the deposited dust and dirt on the slippery coating was readily removed on exposure to the aqueous stream and provided a dry and clean interface, as shown in Figure 5.16D. In the absence of such coating, the glass substrate remained inefficient to provide an instantly dry and clean interface, as shown in Figure 5.16C; rather a muddy and wet interface was recovered at the end for the uncoated glass substrate. Thereafter, the bare fabric and prepared superhydrophobic fabric were exposed to various commercially available hot and cold beverages, including milk, cold (4 °C) soft drink, fruit juice and hot coffee (60 °C) to examine its ability to protect the selected porous/fibrous and inherently hydrophilic substrates from unwanted aqueous exposures, as shown in Figure 5.16E-T. While the bare fibrous substrate soaked all the beaded droplets of the selected beverages, (Figure 5.16E-L) the small molecule derived coating repelled the same aqueous droplet with extreme repellence, having a CA of above 150°. Thereafter, the streams of selected cold and hot beverages were poured on the prepared superhydrophobic coating and the liquids were extremely repelled and readily removed, without having any trace of these used liquids on the coated fabric, as shown in Figure 5.16M-T.

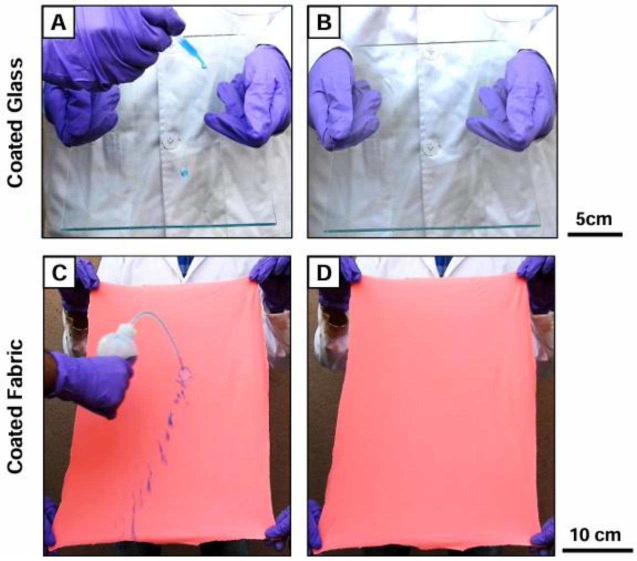

Figure 5.17 A-D) Digital images demonstrating the solid slippery (A-B) and superhydrophobic (C-D) coatings on large objects.

Further, this coating strategy was successfully applied to coat on large substrates with the slippery and superhydrophobic property, as depicted in Figure 5.17A-D. Thus, I have introduced a scalable and facile chemical approach to develop an optically transparent slippery and superhydrophobic coating, which remained appropriate to survive various practically relevant and challenging conditions, and thus, such coating would be useful in relevant and realistic applications.

5.4. Conclusion

To conclude, I report a simple design for aqueous processing of some important chemical parameters to achieve coating with desired and relevant 'output', including optical transparency, physical & chemical durability, slippery property and superhydrophobicity. In the current design, a thioester molecule (R-1) that is associated with both hydrophobic (heptadecyl) and hydrophilic (sulfonate) moieties was reacted with another small molecule, i.e. AEPTS (R-2) in DI water to achieve a stable (for 30 days) dispersion of NPs (size 210 nm), where the thioester and primary amine groups were mutually reacted to form an amide linkage and it caused the release of the hydrophilic (sulfonate) moiety. The reaction mixture of selected reactants (R-1 and R-2) was extended to develop an optically transparent (above 85%), non-fluorinated and lubrication-free slippery coating for effortless sliding (below 15° tilting angle) of various polar and nonpolar liquids having a wide range of surface tensions. Such interface remained efficient to perform at extremes of temperatures (120 °C to 5 °C) and remained tolerant to survive various and severe abrasive exposures, including sand drop (250 g) test, sand paper abrasion distance of 500 cm (applied load of 25 KPa), adhesive tape peeling test (for 500 cycles), knife scratch test, pencil hardness test (6H pencil, applied load of 1 Kg) and prolonged (15 days) treatments with extremes of pH, sea water, river water, different surfactants (1 mM) contaminated water etc. The same reaction solution was also successfully explored to develop a physically deformable (stretchable and compressible) superhydrophobic coating on fibrous and porous substrates with a water contact angle above of 150° and contact angle hysteresis below 10°. The prepared coating sustained repetitive compressive (70%) and tensile (150%) strains for 3000 and 2500 cycles, respectively, without compromising the embedded extremes of water repellence. Further, such coatings remained appropriate to sustain different and severe abrasive physical and chemical exposures. Such slippery and superhydrophobic coating were also utilized to demonstrate the abilities of 1) self-cleaning of deposited dust, 2) protecting the underneath hydrophilic substrate from unwanted exposures of commercially available 'permanent ink' and aqueous beverages, respectively.

5.5. References

1 S. Wang, K. Liu, X. Yao and L. Jiang, *Chem. Rev.*, 2015, **115**, 8230-8293.

2 Z. Chu, Y. Feng and S. Seeger, *Angew. Chem. Int. Ed.*, 2015, **54**, 2328-2338.

3 B. Su, Y. Tian and L. Jiang, *J. Am. Chem. Soc.*, 2016, **138**, 1727−1748.

4 Y. Si, Z. Dong and L. Jiang, *ACS Cent. Sci.*, 2018, **4**, 1102-1112.

5 C. Howell, A. Grinthal, S. Sunny, M. Aizenberg and J. Aizenberg, *Adv. Mater.*, 2018*,* **30**, 1802724.

6 J. Li, E. Ueda, D. Paulssen and P. A. Levkin, *Adv. Funct. Mater.*, 2019*,* **29***,* 1802317.

7 M. Villegas, Y. Zhang, N. A. Jarad, L. Soleymani and T. F. Didar, *ACS Nano*, 2019, **13**, 8517-8536.

8 Y. Wang, S. Gao, W. Xu, and Z. Wang, *Adv. Funct. Mater.*, 2020*,* **30***,* 1908252.

9 S. William, Y. Wong, A. Naga, L. Hauer, P. Baumli, H. Bauer, K. I. Hegner, M. D'Acunzi, A. Kaltbeitzel, H. J. Butt and D. Vollmer, *Nat. Commun.*, 2021, **12**, 5358.

10 M. Tenjimbayashi and M. Naito, *Adv. Funct. Mater.*, 2022, **32**, 2204681.

11 Y. Xu, A. M. Rather, Y. Yao, J. C. Fang, R. S. Mamtani, R. K. A. Bennett, R. G. Atta, S. Adera, U. Tkalec and X. Wang, *Sci. Adv.*, 2021, **7**, eabi7607.

12 A. Shome, A. Das, A. Borbora, M. Dhar and U. Manna, *Chem. Soc. Rev.*, 2022, **51**, 5452-5497.

13 L. Wang and T. J. Mccarthy, *Angew. Chem. Int. Ed.*, 2016, **55**, 244.

14 A. Baidya, M. A. Ganayee, S. J. Ravindran, K. C. Tam, S. K. Das, R. H. A. Ras and T. Pradeep, *ACS Nano*, 2017, **11**, 11091-11099.

15 C. Peng, Z. Chen and M. K. Tiwari, *Nat. Mater.*, 2018, **217**, 355-360.

16 K. Zhang, S. Huang, J. Wang and G. Liu, *Angew. Chem. Int. Ed.*, 2019, **58**, 12004.

17 M. Liu, Z. Wang, P. Liu, Z. Wang, H. Yao and X. Yao, *Sci. Adv.*, 2019, **5**, eaaw5643.

18 X. Dong, S. Gao, J. Huang, S. Li, T. Zhu, Y. Cheng, Y. Zhao, Z. Chen and Y. Lai, *J. Mater. Chem. A*, 2019, **7**, 2122-2128.

19 X. Wang, J. Wang, L. Heng and L. Jiang, *Adv. Funct. Mater.*, 2020, **30**, 1902686.

20 G. Han, T. B. Nguyen, S. Park, Y. Jung, J. Lee and H. Lim, *ACS Nano*, 2020, **14**, 10198-10209.

21 D. Wang, Q. Sun, M. J. Hokkanen, C. Zhang, F.Y. Lin, Q. Liu, S. P. Zhu, T. Zhou, Q. Chang, Bo He, Q. Zhou, L. Chen, Z. Wang, R. H. A. Ras and X. Deng, *Nature*, 2020, **4**, 582.

22 J. Ma, T. Ma, W. Duan, W. Wang, J. Cheng and J. Zhang, *J. Mater. Chem A*, 2020, **8**, 22315-22326.

23 C. H. Xuea, L. L. Zhao, X. J. Guo, Z. Y. Ji, Y. Wu, S. T. Jia and Q. F. An, *Chem. Eng. J.*, 2020, **396**, 125231.

24 M. Ge, C. Cao, F. Liang, R. Liu, Y. Zhang, W. Zhang, T. Zhu, B. Yi, Y. Tang, and Y. Lai, *Nanoscale Horiz.*, 2020, **5**, 65-73.

25 J. Liu, Y. Sun, X. Zhou, X. Li, M. Kappl, W. Steffen and H. J. Butt, *Adv. Mater.*, 2021, **33**, 2100237.

26 V. Singh, X. Men and M. K. Tiwari, *Nano Lett.*, 2021, **21**, 3480-3486.

27 L. Zhang, A. G. Zhou, B. R. Sun, K. S. Chen and H. Z. Yu, *Nat. Comm.*, 2021, **12**, 982.

28 K. Han, Z. Wang, L. Heng and L. Jiang, *J. Mater. Chem. A*, 2021, **9**, 16974-16981.

29 W. Niu, G. Y. Chen, H. Xu, X. Liu and J. Sun, *Adv. Mater.*, 2022, **34**, 2108232.

30 M. Dhar, A. Das, D. Parbat and U Manna, *Angew. Chem. Int. Ed.*, 2022, **61**, e202116763.

31 Y. Wang, W. Zhao, M. Han, L. Guan, L. Han, A. Hemraj and K. C. Tam, *Angew. Chem. Int. Ed.*, 2022, **61**, e202115238.

32 H. Luo, H. Wei, L. Wang, Q. Gao, Y. Chen, J. Xiang and H. Fan, *J Colloid Interface Sci.*, 2022, **628**, 1070-1081.

33 J. Wen, Z. Sun, F. Zhu and H. Fan, *Prog. Org. Coat.*, 2023, **174**, 107254.

34 S. Huang, G. Liu, H. Hu, J. Wang, K. Zhang and J. Buddingh, *Chem. Eng. J*, 2018, **351**, 210-220.

35 Z. Ha, L. Lei, M. Zhou, Y. Xia, X. Chen, P. Mao, B. Fan and S. Shi, *ACS Appl. Mater. Interfaces*, 2023, 15, 7427-7441.

36 J. Sarma, L. Zhang, Z. Guo and X. Dai, *Chem, Eng. J.*, 2022, **431**, 133475.

37 L. Zhang, Z. Guo, J. Sarma and X. Dai, *ACS Appl. Mater. Interfaces*, 2020, **17**, 20084-20095.

38 S. P. Chapman, J. K. Hong, A. Waterhouse and C. Neto, *Chem. Soc. Rev.*, 2020, **49**, 3688-3715.

39 C. Ghobril, K. Charoen, E. K. Rodriguez, A. Nazarian and M. W. Grinstaff, *Angew. Chem. Int. Ed.*, 2013, **52**, 14070-14074.

40 J. Franke and C. Hertweck, *Cell. Chem. Biol.*, 2016, **23**, 1179-1192.

41 A. K. Rudd, R. J. Brea and N. K. Devaraj, *J. Am. Chem. Soc.*, 2018, **140**, 17374-17378.

42 M. Podgórski, S. Mavila, S. Huang, N. Spurgin, J. Sinha and C. N. Bowman, *Angew. Chem. Int. Ed.*, 2020, **59**, 9345-9349.

43 S. Mavila, H. R. Culver, A. J. Anderson, T. R. Prieto and C. N. Bowman, *Angew. Chem. Int. Ed.*, 2022, **61**, e202110741.

44 M. F. Pinter, M. Bouza, F. M. Fernández, L. J. Leman, L. D. Williams, N. V. Hud and A. G. Martinez, *Nat. Commun.*, 2022, **13**, 2569.

45 B. J. Carberry, J. J. Hernandez, A. Dobson, C. N. Bowman and K. S. Anseth, *Macromolecules*, 2022, **55**, 2123-2129.

46 Y. Qing, C. Long, K. An and C. Liu*,* *Composites Part B*, 2022, **236**, 109797.

47 X. Xu, Y. Qing, N. Liu, C. Long, J. Ma, M. Cui, Y. Yao, W. Yao and C. Liu, *ACS Appl. Mater. Interfaces*, 2022, **14**, 37039-37050.

48 W. Zhang, D. Wang, Z. Sun, J. Song and X. Deng, *Chem. Soc. Rev.*, 2021, **50**, 4031-4061.

49 S. S. Latthea, R. S. Sutar, A. K. Bhosale, S. Nagappanc, C.-S. Hac, K. K. Sadasivunid, S. Liua and R. Xing, *Prog. Org. Coat.*, 2019, **137**, 105373.

50 R. S. Sutar, S. Nagappan, A. K. Bhosale, K. K. Sadasivuni, K.-H. Park, C.-S. Ha and S. S. Latthe, *Coatings*, 2021, **11**, 1162.

51 R. S. Sutar, S. S. Latthe, S. Nagappan, C.-S. Ha, K. K. Sadasivuni, S. Liu, R. Xing, A. K. Bhosale, *J. Appl. Polym. Sci.*, 2021, **138**, e49943.

52 R. S. Sutar, S. S. Latthe, A. M. Sargar, C. E. Patil, V. S. Jadhav, A. N. Patil, K. K. Kokate, A. K. Bhosale, K. K. Sadasivuni, S. V. Mohite, S. Liu and R. Xing, *Macromol. Symp.*, **393**, 2020, 2000031.

53 R.S. Sutar, S. D. Manadeshi, S. S. Latthe, S. R. Kulal, G. D. Salunkhe, K. K. Rangar, R. A. Lavate, S. B. Raut, A. C. Sapkal, A. K. Bhosale, K. K. Sadasivuni, S. Liu, R. Xing, *Macromol. Symp.*, 2020, **393,** 2000033.

54 R. S. Sutar, S. S. Gaikwad, S. S. Latthe, V. S. Kodag, S. B. Deshmukh, L. P. Saptal, S. R. Kulal, A. K. Bhosale, *Macromol. Symp.*, 2020, **393**, 2000116.

Chapter 6. Conclusion and Future Directions

This chapter presents a summary of the entire thesis work discussed in the previous chapters and outlines potential future directions related to this thesis work. I have strategically applied aqueous and non-aqueous liquid wettability to derive various functional customized materials and interfaces through the adoption of facile fabrication methods. In Chapter 1, I provided a brief overview of bio-inspired liquid wettability, exploring the conventional techniques used to prepare different artificial anti-wetting surfaces, highlighting existing relevant challenges, and outline the objectives of this thesis work. Chapter 2 demonstrates the post-modification of porous and reactive crystalline nano material (MOFs) with selected alkyl amines through 1,4-conjugate addition reaction to tailor the liquid wettability from hydrophobic to superhydrophobic. It allowed to develop liquid marbles (LMs) for on-demand and customized release of the inner liquid in the presence of different pH of the water pool. In Chapter 3, I have introduced omniphobic capsules/colloidosomes from crystalline and hydrophobic comb-polymer to prevent loss of inner liquid because of surface adhesion and evaporation of encapsulated volatile liquid. Chapter 4 accounts for the fabrication of chemically reactive superhydrophobic polymeric coating on a textile to develop a chemically modulated wettability pattern for antigravity unidirectional water transport. In Chapter 5, I have introduced a completely waterborne, highly transparent, abrasion-tolerant, and substrate-independent solid slippery and superhydrophobic interface through an amidation reaction between a thioester and aminosilane.

In this thesis, I have introduced different types of anti-wettable materials/interfaces, which can be further used for various relevant applications. LMs and colloidosome (discussed in chapters 2 and 3) have been used in various “droplet-scale” applications, like on-demand drug release, miniaturized chemical reaction, sensing of toxic pollutants, etc. Further, these materials could be extended for catalytic miniature reactors, lab-on-a-chip devices, etc. Moreover, in the recent past, LMs have been used in 3D cell culture applications. A 3D cell culture is an advanced engineered system that enables biological cells to grow and interact with their surrounding environment in all three dimensions. LMs are potential candidates for 3D cell culture due to non-sticking, permeability, easy transportation, and a confined environment. However, LMs often suffer from weak mechanical properties. So, it is difficult to monitor cell culture for a long duration. On the other side, colloidosomes are mechanically stable but lack porosity. To achieve the desired mechanical property while retaining the property of LMs, i.e., porous shell structure, it could be possible to develop a hybrid material combining the key properties of both LMs and colloidosome, adequately.

Furthermore, the patterned Janus textile, discussed in Chapter 4, is used to demonstrate directional liquid transport and can also be extended to various applications. The asymmetric wettability of patterned Janus textile and the fast ejection rate of water droplets could make them efficient for water harvesting, wound healing, sensing, etc. In the recent past, researchers have made efficient progress in developing patterned Janus fabric for unidirectional liquid transport properties for real-life applications. However, the slow rate of unidirectional liquid transport properties and the use of sophisticated instruments restrict the industry requirements. So, this patterned Janus textile with facile fabrication, instrument-free, and high unidirectional liquid transport properties could be used in the near future for water harvesting, wound healing, and sensing applications in real-life scenarios.

I have successfully introduced a robust, complete waterborne, transparent, scalable, non-fluorinated dry solid slippery interface as discussed in Chapter 5, which can be further used in solar panels, smart windows, spectacles, airplane wings, and other applications to prevent unwanted fouling by liquids and dust particles. Moreover, a highly deformable complete waterborne superhydrophobic coating on porous and fibrous substrates was developed following the same chemistry, which was also discussed in this chapter. The porous and fibrous robust superhydrophobic coating has potential for various applications such as oil-water separation and anti-icing. Therefore, the developed materials could be beneficial for a wide range of future applications.

Publications Related to Thesis

1. **S. Kumar**, N. Barman, A. Borbora, P. Mondal, M. Tenjimbayashi and U. Manna**,** *J. Mater. Chem. A*, 2024, **12**, 3362-3372.
2. K. Jain,$^{\perp}$ **S. Kumar**,$^{\perp}$ M. dhar, H. Ali, D. Sarkar, N. Barman, M. Tenjimbayashi and U. Manna, *Chem. Mater.*, 2024, **36**, 8692-8703.
3. **S. Kumar**, A. Borbora, P. Chakraborty, H. Sarma, A. Bose, M. Tenjimbayashi and U. Manna**,** *Adv. Funct. Mater.*, 2024, **34**, 2410955.
4. **S. Kumar**, M. Dhar, B. M. Prusty, D. Sarkar, A. Das, D. Manna and U. Manna, *Chem. Eng. J.*, 2023, **465**, 142776

Other Publications

5. A. Rana, C. Gogoi, S. Ghosh, S. Nandi, **S. Kumar**, U. Manna and S. Biswas, *New J. Chem.*, 2021, **45**, 20193-20200.
6. S. Ruidas, A. Das, **S. Kumar**, S. Dalapati, U. Manna and A. Bhaumik, *Angew. Chem. Int. Ed.*, 2022, **61**, e2022105.
7. S. Ghosh, A. Rana, **S. Kumar**, C. Gogoi, S. Mukherjee, U. Manna and S. Biswas *Mater. Chem. Front.*, 2022, **6**, 2051-2060.
8. N. Barman, A. Shome, **S. Kumar**, P. Mondal, K. Jain, M. Tenjimbayashi and U. Manna, *Adv. Funct. Mater.*, 2023, **33**, 2214840.
9. H. Sarma, S. Mandal, A. Borbora, A. Phukan, **S. Kumar**, M. Dhar, D. Sarkar and U. Manna, *Adv. Funct. Mater.*, 2024, **34**, 2403607.
10. H. Sarma, S. Mandal, **S. Kumar** and U. Manna, *Chem Comm.*, 2024, **60**, 13871.
11. H. Sarma, S. Mandal, A. Borbora, J. Das, **S. Kumar** and U. Manna, *Small*, 2024, **20**, 2309359.
12. C. Mishra, D. Sarkar, N. Barman, **S. Kumar**, M. Tenjimbayashi and U. Manna, *Adv. Mater.*, 2025, **37**, 2420342.
13. N. Barman, K. Jain, A. Borbora, **S. Kumar**, M. Tenjimbayashi and U. Manna, *Adv. Funct. Mater.*, 2025, e05295.

Patents

1. U. Manna, **S. Kumar**, M. Dhar "A waterborne, lubrication-free optically transparent solid slippery and superhydrophobic coating and method of production thereof" Indian Patent, Application No.: 202331008591 A, Date: February 09, 2023.

Conferences Attended

1. Poster presentation at **International Conference on Frontiers in Chemical Sciences 2022** (FICS - 2022) from 2nd to 4th December 2022, organized by IIT Guwahati, India.
2. Poster presentation at **Frontiers in Nano-Sciences 2024** (FINS 2024) from 1st - 2nd November, 2024, organized by IIT Guwahati, India.
3. Oral presentation at **International Conference on Innovation and Advances in Chemical Sciences** (IACS - 2025) from 24th to 25th January 2025, organized by Cotton University, India.